

Placing Limits on the Higgs Production Cross Section at the Tevatron using the $H \rightarrow W^+W^- \rightarrow \ell^+\ell^-$ Decay Channel

Toby Davies
Department of Physics and Astronomy
University of Glasgow

Thesis submitted in December 2008 for the degree of
Doctor of Philosophy
at the University of Glasgow

Abstract

Limits on the Higgs production cross section at the Tevatron were placed using data with an integrated luminosity of 2.4 fb^{-1} from CDF. Limits over a Higgs mass range between 110 GeV and 200 GeV were determined, by calculating a limit at ten mass points distributed over this region. The analysis exclusively searches for Higgs produced by top-quark mediated gluon fusion and then decaying into two W bosons. Only leptonic decay channels of the W are considered, such that the final event signature consists of ee , $e\mu$, or $\mu\mu$ with missing energy from undetected neutrinos.

After an evaluation of alternative techniques, a neural net was selected as the best method for increasing the sensitivity of the measurement. The BFGS neural net training technique was selected as the most efficient method.

A Bayesian Likelihood technique was used to place limits on the observed Higgs production cross section, and an expected limit was calculated by running 10,000 pseudo experiments.

The 160 GeV mass point was the most most sensitive, achieving an expected limit 4.1 times the Standard Model prediction cross section at a 95% Confidence Level. Observed limits are within 1σ of the expected limit below a mass point of

160 GeV. Above this, observed limits are higher than the expected limits, within 2σ . The lowest observed limit was also at $M_H=160$ GeV with a limit of 6.85 times the Standard Model prediction at a 95% Confidence Level.

A new method for increasing the sensitivity of the measurement was proposed and investigated, but unused in the analysis.

Acknowledgements

I would like to thank the both the University of Glasgow and Fermi National Laboratory for the use of their facilities, and the Science and Technology Facilities Council for the funding I have received.

I would like to thank my supervisors Peter Bussey and Richard St.Denis for their invaluable help and advice during my research, and for their encouragement.

I owe many thanks also to Aidan Robson for his aid, and Dean Hidas for his counselling. I would also like to thank Stan Thompson, Doug Benjamin, Mark Kruse, Paul Millar, Savario D'Aurio, Ken Strain, and Tom Junk for their support, and Sam Harper and Troy Vine for their role as coding mentors.

Lastly, I am indebted to my parents, brother, family and friends for their optimistic encouragement.

Declaration

All analysis in this dissertation was performed by the author unless indicated in the text, by reference or noted here. No original work by the author appears in the Theory or Experimental Equipment chapters. The author has written code for the selection of the events but these have since been modified. Actual processing of the datasets used in this dissertation along with the final estimation of all scale factors noted in the Event Selection chapter were performed by other parties as referenced apart from the fake rates and muon scale factors which were measured by Aidan Robson. Estimation of the ISR and fake error rates in the Systematic Uncertainties chapter were also performed by Aidan Robson. The thesis has not been submitted for another qualification to this or any other institution.

Toby Davies

Contents

1	Introduction	1
2	Theory	3
2.1	Yang-Mills model of the forces	4
2.2	Motivation For the Higgs Mechanism	7
2.3	Higgs Mechanism	8
2.4	The Standard Model	13
2.5	Higgs production and decay at the Tevatron	15
2.6	Backgrounds in the lepton and neutrino channel	19
2.7	Background Legend	20
2.8	Current limits from theory and searches	21
3	Experimental Equipment	28
3.1	Accelerator Chain	28
3.1.1	Cockroft Walton	30
3.1.2	Linear Accelerator	30
3.1.3	Booster	30
3.1.4	Main Injector	30

3.1.5	Antiproton Source	31
3.1.6	Tevatron	32
3.1.7	Recycler	32
3.2	Luminosity	32
3.3	Collider Detector at Fermilab	34
3.3.1	Co-ordinate system	34
3.3.2	Tracking and momentum measurement	35
3.3.3	Calorimeters	39
3.3.4	Muon Detection Systems	42
3.4	Trigger Systems	44
4	Event Selection	46
4.1	Variable definitions	48
4.2	Trigger requirements	54
4.3	Lepton Selection Cuts	55
4.3.1	Tight Central Electron (TCE)	56
4.3.2	Phoenix Electron (PHX)	56
4.3.3	CMUP muon	57
4.3.4	CMX muon	58
4.3.5	CMU muon	58
4.3.6	CMP muon	58
4.4	Jet Selection	58
4.5	Transverse Missing Energy	60
4.6	Run range selection	61
4.7	Data Samples	62

4.8	Monte Carlo Samples	62
4.8.1	Fakes	63
4.9	Trigger efficiencies and scale factors	66
4.10	Primary Vertex position efficiency	70
5	Sample Composition Checks	74
5.1	Z cross-section measurement	74
5.2	Z Mass measurement	78
5.3	W^+W^- background cross-section measurement	80
5.4	Fake background cross checks	84
6	Analysis Method Overview	86
6.1	Pre-analysis Cuts	87
6.2	Multivariate Techniques	89
6.3	Neural Nets	91
6.4	Input Variables	98
6.5	Method	100
6.6	Neural net output plots	105
6.7	Limit calculation using likelihood estimator	112
6.8	Neural Net improvement investigations	117
6.9	Method Summary	120
7	Systematic Uncertainties	121
7.1	Shape Errors	122
7.1.1	Jet Energy Scale	122
7.1.2	Lepton Energy Scale	123

7.1.3	Initial State Radiation	124
7.1.4	Parton Distribution Function	126
7.1.5	Fakes	127
7.2	Other Errors	128
7.2.1	Luminosity	128
7.2.2	Higgs $\rightarrow W^+W^-$ cross section @ NNLO	129
7.2.3	Drell Yan Neural Net Cut Efficiency	129
7.2.4	Lepton ID, reconstruction and trigger efficiencies	129
7.2.5	Generator	131
7.2.6	$W\gamma$ conversion error	131
7.2.7	Cross section	131
7.2.8	Next-to-leading-order acceptance	132
7.2.9	Summary	132
8	Measurement	135
8.1	Results	135
9	Conclusion	140
A	Acceptance Tables	153
B	Detailed Input plots	174
C	Detailed Input plots after the Drell Yan cut	181
D	Neural net training outputs	188
E	Likelihood Input Plots (linear)	192

F Likelihood Input Plots (log)

196

List of Figures

2.1	Higgs Lagrangian energy density	9
2.2	The standard model tree level Higgs couplings	15
2.3	Higgs production mechanisms at the Tevatron	16
2.4	Relative cross sections for Higgs production processes at the Tevatron ⁶	17
2.5	Branching ratios for Higgs decay at the Tevatron ²²	18
2.6	Background Legend	21
2.7	Theoretical limits on M_H	22
2.8	LEP2 limit from direct searches	23
2.9	Best fit for the Higgs mass at LEP2	24
2.10	Combined limits from CDF and D0	25
2.11	Combined limits from CDF and D0 in the high mass region	26
2.12	Limits from CDF in the $gg \rightarrow H \rightarrow W^+W^-$ channel	27
3.1	Fermilab accelerator chain	29
3.2	The CDF Detector	33
3.3	The SVX silicon detector	37
3.4	A schematic diagram of a Central Outer Tracker segment	37
3.5	A cross section of the CDF detector	40

3.6	CMX Arches	43
3.7	A schematic diagram of the CDF trigger system	43
5.1	Drell Yan mass peaks	77
5.2	Measured $\sigma_{q\bar{q}\rightarrow Z^*}BR(Z\rightarrow\ell\ell)$	79
5.3	Measured Z masses	81
5.4	$E_{unclustered}$	82
5.5	W^+W^- -cross checks	83
5.6	Same sign cross check	85
6.1	Jet energy and multiplicity plots	88
6.2	Comparison of multivariate technique strengths	92
6.3	Schematic diagram of a neural net architecture	93
6.4	The sigmoid function	94
6.5	Neural net training method comparisons	97
6.6	Neural net strength using de-correlated input variables	98
6.7	Plots of the input variables	101
6.8	Plots of the input variables	102
6.9	Background and Signal separation plots with Drell Yan as background	106
6.10	Background rejection vs. signal efficiency with Drell Yan as back- ground	107
6.11	Background and Signal separation plots with W^+W^- as background	108
6.12	Drell Yan neural net cut plots	109
6.13	Input variables plots with the Drell Yan neural cut applied	110
6.14	Input variables plots with the Drell Yan neural cut applied	111

6.15	Plots of the W^+W^- -trained neural net scores before and after the Drell Yan trained neural net has be cut upon	113
7.1	Jet energy systematic plots	123
7.2	Lepton energy systematic plots	124
7.3	Initial state radiation systematic plots	125
7.4	PDF systematic plots	127
7.5	Fakes systematic plots	128
8.1	Plots of the limits set by the pseudo experiments	137
8.2	Plots of the limits set by the pseudo experiments	138
8.3	Expected and observed limits on $gg \rightarrow H$	139
B.1	Input variable plots with ee	175
B.2	Input variable plots with ee	176
B.3	Input variable plots with $e\mu$	177
B.4	Input variable plots with $e\mu$	178
B.5	Input variable plots with $\mu\mu$	179
B.6	Input variable plots with $\mu\mu$	180
C.1	Input variable plots with ee after the cut on the Drell Yan neural net	182
C.2	Input variable plots with ee after the cut on the Drell Yan neural net	183
C.3	Input variable plots with $e\mu$ after the cut on the Drell Yan neural net	184
C.4	Input variable plots with $e\mu$ after the cut on the Drell Yan neural net	185
C.5	Input variable plots with $\mu\mu$ after the cut on the Drell Yan neural net	186
C.6	Input variable plots with $\mu\mu$ after the cut on the Drell Yan neural net	187
D.1	W^+W^- -neural net training plots at $M_H = 110$ GeV.	188

D.2	W^+W^- -neural net training plots at $M_H = 120, 130$ and 140 GeV. . .	189
D.3	W^+W^- -neural net training plots at $M_H = 150, 160$ and 170 GeV. . .	190
D.4	W^+W^- -neural net training plots at $M_H = 180, 190$ and 200 GeV. . .	191
E.1	Plots of the W^+W^- -trained neural net scores before and after the Drell Yan trained neural net has be cut upon	193
E.2	Plots of the W^+W^- -trained neural net scores before and after the Drell Yan trained neural net has be cut upon	194
E.3	Plots of the W^+W^- -trained neural net scores before and after the Drell Yan trained neural net has be cut upon	195
F.1	Plots of the W^+W^- -trained neural net scores before and after the Drell Yan trained neural net has be cut upon	197
F.2	Plots of the W^+W^- -trained neural net scores before and after the Drell Yan trained neural net has be cut upon	198
F.3	Plots of the W^+W^- -trained neural net scores before and after the Drell Yan trained neural net has be cut upon	199

List of Tables

2.1	Breakdown of the expected signal cross section calculation in the channel $\sigma(gg \rightarrow H \rightarrow W^*W) \cdot \text{BR}(W \rightarrow \ell_{e,\mu} + \nu)^{26}$	19
4.1	Values for the FidEle function	49
4.2	Triggers used and their associated lepton types	55
4.3	Selection cuts for TCE electrons	56
4.4	Selection cuts for phoenix electrons	57
4.5	Muon selection cuts	59
4.6	Run ranges of the various dilepton types	61
4.7	Data run ranges	62
4.8	Data samples used in the analysis. The trigger name is shown with the dataset ids, and number of events.	63
4.9	$gg \rightarrow H \rightarrow WW$ Monte Carlo samples. The $\sigma \cdot \text{Br}$ is taken from a recent report??.	64
4.10	Background Monte Carlo samples used in the analysis. All are generated with Pythia 6.2. Factors marked with an asterisk are filter factors but have been included here for brevity.	65
4.11	Cuts for the fakeable object denominator	67

4.12 Fake Rates	68
4.13 Trigger efficiencies used in the analysis	71
4.14 Electron scale factors	71
4.15 Muon reconstruction scale factors	72
4.16 Muon ID scale factors	73
5.1 Drell Yan cross sections	78
5.2 Measured Z masses for the different same-type di-lepton combina- tions. Only statistical error are displayed	80
5.3 Cuts for the WW normalisation cross check	82
6.1 Cuts placed on the input variables before the multivariate analysis .	87
6.2 Multivariate analyses available and investigated with TMVA	89
6.3 Cuts placed on the input variables before the multivariate analysis .	96
6.4 Input variables used in the multivariate analysis.	100
6.5 Events passing Drell Yan neural net cuts. Statistical and systematic errors are displayed.	112
7.1 Average errors on the yield from varying the jet energy scale	122
7.2 Average errors on the yield from varying the lepton energy scale . .	124
7.3 Average errors on the yield from varying the ISR parameters	125
7.4 Average errors on the yield from varying the PDF parameters . . .	127
7.5 Average errors on the yield from varying the Fake parameters . . .	128

7.6	Evaluation of the Drell Yan neural net cut error is evaluated by varying the ee cut around the analysis cut value of 0.993. The ee channel is chosen because it shows the largest differences between data and Monte Carlo. The largest ratio between the data and Monte Carlo acceptances is found at a cut value of 0.991, and is 20%	130
7.7	Average errors from uncertainties in lepton scale factors, trigger efficiencies and reconstruction	130
7.8	Summary of average systematic errors on the yield used in the analysis	133
7.9	Expected limits to 95% C.L. on $\sigma_{gg \rightarrow H} \cdot BR(H \rightarrow W^+W^- \rightarrow \ell\ell)$ with statistical errors and only one systematic error applied. The results are expressed in pb, and $M_H = 160$ GeV	134
7.10	Expected limits to 95% C.L. on $\sigma_{gg \rightarrow H} \cdot BR(H \rightarrow W^+W^- \rightarrow \ell\ell)$ with statistical errors and only one systematic error applied. The results are expressed as a fraction of the theoretical $\sigma_{gg \rightarrow H}$, and $M_H = 160$ GeV	134
8.1	Measured observed and expected limits to 95% C.L. on $\sigma_{gg \rightarrow H} \cdot BR(H \rightarrow W^+W^- \rightarrow \ell\ell)$ expressed in pb	136
8.2	Measured observed and expected limits to 95% C.L. on $\sigma_{gg \rightarrow H}$ expressed as a fraction of the theoretical $\sigma_{gg \rightarrow H}$	136
8.3	Measured observed and expected limits to 95% C.L. on $\sigma_{gg \rightarrow H} \cdot BR(H \rightarrow W^+W^- \rightarrow \ell\ell)$ expressed in pb at $M_H = 160$ GeV and split into channels	136

8.4	Measured observed and expected limits to 95% C.L. on $\sigma_{gg \rightarrow H}$ expressed as a fraction of the theoretical $\sigma_{gg \rightarrow H}$ at $M_H = 160$ GeV and split into channels	137
A.1	$Z \rightarrow \mu^- \mu^+$ acceptances	154
A.2	$Z \rightarrow e^- e^+$ acceptances	155
A.3	$W^\pm Z^0$ acceptances	156
A.4	fake acceptances	157
A.5	data acceptances	158
A.6	$Z \rightarrow \tau^- \tau^+$ acceptances	159
A.7	$W^+ W^-$ acceptances	160
A.8	$Z^0 Z^0$ acceptances	161
A.9	$t\bar{t}$ acceptances	162
A.10	$W\gamma$ acceptances	163
A.11	$gg \rightarrow H \rightarrow W^+ W^-$ acceptances, assuming $M_H^{\text{SM}} = 110$ GeV	164
A.12	$gg \rightarrow H \rightarrow W^+ W^-$ acceptances, assuming $M_H^{\text{SM}} = 120$ GeV	165
A.13	$gg \rightarrow H \rightarrow W^+ W^-$ acceptances, assuming $M_H^{\text{SM}} = 130$ GeV	166
A.14	$gg \rightarrow H \rightarrow W^+ W^-$ acceptances, assuming $M_H^{\text{SM}} = 140$ GeV	167
A.15	$gg \rightarrow H \rightarrow W^+ W^-$ acceptances, assuming $M_H^{\text{SM}} = 150$ GeV	168
A.16	$gg \rightarrow H \rightarrow W^+ W^-$ acceptances, assuming $M_H^{\text{SM}} = 160$ GeV	169
A.17	$gg \rightarrow H \rightarrow W^+ W^-$ acceptances, assuming $M_H^{\text{SM}} = 170$ GeV	170
A.18	$gg \rightarrow H \rightarrow W^+ W^-$ acceptances, assuming $M_H^{\text{SM}} = 180$ GeV	171
A.19	$gg \rightarrow H \rightarrow W^+ W^-$ acceptances, assuming $M_H^{\text{SM}} = 190$ GeV	172
A.20	$gg \rightarrow H \rightarrow W^+ W^-$ acceptances, assuming $M_H^{\text{SM}} = 200$ GeV	173

Chapter 1

Introduction

The Higgs boson is the last unobserved particle in the Standard Model of particle physics, and therefore its discovery is of high importance to the physics community. It is necessary for giving mass to the W and Z weak bosons via the Higgs mechanism, independently proposed by Englert and Brout in 1964²⁷, and also Higgs in October of the same year⁵⁸. The Higgs also allows these terms to be renormalisable, cancels inconvenient terms in the gauge bosons' self energy corrections. In 1973, the Z boson was observed and the agreement with the predicted relationship between the W and Z masses confirmed the surrounding electroweak unification system in which the Higgs field plays a central role. The presence of the Higgs field itself presents subtle inadequacies in Quantum Field Theory (QFT) such as the Hierarchy Problem, which has in part led to variations of the standard model being proposed such as Supersymmetry. However, many of these extensions employ the Higgs mechanism to bring about the electroweak symmetry breaking, and so include within them a Higgs-like field which has similar properties to a Standard Model Higgs. Thus, a search for the Higgs is important in order to verify the

understood electroweak symmetry breaking in many particle theories.

The theoretical prediction for the $gg \rightarrow H$ cross section indicates that observation of direct evidence of the Higgs will be unlikely at the luminosities presently available at the Tevatron collider, but an analysis placing continually more stringent limits on the cross section is important for testing and progressively refining advanced recognition techniques. Direct Higgs production via gluon fusion and subsequent decay to W bosons provides the most promising channel for finding a high mass Higgs at the Tevatron.

This dissertation places a limit on the $gg \rightarrow H$ cross section using 2.4 fb^{-1} integrated luminosity of $p\bar{p}$ collisions at the Tevatron with $\sqrt{s} = 1.96 \text{ TeV}$ taken between the years of 2002-2007. It uses neural nets to improve the limit by discriminating the Higgs signal more strongly than a cut based analysis.

Chapter 2

Theory

In the first half of the 20th century, particle theory made the great leap from a deterministic theory of point-like particles to a field theory where forces and matter are described by quantum disturbances in fields. The formalism has progressed through ‘first quantisation’, where particle properties are found by applying operators to the fields, to ‘second quantisation’ where the fields themselves are represented by operators which act upon the vacuum state to create (and destroy) states that correspond to particles.

In ‘canonical quantisation’, the ‘Hamiltonian’ describes an overall energy density function for the system and is defined in terms of the fields. Perturbation theory then applies this to states to describe their development in time. The Hamiltonian may undergo a co-ordinate transformation into the ‘Lagrangian’; minimising this integrated over all space-time (the action) dictates the physical development of the system. In a later formalism known as ‘path integration’, the action is integrated over many possible particle paths to calculate real quantities; therefore, defining the Lagrangian effectively defines the particle system that describes

reality, and consequently the present chapter will mostly work at that level.

As new forces were discovered throughout the 20th century, they were added into the Lagrangian in an ad-hoc fashion until in 1954 Yang and Mills recognised that the forces' forms within the Lagrangian could be generated by requiring that it remained invariant under local transformations⁴. Group theory can be used to describe and relate the transformations; the different sets of transformations over which the Lagrangian remains symmetrical (named 'groups') generate the different forces seen in reality.

2.1 Yang-Mills model of the forces

Yang and Mills found that forces in Quantum Field Theory^{61,71} could be modelled by requiring the Lagrangian to remain invariant under a local gauge transformation. A rotation transformation in an arbitrary space ($U(x)$) can be expressed as a complex exponential:

$$U(x) = e^{(-iG^a\theta^a(x))} \approx 1 - iG^a\theta^a(x) \quad (2.1)$$

Here, G describes the 'generators' of the rotation which are a set of rotation matrices, and the components of theta vector give the magnitude of the rotation in the corresponding direction. This a 'local' transformation as the rotation depends on the space-time position, x . As the exponential is Taylor expanded, the higher terms can be dropped in the case of an infinitesimally small transformation. The transformation can then be applied to a Lagrangian. In a Lagrangian containing a massless fermionic field, the kinetic energy enters as prescribed by the Dirac

equation:

$$\mathcal{L}_{\text{fermionic}} = \bar{\psi} i \gamma^\mu \partial_\mu \psi \quad (2.2)$$

The Lagrangian is transformed on a local basis by applying the transform to the fields, ψ . However, the transformation itself is dependent on space-time and so is acted on by the differential with respect to space-time; the result is an extra term involving the differential of the transform. To ensure invariance, the differential is replaced by a ‘covariant’ differential, which includes in it a new field, A :

$$D_\mu \equiv \left(\partial_\mu - ig G^a A_\mu^a \right) \quad (2.3)$$

This ensures invariance of the Lagrangian simply by forcing the transformation rule of A to explicitly remove the differential of the transform as it itself transforms:

$$G^a A_\mu^a \rightarrow G^a A'^a_\mu = U(x) G^a A_\mu^a U(x)^{-1} - \frac{i}{g} (\partial_\mu U(x)) U(x)^{-1} \quad (2.4)$$

The field A will accurately describe different fundamental forces depending upon the group to which the generators belong. A field strength term is also included in the Lagrangian to describe the observed free fields of the forces:

$$F_{\mu\nu}^a = \partial_\mu A_\nu^a - \partial_\nu A_\mu^a + g \varepsilon^{abc} A_\mu^b A_\nu^c \quad (2.5)$$

it is introduced into the Lagrangian squared, such that it is Lorentz invariant. To retain renormalisability, any cross terms describing the kinetic energy and self-interaction of the force field are of less than the fourth power. A simple model including only a $U(1)$ symmetry quickly describes the electromagnetic force as

the result of the requirement that the Lagrangian remain invariant under a local complex phase transformation:

$$\mathcal{L}_{\text{EM}} = -\frac{1}{4}G_{\nu\mu}G^{\mu\nu} + \bar{\psi}i\gamma^\mu D_\mu\psi \quad (2.6)$$

for a $U(1)$ symmetry, the generators are Abelian scalars such that they commute, and the electromagnetic covariant derivative:

$$D_\mu \equiv (\partial_\mu - ieB_\mu) \quad (2.7)$$

expands the kinetic fermionic portion of the Lagrangian to give the classical interaction energy of the the fermion with the electromagnetic field, B . In addition, the field strength term for the free field only contributes kinetic terms, and the self-interaction terms which correspond to mass are (correctly) missing for the photon. To include the weak force, an $SU(2)$ symmetry is added by simply including the appropriate field in the covariant derivative:

$$D_\mu \equiv \left(\partial_\mu - ig\frac{\tau^a}{2}A_\mu^a - i\frac{g'}{2}B_\mu \right) \quad (2.8)$$

and including the appropriate field strength term in the Lagrangian:

$$\mathcal{L}_{\text{EW}} = -\frac{1}{4}F_{\nu\mu}^a F^{a\mu\nu} - \frac{1}{4}G_{\mu\nu}G^{\mu\nu} + \bar{\psi}i\gamma^\mu D_\mu\psi \quad (2.9)$$

This system is now said to possess a $SU(2) \times U(1)$ symmetry, afforded by its invariance under both local transformations.

2.2 Motivation For the Higgs Mechanism

Experimentally, the weak force is shown to correspond to massive free field particles, the W and Z bosons, but expanding Eqn. 2.9 will yield no squared terms of the weak field which would signify mass. Solutions to this problem originated in the BCS theory of superconductivity, where electron condensation into Cooper pairs causes the photons to acquire an effective mass. Building on this idea, Higgs introduced a scalar field with a non-zero vacuum expectation value in an analogy to the Bose-Einstein condensate of Cooper pairs. As a consequence, mass terms for force bosons are generated and the symmetry that the force had mediated is broken. This was later applied to an $SU_L(2) \times U_Y(1)$ electroweak symmetry by Glashow, Weinberg and Salam to describe experimental findings accurately, and has become the standard solution to the massive weak boson problem. As a simple solution, it is not without problems. Its requirement for an extra unseen field has been considered unnatural, so alternatives involving condensations of fermions to replace the Higgs field have been proposed, inspired by BCS superconductivity. Topcolor depends on a condensation of top quarks and has yet to be verified; Technicolor introduces new families of techniquarks which condense into symmetry breaking technipions, but disagreement with precision measurements have ruled out simpler technicolor models. The simplest Higgs Mechanism also suffers from the Hierarchy Problem, where radiative loop corrections to the self-energy of the Higgs are large and the parameters of the theory need to be continually fine-tuned at each perturbative iteration in order to keep them well behaved. This unnaturalness has inspired extensions to the standard model, notably Supersymmetry, which solves this problem by introducing counter-corrections to the self energy. In

many of the supersymmetric theories, a Higgs boson with the same characteristics as a standard model Higgs boson can be found.

2.3 Higgs Mechanism

The Higgs Mechanism introduces the Higgs field, a scalar field ϕ' that has kinetic energy and mass, and can self-interact:

$$\mathcal{L}_\phi = (D_\mu \phi')^\dagger (D^\mu \phi') - \frac{\mu^2}{2!} (\phi'^\dagger \phi') - \frac{\lambda}{4!} (\phi'^\dagger \phi')^2 \quad (2.10)$$

It appears with a prime here to avoid confusion later. To induce the symmetry breaking, the field's mass term is allowed to become positive.

In the lowest energy state where \mathcal{L} is minimised, the field has a constant magnitude v in any phase direction. All phase directions are equivalent, but the field must choose one of them to minimise its energy, which breaks the symmetry. The value the field takes is known as the Higgs field's vacuum expectation value: in the lowest energy states, the field will have that amplitude:

$$\langle 0 | \phi' | 0 \rangle = \langle \phi' \rangle = v \quad (2.11)$$

To make the equations clearer, the field is split into two components, the vacuum expectation value v (v.e.v.) and a shifted field, which from now on will now be referred to as the Higgs field:

$$\phi' = \phi + v \quad (2.12)$$

In the Higgs mechanism, the Higgs is represented by a doublet, comprising two

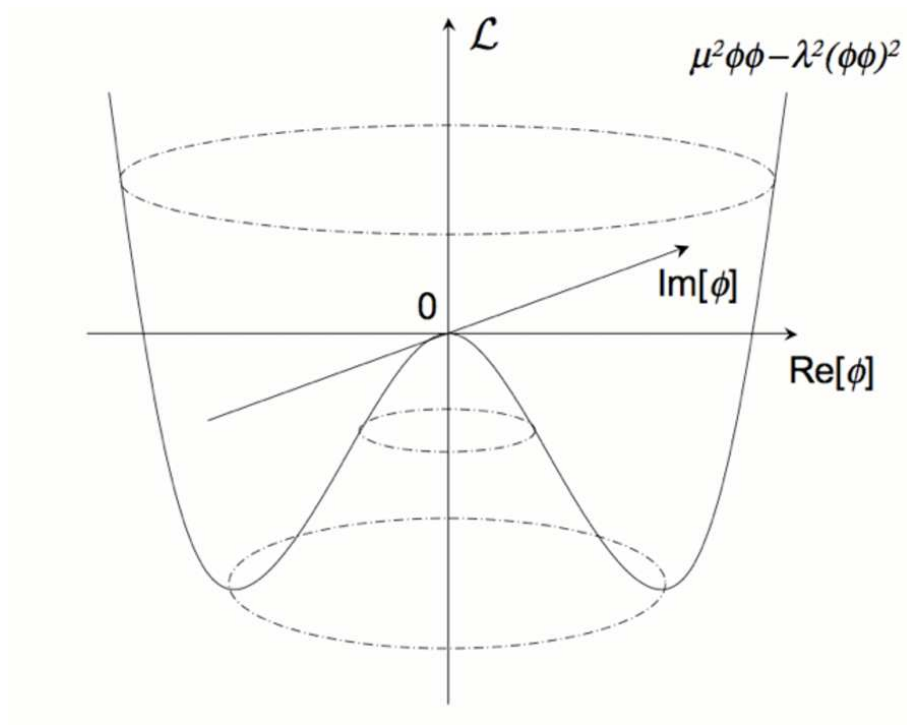


Figure 2.1: This plots the Lagrangian energy density in terms of the real and imaginary components of a singlet Higgs field with imaginary mass. The minimum is not at $\phi=0$, but occurs at a ring, $|\phi| = v$. Any choice of minimum is acceptable, but only one can be chosen, breaking the symmetry. This is known as the ‘Mexican hat’ plot.

complex fields, each of which can be separated into its imaginary and real components:

$$H = \begin{pmatrix} \xi'^2(x) + i\xi'^1(x) \\ \eta'(x) + i\xi'^3(x) \end{pmatrix} \quad (2.13)$$

The real component of the lower field has been singled out, as this is where the v.e.v. is chosen to occur (in the current $SU(2) \times U(1)$ -symmetrical Lagrangian, all directions are equivalent) resulting in a shifted field:

$$H = \begin{pmatrix} \xi'^2 + i\xi'^1 \\ \eta' + i\xi'^3 \end{pmatrix} \rightarrow H = \begin{pmatrix} \xi^2 + i\xi^1 \\ \eta + v + i\xi^3 \end{pmatrix} \quad (2.14)$$

The interaction of the force fields within the partial differential with the shifted Higgs field now yield normal interactions of the shifted Higgs field with the force fields, but the extra v term now expands with the force fields \mathbf{A} and B to produce quadratic field cross terms:

$$\begin{aligned} \mathcal{L}_{H_{K.E}} &= (D_\mu H)^\dagger (D^\mu H) = v^2 \left(\left(\frac{g}{2} \boldsymbol{\tau} \cdot \mathbf{A}_\mu + \frac{g'}{2} B_\mu \right) \begin{pmatrix} 0 \\ 1 \end{pmatrix} \right)^\dagger \left(\left(\frac{g}{2} \boldsymbol{\tau} \cdot \mathbf{A}^\mu + \frac{g'}{2} B^\mu \right) \begin{pmatrix} 0 \\ 1 \end{pmatrix} \right) \\ &= \frac{v^2}{4} \left\{ g^2 [(A^1)^2 + (A^2)^2] + (gA^3 - g'B)^2 \right\} \\ &= \frac{v^2}{4} \left\{ g^2 [(A^1)^2 + (A^2)^2] + \begin{pmatrix} A^3 & B \end{pmatrix} \begin{pmatrix} g^2 & gg' \\ gg' & g'^2 \end{pmatrix} \begin{pmatrix} A^3 \\ B \end{pmatrix} \right\} \end{aligned} \quad (2.15)$$

(Only the v component of the Higgs doublet has been expanded here.) So far, this equation has terms which mix the third component of the weak field and the electromagnetic field, B ; the mixing matrix can be diagonalised by explicitly mixing A^3 and B :

$$\begin{pmatrix} Z \\ A \end{pmatrix} = \begin{pmatrix} \cos \theta_W & \sin \theta_W \\ -\sin \theta_W & \cos \theta_W \end{pmatrix} \begin{pmatrix} A^3 \\ B \end{pmatrix}; \quad (2.16)$$

where θ_W is the weak mixing angle defined as:

$$\tan \theta_W = \frac{g'}{g} \quad (2.17)$$

The first two components of the weak field are also mixed to be complex conjugates of each other, which represent the observed oppositely charged W particles:

$$W^\pm = (A_\mu^1 \mp iA_\mu^2) \quad (2.18)$$

The resultant Lagrangian now contains a mass term for the charged weak W pair, a mass term for the weak neutral Z boson, and a massless field A corresponding to the photon:

$$\begin{aligned} \mathcal{L}_{H_{K.E}} &= \frac{v^2}{4} \left\{ g^2 (A_\mu^1 + iA_\mu^2) (A_\mu^1 - iA_\mu^2) + \begin{pmatrix} Z & A \end{pmatrix} \begin{pmatrix} g^2 + g'^2 & 0 \\ 0 & 0 \end{pmatrix} \begin{pmatrix} Z \\ A \end{pmatrix} \right\} \\ &= \frac{v^2}{4} \left\{ g^2 W_\mu^+ W^{-\mu} + (g^2 + g'^2) Z_\mu Z^\mu \right\} = \frac{M_W^2}{2} W_\mu^+ W^{-\mu} + \frac{M_Z^2}{2} Z_\mu Z^\mu \end{aligned} \quad (2.19)$$

where:

$$M_W^2 = \frac{v^2 g^2}{2}; \quad M_Z^2 = \frac{v^2 (g^2 + g'^2)}{2} \quad (2.20)$$

The system is not yet free of the three massless ξ fields which accompanied the η component of the Higgs field, and are unobserved. These correspond to particles known as Goldstone bosons and are predicted to occur whenever symmetry breaking occurs according to the Goldstone theorem. However, such particles are not observed in practice, so to remove these, an $SU(2)$ transformation can be made which directly complements these fields and leaves the Lagrangian invariant due to the inclusion of the $SU(2)$ weak fields in the covariant derivative:

$$U(x)H = e^{\left(-i\frac{\tau^a \xi^a}{v}\right)} \begin{pmatrix} \xi^2 + i\xi^1 \\ \eta + v + i\xi^3 \end{pmatrix} = e^{\left(-i\frac{\tau^a \xi^a}{v}\right)} e^{\left(i\frac{\tau^a \xi^a}{v}\right)} \begin{pmatrix} 0 \\ \eta + v \end{pmatrix} = \begin{pmatrix} 0 \\ \eta + v \end{pmatrix} \quad (2.21)$$

The Goldstone bosons are said to be ‘eaten’ by the weak bosons. In doing this, the Lagrangian loses its $SU(2)$ invariance, a specific transformation has had to be picked and any further transformation would result in the appearance of the Goldstone bosons once again. This is an example of gauge fixing in which a symmetry is broken by choosing a specific $SU(2)$ rotation to remove the unphysical Goldstone bosons. The end result is that the fields of the electromagnetic and the weak forces have been mixed, resulting in three weak fields gaining mass, and the fourth electromagnetic field remaining massless; this is therefore known as electroweak symmetry breaking, and is schematically denoted $SU_L(2) \times U_Y(1) \rightarrow U(1)$. The η component of the Higgs doublet gains real mass, however, as the v.e.v. in the self-interaction term of the Lagrangian creates squared terms to counteract the negative mass squared value of the original Higgs field:

$$\begin{aligned} \mathcal{L}_H &= (D_\mu H)^\dagger (D^\mu H) - \frac{\mu^2}{2!} (H^\dagger H) - \frac{\lambda}{4!} (H^\dagger H)^2 \\ &= (D_\mu \eta)^\dagger (D^\mu \eta) - \frac{\mu^2}{2!} (\eta + v)^2 - \frac{\lambda}{4!} (\eta + v)^4 \end{aligned} \quad (2.22)$$

The electromagnetic charge is now a combination of the $SU(2)$ and $U(1)$ charges:

$$Q = \frac{Y}{2} + T_3 \quad (2.23)$$

where Y is the weak hypercharge and T_3 is the third component of weak isospin, defined as the commutator of the raising and lowering isospin operators. The

Higgs field is also responsible for giving the fermions mass, since a simple Yukawa coupling will give rise to quadratics in the fermion field:

$$\mathcal{L}_{Yukawa} = \lambda \bar{\psi} H \psi; \quad (2.24)$$

with:

$$m_\psi = \lambda v \quad (2.25)$$

2.4 The Standard Model

The Standard Model (SM) is built out of the electroweak theory by adding the strong force and the fermion families. The strong force arises from an $SU_C(3)$ gauge invariance in color added in the same way as the weak force, by adding an interaction field term to the covariant derivative, and the corresponding field strength term into the Lagrangian. The mediating bosons of the strong force, the gluons, are found to be massless, so this symmetry remains unbroken. Schematically, this written: $SU(3) \times SU(2) \times U(1) \rightarrow SU(3) \times U(1)$. Families of fermions are also added, such that the standard model now comprises distinct sectors and the Lagrangian can be written:

$$\mathcal{L}_{SM} = \mathcal{L}_{FORCES} + \mathcal{L}_{HIGGS} + \mathcal{L}_{FERMIONS} \quad (2.26)$$

where:

$$\mathcal{L}_{FORCES} = \mathcal{L}_S + \mathcal{L}_W + \mathcal{L}_{EM} = -\frac{1}{4}S_{\nu\mu}^a S^{a\mu\nu} - \frac{1}{4}F_{\nu\mu}^a F^{a\mu\nu} - \frac{1}{4}G_{\mu\nu} G^{\mu\nu} \quad (2.27)$$

The fermions are separated into quarks and leptons; for each there are three families. In each family there exists two particles but due to the non-observation of right-helicity neutrinos, the left- and the right-handed helicity particles are separated, and only the left-helicity particles are grouped together in a doublet per family. Recently, neutrinos have been found to have non-zero mass which would allow them to be boosted into right handed neutrinos, but this is not covered here as it requires an extension to the Standard Model. The right-handed fermions exist in the Standard Model only as singlet fields.

$$\begin{pmatrix} v_e \\ e^- \end{pmatrix}_L ; \begin{pmatrix} v_\mu \\ \mu^- \end{pmatrix}_L ; \begin{pmatrix} v_\tau \\ \tau^- \end{pmatrix}_L ; e_R^- ; \mu_R^- ; \tau_R^- ; \quad (2.28)$$

$$\begin{pmatrix} u \\ d \end{pmatrix}_L ; \begin{pmatrix} c \\ s \end{pmatrix}_L ; \begin{pmatrix} t \\ b \end{pmatrix}_L ; u_R ; d_R ; c_R ; s_R ; t_R ; b_R ;$$

In Eqn. 2.28, the top row are leptons which are significantly lighter than the fermions on the second row, the quarks. The upper component fields in the lepton doublets are neutrinos with very small mass; they have no right-handed singlet counterpart, and interact only through weak interactions. The partners to the neutrinos have both electromagnetic and weak charges and can interact with both of these fields. Quarks on the bottom row also have a strong colour charge, and so interact with all three forces. The Lagrangian for each family now follows the same pattern, comprising of a kinetic energy term (in which the covariant derivative provides the interaction terms with the fermions), and a mass term provided by the Yukawa coupling the Higgs to the fermion.

$$\mathcal{L}_{FERMIONS} = \mathcal{L}_{K.E} + \mathcal{L}_{Yukawa} = +\lambda (\bar{L}HR + \bar{R}H^\dagger L) \quad (2.29)$$

2.5 Higgs production and decay at the Tevatron

The tree level interactions with other SM particles can be read off by replacing each v.e.v, one at a time, in Eqn. 2.15 and Eqn. 2.24 with the real Higgs η field, giving couplings seen in Fig. 2.2.

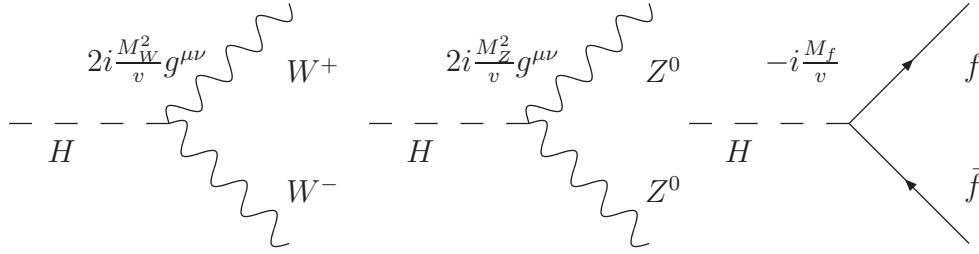


Figure 2.2: The standard model tree level Higgs couplings to the weak bosons and fermions⁷¹

There is also a quartic self-interaction term. Of importance is that the Higgs coupling in these situations is always proportional to the coupling particle's mass in the case of the fermions, and proportional to the coupling particle's mass squared in the case of the weak bosons. This makes the Higgs' couplings to the weak bosons significantly stronger. The Higgs does not directly couple to the gluon or the photon, but this coupling is possible at the one-loop level by including a quark loop. All quarks are involved in the loop, but to first order only the top quark is considered because its high mass ensures it's coupling with the Higgs dominates the other couplings. Protons and anti-protons at the Tevatron contain very small quantities of heavy quarks; however, much of their momentum is occupied in a gluon cloud such that the largest overall Higgs production cross section is the result of top-loop mediated gluon fusion despite there being no tree level coupling of the Higgs to gluons³³. The next largest contributions to production come from

associated production along with a weak boson, or W boson fusion; diagrams for these processes are shown in Fig. 2.3.

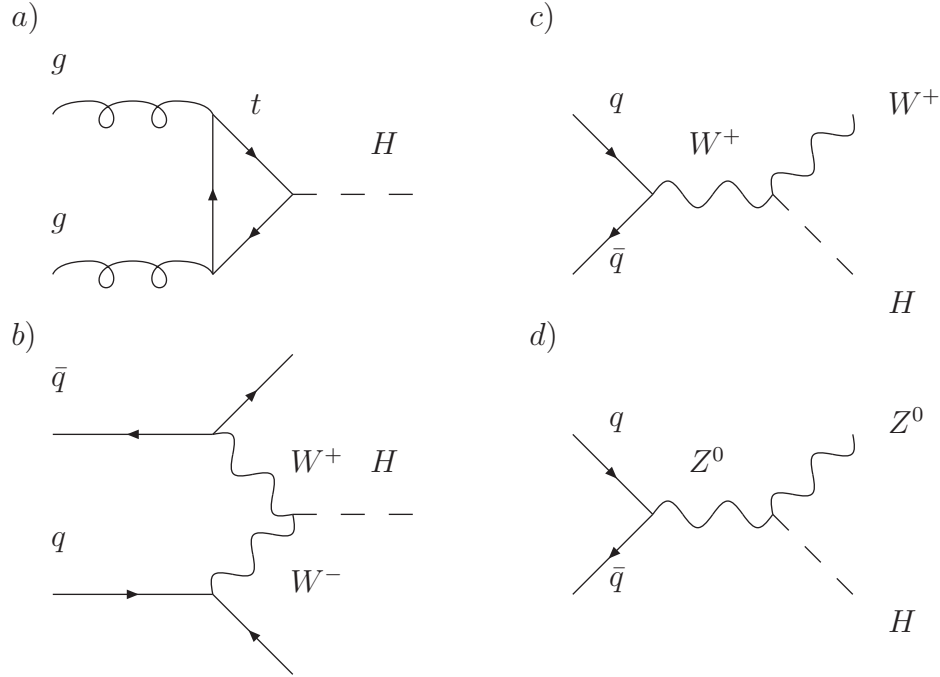


Figure 2.3: Higgs production mechanisms at the Tevatron: a) quark-mediated gluon fusion; b) W boson fusion; c) associated production with a W ; d) associated production with a Z

At the Tevatron the first of these, gluon fusion, is approximately an order of magnitude greater than the other processes (see Fig. 2.4), so for this investigation this is the only production mechanism considered. In the lepton channel described presently, W boson fusion has the next largest contribution, being about 5% of the total Higgs signal in events containing two additional jets.

Additionally, NNLO corrections to the gluon fusion are significant due to the large strong couplings involved with the quark loop, with a correcting factor (a ‘ k ’-factor) of approximately 1.4.¹³ Decay branching ratios can be seen in Fig. 2.5;

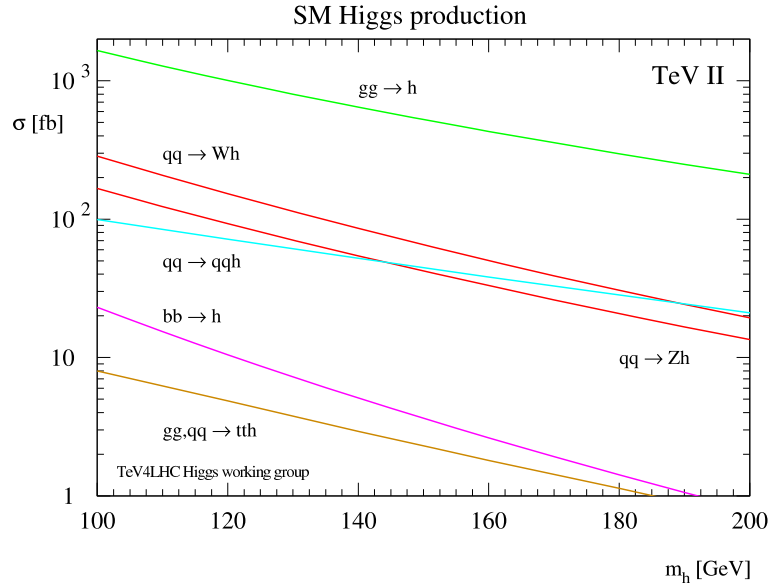
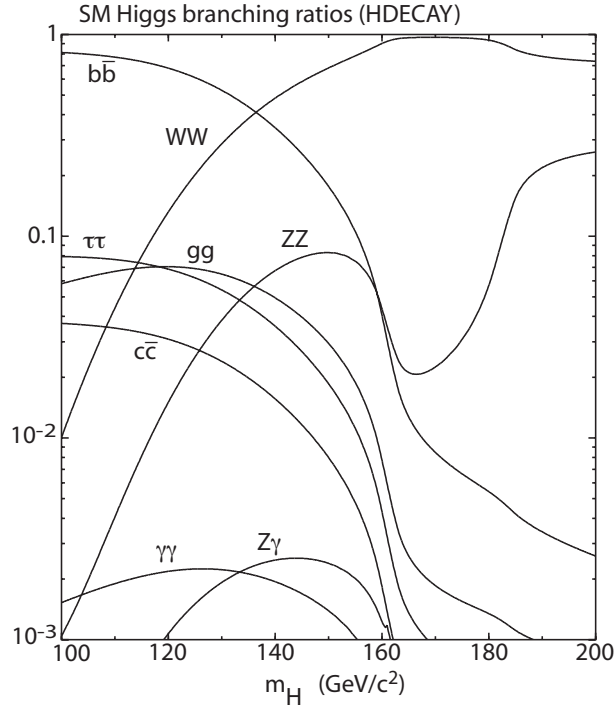


Figure 2.4: Relative cross sections for Higgs production processes at the Tevatron⁶

for a Higgs mass greater than 135 GeV, the dominant decay is to W^*W , which becomes maximal as both W s become on shell in the region of $M_H=160\text{GeV}$. This analysis will concentrate on this decay mode. Above a mass of $M_H=180\text{GeV}$, the Higgs decay into two Z s becomes resonant which reduces the branching ratio into W s.

The W boson decays to a lepton and a neutrino 32.4% of the time and to a quark pair, which are seen as jets, 67.6% of the time. Despite there being a much larger branching ratio to jets, the lepton channels are far cleaner in terms of standard model backgrounds, and so the channel where both W bosons decay to leptons is chosen. The spin 0 of the SM Higgs forces the two oppositely charged W bosons to have opposite spin. As they decay to neutrinos, the ‘V-A’⁵⁰ architecture of the standard model strongly encourages the neutrinos to be emitted in the same direction, as dictated by their helicity⁶⁹. This makes the fully leptonic decay mode even more attractive as a search channel, because the angle between the

Figure 2.5: Branching ratios for Higgs decay at the Tevatron²²

heavy leptons are smaller for this Higgs decay allowing it to be identified more easily. Both the electrons and muons from these decays are easily detected at CDF, but the τ will decay quickly in either a hadronic mode or a leptonic mode. To keep the selection signature consistent only the leptonic decay modes of the τ are considered, which are 35.1% of the τ decay ratio. The total branching ratio of $W^+W^- \rightarrow (\mu\mu, ee, e\mu)$ is $((0.1125 * 0.351) + 0.2132)^2 = 0.064$. A summary of the total cross sections for the $(gg \rightarrow H \rightarrow W^+W^-) \cdot \text{BR}(W^+W^- \rightarrow (\mu\mu, ee, e\mu))$ can be found in Table 2.1.

Higgs Mass (GeV/ c^2)	$\sigma_{gg \rightarrow H}$ (fb)	$\text{Br}(H \rightarrow W^*W)$	$\sigma_{gg \rightarrow H} \cdot \text{Br}(H \rightarrow W^*W)$ (fb)	$\sigma_{gg \rightarrow H} \cdot \text{Br}(H \rightarrow W^*W \rightarrow \ell_{e,\mu} + \nu)$ (fb)
110	1281	0.044	56.4	3.61
120	1006	0.132	133	8.50
130	801	0.287	230	14.7
140	646	0.483	312	20.0
150	525	0.682	358	22.9
160	431	0.901	388	24.9
170	357	0.965	345	22.0
180	297	0.935	278	17.8
190	249	0.776	193	12.4
200	211	0.735	155	9.93

Table 2.1: Breakdown of the expected signal cross section calculation in the channel $\sigma(gg \rightarrow H \rightarrow W^*W) \cdot \text{Br}(W \rightarrow \ell_{e,\mu} + \nu)^{26}$

2.6 Backgrounds in the lepton and neutrino channel

- Drell Yan, $Z/\gamma^* \rightarrow ee, \mu\mu$: this is the largest background in cross section ($\sigma_{DY}=251$ pb), but also the most easily removed. Leptons originating from a Z will be emitted mostly in near-opposite directions to conserve momentum; their combined mass give a very clear peak at the Z mass of 91 GeV/ c^2 ; and the events will contain low amounts of missing energy. They also do not contribute at all to the $e\mu$ decay channel.
- Drell Yan, $Z/\gamma^* \rightarrow \tau\tau$: this is a more problematic background due to its high cross section with no clear Z peak in $M_{\ell\ell}$; also, the decay of the τ to neutrinos will create missing energy and may close the angle between the resulting leptons.
- W^+W^- : Once Drell Yan has been removed, this is the largest and most problematic background due to the strong similarity to the Higgs decay mode and its large relative cross-section ($\sigma_{WW}=130$ fb). The strongest discriminator is

$\phi_{\ell\ell}$ because the spins of the W bosons are not correlated in the background.

- $W + \gamma$: gives rise to dilepton events when the gamma converts to two electrons; these can give the same signal as a lepton in the detector, and be associated with a track by accident. A rejection of same-sign lepton pairs will reduce the background by half because there is a 50% chance that the track that was mistakenly matched will be of the wrong sign.
- Fake: This is any class of event where a jet may fake a lepton. Mainly, these will arise from W +jet events, and again, rejection on the basis of same-sign will reduce the background by half. Its cross-section is estimated by Monte Carlo at $\sigma_{W+fake}=18$ fb, but in the analysis the cross-section uncertainty will be solved by taking the sample directly from data.
- $t\bar{t}$ Each top emits a W and a b quark. The event will contain jets from the b quarks so jet measurement and multiplicities are an important discriminator. The cross-section for this process is $\sigma_{t\bar{t}}=13$ fb.
- WZ, ZZ : these have low total cross-section times branching ratio into leptons ($\sigma_{WZ}^{tot}=4.4$ fb & $\sigma_{ZZ}^{tot}=2.4$ fb) and create dilepton events when a lepton is not detected in WZ , or when one Z decays to neutrinos in ZZ . When both leptons come from a Z , a peak in $M_{\ell\ell}$ will easily differentiate the event, so most background will arise from WZ where a lepton from the Z is lost.

2.7 Background Legend

Due to the large number of significant backgrounds used in the analysis, the legend often interferes with the plots. Therefore, one legend is displayed here and not on

the plots, and will be used throughout.



Figure 2.6: Legend for the plots showing the colour key for the backgrounds used throughout this document in all the plots

Systematic errors found in chapter 7 are displayed on the plots as a hatched region, with the blue hatch representing the shape systematic errors added in quadrature, and the grey hatch representing all errors added in quadrature.

2.8 Current limits from theory and searches

An upper and lower theoretical limit on the mass of the Higgs boson can be placed by requiring the Higgs to satisfy unitary constraints at high mass, and requiring the vacuum to be stable at low masses.^{6,54,73} The limits can be seen in Fig. 2.7 and are given in terms of Λ , the energy scale at which the Standard Model breaks down. They are calculated with a top quark mass of $M_t=175$ GeV and prescribe a range of $120 \text{ GeV} < M_H < 200 \text{ GeV}$ at a cut-off, $\Lambda \approx 10^{12} \text{ GeV}$.

Further limits can be placed using data gained from the LEP2 and Tevatron.

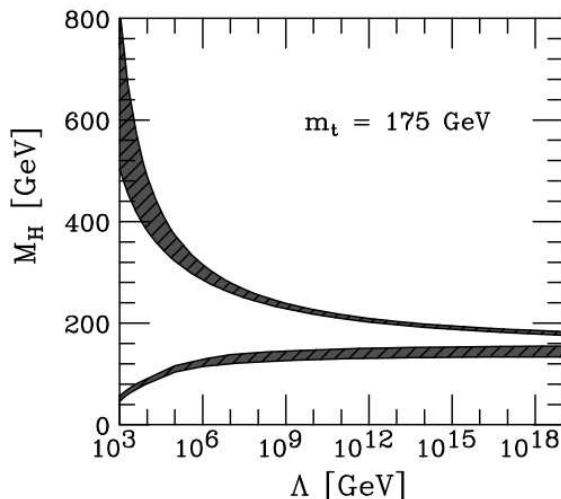


Figure 2.7: Theoretical limits on M_H . Upper bounds come from unitary requirements and lower bounds from vacuum stability requirements.

The direct search in the channel $Z \rightarrow HZ$ at the LEP set a lower limit at 114.4 GeV (see Fig. 2.8).

Electroweak precision data measurements, which place accurate constraints on electroweak values can also be used to estimate the Higgs mass, as the systems are intimately connected. Fits to electroweak data from LEP2 placed an upper limit at 160 GeV at 95% CL, as shown in Fig. 2.9.

However, the combination of the electroweak data and the direct search extended the upper limit to $M_H < 182$ GeV at 95% C.L. Using data from LEP, SLC and the Tevatron an electroweak precision data fit was made to estimate a Higgs mass of $M_H = 76^{+33}_{-24}$ GeV or $M_H < 144$ both at 95% C.L.³³. These estimations mostly anticipate the Higgs mass to be at the low end of the mass spectrum investigated in this analysis.

Unfortunately, the sensitivity in this channel is not strong due to the branching ratio to W^+W^- being low at low Higgs masses. This analysis therefore investigates

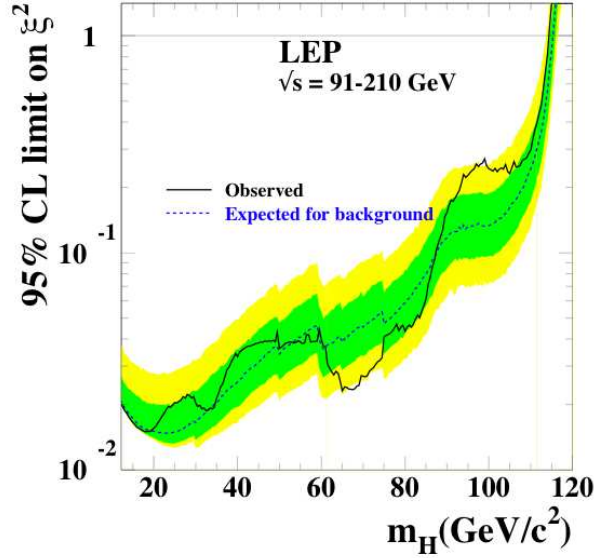


Figure 2.8: Bounds at 95% CL set by LEP2 on the $\xi^2 = (g_{HZZ}/g_{HZZ}^{SM})^2$. The limit is set at 114 GeV where the observed limit (solid black line) crosses the becomes larger than the SM cross section and the mass can not be excluded. The expected limit is displayed as a dotted line, with the 1- and 2- sigma errors displayed using green and yellow bands respectively.

the higher masses with an eventual aim of creating a more precise upper bound on the Higgs mass. However, given the luminosity available in this analysis, it is probable that no exclusion is possible and instead a limit on the Higgs production cross section is calculated. The method in this analysis is therefore to place a limit on the cross section and then look for evidence of exclusion of the Higgs masses if the observed limits are below the theoretical cross section.

Current searches at the Tevatron combine limits from the D0 and CDF detectors. Fig. 2.10⁴³ shows the last analysis over the entire mass range using 2.4 fb⁻¹ data, and Fig. 2.11⁵² shows a more recent combined limit over the high mass region using 3.0fb⁻¹. The latter search excludes a Standard Model Higgs at a $H_M=170$, mainly due to the contribution from the $gg \rightarrow H \rightarrow W^+W^-$ channel

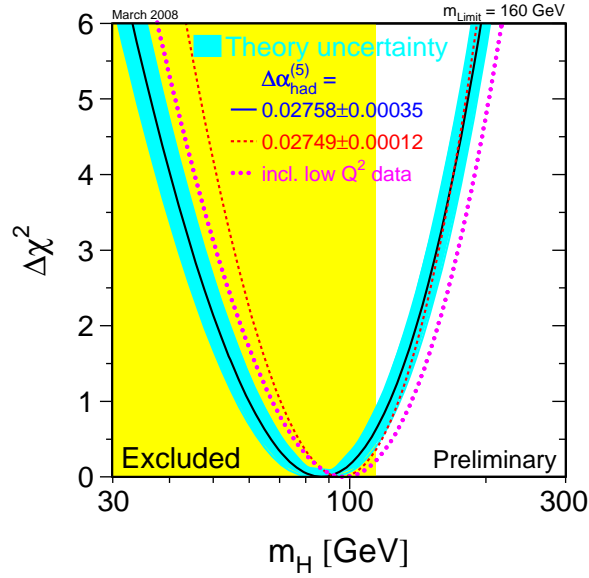


Figure 2.9: Best fit for the Higgs mass placed by electroweak precision data at LEP2. The yellow region shows the excluded limit in direct searches.

also investigated in this analysis.

The contribution from CDF in this channel is also published⁸⁰. The analysis incorporates more lepton types than this analysis to increase acceptance at the cost of higher systematic errors, and combines two techniques, neural nets and a matrix element estimator to improve the sensitivity. It achieves expected limits on the cross section with respect to the theoretical Standard Model as low as $2.2 \cdot \sigma_{SM}$ (0.9 pb) as shown in Fig.2.12. The analysis presented here uses less luminosity, has fewer lepton types and employs only a neural net as a discriminator, and as such does not attempt to lower this limit; instead, it investigates an alternative neural net training method using the most reliable lepton types. It includes the events with two jets, and it also employs an alternative configuration of likelihood templates, including shape errors in the limit calculation.

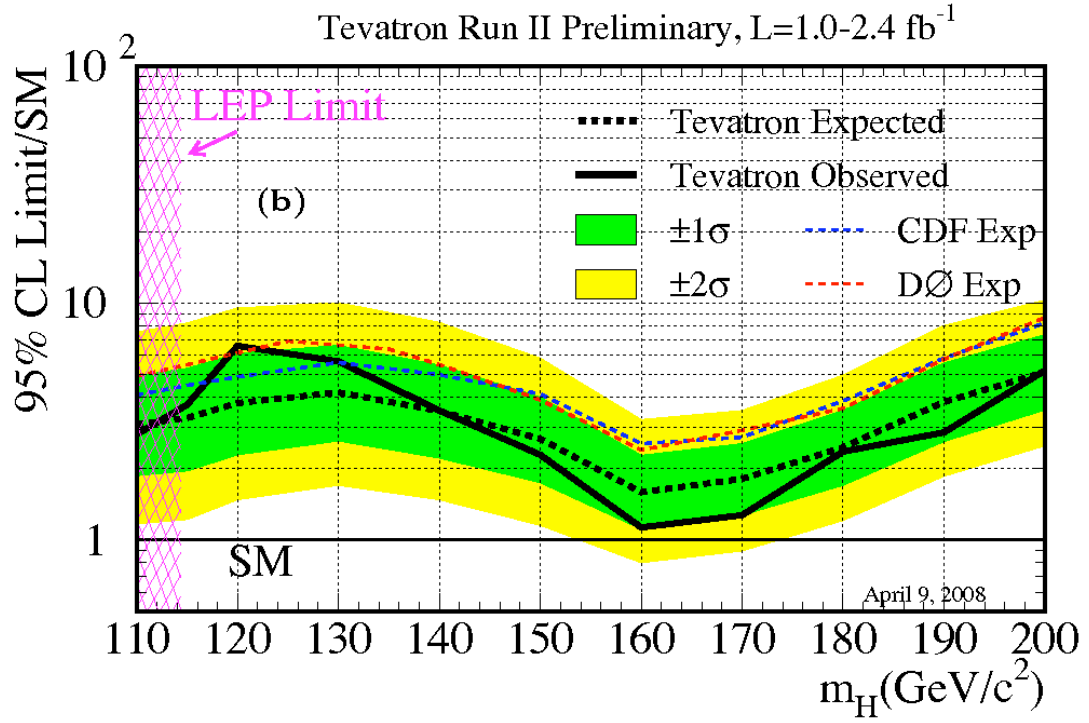


Figure 2.10: Limits placed on the Higgs mass by the combined searches at CDF and D0 at the Tevatron⁴³. The bold black line shows the combined limit, and the dashed black line gives the combined expected limit expressed as a fraction of the Standard Model cross section.

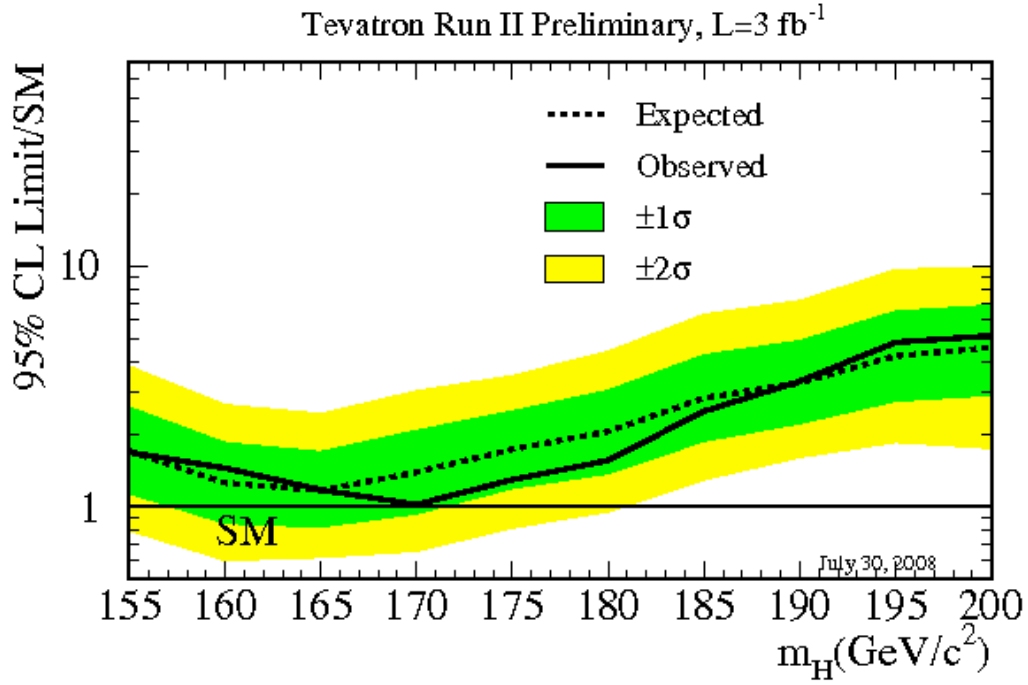


Figure 2.11: Limits placed on the Higgs high-mass region by the combined searches at CDF and D0 at the Tevatron⁵². The bold black line shows the combined limit, and the dashed black line gives the combined expected limit expressed as a fraction of the Standard Model cross section. The observed limit on the cross section is below that of the Standard Model cross section at the $M_H=170$ GeV mass point, excluding a SM Higgs at this mass.

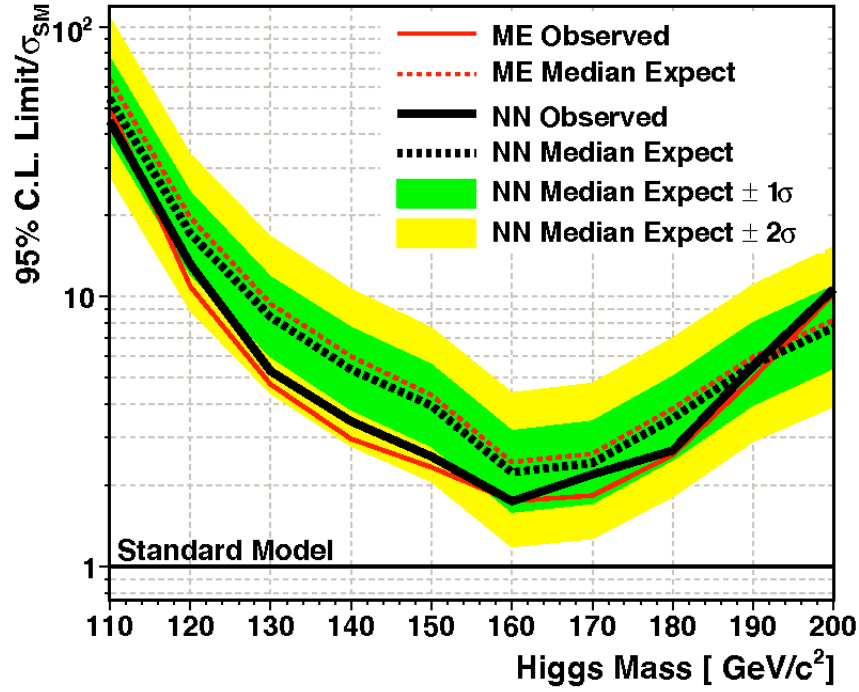


Figure 2.12: Limits placed on the Higgs mass by the $gg \rightarrow H \rightarrow W^+W^-$ search at CDF. The bold black line shows the combined limit, and the dashed black line gives the combined expected limit expressed as a fraction of the Standard Model cross section.

Chapter 3

Experimental Equipment

The experiment was conducted at the Fermilab National Accelerator Laboratory in Batavia, IL, USA. This facility currently houses the world's most powerful active hadron accelerator, the Tevatron. This will be surpassed in the near future by the Large Hadron Collider (LHC) at CERN, which is predicted to commence data taking in 2009. The Tevatron is a proton-antiproton accelerator with two designated positions on the ring where the beams are collided. The two main experiments are housed at these sites, D0 and the Collider Detector at Fermilab (CDF) which are both general purpose detectors. The experiment was conducted with data from CDF.

3.1 Accelerator Chain

The accelerator at Fermilab⁶⁴ utilises a sequence of five accelerators, each increasing the particles' kinetic energy to the maximum for the stage before passing into the next accelerator in the chain, as shown in Fig. 3.1. The process begins with

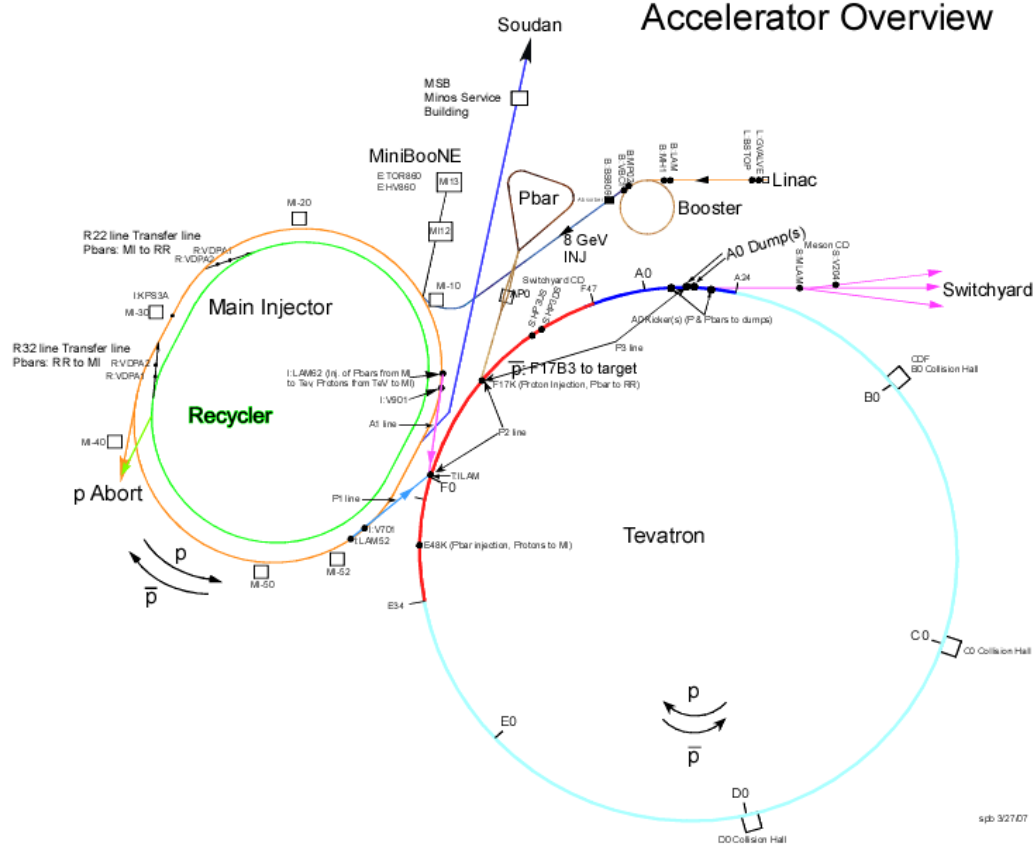


Figure 3.1: A schematic diagram of the Fermilab accelerator chain. The process begins at the Linac, travelling through the Booster and Main Injector before entering the Tevatron.

a Cockroft Walton, with the particles passing through a linear accelerator, the Booster and the Main Injector before final acceleration occurring in the Tevatron ring. There are also rings for creating and storing anti-protons. Data in this analysis is collected at CDF (position B0), but the accelerator also supplies beams for the D0 detector, and other experiments such as MiniBoone and Soudan.

3.1.1 Cockroft Walton

The Cockroft-Walton accelerator^{86,88} is a simple accelerator which uses static electric fields for acceleration. H^- ions are generated from a canister of H_2 gas. These are accelerated to an energy of 750 keV using a series of static electric fields. They are then passed onto the linear accelerator (linac).

3.1.2 Linear Accelerator (linac)

The Linac^{21,66,89,90} is a 500ft long array of radio frequency cavities that utilise oscillating fields at 15 Hz to propel the H^- ions to an energy of 400 MeV. At the end, they are passed through a carbon foil to strip the H^- ions of their electrons producing a beam of protons. From here, the protons are passed on to the Booster.

3.1.3 Booster

The Booster^{91,93,94} is a circular Sychrotron with a circumference of 474m, (75m radius). This utilises alternating radio frequency cavities for acceleration, and bending magnets to maintain the circular trajectory. The protons are gathered into bunches and accelerated to an energy of 8 GeV within 20,000 revolutions. The protons are then passed onto the Main Injector.

3.1.4 Main Injector

The Main Injector^{19,92} is a sychrotron with two straight parallel sections, a total of 3km in circumference. It has two functions, to supply protons for the antiproton source and to store protons to be ready for use in the Tevatron. The protons are supplied to the antiproton source after the main injector has accelerated them to

an energy of 120 GeV. These are debunched and sent via a small linking transport in the Tevatron tunnel to the antiproton source. The rest are accelerated further to 150 GeV ready for injection into the Tevatron.

3.1.5 Antiproton Source

Antiprotons are generated by colliding 120 GeV protons onto a nickel target in the Target hall²⁴. This produces a vast array of secondary particles; the antiprotons are separated out using magnetic spectroscopy, which selects them within a certain momentum range utilising the characteristic curvature of the particles' trajectories when a magnetic field is applied. The process is very inefficient, giving 1 antiproton for every 100,000 protons incident on the target; the generation and storage of antiprotons is the limiting factor in the luminosity of the collisions in the Tevatron. The resulting 8 GeV antiprotons are passed onto a triangular synchrotron named the 'Accumulator' with a mean radius of 90m. Given the chaotic nature of the antiproton production, the resulting beam has too much transverse momentum which is regarded as heat. It is therefore 'cooled' by reducing the electrons' transverse momentum before it is passed into the accumulator. A lithium lens performs the initial \bar{p} collection, which consists of an electromagnetic lens surrounding a lithium core. The beam is then cooled by using 'stochastic cooling', where the excessive momentum of the beam is measured on one side of the accumulator triangle and 'kicked' by magnets in the opposite direction by the time it gets to the next side. The triangular design of the accumulator is such that the measurement and processing needed for the kick to be accurate is performed as the beam is passing around a corner. The antiprotons are stored in the accumulator

and the recycler in readiness for injection into the Tevatron.

3.1.6 Tevatron

The Tevatron⁸⁷ is the final stage of the chain, accelerating the protons and antiprotons to 980 GeV. It is a synchrotron with a circumference of 6.3 km, and contains two collision halls which contain the general purpose detectors CDF and D0. The proton and antiproton beams are accelerated and bent by the same set of super-conducting magnets, possible because of the opposite charges of the particles.

3.1.7 Recycler

The primary role of the recycler is to reclaim antiprotons from old runs. It also stores some freshly generated antiprotons from the accumulator prior to insertion into a new store. The recycler is a permanent magnet ring which occupies the same tunnel as the main injector.

3.2 Luminosity

The quantity of potential particle reactions delivered by the Tevatron is measured in terms of ‘instantaneous Luminosity’,²⁰ which is defined in Eqn. 3.1

$$\mathcal{L} = \frac{N_B N_p N_{\bar{p}} f_0}{4\pi\sigma^2} \quad (3.1)$$

where N_B is the number of bunches, of which there are 36 in three groups of 9, and f_0 is the frequency of the bunch revolutions, 47.7 kHz. N_p and $N_{\bar{p}}$ are the number

per bunch of protons and antiprotons respectively: these have varied greatly over the period of data taking for use in this analysis, but are typically of the order of 10^9 . σ is the average effective width of the bunches in cm, and is typically around 0.007cm. Instantaneous luminosity is integrated over the entire operation of the Tevatron to give a measure of the total luminosity delivered. This analysis uses $\int \mathcal{L} dt = 2.4 \text{fb}^{-1}$. In reality, the luminosity used is that measured by the Cherenkov Luminosity Counters (CLC) located on either side of CDF²⁶.

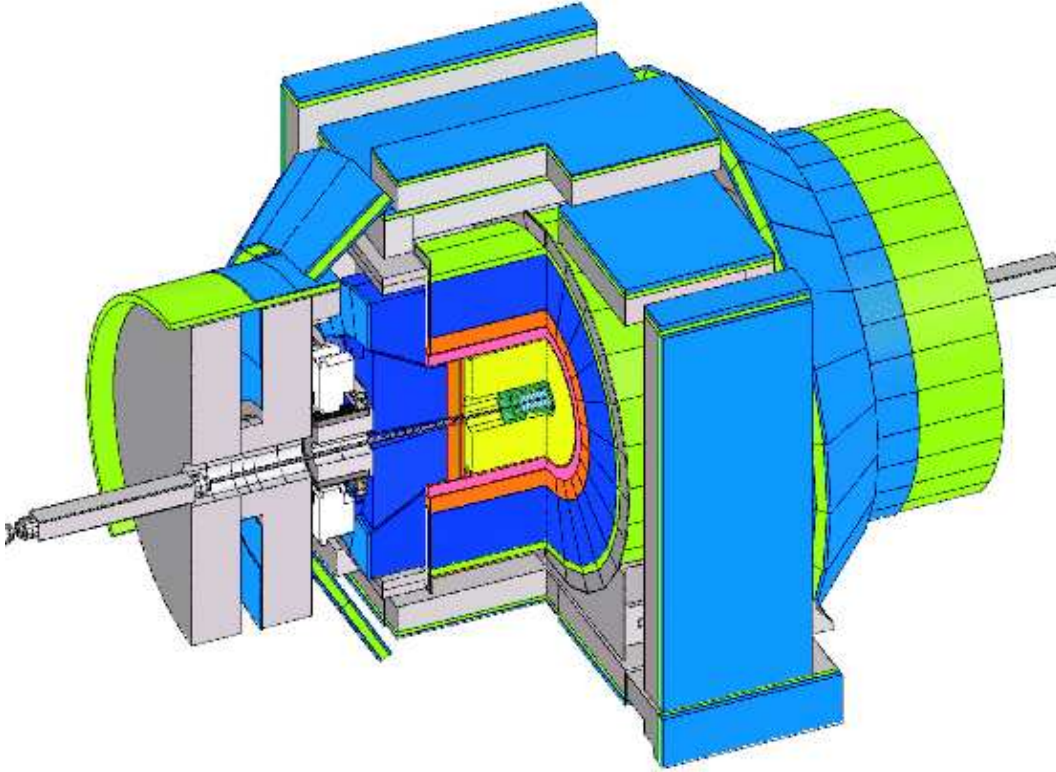


Figure 3.2: A cut-away diagram of the CDF detector showing the silicon detector (light blue and dark green), the COT (yellow), the solenoid (pink), the electromagnetic calorimeters (red), the hadronic calorimeters (dark blue) and muon detectors (light green)

3.3 Collider Detector at Fermilab (CDF)

The Collider Detector at Fermilab³⁵ (CDF) (Fig. 3.2) is a general purpose detector located at the B0 position on the Tevatron ring. Quadropole magnets are located on either side of the detector to focus the two helical beams to a point in the centre of the detector where they collide, called the ‘beam spot’, or ‘primary vertex’. Reflecting this geometry, the detector is approximately 15m long and cylindrically symmetric and forward-backward symmetric. The detector previously had coverage out to ± 1.1 in η (as defined in section 3.3.1) in the central section, but was upgraded in Run II by adding ‘plug’ sections fitting in the front and back which increased the coverage to 3.6 in η . The detector is 85-90% efficient in coverage. CDF consists of a central tracking system surrounded by a solenoid to create a magnetic field. Surrounding this, lie the calorimeters for measuring particle energy and beyond these at the furthest distance from the centre are muon detectors.

3.3.1 Co-ordinate system

CDF is defined using two co-ordinate systems, both with the origin at the interaction point. The first is a standard right handed xyz system, with the z axis pointing along the beam line. Due to the cylindrical nature of the detector, a more convenient system replaces the x and y unit vectors with $\phi = \arctan(y/x)$ and the ‘rapidity’ as defined in Eqn. 3.2.

$$\text{rapidity} = 0.5 \ln \left(\frac{E + p_z}{E - p_z} \right) \quad (3.2)$$

For measuring particle trajectories, η is more convenient than a conventional

$\theta = \arctan(z/\sqrt{x^2 + y^2})$ angle because differences in rapidity between particles are invariant under lorentz boosts; it is often simplified to pseudo-rapidity:

$$\eta = -\ln \left(\tan \left(\frac{\theta}{2} \right) \right) \quad (3.3)$$

which is a good approximation when the particle's momentum is much greater than its mass. In this system, the $\eta - \phi$ separation, R , is defined as:

$$R = \sqrt{\Delta\phi^2 + \Delta\eta^2} \quad (3.4)$$

3.3.2 Tracking and momentum measurement

The first detectors a particle will encounter after being emitted from the primary vertex are the tracking detectors. There are two in CDF, the silicon detector, and a proportional chamber known as the Central Outer Tracker (COT). Both are cylindrical in structure and are composed of multiple detecting layers parallel to the beam line. Centrally emitted particles ($|\eta| < 1$) pass through all the layers and gain the best measurements, whereas particles at higher η experience a loss in efficiency as they traverse fewer layers, and hits from a particle trajectory are more spaced out and so harder to associate with each other. Both the COT and silicon detector are surrounded by a 1.4T solenoid parallel to the beam axis at a distance of 1.5m. This forces charged particles to travel in a helix before they exit the COT, so the curvature of the particles' tracks can be used to measure their momenta.

Silicon Detector

At the centre, closest to the beam spot, lies the silicon vertex detector⁷⁰. It allows precise position resolution of track origins at vertices, which is very valuable for detection of B mesons where the decay vertex is displaced from the primary vertex. As a particle traverses the silicon, it displaces lattice electrons to create electron-hole pairs, which are forced to opposite sides of the detector by an imposed electrical bias. They are collected by a grid of microstrips attached to the surface to create a one dimensional position measurement. A set of strips on both sides, with one set rotated by a relative angle, allows two dimensional measurements to be made.

The detector itself is composed of multiple cylindrical layers of silicon microstrip detectors, which are grouped into sub-detector systems. The main central detector, the SVX³², comprises five layers between a radial distance of 2cm and 10.6cm, 16cm long (See Fig. 3.3).

There are 12 azimuthal wedges on each, each containing two ‘ladders’, which are sets of 3 detectors in series. Each detector is double-sided, with some having a 90° rotation between the filaments on either side, and some 1.2° . Additionally to the SVX is the Layer00³⁴ detector, a single sided detector located on the beam-pipe at a radius of 1.6 cm, and the Intermediate Silicon Layers (ISL)²⁹. The ISL comprises one layer at a radius of 22 cm which covers the $|\eta| < 1$ region, and two layers at a radii of 20 and 28 cm, covering the region $1 < |\eta| < 2$. Overall, there are 722,432 readout channels providing ϕ position measurements with a resolution of 12 μm .

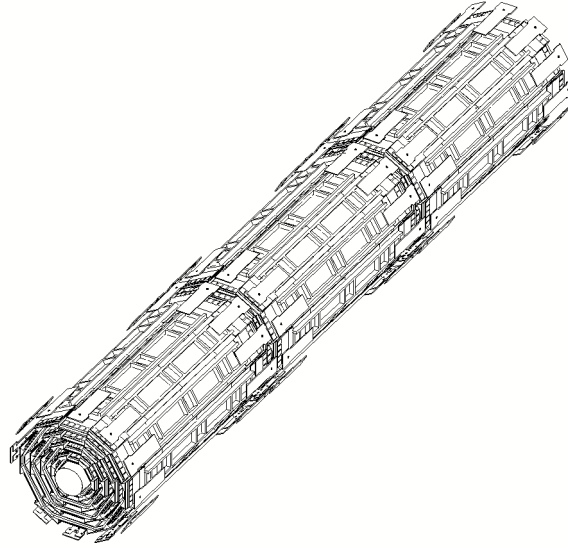


Figure 3.3: The SVX silicon vertex detector, showing the three barrels with five layers of silicon detectors

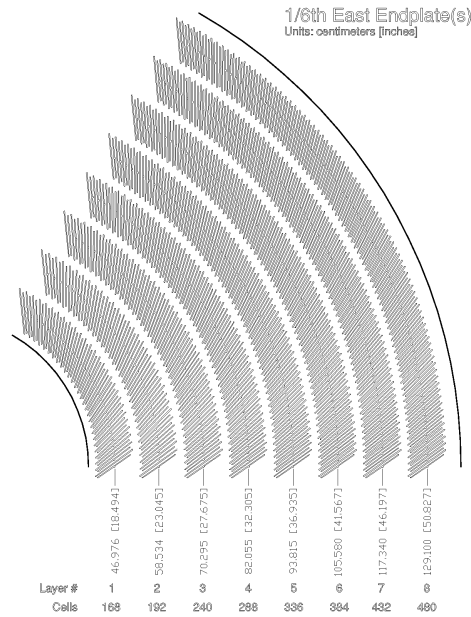


Figure 3.4: A schematic diagram of a segment of the Central Outer Tracker showing the superlayers, and the angled drift cells

Central Outer Tracker

Surrounding the silicon detector is a proportional chamber known as the Central Outer Tracker³⁰ (COT), which is used for tracking, charge resolution and momentum measurement. A segment can be seen in Fig 3.4. The COT is 3m long, covering a radius from 0.43m to 1.32m, and containing 96 layers of 30240 gold plated tungsten wires arranged into 8 ‘superlayers.’ As a charged particle passes through the 1:1 mixture of argon and ethane, the displaced ions they create drift towards the sense wires and deposit a charge⁴². The chamber contains a small amount of oxygen to prevent ageing. The time difference with which the charge arrives at the ends of the chamber can be used for a z measurement of the track. Each layer consists of a series of enclosed cells tilted at a 35° Lorentz angle to compensate for the solenoid’s effect on the drifting ions. Each cell is surrounded with sheets which help create a uniform electric field gradient of 2kV/cm within the cell. At the centre of the cell are sense wires alternated with wires held at a potential. To reduce pileup of signals, the drift time is 177ns with a $100 \mu\text{m}/\text{ns}$ drift velocity and a maximum drift distance of 0.88cm; thus the ions are collected before the next beam crossing. Superlayers alternate between containing axially aligned wires and wires held at a $\pm 2^\circ$ stereo angle. This achieves a position resolution of $140\mu\text{m}$, and an impact parameter (position of the primary vertex) resolution of $40\mu\text{m}$. In addition to tracking, the COT can measure transverse momenta with a resolution of $0.15\% \cdot P_T$.

3.3.3 Calorimeters

The calorimeters are found in both the central section and the plug section, but both follow the same basic design. In the central section ($|\eta| < 1$) the calorimeters are arranged in 24 phi wedges, each divided into 10 η towers. They consist of alternate layers of inert material to interact with the incident particles, and scintillator material. As the incident particles hit the inert material, they create a shower of secondary particles that increases in size to a maximum width and length determined by the particle and the material. The size of the shower is measured by the sampling scintillator layers which create a number of light pulses proportional to the number of particles within the shower. The pulses are transferred using waveguides and ultimately measured with phototubes.

Electromagnetic Calorimeters

The electromagnetic calorimeter is used for the measurement of photon and electron energies. Electromagnetic showers are created by electrons bremsstrahlunging photons and photons creating electron-positron pairs⁴². The length of the showers is therefore proportional to the radiation length (X_0) of the material used in the calorimeter. The positional accuracy of the calorimeter is supplemented by a ‘shower maximum’ detector, located at $5X_0$, which measures the profile of the shower at its maximum width and can help in separating overlapping showers. Pre-radiator detectors are also placed in front of the electromagnetic calorimeters to help differentiate between electrons and pions.

In the central region, the Central Electromagnetic calorimeters (CEM)³⁸ are located beyond the tracking systems and solenoid; they consist of 31 layers of

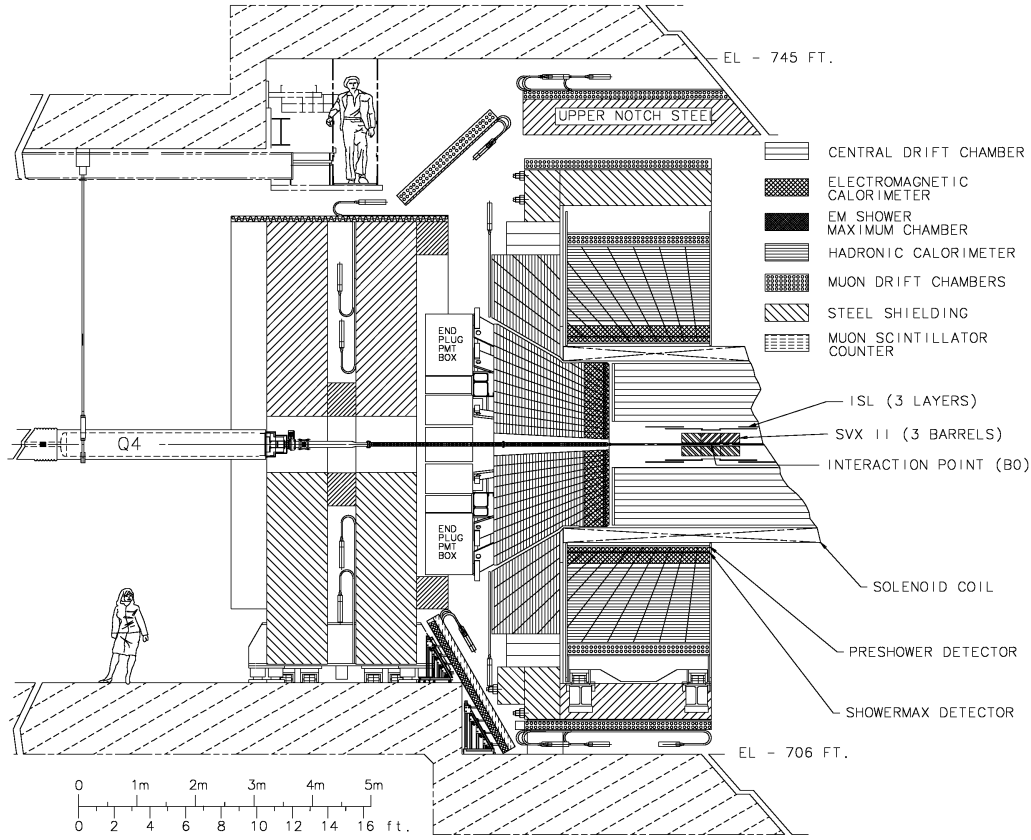


Figure 3.5: A cross section of the CDF detector

aluminium-clad lead alternated with layers of scintillator, a total of $18X_0$, giving it an energy resolution of $\delta E/E$ of $0.14/\sqrt{E}$. At high η , some lead layers are replaced with plastic to maintain the radiation depth apparent to the particle. The Central Shower Maximum detector (CES) is located at the 8th layer of lead ($5X_0$) within the CEM and it consists of two layers of proportional chambers aligned at right angles to each other. A set of proportional chambers constitute the Central Pre-shower Radiator detector (CPR), situated in front of the CES.

The Plug Electromagnetic calorimeter (PEM)³⁹ consists of 23 4.5mm thick lead

layers alternated with 4mm thick scintillator layers. This is $23.2X_0$ deep achieving $\delta E/E$ of $0.16/\sqrt{E}$. Within the PEM at $6X_0$, the Plug Shower Maximum detector (PES)³⁶ comprises of 8 layers of scintillator strips each set at 45° between adjacent layers for position measurements. The first layer of the PEM is read out as the Plug Pre-shower Radiator (PPR).

Hadronic Calorimeters

Hadronic calorimeters⁴¹ are used to measure the energy of hadronic particles, usually in collections of particles called jets resulting from a fragmenting quark released from the primary interaction. Hadronic showers are created from strong force collisions as the particles interact with the inert material's nuclei⁴². The showers are therefore dependent upon interaction length within the calorimeter material. Hadronic showers are greater in length than electromagnetic showers due to the greater mass of incident particles, so the hadronic detector is placed on the outside of electromagnetic one. Hadronic showers may start in the electromagnetic calorimeters.

The Central Hadronic calorimeters (CHA) comprise of 4.7 interaction lengths of 2.5cm steel layers alternated with 1cm thick acrylic scintillator layers covering an $|\eta| < 0.9$. It has a $\delta E/E$ of $0.75/\sqrt{E}$. The CHA's η range is extended to 1.2 by the Wall Hadronic calorimeter (WHA), in which the steel layers are 5cm thick. The Plug Hadronic calorimeter (PHA) comprises of 22 5cm thick layers of iron separated by 6mm thick scintillation layers, for a total of 6.8 interaction lengths. It achieves an energy resolution of $\delta E/E = 0.8/\sqrt{E}$.

3.3.4 Muon Detection Systems

Any particle escaping the calorimeters are considered to be muons or neutrinos. The muons are detected by proportional chambers which do not have full $\eta - \phi$ coverage due to space constraints within collision hall. They are comprised of 4 layers of one-wire drift cells, often offset from each other in ϕ to give more accurate position measurement. Signals from a majority of these layers is usually required to register a signal for a muon hit (a ‘stub’) to be confirmed. A scintillator layer often surrounds the chambers to confirm triggering and make triggers less prone to backgrounds.

In the central region, the Central Muon Detectors (CMU)³⁷ are embedded in the outer layers of CHA, and can detect muons with P_T low as 1.4GeV. They cover a region up to $|\eta| < 0.6$ but contain ϕ and η cracks due to their incorporation into the calorimeter wedges. These are surrounded by a 60cm layer of steel, outside of which lie the Central Muon Upgrade detectors (CMP)⁸⁴. The CMP detects muons above a P_T of 2GeV/c, and has a more complete coverage but also contains gaps due to space constraints. The plug regions have a cylindrical Barrel Muon detector (BMU) beyond the calorimeters, but this remains unused in this analysis due to the lack of correctly simulated Monte Carlo.

Covering the η gap between the CMP and the BMU lies the Central Muon Extension detectors (CMX)²³ which are arranged in annuluses of 24 wedges at each end. The top two wedges of the west CMX arch is known as the ‘keystone’ and the bottom six wedges of each arch are known as the ‘miniskirt’. These were added later than the rest of the CMX detectors and are of reduced efficiency.

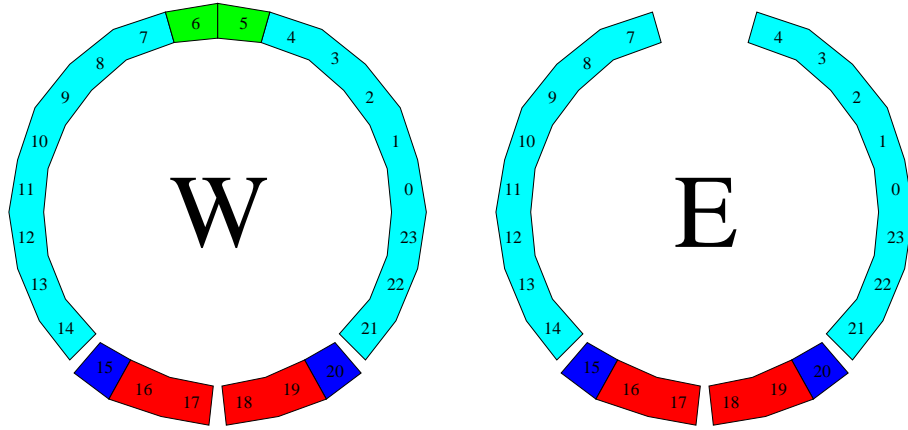


Figure 3.6: A schematic diagram of the CMX arches, with the keystone (wedges 5 and 6) and miniskirt (wedges 15 to 20) regions highlighted

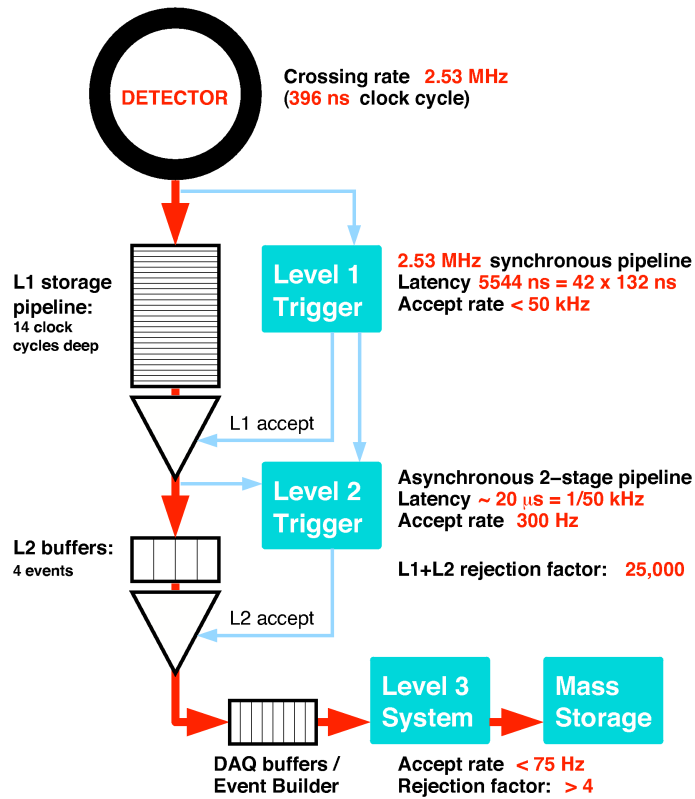


Figure 3.7: A schematic diagram of the CDF trigger system

3.4 Trigger Systems

The crossing rate for the bunches in the beams is 2.53MHz, which is a much higher rate of data uptake than can be computationally processed. To reduce the rate, a trigger system⁸³ is used to isolate events which are physically interesting. CDF employs three levels of trigger systems, shown in Fig. 3.7. The fastest at Level 1 must also be the most basic to assess all logic decisions in time for the next bunch crossing. An electronic storage pipeline stores events while the Level 1 trigger assesses them. Level 1 uses custom made hardware boards which make decisions in parallel on tracking, muon systems and calorimeter information, which are then combined into an overall level 1 trigger decision. Decisions involve, for example, summing all the energy in the calorimeter towers for a quick missing energy decision, or coincidences between muon stub measurements and muon scintillator firings. Level 1 accepts occur at a maximum rate of 50kHz, but are not regular, so another buffer is employed after it. Level 2 consists of programmable logic boards which make more advanced decisions, for example, jet triggers based on calorimeter clustering algorithms, or loose momentum measurements of tracks. This reduces the rate of important events to a maximum of 300Hz, which pass through another buffer before reaching Level 3. Here the events are fully reconstructed in a bank of CPUs; the triggers look for specific physics signatures, and also verify the integrity of the data. Full data events are released from Level 3 at a maximum rate of 75Hz to be stored to disk. Events stored on disk are sorted into ‘datasets’, which are then processed to calculate important quantities, such as identify leptons to create electron or muon collections, or to check for cosmic events. This last stage is called ‘production’.

Triggers with loose requirements fire more often than triggers for rare events, so the rate at which these triggers are allowed to be recorded is artificially restricted with a ‘prescale’. Triggers in this analysis are prescaled in some of the later runs, and this has been accounted for by including the drop in data taking into the luminosity calculation.

Chapter 4

Event Selection

From the raw data, appropriate events are separated which have the basic profile of the signal. Selection centred around isolating events which contained two electrons, two muons, or one of each. Therefore, triggers which trigger on either an electron or a muon were used, and the datasets were searched though for events containing one more lepton. The selection criteria and classifications used in the analysis follow the advised lepton cuts from the Joint Physics Group in CDF, which allows the analysis to use detection efficiencies measured collaboratively. Six lepton types are used: TCE, PHX, CMX, CMUP, CMU, and CMP; they are predominantly named after the detector subsystem that detect them. Their defining selection cuts are discussed in section 4.3.

There is a cut on the run ranges based upon whether the the sub-detectors used to measure the lepton were faulty, or there was reason to doubt the quality of the measurement. This is decided upon by the CDF Data Quality Group who publish good run lists based upon the live evaluations of the data recording. Run range cuts are also placed on Monte Carlo only for certain runs that have been

found to have incorrectly simulated primary vertices.

Each event is required to have two leptons to exclude tri-lepton events. This serves to exclude many backgrounds such as $Z^0 Z^0$ and $W^\pm Z^0$, but also it reduces the acceptance of other Higgs channels such as associated production, which this analysis is not designed to detect.

Finally, the event is required not to have been identified as a cosmic event, which is flagged as the events pass through the production process using a dedicated algorithm.

Alternative analyses carried out by the CDF Higgs Group have used various other lepton types:

- PEM plug electrons are the precursor to PHX electrons (see section 4.3.2), and the two groups are not exclusive. This analysis uses PHX electrons for which the selection method is more precise and achieves a higher acceptance rate for electrons in the plug areas of CDF.
- CMIO are tracks which do not pass through any muon detector, but are not identified as electrons by the electron cuts, and as such are often categorised as muons. These are not used in this analysis because of the lack of certainty as to their identity, which is not in keeping with the grouping of the template plots in chapter 6; in these templates muons and electrons are treated independently. It is also contrary to the neural net training strategy, also in chapter 6, in which the muons and electrons are trained separately. CMIO muons also exhibit widely varying scale factors and inconsistent Drell Yan cross section measurements, as measured in section 5.1, over subsections of run ranges. Due to their loosened selection requirements, they also bring

with them a larger fake background.

- ‘crack tracks’ are another selection of tracks which is not fully identified as electrons or muons due to their path through the detector. They are not exclusive from the CMIO selection, and consequently suffer from the same problems. They additionally suffer from less precise energy measurements which are evident in a broader Z mass peak.

4.1 Variable definitions

These are definitions of the variables used in the trigger and selection criteria.⁶⁸

- Region: for basic categorisation, the detector is split into named η (fiducial) regions which contain different detector systems⁴⁴. Actual categorisation depends on which towers the track is pointing at. Essentially, only two are used for classifying electrons, and the variable is a basic η cut:

0=CEM (central region): $|\eta| < 1$

1=PEM (plug region): $1 < |\eta| < 2.6$

- Fiducial: this is a tighter fiducial categorisation which maps out where detector systems lie in $\eta - \phi$. A lepton is ‘fiducial’ to a system if it is within the $\eta - \phi$ space assigned to that detector system, and is assigned a Fiducial code during production. For electrons, the ‘FidEle’ function routine⁴⁵ is used, the codes of which are shown in Table 4.1. Each calorimeter tower has a local x and z co-ordinate on its surface; fiduciality uses this to ensure that the track lies within a certain distance from the edges of the tower where the efficiency

FidEle Code	Condition
-1	error (null strip/wire cluster)
0	not fiducial in central or plug
1	fiducial in central or plug
2	fiducial, but in CEM Tower 9
3	fiducial, but in Chimney wedge tower 7
4	fiducial in CEM using max P_T track extrapolated to plane of CES
5	fiducial in PEM using PES
6	fiducial in PEM using max P_T track extrapolated to plane of PES

Table 4.1: Values for the FidEle function ensuring that the track lies with the linear response area of the calorimeter tower. Different codes denote whether the track points at towers identified as ‘bad’.

is non-linear. Various fiducial codes check that bad calorimeter towers are not used.

- x -fid, z -fid for CMU, CMP & CMX: each muon detector is assigned a local x - z co-ordinate system. x -fid and z -fid are measurements of the position of the extrapolated track as it intersects with the relevant detector. The cut is placed to exclude the edges of the detector where the measurement efficiency is not well modelled.
- E_T : transverse energy. In a hadronic collider where the particles are composite, the total P_z of the interacting sub-particles is unknown even if the total momentum of the hadron, set by the accelerator, is known. The proton remnants, which often have P_z information but little P_T normally escape down the beam line. Therefore, transverse quantities are used as they are more physically interesting. The energy of a central electron is given as the sum of the electromagnetic calorimeters’ and hadronic calorimeters’ measured en-

ergies $(E_{em} + E_{had})$ ⁴⁶. The phoenix electron's energy (see section 4.3.2) is just the electromagnetic calorimeter's energy, E_{em} ⁸. This is then scaled by $\sin(\theta)$ as measured from the best track pointing to the cluster.

- Track P_T : transverse momentum as measured from the track. The momentum as calculated from the curvature of the track.
- P_T : transverse momentum. For muons, this momentum is equal to the Track P_T , because muons punch through the calorimeter and so no energy information can be gained from it. For electrons, the calorimeter energy is more accurately measured than the momentum magnitude from the track curvature, so the magnitude of the momentum is taken to be equal to the electromagnetic calorimeter energy. (At high energies, the mass of the lepton can be neglected and is considered to be zero, such that the energy of the lepton is equal to the momentum magnitude.) The momentum direction is taken from the track⁴⁷. As with E_T , the transverse measurement is predominantly used.
- Track Z_0 : This is the distance in centimetres of the track intersection from the detector central point in the z direction⁶⁸. This is cut upon to make sure the track originates from within the detector, as many systems are calibrated to measure accurately only when the particle originates from near the detector centre. However, the luminosity is measured over all z , so a correction is applied (see section 4.10).
- COT Axial segments: This is the number of Axial superlayers that the track must pass through for the measurement of the track to be valid. The track

must trigger 5 wires in each superlayer before it is counted.

- COT Stereo segments: This is the number of Stereo superlayers that the track must pass through for the measurement of the track to be valid. Stereo layers are required along with axial superlayers to validate the z-position of the track. The track must trigger 5 wires in each superlayer before it is counted.
- conversion: this is a flag to identify whether the lepton is the result of a photon converting into an e^+e^- pair within the detector rather than a prompt lepton. The algorithm looks for an additional oppositely charged lepton which has a very small separation between the tracks at a possible conversion point ($|R\Delta\phi| < 0.2cm$), and also a very small opening angle between the tracks ($|\Delta\cot\theta| < 0.04$); these conditions are typical of lepton pairs originating from a photon²⁵. A value of 1 for this variable denotes a conversion.
- E_{had}/E_{em} : this is the ratio of the energy as measured by the hadronic calorimeter to the energy as measured by the electromagnetic calorimeter. A low cut on this will filter out hadronic particles such as pions from the selection which are expected to deposit more energy in the hadronic calorimeter than electrons. The cut slides with energy as more hadronic energy will be expected from a more energetic electron.
- Calorimeter Isolation: this is the energy in a cone of radius $\delta R = \sqrt{\Delta\eta^2 + \Delta\phi^2} < 0.4$ around the electromagnetic calorimeter cluster (excluding the cluster) divided by the energy in the cluster. Isolation is important in rejecting jets, which contain many particles in the cone. High energy jets can fake or con-

tain leptons, so requiring the lepton to be isolated will reduce the number of jet-faked leptons or leptons originating from within jets⁶⁸.

- *Lshr*: An electron will deposit some energy in adjacent towers to the calorimeter tower in which the cluster is located. This variable is a sum over adjacent towers of the difference between the amounts found and those expected from test beams².
- E/P : this is the ratio E_{em}/P_{track} ⁴⁸. It is expected to be reasonably close to one for leptons which have negligible mass compared to their momenta.
- CES ΔZ : distance in the z direction between the track extrapolation to the shower max detector and the centre of the shower max electromagnetic cluster associated with the track. It is used to validate the association of the track and the calorimeter cluster.
- Signed CES ΔX : This is the same as for CES ΔZ in the ϕ direction but local to the detector. The cuts are asymmetric and reversed for the opposite sign of electron charge. If the electron radiates a photon as it traverses the COT, the electron's path will be diverted and cluster displaced from the position predicted by the track. Measuring the displacement of the cluster center from the track projection detects this.
- χ^2_{strip} : this is a χ^2 : comparison of the central shower maximum detector's (CES) shower profile compared with a distribution from a test beam⁶⁸.
- PEM 3x3 Fit Tower: 3x3 refers to the number of plug towers used in the plug cluster algorithm. For plug based lepton types, the check is trivial, just making sure that at least one is used⁸.

- PEM 3x3 χ^2 : similar to χ^2_{strip} , this is a goodness of fit of the calorimeter shower profile in the PEM (the plug electromagnetic calorimeter) compared with that from a test beam. 3x3 specifies that the fit be performed over a 3x3 grid of towers^{49 8}.
- PES5by9v, PES5by9u: within the PES, there are two sets of strips set at an angle for position detection; they are labelled ‘v’ and ‘u’, so these measurements are equivalent except applicable to the different set of strips. The variables are a ratio of the shower response in the 5 central strips compared to 9 total strips centred around the cluster centre. It is therefore a measure of the shower profile.
- PES2d η : this is the eta range in which the plug shower maximum detector (PES) clusters are valid.
- N_{hits}^{is} : number of hits of the track in the silicon detector. This is only used in the phoenix selection as the phoenix track requires silicon hits. A minimum amount of hits are required for the PHX algorithm to be valid.
- $|z_0^{PHX}|$: this is equivalent to $TrackZ_0$, but is applicable to the phoenix track found.
- ΔR_{PHX} : this is equivalent to CES ΔZ for central electrons, as it is the separation between the phoenix track extrapolation and the calorimeter cluster in R .
- Δx_{CMP} , Δx_{CMP} , Δx_{CMX} : this is the distance in centimetres between the stub and the extrapolated track’s intersection with the muon detector in the

local x direction. The muon stub needs to be close to the track of the muon.

The association of a stub with a track is called reconstruction, and carries with it an efficiency discussed in section 4.9.

- Track $|d_0|$: closest distance of the track to the primary vertex.
- ρ_{COT} : this is the radial distance from the z axis of the track as it exits the central outer tracker (COT).
- \vec{E}_T^{raw} : raw transverse missing energy is represented by the vector sum of the towers' calorimeter energies in the direction of the tower. This is represented in Eqn. 4.1, where the sum is over the towers within the detector up to an $|\eta| < 3.6$.

$$\vec{E}_T^{raw} = - \sum_i [(E_i^{em} + E_i^{had}) \sin \theta_i] \times \hat{n}_i \quad (4.1)$$

4.2 Trigger requirements

Four trigger paths were used to select events as shown in Table 4.2.

Each trigger ‘path’ is a combination of Level one, Level two and Level three triggers. Triggers of levels one and two are used to reduce the rate of candidates arriving at level three, such that they are progressively more restrictive up to Level 3 which completely reconstructs the event off-line for the most accurate measurements and thus most restrictive cuts. The cuts in Table 4.2 are the Level 3 trigger cuts within the trigger path specified. Over time, the trigger path definitions have been modified such that the Level 1 and Level 2 triggers within the paths have differed between trigger path versions, but the most restrictive Level 3 trigger has

trigger path	requirements	resulting triggerable lepton
ELECTRON_CENTRAL_18	Region = 0 $E_T > 18.0$ GeV $E_{had}/E_{em} < 0.125$ Track $P_T > 9.0$ GeV	TCE
MUON_CMV18 (includes MUON_CMV18_L2_PT15)	$P_T > 18.0$ GeV $ \Delta x_{CMV} < 10$	CMV
MUON_CMUP18 (includes MUON_CMUP18_L2_PT15)	$P_T > 18.0$ GeV $ \Delta x_{CMP} < 20$ $ \Delta x_{CMU} < 10$	CMUP
MET_PEM	$\cancel{E}_T^{raw} > 15.0$ GeV Region = 1 $E_T > 20.0$ GeV $E_{had}/E_{em} < 0.125$	PHX

Table 4.2: Triggers used and their associated lepton types

remained the same. Small differences in the trigger paths are accounted for along with changes in detector performance by using a time-dependent (based on run number) trigger efficiency. These are discussed in section 4.9.

4.3 Lepton Selection Cuts

Lepton categorisation relies heavily on the detector that the lepton hits. Accordingly, the triggers used strongly influence the lepton classification scheme, to the extent that the trigger used to record the lepton lends its name to the first four triggerable lepton types.

When triggered events are stored, all minimum ionising tracks within the detector are stored in data-collections of objects. A given track may appear in more than one collection, so the classification of lepton type is done in the order that they are described in this section, with a selection test being performed only if the track has been rejected for all previous categories.

variable	cut
Region	== CEM
Fiducial	== 1
E_T	≥ 20 GeV
Track $ Z_0 $	≤ 60 cm
Track P_T	≥ 10 GeV
COT Axial Segments	≥ 3
COT Stereo Segments	≥ 2
conversion	$\neq 1$
E_{had}/E_{em}	$\leq (0.055 + (0.00045 \cdot E))$
Isolation	≤ 0.1
$Lshr$	≤ 0.2
E/P	≤ 2.0 unless $P_T \geq 50\text{GeV}/c$
$CES\Delta Z$	$\leq 3.0\text{cm}$
Signed CES ΔX	$-3.0 \leq q \cdot \Delta X \leq 1.5$
$CES\chi^2_{strip}$	≤ 10.0

Table 4.3: Selection cuts for TCE electrons

Firstly, there are four triggerable leptons used:

4.3.1 Tight Central Electron (TCE)

These are electrons within the central section of the detector. They are efficiently measured, and encompass all the used electrons used in the eta range $-1 < \eta < 1$. TCE electrons are essentially a track which matches an identified cluster in the electronic calorimeter, and pass the cuts found in Table 4.3⁸¹.

4.3.2 Phoenix Electron (PHX)

These are electrons from the plug area in the eta range $1.2 \leq |\eta| \leq 2.8$. They are electrons originating from the phoenix electron collection. Electrons allowed in this collection are identified in a different way from TCE electrons due to the

variable	cut
E_T	$\geq 20 \text{ GeV}$
PES2d η	$1.2 < \eta < 2.8$
E_{had}/E_{em}	≤ 0.05
PEM3x3FitTow	> 0
PEM3x3 χ^2	≤ 10
PES5by9U, PES5by9V	≥ 0.65
Isolation	≤ 0.1
ΔR_{PHX}	$\leq 3.0\text{cm}$
N_{hits}^{si}	≥ 3
$ Z_0^{PHX} $	$\leq 60\text{cm}$

Table 4.4: Selection cuts for phoenix electrons

reduced efficiency of the tracking from the COT in the plug area; this reduction in efficiency is itself due to the lessened amount of COT layers the electron passes through within the plug η range. The Phoenix algorithm takes well-measured plug calorimeter clusters and hypothesises where the track would have originated in the silicon detector. It then searches for tracks in the silicon detectors, which become the tracks with which the clusters are associated. The silicon detector is therefore used for tracking to amend the mis-measurement of COT tracks in the plug. The cut requirements for phoenix are found in Table 4.4⁸¹.

4.3.3 CMUP muon

CMUP muons follow the muon cuts in Table 4.5. They are fiducial to both the CMP and CMU detectors and are required to leave a stub in both. Muons which pass through both detectors but leave only one stub (or only become associated with one stub due to inefficiencies) are completely discounted. There is a ‘blue-beam’ section of the detector which is unused for runs earlier than 154449 (Spring 2003) as it was un-comissioned. See section 4.6 for more details on run ranges.

4.3.4 CMX muon

CMX muon is the last triggerable type. It leaves a stub in the CMX muon detector and passes the cuts in Table. 4.5. Different parts of the CMX detector were commissioned at different times; the majority of the CMX detector is used after run 150144 (Autumn 2002); the areas of the ‘miniskirt’ and the ‘keystone’ are unused before 190697 (Winter 2004). Wedge 14 of the CMX detector was faulty between the runs of 190697 and 209760 (Winter 2006). See section 4.6 for more details on run ranges.

There remains two non-triggerable leptons:

4.3.5 CMU muon

A muon which is fiducial to the CMU but not the CMP that leaves a muon stub becomes a CMU muon; it must pass the CMU cuts in Table. 4.5.

4.3.6 CMP muon

A track that is fiducial only to the CMP and leaves a stub becomes a CMP muon if it passes the CMP cuts in Table. 4.5.

4.4 Jet Selection

Jets are collections of particles projected in the same direction from the interaction vertex and are the result of a colour octet breaking away from the underlying event. The resulting fragmentation of the quark as it attempts to leave the hadron

Muon Type	variable	cut
All	P_T $Track Z_0 $ E_{em} E_{had} $Track d_0 $ E_T^{isol}/P_T COT Axial Segments COT Stereo Segments	> 20 GeV < 60 cm $< 2 + Max(0, 0.0115 \cdot (P - 100))$ GeV $< 6 + Max(0, 0.028 \cdot (P - 100))$ GeV < 0.2 cm with no silicon hits < 0.02 cm with silicon hits < 0.1 ≥ 3 ≥ 2
CMX	$ \Delta x_{CMX} $ x-fid $_{CMX}$ z-fid $_{CMX}$ runs keystone and miniskirt runs Wedge 14 runs ρ_{COT}	< 6 cm < 0 cm < -3 cm > 150144 > 190697 (< 190697 or > 209760) > 140 cm
CMUP	bluebeam runs	> 154449
CMUP, CMU	$ \Delta x_{CMU} $ x-fid $_{CMU}$ z-fid $_{CMU}$	< 3 cm < 0 cm < 0 cm
CMUP, CMP	$ cmp\Delta x_{CMP} $ x-fid $_{CMP}$ z-fid $_{CMP}$	< 5 cm < 0 cm < -3 cm

Table 4.5: Muon selection cuts

produces a jet of particles. They are selected and quantified using a jet clustering algorithm that groups calorimeter energy clusters together in a cone of $\Delta R < 0.4$. The jet energy estimation and correction is also applied in a standard way, and is estimated using di-jet events in which the jets must balance each other. Jets above 15 GeV are included in this analysis; anything below this is not considered a jet. Jets are also isolated from selected leptons to ensure that the object is not included twice. High energy jets can be falsely identified as electrons or can ‘punch through’ the electromagnetic and hadronic calorimeters to leave a stub in a muon detector which will fake a muon. The estimation of this occurrence and its contribution to the backgrounds is the origin of the fakes sample in section 4.8.1.

4.5 Transverse Missing Energy

The transverse missing energy, \cancel{E}_T , is the deficit of energy in the transverse direction due to undetected particles such as neutrinos exiting the detector. It is a corrected version of the raw missing energy as defined in Eqn. 4.1, except the unit vectors of the towers are modified to originate from the measured interaction point rather than the default co-ordinate origin. Additionally, muons punch through the hadronic calorimeter so their energy must be added into the sum because it can be attributed to a visible particle. Finally, any energy correction to jets, muons or electrons made during off-line processing must be accounted for in the \cancel{E}_T .

dilepton type	bit	run range	name	$\int Ldt$ (pb ⁻¹)
TCE-TCE	1001	141544-236132	em_nosi	2405 ± 144
TCE-PHX	1101	141544-236132	em_si	2273 ± 136
TCE-CMX	1021	150145-236132	em_cmx	2304 ± 138
TCE- (CMUP, CMU, CMP)	1031	141544-236132	em_cmup	2364 ± 141
PHX-CMX	1121	150145-236132	em_cmx_si	2182 ± 131
PHX- (CMUP, CMU, CMP)	1131	141544-236132	em_cmup_si	2234 ± 134
CMUP- (CMUP, CMU, CMP)	0031	141544-236132	cmup_nosi	2420 ± 145
CMX- (CMX, CMUP, CMU, CMP)	0011	150145-236132	mu_nosi	2324 ± 139

Table 4.6: Run ranges of the various dilepton types

4.6 Run range selection

Data up to and including run 236132 was included in the present analysis, a total of 2405 ± 144 pb⁻¹ integrated luminosity which was summed up individually from each run selected. As the data is taken it is labelled as being a good or bad run by the shift crew who decide based on whether there has been any problems with the detector during the run. For each sub-detector, a data bit is set in the collected data to reflect this. The data used in this analysis is therefore only selected from good runs using a list compiled by the Data Quality Management group (DQM) that checks for these bits. For example, if an event contains a phoenix electron, it must have the silicon detector working, and a corresponding data bit set. Also, there are restrictions placed on the run-ranges for certain lepton types due to the particular detector not being operational. Table 4.6 shows the required bits, run-ranges and internal CDF name for each run list. This analysis uses version 17 of the DQM good run lists.

minimum run	maximum run	run period
141544	186599	0d
186599	203799	0h
203799	233079	0i
233133	254686	0j

Table 4.7: Data run ranges. Data is grouped into datasets once it has been taken, with a suffix 0-d,h,i,j denoting the runs which were taken within the period.

During the time that data was taken, the detector underwent changes in set-up and calibration, resulting in periods of stable detector efficiency which vary from period to period. Runs are therefore grouped together (see Table. 4.7) to reflect this, with data sets organised to contain a certain period of stable data taking.

4.7 Data Samples

Data samples are organised into datasets based on which trigger fired to collect the event. An event can therefore be included in more than one dataset if it contained two different triggerable lepton types, and a duplicate check must be made when running over more than one dataset. A list of the data sets used appears in Table 4.8

4.8 Monte Carlo Samples

Standard CDF-generated Monte Carlo samples were used for all the major background covering the entire runrange. $gg \rightarrow H \rightarrow WW$ samples were generated with the Monte Carlo simulator Pythia 6.2⁷⁸; the samples are listed in Table. 4.9. It is more desirable to generate a predetermined number of events to ensure the sample is not statistically limited than it is to use a realistic cross section during

Sample	Triggers Paths	Dataset ID	Run period	# Events
electron	ELECTRON_CENTRAL_18	bhel0d	0d	26499561
		bhel0h	0h	20026640
		bhel0i	0i	40529045
		bhel0j	0j	10420577
muon	MUON_CMx18, MUON_CMUP18	bhmubd	0d	6629080
		bhmu0h	0h	5769254
		bhmu0i	0i	13566019
		bhmu0j	0j	4536149
plug electron	MET_PEM	bpel0d	0d	21755618
		bpel0h	0h	18463953
		bpel0i	0i	33232819
		bpel0j	0j	8551961

Table 4.8: Data samples used in the analysis. The trigger name is shown with the dataset ids, and number of events.

generation, so the actual cross section of the process used in generation is read out of the Monte Carlo log files. The sample is then normalised by calculating a sample-luminosity from the number of events and the cross section, and scaling the sample to the luminosity of the data. Each Monte Carlo sample may also be filtered at generator level to cut out unimportant events, so some cross sections are also modified by a filter efficiency. After generation, the Monte Carlo is passed through a detector simulation but it is not passed through a full trigger simulation. The effect of the trigger is imitated by including a trigger efficiency which is the trigger acceptance for a given fiducial region. It is included within in the event weight.

4.8.1 Fakes

Events in which a jet faked a lepton were estimated from data events¹⁷. Given that the events are already required to have a second lepton and a quantity of

Process	M_H	Run Range	Dataset ID	$\sigma \cdot \text{Br}$ (pb)	#Events
$gg \rightarrow H \rightarrow WW$	110	138809 to 246226	dhgs4a	0.006	1219446
$gg \rightarrow H \rightarrow WW$	120	138809 to 246226	dhgs4b	0.014	1224547
$gg \rightarrow H \rightarrow WW$	130	138809 to 246226	dhgs4c	0.024	1205622
$gg \rightarrow H \rightarrow WW$	140	138809 to 246226	dhgs4d	0.033	1219279
$gg \rightarrow H \rightarrow WW$	150	138809 to 246226	dhgs4e	0.038	1200087
$gg \rightarrow H \rightarrow WW$	160	138809 to 246226	dhgs4f	0.041	1214004
$gg \rightarrow H \rightarrow WW$	170	138809 to 246226	dhgs4g	0.036	1220536
$gg \rightarrow H \rightarrow WW$	180	138809 to 246226	dhgs4h	0.029	1199916
$gg \rightarrow H \rightarrow WW$	190	138809 to 246226	dhgs4i	0.020	1214201
$gg \rightarrow H \rightarrow WW$	200	144428 to 246226	dhgs4j	0.016	1209697

Table 4.9: $gg \rightarrow H \rightarrow WW$ Monte Carlo samples. The $\sigma \cdot \text{Br}$ is taken from a recent report??.

missing energy, these events are mostly W +jet events. First, a fake rate for each lepton type was determined by creating a set of cuts which would define a ‘fakeable object’ for each lepton. These cuts are a subset of the total lepton identification cuts; they are mostly kinematic in nature as the kinematic properties of the leptons are not used to directly identify the leptons. Instead, they are used to reduce the sample from which the fake leptons might come. These fakeable objects comprise a wide variety of phenomena in the detector which have the possibility to pass the lepton identification cut falsely. The fraction of these objects which passed all lepton cuts including the ID-like selection cuts is taken to be the fake rate. The denominator cuts of this process are shown in Table. 4.11; the numerator cuts are the normal lepton cuts.

Along with the lepton datasets used in this analysis, CDF also stores datasets where a jet may trigger. In a similar way to the lepton data, these are sorted according to the trigger that was used to flag the event to be taken. This is performed on four jet samples of increasing jet P_T which come from four triggers which trigger depending upon jet P_T ; these are separated so that they can be

Process	Run Range	Dataset ID	sample ($\sigma \cdot \text{Br}$) (pb)	k-factor	#Events
$Z/\gamma^* \rightarrow ee$ $M_{\ell\ell} > 20 \text{ GeV}/c^2$	141572 to 186598	zewk6d	355 ± 3	1.4	3201770
	190753 to 212133	zewkad	355 ± 3	1.4	6931813
	218180 to 222418	zewkcd	355 ± 3	1.4	1958572
	222426 to 228596	zewkdd	355 ± 3	1.4	1651445
	228664 to 233111	zewked	355 ± 3	1.4	2647205
	233133 to 237795	zewkee	355 ± 3	1.4	2367948
	237850 to 241657	zewkeh	355 ± 3	1.4	1551570
	241665 to 246231	zewkej	355 ± 3	1.4	3004493
$Z/\gamma^* \rightarrow \mu\mu$ $M_{\ell\ell} > 20 \text{ GeV}/c^2$	141572 to 186598	zewk6m	355 ± 3	1.4	3252143
	190753 to 212133	zewk9m	355 ± 3	1.4	6937820
	218180 to 222418	zewkbm	355 ± 3	1.4	1950572
	222426 to 228596	zewkcm	355 ± 3	1.4	1614578
	228664 to 233111	zewkdm	355 ± 3	1.4	2615604
	233133 to 237795	zewkem	355 ± 3	1.4	2379517
	237850 to 241657	zewkfm	355 ± 3	1.4	1546529
	241665 to 246231	zewkgm	355 ± 3	1.4	2982695
$Z/\gamma^* \rightarrow \tau\tau$ $M_{\ell\ell} > 20 \text{ GeV}/c^2$	141572 to 186598	zewk8t	355 ± 3	1.4	9219648
	190753 to 212133	zewkat	338 ± 3	1.4	6916050
WW	141572 to 186598	wewk5d	1.27	1	1652395
	190753 to 212133	wewkbd	1.27	1	3469910
	218180 to 233111	wewkgd	1.27	1	3000603
	233133 to 237795	wewkkd	1.27	1	1100548
WZ	141572 to 186598	wewk6d	0.36	0.76*	1731615
	190753 to 212133	wewkcd	0.36	0.76*	3598792
	218180 to 233111	wewkhd	0.36	0.76*	3192141
	233133 to 237795	wewkld	0.36	0.76*	1279612
ZZ	141572 to 186598	wewk7d	2.01	0.23*	1572769
	190753 to 212133	wewkdd	2.01	0.23*	3456173
	218180 to 233111	wewkdd	2.01	0.23*	3087087
	233133 to 237795	wewkdd	2.01	0.23*	1216664
$W\gamma \rightarrow e\nu\gamma$	141572 to 186598	rewk38	21.48	1.34	328205
	190753 to 212133	rewk28	21.48	1.34	661901
	218180 to 237795	rewk48	21.48	1.34	297846
$W\gamma \rightarrow \mu\nu\gamma$	141572 to 186598	rewk39	21.48	1.34	330468
	190753 to 212133	rewk29	21.48	1.34	688901
	218180 to 237795	rewk49	21.48	1.34	835491
$W\gamma \rightarrow \tau\nu\gamma$	141572 to 186598	rewk2a	21.48	1.34	328166
	190753 to 212133	rewk1a	21.48	1.34	684628
	218180 to 237795	rewk4a	21.48	1.34	828700
$t\bar{t}$	141572 to 237795	tewk2z	6.7	1	1722139

Table 4.10: Background Monte Carlo samples used in the analysis. All are generated with Pythia 6.2. Factors marked with an asterisk are filter factors but have been included here for brevity.

prescaled to keep the rates of the lower P_T jet triggers down.

The overall fake rate was calculated for each of the jet P_T triggered samples. The jet $P_T > 50$ GeV fake rates were found to be the most consistent with the averages of the jet samples, and so these are used in this analysis. The errors on the fake rates are the statistical errors involved in calculating the fake rates.

To avoid contamination from real leptons when measuring fake rates, the mass Z-peak is avoided by excluding the region $76.0 < M_{f,\ell} < 106.0$. Fake rates used in this analysis are listed in Table. 4.12.

Once a fake rate is calculated, a fake sample must be generated by applying the fake rate to fakeable objects within the data. To get the fake sample used in the analysis, events with only one identified lepton are searched through for fakeable objects. These fakeable objects are then artificially made to pass the lepton identification cuts, and are weighted by the appropriate fake rate to create a sample of two-lepton faked events. Should two fakeable objects be found, two fake events are created and both contribute to the fake sample.

4.9 Trigger efficiencies and scale factors

Using well defined lepton types allows trigger efficiencies and scale factors which have been measured by the central CDF Joint Physics group to be used. Trigger efficiencies are shown in Table. 4.13, and scale factors are shown in tables 4.14 and 4.16. Scale factors and reconstruction efficiencies for the muons were re-evaluated for this sample. The TCE Trigger is separated into a tracking efficiency and two E_T dependent efficiencies for the Level 2 and Level 3 components of the trigger path, as in Eqn. 4.2.

lepton type	variable	fakeable object cut
TCE	Region Fiducial E_T Track $ Z_0 $ Track P_T conversion E_{had}/E_{em} Isolation	$==$ CEM $==$ 1 ≥ 10 GeV ≤ 60 cm ≥ 0 GeV $\neq 1$ ≤ 0.125 ≤ 0.2
PHX	E_T $Pes2d\eta$ E_{had}/E_{em} $ Z_0^{PHX} $ Isolation	≥ 10 GeV $1.2 < \eta < 2.0$ ≤ 0.125 ≤ 60 cm ≤ 0.2
all muons	Track $ d_0 $ Track $ Z_0 $ E_T^{isol}/P_T $E_{had} + E_{em}/P$	< 0.2 cm with no silicon hits < 0.02 cm with silicon hits < 60 cm < 0.2 > 0.1 GeV
CMX	P_T ρ_{COT} x-fid $_{CMX}$ z-fid $_{CMX}$ runs keystone and miniskirt runs Wedge 14 runs	> 10.0 GeV > 140 cm < 0 cm < -3 cm > 150144 > 190697 ($< 190697 > 209760$)
CMUP	P_T x-fid $_{CMU}$ z-fid $_{CMU}$ x-fid $_{CMP}$ z-fid $_{CMP}$ bluebeam runs	> 10.0 GeV < 0 cm < 0 cm < 0 cm < -3 cm > 154449
CMU	P_T x-fid $_{CMU}$ z-fid $_{CMU}$	> 20.0 GeV < 0 cm < 0 cm
CMP	P_T x-fid $_{CMP}$ z-fid $_{CMP}$	> 20.0 GeV < 0 cm < -3 cm

Table 4.11: Cuts for the fakeable object denominator. These are a subset of the lepton identification cuts and they are kinematic or fiducial (making sure the object hit the detector) in nature. A fake rate is calculated using the ratio of fully identified leptons to fakeable objects within the sample triggered by jet of $P_T > 50$ GeV. This is then applied to fakeable objects in the data to create a fake sample.

lepton	run period	fake rate (%)		
		20-40 GeV	40-80 GeV	> 80 GeV
TCE	0d	1.0±0.07	1.8±0.13	1.3±0.49
PHX		7.4±0.35	6.7±0.35	7.1±1.7
CMUP		1.0±0.15	2.7±0.38	3.8±0.86
CMX		1.0±0.19	2.8±0.47	1.4±0.62
CMU		1.4±0.35	1.4±0.55	3.8±1.7
CMP		2.2±0.42	4.3±0.88	4.2±1.6
TCE	0h	1.0±0.09	1.7±0.18	1.5±0.72
PHX		7.1±0.45	7.0±0.49	10±2.7
CMUP		0.68±0.15	1.9±0.36	2.5±0.74
CMX		0.68±0.16	1.3±0.30	1.3±0.5
CMU		0.66±0.29	0.92±0.53	0.84±0.84
CMP		1.2±0.37	2.2±0.7	1.4±1.0
TCE	0i	0.75±0.06	1.8±0.12	1.8±0.53
PHX		6.9±0.3	7.1±0.33	9.5±1.8
CMUP		0.47±0.07	1.1±0.13	0.51±0.15
CMX		0.43±0.07	0.75±0.12	0.56±0.16
CMU		0.39±0.12	0.58±0.20	0.59±0.34
CMP		0.44±0.13	0.89±0.23	0.57±0.33
TCE	0j	0.85±0.09	1.6±0.18	1.3±0.75
PHX		6.9±0.48	7.9±0.56	10±2.9
CMUP		0.23±0.06	0.61±0.11	0.27±0.12
CMX		0.25±0.06	0.32±0.09	0.27±0.12
CMU		0.11±0.08	0.58±0.22	0.58±0.34
CMP		0.52±0.16	0.84±0.25	0.37±0.26

Table 4.12: Fake rates applied to the fakeable objects to estimate the fakes sample.

$$\varepsilon_{TCE}^{trig} = \varepsilon_{tracking}^{trig} \cdot \varepsilon_{Level2}^{trig} \cdot \varepsilon_{Level3}^{trig} \quad (4.2)$$

The separate efficiencies are evaluated by using backup triggers which have a subset of cuts of the main path to create denominator objects. The proportion of these passing the total set of trigger requirements in an off-line evaluation gives the efficiencies for those cuts³. Similarly for the ‘MET_PEM’ trigger, the efficiency is a product of the ‘MET’ trigger efficiency and the plug electron trigger’s efficiency (PEM) at each level which are evaluated by comparing them with backup triggers which are less stringent⁵⁶. They comprise a series of turn-on curves so they are dependent on E_T (for the plug electron trigger part of the triggers) and \cancel{E}_T (for the \cancel{E}_T part of the trigger). Muon trigger efficiencies are measured using Drell Yan events with two leptons in an $M_{\ell\ell}$ Z peak window, where one lepton is triggered. The trigger efficiency is the probability for the second lepton to trigger also, so it must be measured using two different triggers as there is no record as to which lepton triggers if there are two candidates. Ideally, the efficiencies of each trigger level would be measured and then multiplied, but triggers are grouped due to technical issues⁸⁵. The Monte Carlo does not have a simulated trigger, so the data’s trigger efficiency is directly applied to the Monte Carlo as a scaling factor. Should there be two triggerable leptons in an event, the efficiency in Eqn. 4.3 is used.

$$\varepsilon_{1\&2}^{trig} = 1 - (1 - \varepsilon_1^{trig}) \cdot (1 - \varepsilon_2^{trig}) \quad (4.3)$$

Lepton ID selection efficiencies are performed in a similar way. Trigger efficiencies used in this analysis are shown in Table 4.13. The Trigger efficiencies for the

electrons are functions modelled on turn-on curves which depend upon the lepton E_T , the precise formulations of which are not listed here. A Drell Yan sample is used with a dilepton mass cut focusing on the Z peak, as these events will overwhelmingly contain two leptons of the same identity. These efficiencies are just the fraction of leptons that pass the ID cuts. For muons the overall efficiency is an ID efficiency multiplied by a ‘reconstruction’ efficiency which is the chance for a track to be associated correctly with its stub. The ID efficiencies are calculated separately for data and Monte Carlo due to the fact that the Monte Carlo has been passed through a detector simulation. The ratio between the two is applied to the simulated events as the resulting ID scale factor. Muon ID scale factors used in this analysis are found in Table 4.16, and muon reconstruction efficiencies are found in Table 4.15. Electron scale factors are found in Table 4.14. A scale factor is applied for both leptons.

4.10 Primary Vertex position efficiency

For the tracking and calorimeter measurements to be accurate, the data must satisfy $z_0 < |60|$ where z_0 is the distance in cm of the event’s primary interaction vertex from the centre of the detector. This is required for the event to remain within the physical core of the COT. However, the luminosity is measured over the whole range, so a factor, ϵ_{vtx} is applied to each Monte Carlo event to correct the luminosity. The average ϵ_{vtx} in this analysis has been measured to be 0.958^{76} .

lepton type	efficiency	run range	value
TCE	ε_{TCE}^{trig}	-	(varies with E_T)
PHX	ε_{PHX}^{trig}	-	(varies with E_T)
CMX ⁵³	ε_{CMX}^{trig}	141544 to 190697	0.97 ± 0.0036
		190697 to 203819	0.96 ± 0.0039
		203819 to 217990	0.95 ± 0.0046
		217990 to 222529	0.95 ± 0.0073
		222529 to 228664	0.94 ± 0.01
		228664 to 233133	0.97 ± 0.0078
		233133 to 237845	0.96 ± 0.0087
		237845 to 241665	0.94 ± 0.013
CMUP ⁵³	$\varepsilon_{CMUP}^{trig}$	141544 to 190697	0.90 ± 0.0044
		190697 to 203819	0.92 ± 0.0039
		203819 to 217990	0.92 ± 0.0048
		217990 to 222529	0.91 ± 0.0067
		222529 to 228664	0.93 ± 0.0067
		228664 to 233133	0.92 ± 0.0056
		233133 to 237845	0.92 ± 0.0061
		237845 to 241665	0.92 ± 0.0078

Table 4.13: Trigger efficiencies used in the analysis. For the electrons, functions are created to mimic the turn-on curves of the trigger with respect to the lepton E_T , the precise formula of which is not listed here.^{3,55,56,59}

lepton type	run range	ID scale factor
PHX	138425 to 186598	0.93 ± 0.006
	190697 to 203799	0.94 ± 0.006
	203819 to 222426	0.94 ± 0.006
TCE	138425 to 186598	0.99 ± 0.004
	190697 to 203799	0.99 ± 0.004
	203819 to 212133	0.97 ± 0.004
	217990 to 222426	0.98 ± 0.006
	222529 to 228596	0.98 ± 0.006
	228664 to 233111	0.98 ± 0.005
	233133 to 237795	0.97 ± 0.007
	237845 to 246231	0.96 ± 0.007

Table 4.14: Electron scale factors applied to the Monte Carlo in the analysis^{14,15,79}. The scale factor is applied as an event weight, and so modifies the overall yield.

lepton type	run range	reconstruction scale factor
CMUP	141544 to 186598	0.95 ± 0.0034
CMX		1.0 ± 0.0007
CMU		0.99 ± 0.003
CMP		0.96 ± 0.0057
CMUP	190697 to 198379	0.94 ± 0.0045
CMX		1.0 ± 0.0011
CMU		0.99 ± 0.0039
CMP		0.97 ± 0.0065
CMUP	233133 to 241664	0.94 ± 0.0036
CMX		1.0 ± 0.001
CMU		0.99 ± 0.0033
CMP		0.95 ± 0.0062
CMUP	241665 to 246231	0.94 ± 0.0042
CMX		0.99 ± 0.0019
CMU		1.0 ± 0.0023
CMP		0.96 ± 0.0067
CMUP	198380 to 203799	0.94 ± 0.0051
CMX		1.0 ± 0.0022
CMU		0.99 ± 0.0039
CMP		0.96 ± 0.0078
CMUP	203819 to 210011	0.94 ± 0.0046
CMX		1.0 ± 0.0015
CMU		1.0 ± 0.0026
CMP		0.96 ± 0.0074
CMUP	210012 to 222426	0.96 ± 0.0042
CMX		1.0 ± 0.0006
CMU		0.99 ± 0.0041
CMP		0.95 ± 0.0076
CMUP	222529 to 233111	0.95 ± 0.0033
CMX		1.0 ± 0.0011
CMU		0.99 ± 0.0029
CMP		0.93 ± 0.0066

Table 4.15: Muon reconstruction scale factors applied to the Monte Carlo in the analysis. The scale factor is applied as an event weight, and so modifies the overall yield.

lepton type	run range	ID scale factor				
		20-30 GeV	30-40 GeV	40-60 GeV	60-100 GeV	> 150 GeV
CMUP	141544 to 186598	0.92±0.063	0.92±0.013	0.94±0.005	0.91±0.03	1.1±0.03
CMX		1.0±0.038	1.0±0.01	1.0±0.006	0.98±0.04	1.1±0.042
CMU		0.86±0.095	0.99±0.019	0.97±0.01	0.82±0.074	1.1±0.047
CMP		0.87±0.12	0.97±0.023	0.96±0.0085	0.97±0.044	1.1±0.049
CMUP	190697 to 198379	0.87±0.077	0.95±0.016	0.94±0.0064	0.93±0.03	0.85±0.25
CMX		0.93±0.053	1.0±0.013	0.98±0.0088	0.93±0.052	0.0±0.0
CMU		0.63±0.19	0.89±0.033	0.95±0.014	1.0±0.06	1.2±0.12
CMP		0.95±0.16	0.93±0.029	0.95±0.011	0.91±0.061	1.0±0.039
CMUP	233133 to 241664	0.76±0.065	0.89±0.014	0.93±0.0054	0.95±0.026	1.1±0.0233
CMX		0.94±0.04	0.97±0.011	0.98±0.0066	0.99±0.039	1.1±0.049
CMU		0.57±0.13	0.96±0.023	0.94±0.011	0.96±0.065	1.1±0.04
CMP		0.91±0.12	0.92±0.026	0.96±0.0086	0.9±0.053	1.1±0.046
CMUP	241665 to 246231	0.77±0.073	0.95±0.014	0.94±0.006	0.89±0.037	0.73±0.21
CMX		0.94±0.056	0.97±0.013	1.0±0.0077	0.95±0.051	0.93±0.22
CMU		0.76±0.13	0.97±0.023	0.94±0.013	0.85±0.091	0.0±0.0
CMP		0.94±0.17	0.91±0.028	0.95±0.0099	0.96±0.054	1.1±0.044
CMUP	198380 to 203799	0.99±0.089	0.96±0.018	0.93±0.0075	0.9±0.04	1.1±0.0408
CMX		0.91±0.07	0.97±0.016	1.0±0.0094	0.81±0.084	1.1±0.088
CMU		0.89±0.18	0.98±0.03	0.97±0.015	0.9±0.11	1.0±0.0
CMP		0.82±0.18	0.98±0.035	0.97±0.012	1.0±0.033	0.0±0.0
CMUP	203819 to 210011	0.77±0.094	0.91±0.017	0.93±0.0068	0.96±0.034	1.1±0.052
CMX		0.95±0.052	0.99±0.014	1.0±0.0076	0.88±0.068	0.0±0.0
CMU		0.93±0.14	0.98±0.028	0.98±0.013	0.98±0.066	1.1±0.13
CMP		0.9±0.18	0.95±0.03	0.97±0.011	0.99±0.04	1.0±0.0
CMUP	210012 to 222426	0.7±0.086	0.94±0.016	0.94±0.0067	0.93±0.039	0.73±0.3
CMX		0.91±0.054	1.0±0.013	1.0±0.008	0.95±0.055	0.54±0.38
CMU		0.83±0.14	0.92±0.033	0.96±0.014	0.85±0.12	1.1±0.074
CMP		1.1±0.13	0.88±0.033	0.97±0.01	1.1±0.011	1.1±0.049
CMUP	222529 to 233111	0.83±0.061	0.94±0.012	0.94±0.0049	0.91±0.025	0.96±0.11
CMX		0.87±0.038	0.98±0.0095	0.99±0.0058	1.0±0.031	0.0±0.0
CMU		0.74±0.1	0.9±0.022	0.96±0.01	0.95±0.052	1.1±0.038
CMP		0.79±0.12	0.95±0.023	0.97±0.0076	1.0±0.031	1.1±0.039

Table 4.16: Muon ID scale factors applied to the Monte Carlo in the analysis. The scale factor is applied as an event weight, and so modifies the overall yield.

Chapter 5

Sample Composition Checks

Checks were made to confirm the modelling of the data by the Monte Carlo and the validity of the trigger efficiencies and scale factors. It is important for the Monte Carlo to be normalised correctly, as too many or too few data events due to badly normalised Monte Carlo may be incorrectly interpreted as a real absence or abundance of signal events. Similarly, if the Monte Carlo is mis-modelled in the variables utilised by the analysis, an apparent excess or deficiency may be caused by a mismatch of data events lying in the wrong phase space region.

5.1 Z cross-section measurement

The Z cross section was measured for every appropriate combination of leptons (ee or $\mu\mu$) in order to confirm the validity of the scale factors and trigger efficiencies used. The cross section was measured using the following formula in Eqn. 5.1.

$$\sigma \cdot BR(Z \rightarrow l^+l^-) = \frac{I_2}{I_1} \frac{N_{obs} - N_{bg}}{A_Z^{weighted} \cdot \epsilon_{zvtz} \cdot \int L dt} \quad (5.1)$$

where:

- I_2/I_1 : Converts the calculation for $Z/\gamma^* \rightarrow l^+l^-$ over the mass region 66-116 GeV into that for $Z \rightarrow l^+l^-$ over the whole invariant mass range. The Drell Yan Monte Carlo only models the Z production and decay, but γ^* possesses the same quantum numbers as the Z; thus the Drell Yan contains both modes, with the indistinguishable γ^* contribution prominent at low di-lepton mass. The proportion of γ^* events is much lower at the higher di-lepton masses where the Z peak occurs, but it is still present in the data. Within the Z peak di-lepton mass window, there is 0.004% extra contribution from γ^* . I_2/I_1 is the ratio over of the integral Monte Carlo yields with and without the γ^* contribution taken in the Z peak di-lepton mass window.
- N_{obs} : the number of signal events is the number of selected data events in which the leptons are oppositely charged.
- N_{bg} : the number of background events estimated by counting the number of selected data events in which the leptons have the same charge.
- $A_Z^{weighted}$: a weighted acceptance is calculated using events which are weighted event by event with $A_Z^{weighted} = A_Z \cdot SF \cdot \epsilon_{trig}$. It is the number of selected, weighted Monte Carlo events divided by the total number of generator-level good Monte Carlo events.
- ϵ_{vutz} : This is the scale factor applied to account for the change in luminosity due to the $|z_0| < 60$ cut. See section 4.10.

- A_Z : Monte Carlo Z acceptance fraction: The numerator is the number of Z events with the measured M_Z in the Z mass window. The total number of generator level good Monte Carlo events is the denominator of the acceptance. It is found by counting the events in which the generator level M_Z lies in the Z mass window, and the primary interaction vertex lies within 60 cm of the detector centre, as measured at the hepg (generator or ‘truth’) level.
- SF : the scale factor corrects for the difference in efficiency of the ID selection cuts between the Data and Monte Carlo. For muons, this is also multiplied by the reconstruction efficiency, SF_{rec} , which accounts for the difference in probability for the muon stubs to be associated with a track correctly within data and Monte Carlo.
- ϵ_{trig} : is the trigger efficiency measured in data to re-weight the Monte Carlo events.
- $\int Ldt$: the integrated luminosity

The Drell Yan cross section values were found to be consistent apart from dileptons containing CMU, which were found to be low in all combinations. The scale factor for CMU was therefore re-weighted by 1.06 such that the average of the cross sections coincides with the weighted average of the remaining dilepton pairs, 256.8 pb. This re-weighting will be accounted for in the error evaluation in Chapter 7. The resulting measured cross sections are shown in Table. 5.1 and in Figure 5.2, with statistical errors shown only. The cross sections are consistent with the CDF measurements of $\sigma_{q\bar{q} \rightarrow Z} \cdot BR(Z \rightarrow \mu\mu) = 260.5 \pm 1.5_{-6.7}^{+5.5} \text{pb}^{16}$ and

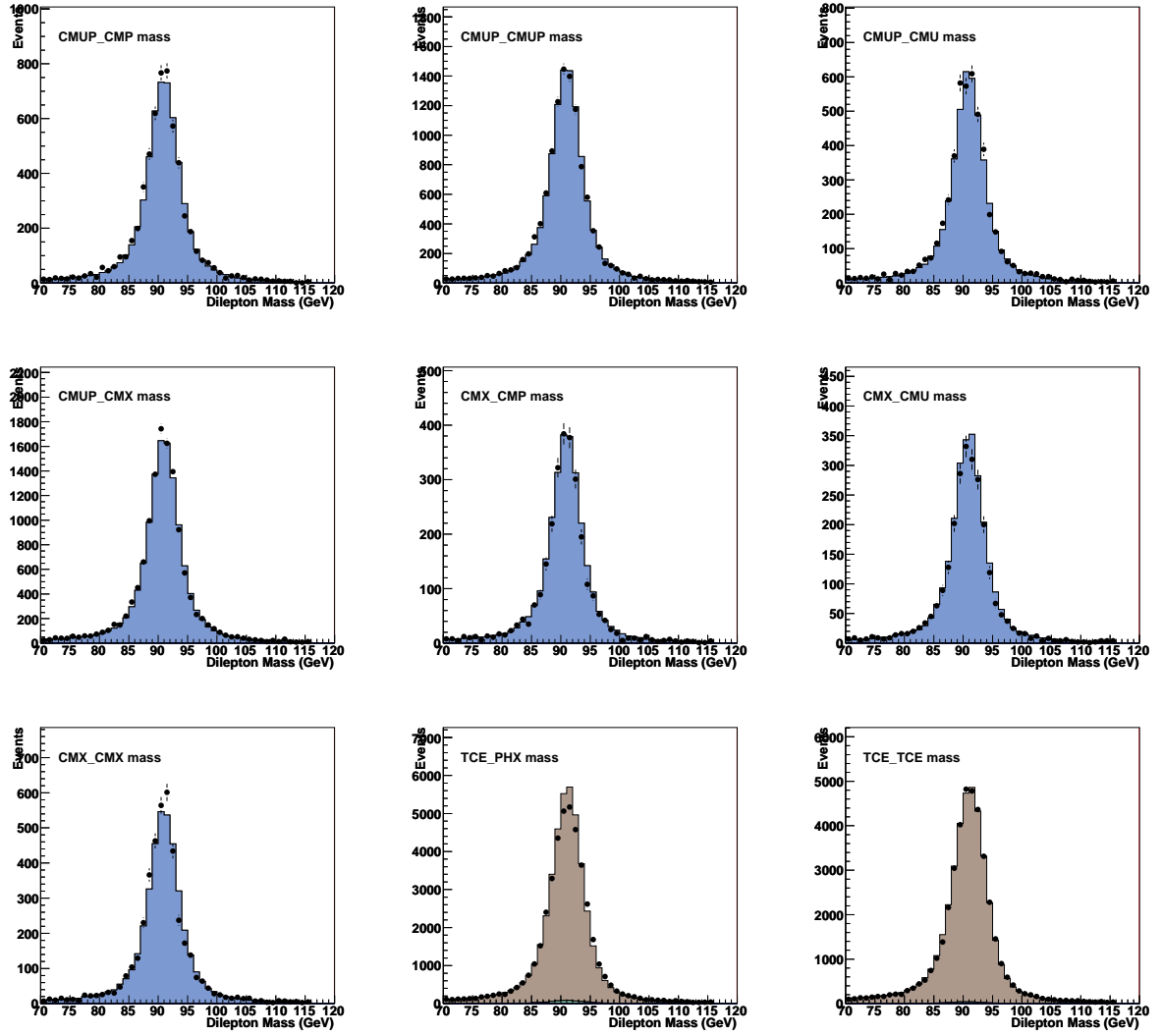


Figure 5.1: Plots of the di-lepton mass showing the Z boson mass peak for di-lepton types used within the analysis. Please refer to section 2.7 for a legend.

Di-lepton combination	$\sigma_{q\bar{q}\rightarrow Z} * BR(Z \rightarrow \ell\ell)$ (pb ⁻¹)
TCE-TCE	258.6 ± 1.4
TCE-PHX	258.4 ± 1.3
CMUP-CMUP	261.0 ± 2.5
CMUP-CMU	266.3 ± 4
CMUP-CMP	263.6 ± 3.5
CMUP-CMX	262.6 ± 2.4
CMX-CMX	255.9 ± 4.2
CMX-CMU	243.8 ± 5
CMX-CMP	247.0 ± 4.8
Average	255.8 ± 3.9

Table 5.1: Drell Yan cross sections

$\sigma_{q\bar{q}\rightarrow Z} \cdot BR(Z \rightarrow ee) = 255.8 \pm 3.9 \pm 5.5\text{pb}^{65}$ and in good agreement with the theoretical value of $\sigma_{q\bar{q}\rightarrow Z} \cdot BR(Z \rightarrow \ell\ell) = 251.3 \pm 5.0\text{pb}^{40}$ once the luminosity errors of 6% on the measured value are included.

5.2 Z Mass measurement

Within the CDF framework, leptons are taken to be massless such that the lepton energy is directly proportional to the momentum magnitude; an energy and a direction can therefore fully describe a lepton. Of these two unknowns, the direction is measured to a far greater precision by the tracking, so the largest uncertainty comes from the energy measurement. Quantities which are proportional to the leptons' four-vectors are consequentially useful for correcting the lepton energies, as this is where any discrepancy is assumed to originate. The mass of the Z boson can be re-created from the two leptons' four-vectors, and can therefore be used to calibrate the lepton energies. To do this, a double Gaussian is fitted to the mass peak shown in Fig. 5.1. The measured M_Z in the Drell Yan Monte Carlo

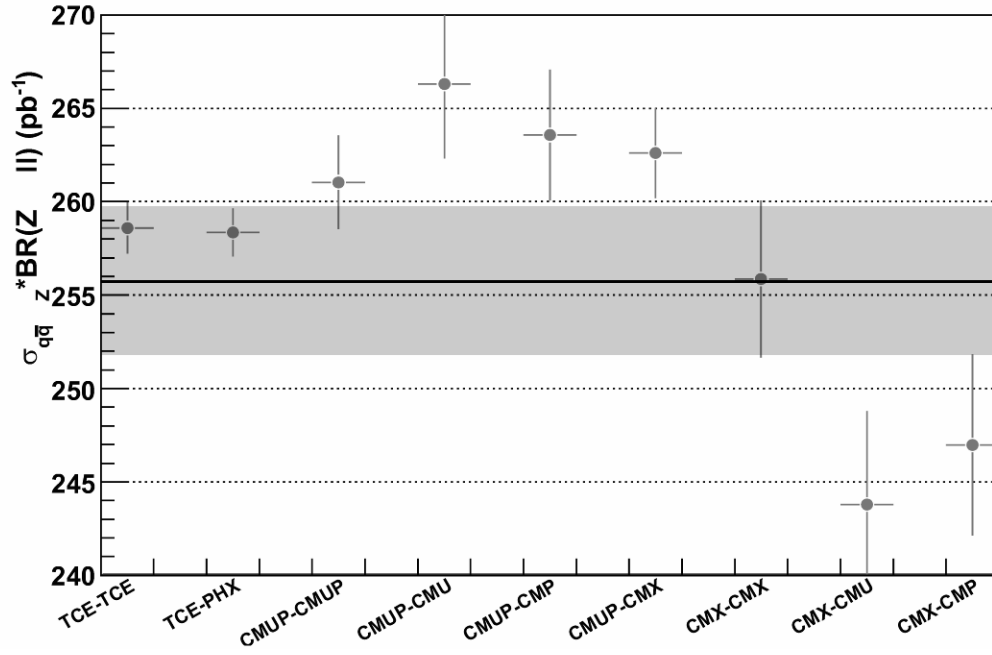


Figure 5.2: Measured $\sigma_{q\bar{q} \rightarrow Z}^* BR(Z \rightarrow \ell\ell)$ separated by di-lepton type with statistical errors only

Dilepton type	Z Mass (GeV/c ²)	Z Mass (GeV/c ²)
	Monte Carlo	Data
TCE-TCE	91.08 \pm 0.01	91.11 \pm 0.02
TCE-PHX	91.08 \pm 0.00	91.16 \pm 0.02
CMUP-CMUP	90.96 \pm 0.01	90.90 \pm 0.04
CMUP-CMU	90.96 \pm 0.01	90.88 \pm 0.05
CMUP-CMP	90.94 \pm 0.01	90.80 \pm 0.05
CMUP-CMX	90.97 \pm 0.01	90.90 \pm 0.03
CMX-CMX	90.97 \pm 0.01	90.72 \pm 0.05
CMX-CMU	90.96 \pm 0.02	90.94 \pm 0.07
CMX-CMP	90.95 \pm 0.01	90.86 \pm 0.06
Average	91.03 \pm 0.00	91.02 \pm 0.01

Table 5.2: Measured Z masses for the different same-type di-lepton combinations. Only statistical error are displayed

is compared with the Monte Carlo pole mass value of 91.0 GeV/c², and thus the data is required to match. All values were within 0.4% of 91.0 GeV/c² except masses containing PHX electrons, which were around 1% high. The PHX lepton energies were corrected by 1.4% to correct the TCE-PHX Z mass; the correction is included in the error estimation of the lepton energy (see section 7.1.2). Measured values of M_Z are shown in Table. 5.2 and Fig. 5.3

5.3 W^+W^- background cross-section measurement

A cross check of the W^+W^- sample normalisation was achieved by applying cuts in Table 5.3 similar to those from a recent analysis which isolates the W^+W^- background in order to measure the W^+W^- cross section⁷. The actual cuts used here are not quite the same, as the cuts in the cross section analysis include a cut on $\cancel{E}_T^{significance}$, which is defined as $\cancel{E}_T/\sqrt{\sum E_{unclustered}}$. $E_{unclustered}$ is energy detected and measured in the calorimeter which is not grouped into a cluster (which would

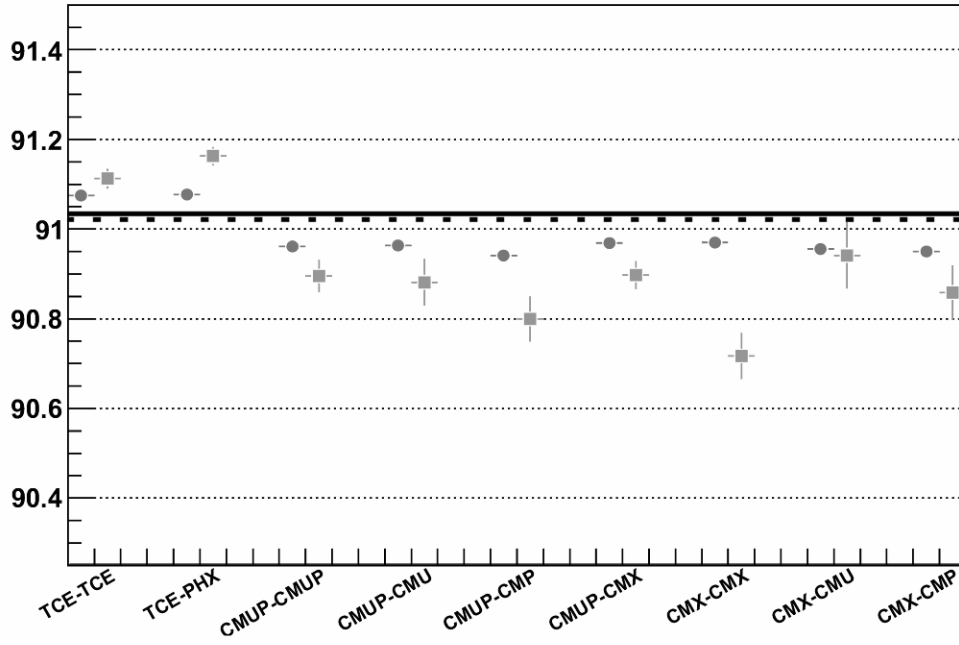


Figure 5.3: Measured Z masses for the different same-type di-lepton combinations. The round points represent values from Monte Carlo, and the square points are measured from data. Only statistical errors are shown.

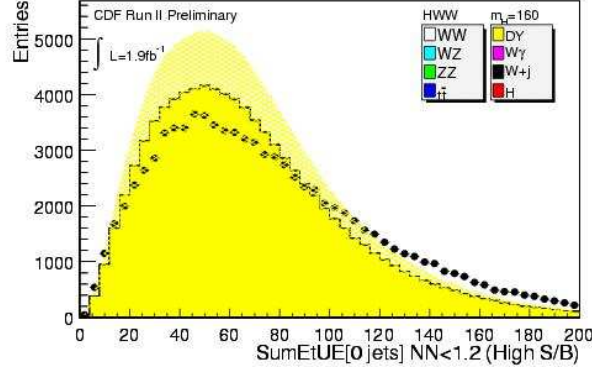


Figure 5.4: $E_{unclustered}$, the sum of the unclustered energy in the detector, is more peaked in the montecarlo simulation than in data⁵¹. The data is the black points, and the Monte Carlo is the filled region, which is dominated by the yellow Drell Yan. A hashed yellow region represents the errors used in the studies. This excludes the variable $\cancel{E}_T^{significance} = \cancel{E}_T / \sqrt{\Sigma E_{unclustered}}$ from the analysis.

cut
2 leptons $E_T > 20$ GeV
$\cancel{E}_T > 25$ GeV
no standard jets ($E_T > 20$ GeV, $ \eta < 2.5$)
leptons of opposite charge
if $\cancel{E}_T < 50$ GeV, $\Delta\phi_{\cancel{E}_T, \ell j} > 0.3$

Table 5.3: Cuts for the WW normalisation cross check

signify a high energy particle's collision). In a parallel analysis⁵¹, $E_{unclustered}$ was found to be badly modelled, mainly due to the inclusion of events with higher jet multiplicity. Figure 5.4 shows the data distribution to be more flat with a greater tail.

Consequently, \cancel{E}_T is substituted into the final cuts instead of $\cancel{E}_T^{significance}$. Plots of \cancel{E}_T , $M_{\ell\ell}$, $\Delta\phi_{\ell\ell}$ and $\Delta\phi_{\cancel{E}_T, \ell j}$ are shown in Figure 5.5, and the data and Monte Carlo agree within errors.

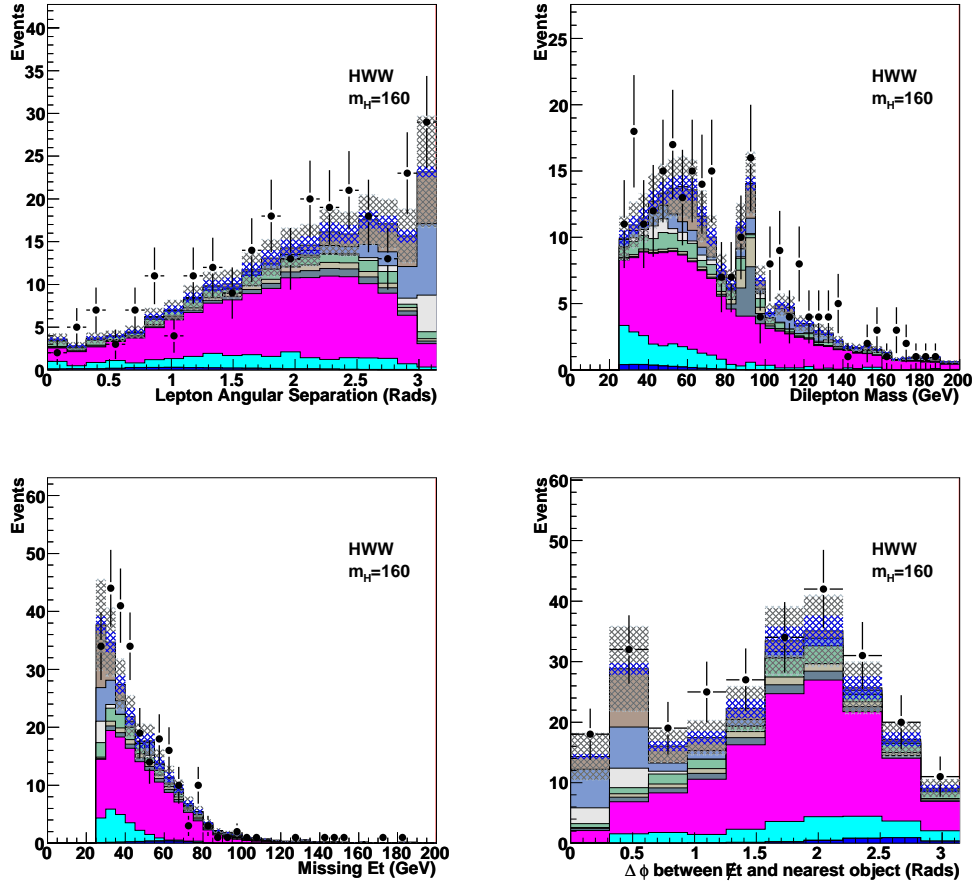


Figure 5.5: Plots of four input variables used in the multivariate analysis once the W^+W^- normalisation cross check cuts have been applied. The plots show good agreement between data and Monte Carlo within the systematic errors found in chapter 7. A guide to the backgrounds can be found in section 2.7. The dominant magenta background is W^+W^- . Please refer to section 2.7 for a legend.

5.4 Fake background cross checks

The fake background contains as many same-sign events as opposite-sign events due to the nature of the fake lepton which not physically constrained to be of any charge. This is not true of the other backgrounds, so looking at events where the leptons are the same sign will isolate the fakes, and can be used to check the fake normalisation. Figure. 5.6 shows plots of \cancel{E}_T , $M_{\ell\ell}$, $\Delta\phi_{\ell\ell}$ and $\Delta\phi_{\cancel{E}_T,\ell j}$ in the same sign region; the $e\mu$ channel is shown in which the larger contribution from $Z \rightarrow ee$ (where the PHX lepton charge is mis-measured) is not present. The plots show the fakes are well behaved and within the large fake errors.

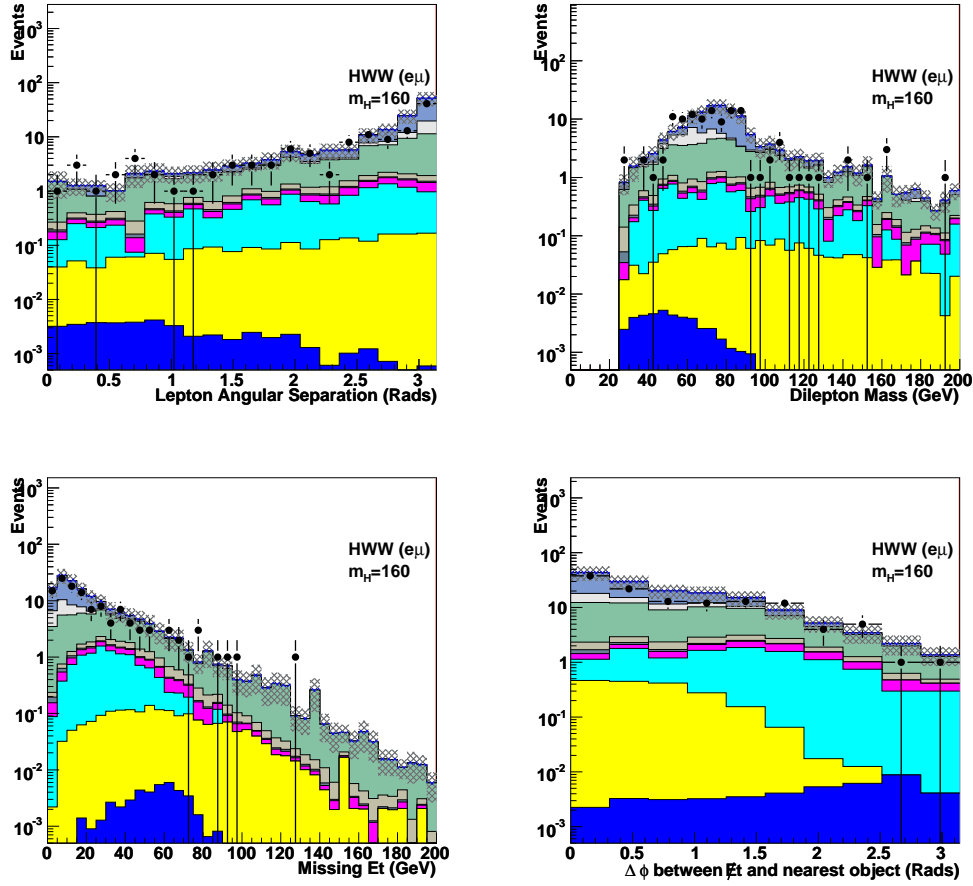


Figure 5.6: Same sign cross check plots of four of the input variables for the main analysis. The plots show good agreement between data and Monte Carlo, signifying that the fake background is well understood and normalised correctly. A guide to the backgrounds can be found in section 2.7. The dominant green background is the fake background. Please refer to section 2.7 for a legend.

Chapter 6

Analysis Method Overview

The three major backgrounds to the $gg \rightarrow H \rightarrow W^+W^-$ signal are $t\bar{t}$, W^+W^- and Drell Yan. The $t\bar{t}$ signal has been found in a previous analysis¹ to be efficiently removed with jet cuts in Table. 6.1. A break down of the effect of the cuts can be found in Appendix A. Two neural nets are then trained using Monte Carlo to reject the two largest backgrounds, Drell Yan and W^+W^- . Once the samples are applied to the neural net, the score plot is cut upon to reject the background. The remaining events are then run through the second neural net to discriminate between $gg \rightarrow H \rightarrow W^+W^-$ and W^+W^- -background. The sample was split by lepton type into ee , $e\mu$ and $\mu\mu$, with neural nets trained separately on each, as the different combinations exhibit different characteristics and systematic errors. A likelihood test is performed on the resulting plots.

Index	Sample Selection Cut
1	two leptons with $p_T > 20$ GeV
2	$M_{\ell\ell} > 16$ GeV
3	$N_{Jets}(E_T > 15 \text{ GeV}) = 0 \parallel N_{Jets}(E_T < 55 \text{ GeV}) = 1 \parallel N_{Jets}(E_T < 40 \text{ GeV}) = 2$
4	opposite lepton charge signs

Table 6.1: Cuts placed on the input variables before the multivariate analysis

6.1 Pre-analysis Cuts

Initial cuts are placed before a multivariate analysis is performed to remove irrelevant phase space areas or areas known to be beyond the modelling capabilities of the Monte Carlo used (Table 6.1). A cut on the lepton E_T is placed at 20 GeV. A lower $M_{\ell\ell}$ cut is placed to remove contributions from γ^* contamination in the Drell Yan process which is not modelled in the Monte Carlo, and also to remove any J/ψ backgrounds. In samples with one jet, a E_T^{jet} cut is placed at 55 GeV, and in two jet events, this is tightened to $E_T^{jet} < 40$ GeV for both jets to remove $t\bar{t}$ (and $b\bar{b}$) backgrounds which are not trained upon and would otherwise be substantial. This will affect the signal minimally as the jets in the signal sample originate from initial state radiation and are therefore softer. Finally, a requirement that the leptons to be oppositely charged is made.

Plots of the jet multiplicity and transverse energies of the jets cut upon in Table 6.1 are shown in Fig. 6.1. Regions accepted by the cuts show good agreement between data and Monte Carlo within the accepted regions, and so the multivariate analysis can proceed with confidence.

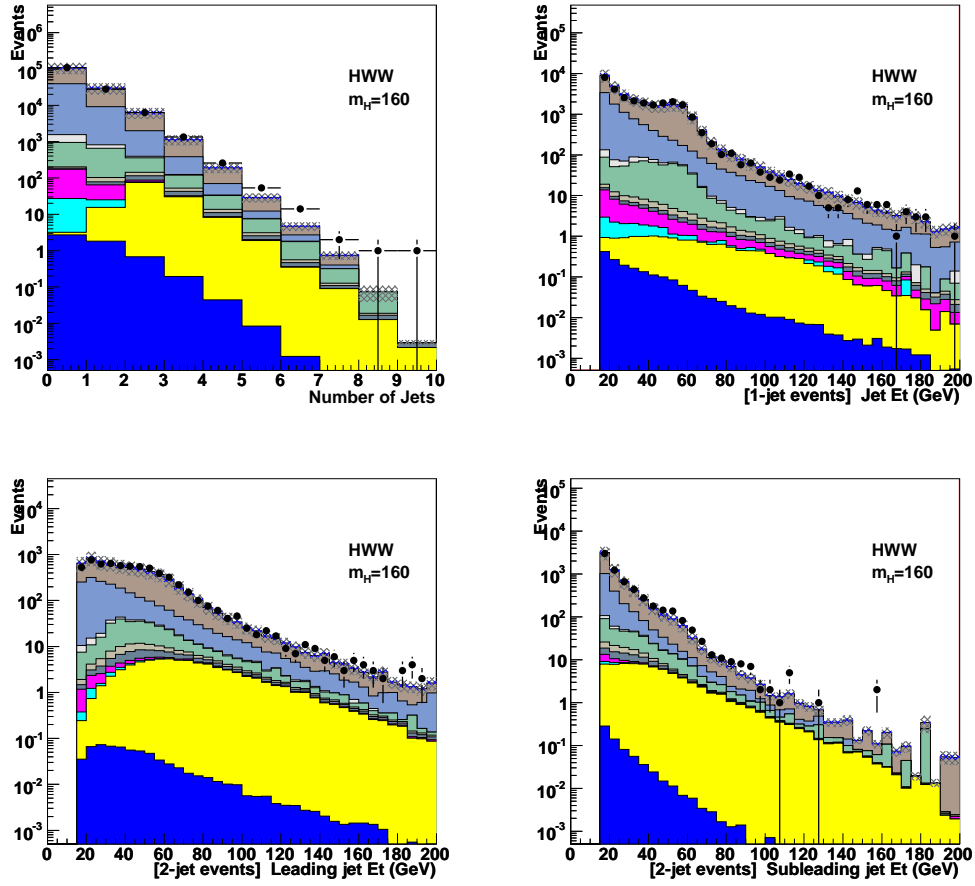


Figure 6.1: Plots of the jet multiplicity and the energies of the primary and secondary jets (if present).

TMVA Method Name	description
Likelihood	simple likelihood test on each variable
LikelihoodD	likelihood test with the input variables de-correlated
Fisher	Fisher discriminate analysis
CFMlpANN	Clemont Ferrand Neural Net
H Matrix	Hessian Matrix element Method
PDERS	Multi-dimensional Likelihood fit
BDTGini	Boosted Decision Tree Method

Table 6.2: Multivariate analyses available and investigated with TMVA

6.2 Multivariate Techniques

The methods contained in a computer package named T-MultiVariableAnalyser (TMVA) were used to increase the signal to background separation over more traditional cut based analyses³¹. TMVA is packaged with the ROOT program from version 5.00 onwards, and implements a range of multivariable discrimination techniques which can be compared to find the best techniques for the data. When using TMVA, the training and testing were performed within a ROOT macro environment; the implementation of the TMVA weights in the analysis was performed in stand-alone code fully compiled outside of root, but using root libraries.

All the techniques in Table. 6.2 were initially compared together to see which method would produce the best overall results. An outline of the methods compared are as follows:

- Likelihood tests use a simple probabilistic technique based in which bin of the input variable histograms the event lies. It then generates a probability using the number of predicted signal and background events in the bin and evaluates them all to gain an over all probability of signal.
- The Fisher technique finds a combination of the variables (similar to a single

first level neural net node - see section 6.3) which is found by assessing the correlation of the signal and background variables in each input variable. This is then used to find the optimal combination of variables in order to separate the signal and background.

- Neural nets comprise a network of nodes which represent weighted sums of the input variables and is discussed further in section 6.3.
- The H Matrix is similar to the Fisher method but more basic; it uses a covariant Hessian matrix which consists of all the correlations of the variables, but models the variables as Gaussian distributions around the correlation directions in the Hessian matrix, and performs a χ^2 on the data relative to either signal or background Monte Carlo to evaluate a likelihood.
- The Multi-Dimensional likelihood fit is similar to the likelihood method, except that the probability is evaluated by counting signal and background events in a volume of the variable hyperspace around the event, thus evaluating the probability in all the dimensions. The technical difficulties in this lie in choosing the volume size in the space, akin to the bin size in the normal one-dimensional likelihood test.
- The boosted decision tree method creates a series of decision trees. Each of these is a random sequence of cuts placed on the input variables, with each new variable's cut varying depending on whether the event passed the previous cut or not. This creates per tree a random set of bins which are independent and contain different proportions of signal and background. An overall likelihood test is performed on all the bins created by a number of such

decision trees called a ‘forest’. To optimise this forest, poorly-discriminating trees are removed or ‘pruned’. Boosting refers to weighting the events in importance such that trees which separate difficult events are kept.

The investigation was performed with W^+W^- as background and $H \rightarrow W^+W^-$ with $M_H = 160$ GeV as signal, because the differentiation between these is the most crucial. As an investigative measure, the procedure was done with only 1000 events of each, and with standard settings for the various techniques. Fig. 6.2 reveals that the neural net is no worse than the other methods, and was chosen for the analysis.

6.3 Neural Nets

A neural net is essentially a series of weighted sums of the input variables⁷⁴. Conceptually, it is based upon a model of the brain as a network of neurons linked together with synapses; each neuron has a response to stimuli from inputs⁶⁷. The architecture is shown in Fig. 6.3. The input variables’ values per event are represented by the first line of circles in the diagram.

In analogy to the brain, each of the sums is given the term ‘node’ or ‘neuron’, of which the result is represented by a circle in Fig. 6.3 denoted by HN_i . Each coefficient in a sum is known as a ‘synapse’, and are represented in the figure by lines linking the nodes. Additionally, each node imposes an ‘activation function’ on the sum of the weighted synapse scores it receives. The activation function gives an output from 0 to 1 and is usually easily differentiable, for reasons explained later; the sigmoid function (Fig. 6.4) is the most common choice. The activation functions allow the neural net to exhibit non-linear behaviour. A neural net is

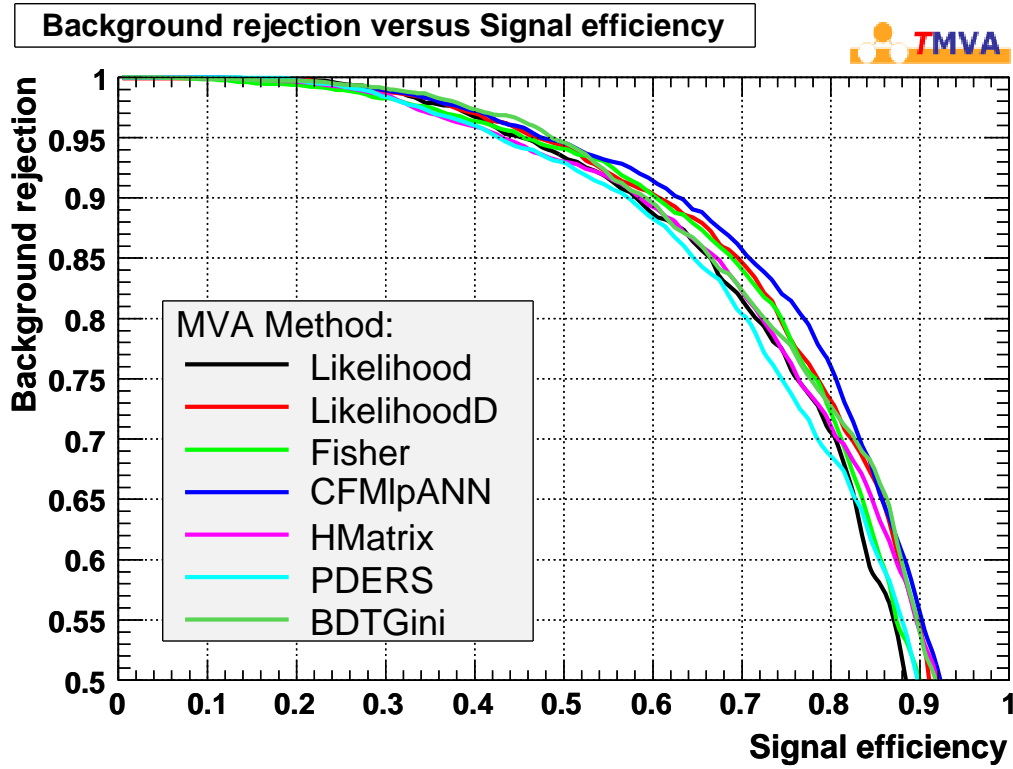


Figure 6.2: Background rejection vs. signal efficiency plots for the methods available in TMVA v2.1 after training on Higgs \rightarrow WW (signal) and WW (background) Monte Carlo samples from run periods 0d+0h at M_h of 160 GeV. A key to the methods is found in Table. 6.2

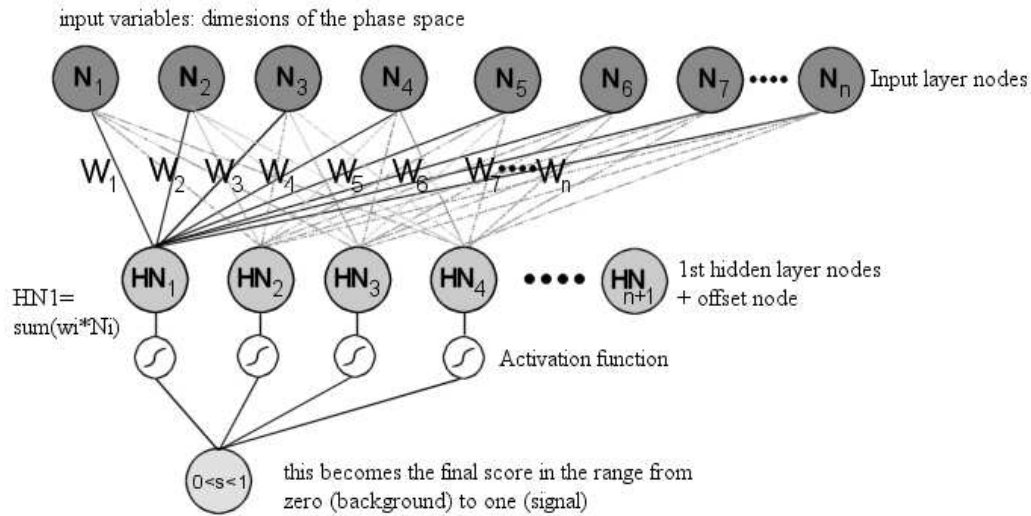


Figure 6.3: A schematic diagram of the neural net architecture. It comprises of layers of nodes, in this case there is one input layer, one hidden layer and one output layer. The input nodes are the input variable values. These are connected to all nodes in the hidden layer by means of synapses, displayed as lines in the diagram, which weight the input variable by a weight which is changed during training to achieve the best overall result. The synapse weights multiplied by the variables' values are summed in each of the hidden layer nodes, and each subjected to the activation function (see Fig. 6.4). These are then summed in a similar fashion in the output node to give a score.

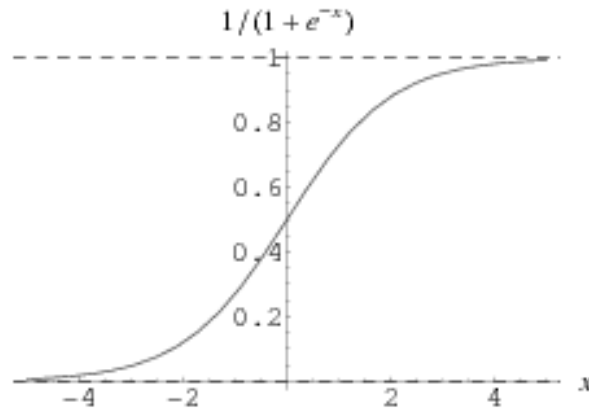


Figure 6.4: A plot of the sigmoid function. The nodes in a neural net often require an ‘activation function’ to be applied to the weight that they calculate to attempt to mimic the response of neurons in the brain. The most common is the sigmoid function as its simple derivative is useful in the back propagation of errors.

often arranged in layers of sums, such that the first set of sums are performed in parallel, and these form the input variables to the next layer. The neural nets in this analysis contain only one intermediate layer of nodes, often called a ‘hidden layer’, and an output layer which is only one node long for the output node. The value calculated by the output node becomes the neural net score for the event being considered, and in the following discussion, ‘output’ and ‘neural net score’ will be used interchangeably. However, it is permitted for neural nets to contain more than one hidden layer, or to possess a non-layer architecture.

The net works by tuning the coefficients of the sums (the weights in the synapses) such that a set of input values from a background event will, averaged over a sample set, give a score from the output node different to that when using a set of input values from a signal event. In particular, the output node is encouraged to give a 0 score from a background event, and a 1 score from a signal event. Thus, the efficiency of the net is the average absolute difference of

the event's actual scores from their intended scores. This is called the 'total error' which will be named ϵ_T from now on to avoid confusion with other errors.

The minimisation of ϵ_T or 'training' is an iterative process over a sample set containing signal and background events, with each iteration being labelled an 'epoch'. This is usually one cycle through all the events, or a sub-set of the training events. Training usually employs 'back propagation of errors' which distributes ϵ_T backwards through the nodes, assigning each node a local error, ϵ_L , which is proportional to their previous nodes' ϵ_L by the weight of the synapse which links them.

In summary, the training fixes the coefficients of multiple sums of the input variables' values. This is optimised by the training such that variable values from signal events produce sums scores close to 1, and background events' variable values produce sum scores close to 0.

After each epoch, the weights are modified to reduce ϵ_T . The technique involved in reducing the error depends on the neural net type. Many neural nets view the minimisation of ϵ_T as the minimisation of the ϵ_L s as a function of the weights. Thus, many training methods seek to modify the weights based upon steepest decent algorithms, with $\delta\epsilon_{Li}/\delta w_i$ as the gradients of the function. This is why neural nets prefer easily differentiable activation functions. Once a direction of steepest descent is identified, a line search for the lowest ϵ_T is performed to find the next set of weights by following the steepest descent direction until ϵ_T starts to increase.

TMVA incorporates three neural nets, of which the ROOT neural net, TMulti-LayerPerceptron (TMLP) was the fastest and most effective. TMLP itself incorporates five minimisation techniques as listed in Table. 6.3, and these were compared

TMVA Method Name	description
TMLpBat	Batch Learning
TMLpSD	Steepest Descent
TMLpRP	Ribiere Polak Learning algorithm
TMLpFR	Fletcher Reeves Learning algorithm
TMLpBFGS	Broyden, Fletcher, Goldfarb, Shanno (BFGS)

Table 6.3: Cuts placed on the input variables before the multivariate analysis

to find the best technique.

- Batch learning is a stochastic learning process in which each weight is guessed by adding a small change to the previous guessed weight based upon the change in the error of the weight. ‘Batch’ refers to the fact that the update is performed after all the events are processed in one epoch.
- In steepest descent minimisation, a line search is performed in the direction of the steepest descent as prescribed by the $\delta\epsilon_{Li}/\delta w_i$. The new weights become the weights at this lowest ϵ_T error point, and the process is repeated to find a new steepest descent direction.
- The steepest descent method will suffer when a valley is found in the function, as it will choose directions which cross the valley continually, without finding the vector pointing down the valley. The Ribiere Polak Learning algorithm and the Fletcher Reeves Learning algorithm are both methods which seek to correct this by modifying the steepest descent vector by a small amount to create a conjugate direction along which the line search is performed. The change in the steepest descent vector in both cases is calculated from the last but one set of weights so that an element of second order change in the steepest descent can be evaluated.

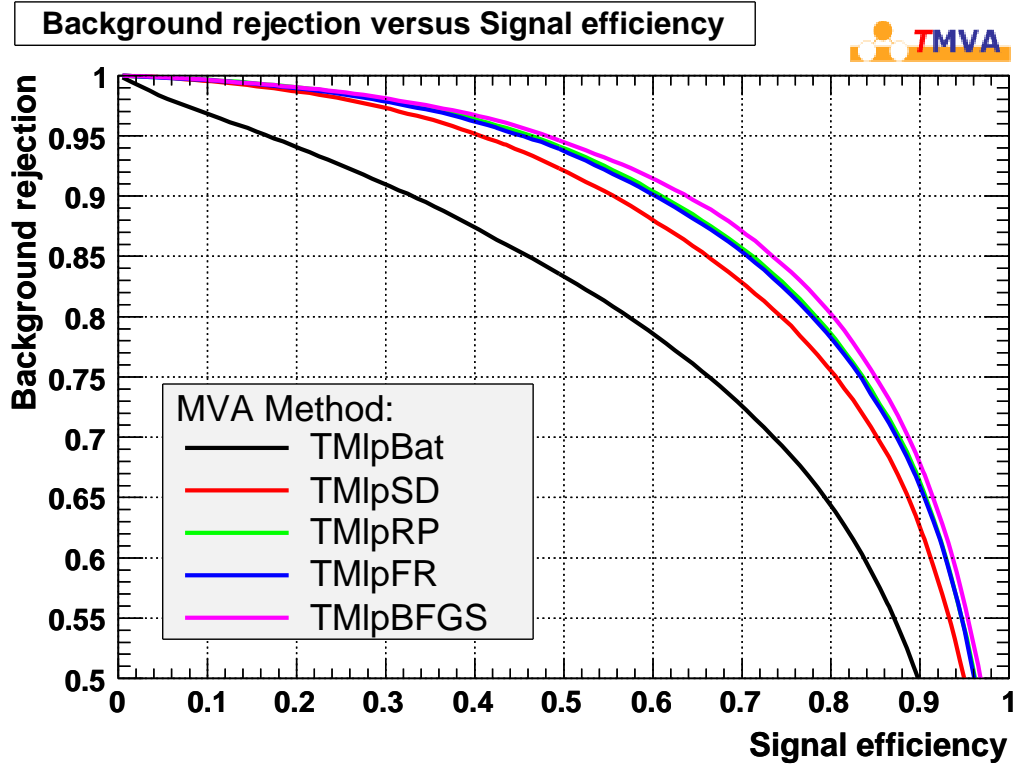


Figure 6.5: Background rejection vs. signal efficiency plots for the training methods available with TMLP using TMVA v3.3.3 after training on Higgs \rightarrow WW (signal) and WW (background) Monte Carlo samples from the 0d+0h run range at at M_h of 160 GeV. A guide to the training methods can be found in table 6.3

- The Broyden, Fletcher, Goldfarb, Shanno method seeks to evaluate this second order change in the steepest descent direction directly by approximating the Newton method. Second order differential information is collated in a hessian matrix to more accurately guess the most optimal direction for descent.

Fig. 6.5 shows that the Broyden-Fletcher-Goldfarb-Shanno (BFGS) method gave the best results.

TMVA also gives the option of pre-processing which creates an alternative set of de-correlated variables from the standard input variables. The difference in

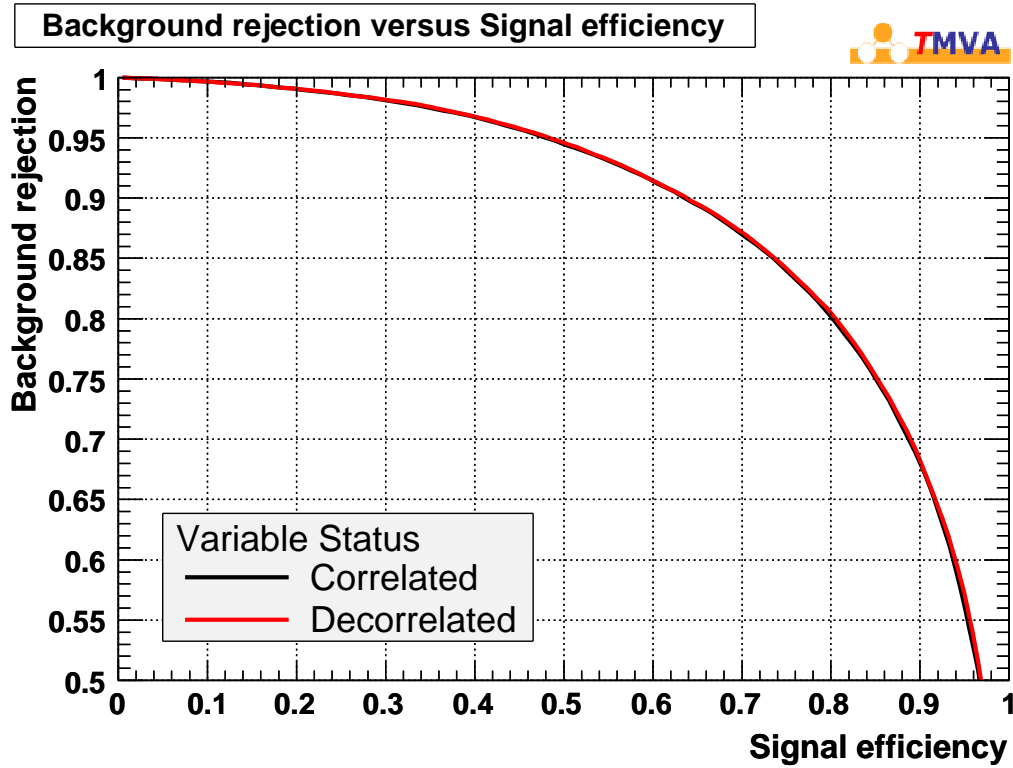


Figure 6.6: Background rejection vs. signal efficiency plots for the TMLP using the BFGS training method, showing the improvement afforded by de-correlating the input variables. This uses TMVA v3.3.3 and is trained on Higgs \rightarrow WW (signal) and WW (background) Monte Carlo samples from the 0d+0h run range at M_h of 160 GeV.

performance of using de-correlated variables to the standard variables is shown to be negligible in Fig. 6.6. Standard variables with no pre-processing were therefore used, as they required less processing time.

6.4 Input Variables

Input variables were based on values used in a previous analysis¹ which used cuts to increase the signal to background ratio of the cut sample, and improved upon a study into finding a Higgs in this channel at the Large Hadron Collider¹⁸. The

neural net was used to implement the variables in a more efficient way, so any variable used in a cut was used as an input variable to the neural net. The input variables used are those in Table 6.4. A number of other variables were also tested, but resulted in no significant improvement in discrimination of the neural net:

- Missing E_T Significance. This is defined as the missing energy magnitude divided by the square of the sum of the unclustered energy from the calorimeters in the event, ‘SumEt’. This has been used in analyses used to isolate W^+W^- . It was found that in events with 2 jets the SumEt was badly modelled in the Drell Yan Monte Carlo, and so this variable was removed from the analysis.
- Number of jets.
- The dilepton transverse mass. This is the mass of the addition of the leptons’ four-vectors with P_z set to 0. It was thought that using a transverse quantity may be more accurate due to the exclusion of poor P_z measurements and less likely to hinder the training process due to a smearing of the proper values.
- The dilepton + \cancel{E}_T transverse mass. This is the same as before with the four-vector of the missing energy also included in the four-vector sum. This was thought to potentially contain more information on recreating the W bosons masses.
- The mass of the vector sum of all transverse quantities measured in the event including leptons, jets, and \cancel{E}_T . This was thought to reflect the momentum of the underlying event system. The rest mass of the vector sum was also calculated by boosting the summed vector.

Variable Label	quantity
LepAEn	Energy of the most energetic lepton
LepBEn	Energy of the other lepton
dilmass	Mass of the 4 vector sum of the leptons
metmag	Missing transverse energy (\cancel{E}_T)
addEt	scalar sum of the leptons' E_T and \cancel{E}_T
dPhiMetLJ	Azimuthal angle between \cancel{E}_T and the nearest lepton or jet in azimuth.
jet1_Et	transverse energy of the first jet
jet2_Et	transverse energy of the second jet
dildphi	separation in ϕ of the two leptons ($\delta\phi_{\ell\ell}$)
lepR	separation in R of the two leptons $\sqrt{\delta\phi_{\ell\ell}^2 + \delta\eta_{\ell\ell}^2}$

Table 6.4: Input variables used in the multivariate analysis.

Plots of these variables can be seen in Figs. 6.7 and 6.8, and the data and Monte Carlo are seen to agree within errors. Plots of the input variables separated into ee , $e\mu$ and $\mu\mu$ are available in Appendix B

6.5 Method

To avoid confusion, the term ‘physical background’ will refer to a sample containing a simulation of a physical process which may be confused with the Higgs sample. The term ‘sample background’ will refer to the sample of events which is presented to the neural net to train against a ‘signal’ sample. The training background sample may contain one or more physical background samples, or may consist of different physical backgrounds in different neural nets. The neural net is used twice within the analysis, once to remove the largest background after initial cuts, namely Drell Yan; the score distribution from this was then cut on to remove Drell Yan events, and a second neural net was used to differentiate the signal from the next largest background, W^+W^- . The W^+W^- trained neural net was

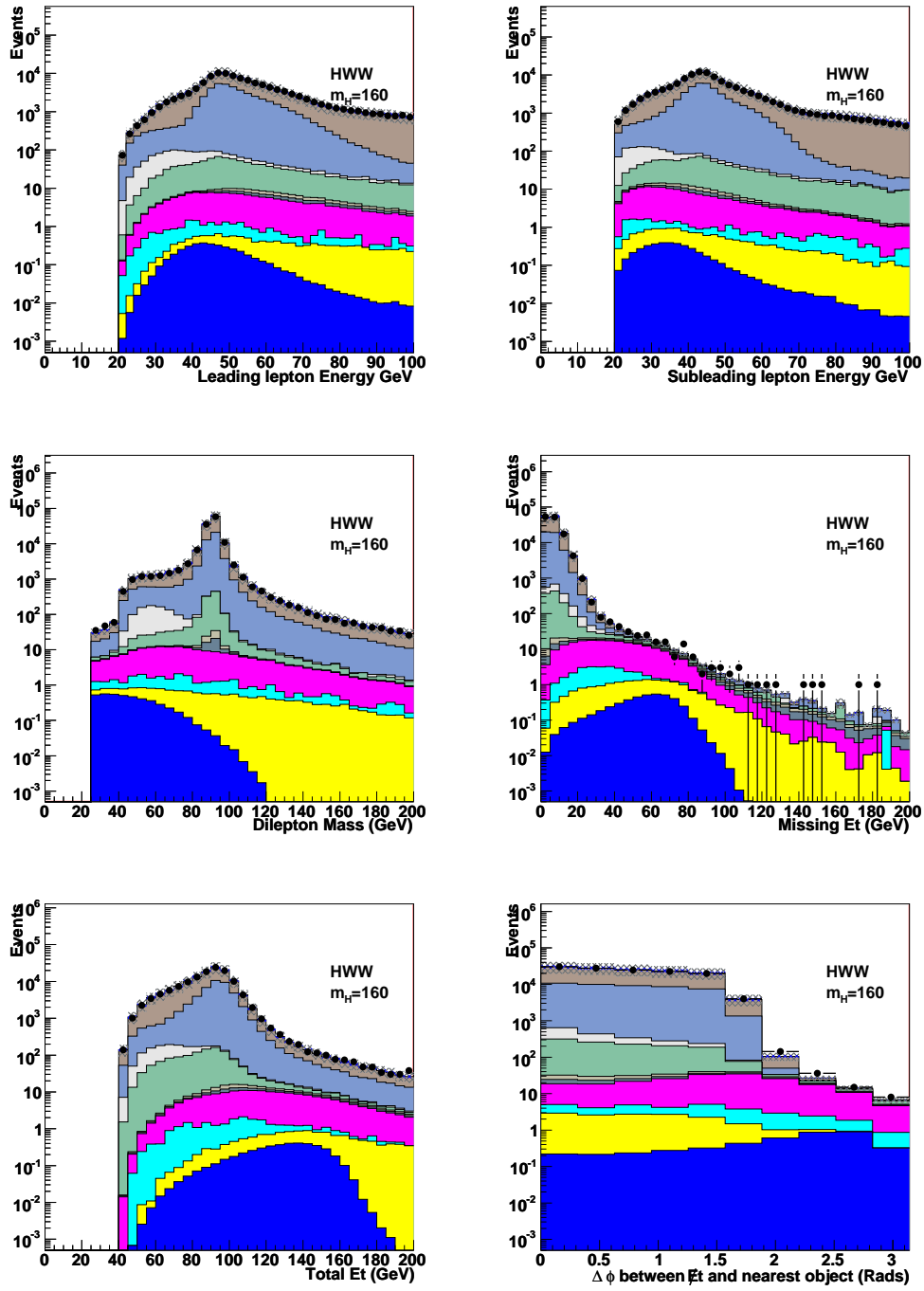


Figure 6.7: Plots of input variables used in the multivariate analysis. This is to check the modelling of the Monte Carlo can be trusted before the neural net is trained. Although all backgrounds are shown here, only the Drell Yan, W^+W^- , and $gg \rightarrow H \rightarrow W^+W^-$ components are used in the training. Please refer to section 2.7 for a legend.

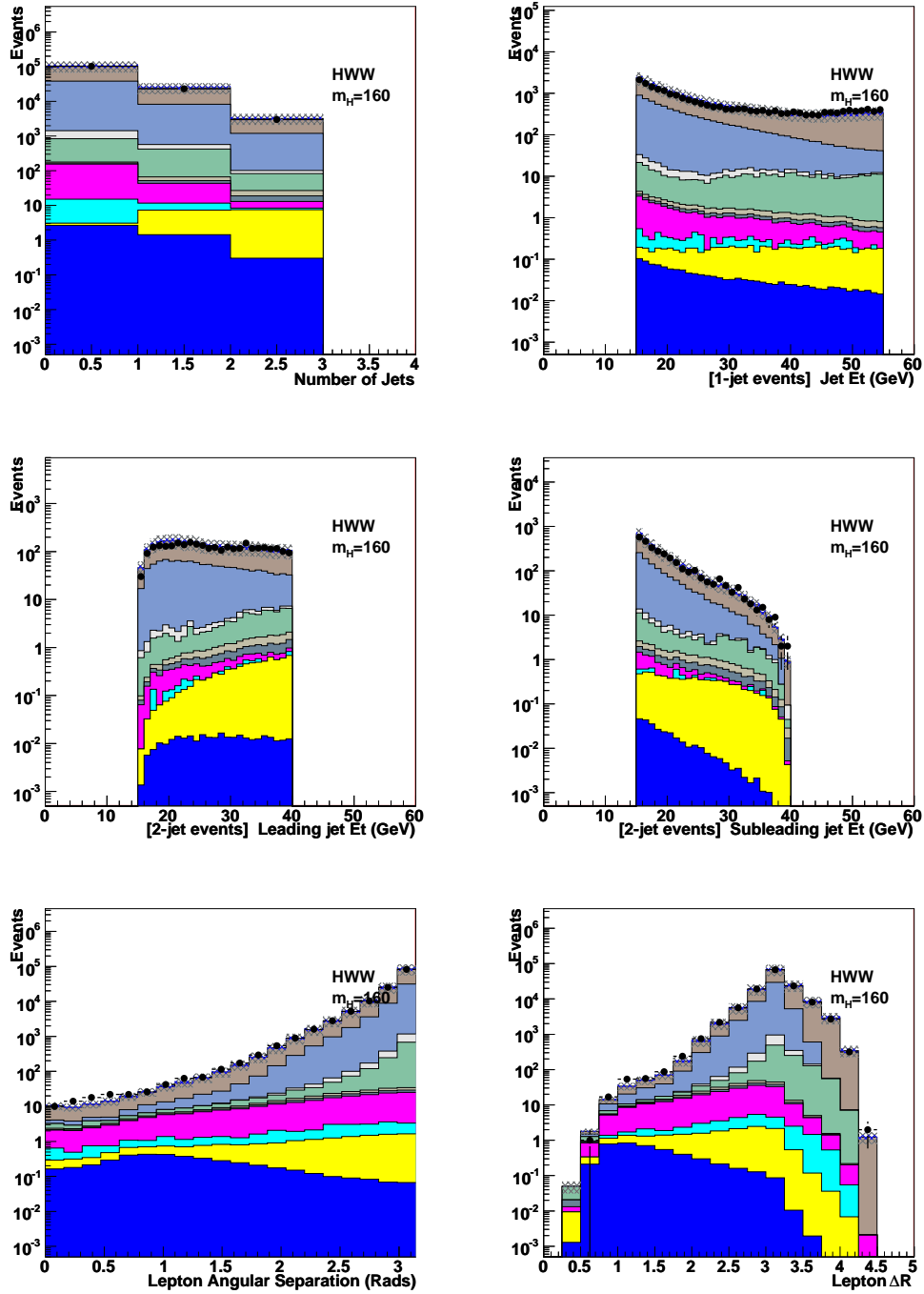


Figure 6.8: Plots of input variables used in the multivariate analysis. This is to check the modelling of the Monte Carlo can be trusted before the neural net is trained. Although all backgrounds are shown here, only the Drell Yan, W^+W^- , and $gg \rightarrow H \rightarrow W^+W^-$ components are used in the training. Please refer to section 2.7 for a legend.

trained with all available events because the training sample would be too small if the cut was Drell Yan neural net cut was placed on the samples. Limits on the Higgs signal cross-section are calculated from the resulting distributions from the W^+W^- neural net. It is undecided as to the benefits of training the neural net over each individual background. Three other scenarios were considered:

- Many neural nets could be trained, one using each of the physical backgrounds listed in the experiment against the Higgs signal. These would be combined in some way to give an overall score. Given the results from the current analysis, it was considered that this would give only minor increases in discrimination, given that the two neural nets presently used remove nearly all of the other backgrounds from the signal area. It would also introduce larger systematic errors, which are not necessary given the modest increase in discrimination power they might achieve.
- Each physical background is trained against each other physical background (including the signal), such that there is a neural net dedicated to separating each physical background from every other physical background. This suffers from the same problems of the scenario described above, where two nets are sufficient to reduce the other physical backgrounds to insignificant amounts, and more neural nets would introduce extra errors and higher processing time, which are not viable given the improvement they might achieve.
- All the physical backgrounds are included in the the background sample within one neural net, all trained against the Higgs Monte Carlo as the signal sample in the neural net. This is subject to some technical difficulties: firstly, the physical backgrounds must be introduced to the neural net in

the proportions that they have in reality. This is because the neural net cannot distinguish between different physical backgrounds, as they are all labelled as 'background' within the neural net; thus, a background such as $t\bar{t}$ may influence the neural net score to the same degree as a much larger background, such as Drell Yan. The resulting neural net will be equally as good at discriminating these, but this would give a worse result, because there is far more Drell Yan to remove.

Therefore:

- The proportion of the events used in the training background must be varied to get the correct mix of physical backgrounds. This does not work, given that the Drell Yan is far more dominant than the other physical backgrounds, and so these would therefore be represented by one or two events in the neural net background sample, which is not enough to get any handle on the smaller physical backgrounds' kinetic properties.
- The background events must be weighted according to their cross section. This method has been tried and has achieved improved discrimination, but it involves training far more background events compared to signal events. Neural nets are recommended to be trained with equal amounts of signal and background events, such that the amount of information supplied to the neural net is the same for the signal and the training backgrounds.

The dangers of a combination of these issues has not been completely studied, and it is for this reason that it is not chosen as the principal training method

for this analysis.

Both the Drell Yan and W^+W^- neural nets were trained on 4000 back-ground and signal events, where the signal Monte Carlo was always the Higgs Monte Carlo; in the Drell Yan neural net the background comprised the $Z \rightarrow ee, \mu\mu, \tau\tau$ samples in proportion to their cross-sections; the W^+W^- neural net solely uses W^+W^- Monte Carlo for background. Each was trained for 200 epochs, and each training sample had initial analysis cuts placed only. Plots of the output scores from the neural net are shown in Fig. 6.9 for the weights trained on Drell Yan background, and in Fig 6.11 for samples trained on W^+W^- background. Plots of the signal to background efficiency for the Drell Yan neural net are shown in Fig. 6.10. Plots of all the W^+W^- neural net trainings and their efficiencies can be found in Appendix D.

6.6 Neural net output plots

Score plots from the Drell Yan neural net show good agreement between data and Monte Carlo as in Fig. 6.12. Cuts are chosen to reject Drell Yan by finding the cut with highest signal acceptance to background rejection ratio. Choosing the cut based upon the end limit is more powerful, but it is less practical due to excessive processing. Plots of signal-background rejection and the optimum values are also displayed in Fig. 6.12.

The input variables are again plotted after this cut and show agreement between data and Monte Carlo (see Figs. 6.13 and 6.14). Plots of the input variables after the Drell Yan neural net has been cut upon separated into ee , $e\mu$ and $\mu\mu$ are available in Appendix C.

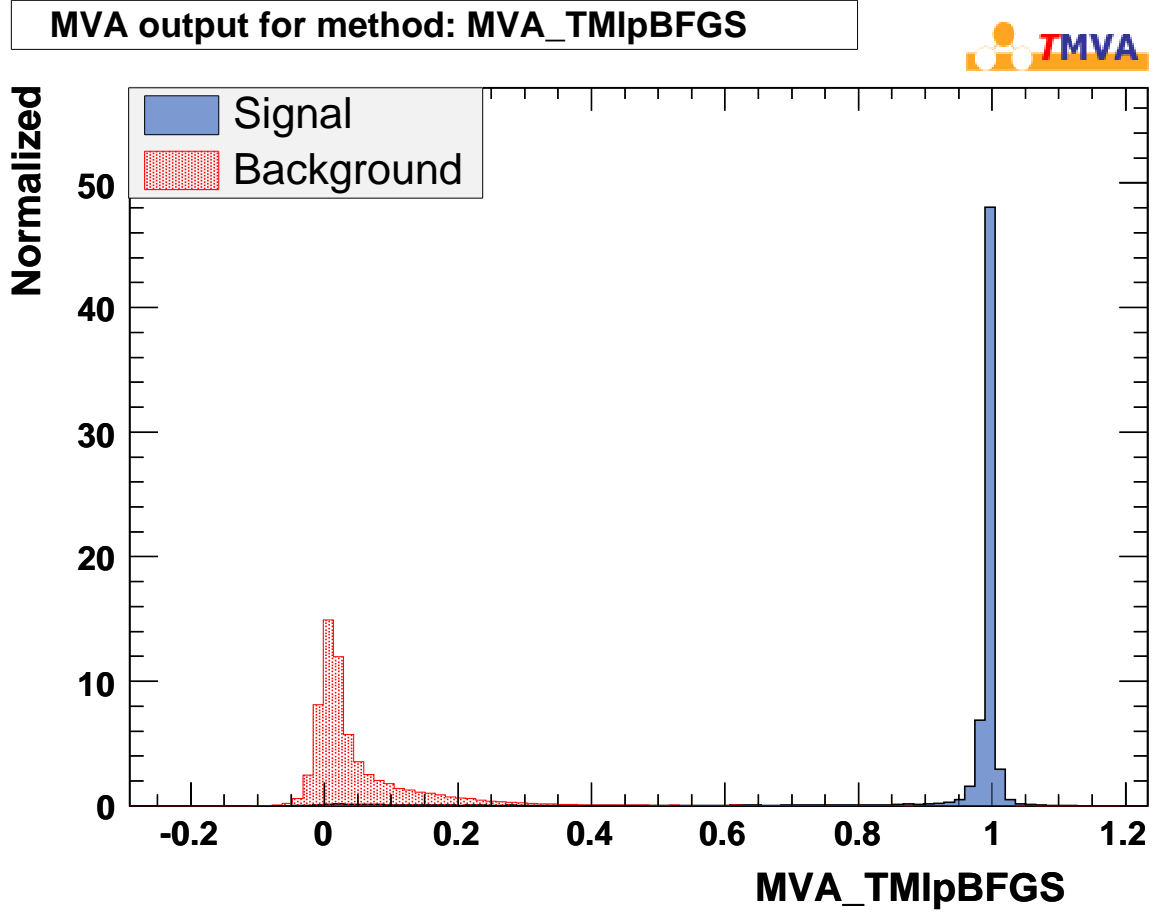


Figure 6.9: Drell Yan background and Higgs signal separation plots for the TMLP using the BFGS training method. This uses TMVA v3.3.3 and is trained on Higgs \rightarrow WW (signal) and $Z \rightarrow ee$, $Z \rightarrow \mu\mu$, and $Z \rightarrow \tau\tau$, (background) Monte Carlo samples with M_H of 160 GeV.

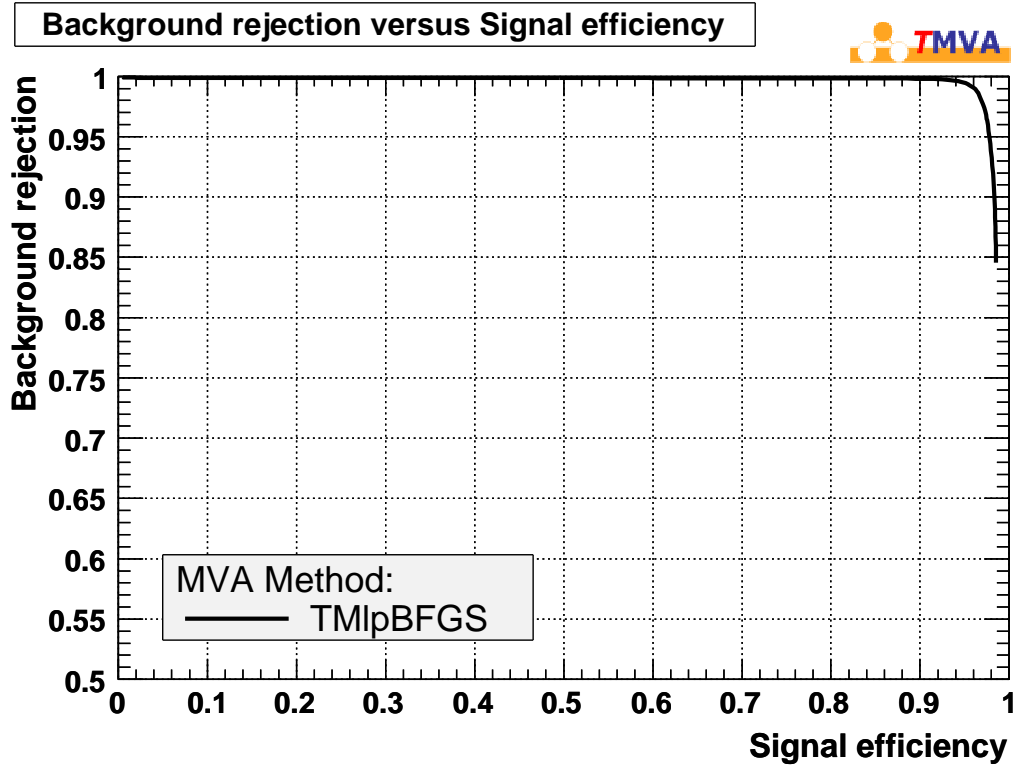


Figure 6.10: Drell Yan background rejection vs. Higgs signal efficiency plots for the TMLP using the BFGS training method. This uses TMVA v3.3.3 and is trained on Higgs \rightarrow WW (signal) and $Z \rightarrow ee$, $Z \rightarrow \mu\mu$, and $Z \rightarrow \tau\tau$, (background) Monte Carlo samples with M_H of 160 GeV.

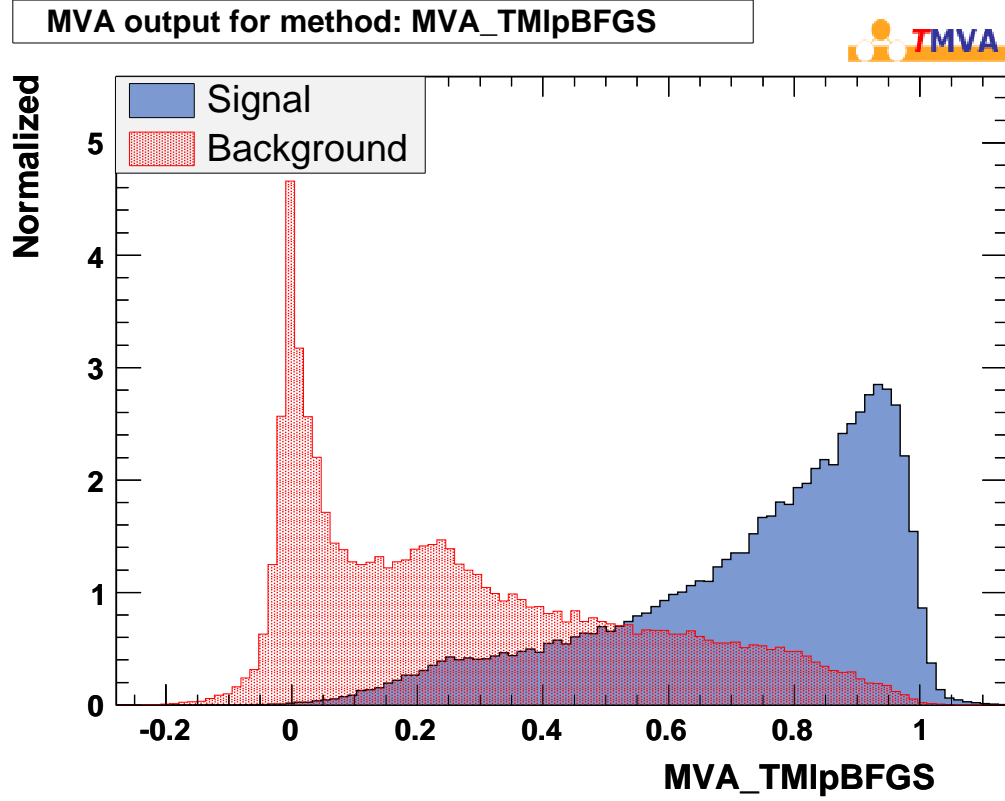


Figure 6.11: W^+W^- background and higgs signal separation plots for the training methods available with TMLP using TMVA v3.3.3 after training on Higgs \rightarrow WW (signal) and W^+W^- (background) Monte Carlo samples with M_H of 160 GeV. All lepton types are included here, for plots of all the W^+W^- neural net trainings and their efficiencies, see Appendix D.

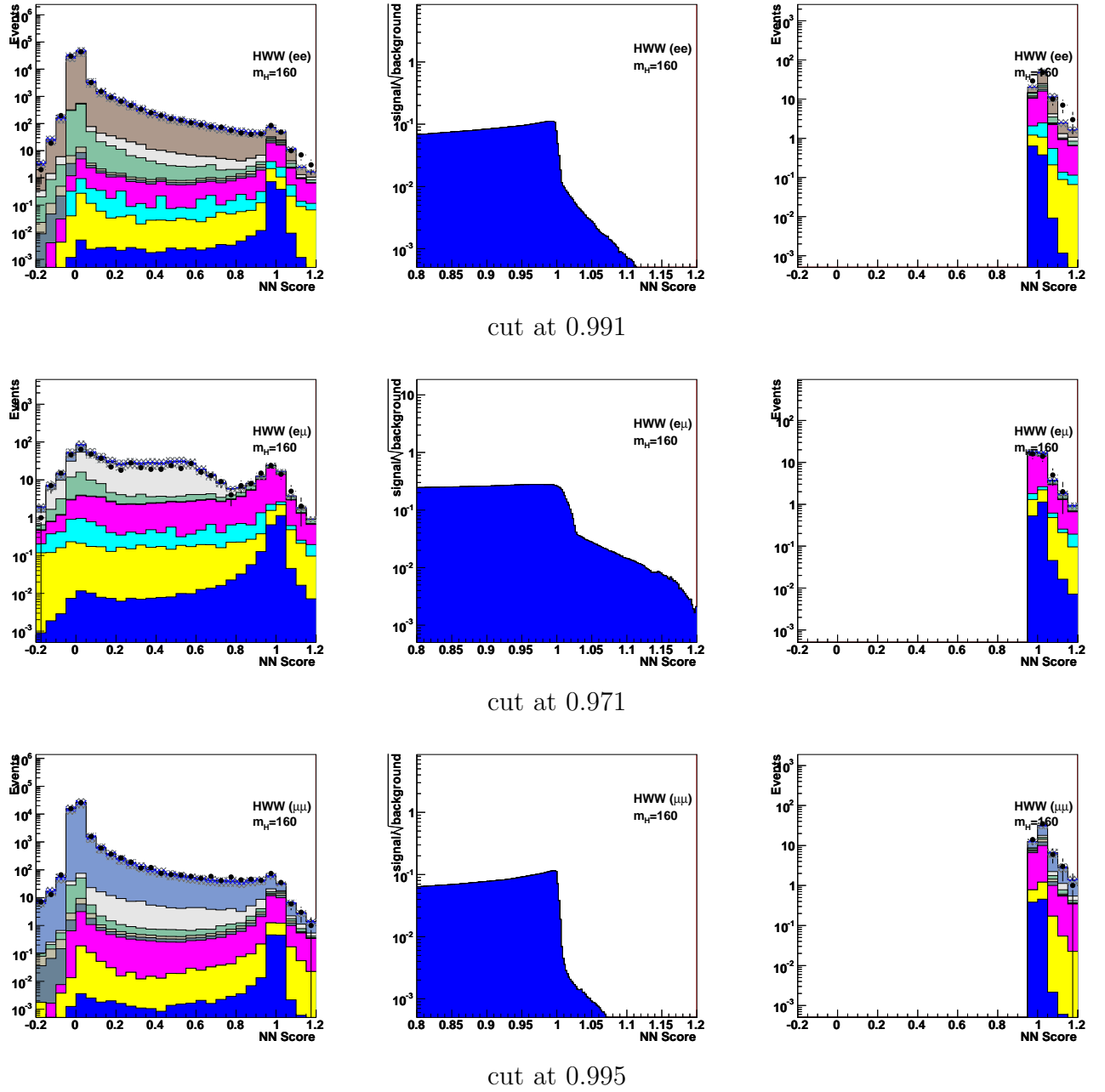


Figure 6.12: Plots of the Monte Carlo and data neural net scores obtained using the neural net trained with Drell Yan as background and $gg \rightarrow H \rightarrow W^+W^-$ and signal. The top set of plots correspond to ee , the middle to $e\mu$, and at the bottom, $\mu\mu$. The second plot in each row depicts the $N_{signal}/\sqrt{N_{background}}$ of a cut made at the corresponding neural net score. The last column of plots have a cut placed on them at the score which achieves the highest $N_{signal}/\sqrt{N_{background}}$ in the remaining events. Please refer to section 2.7 for a legend.

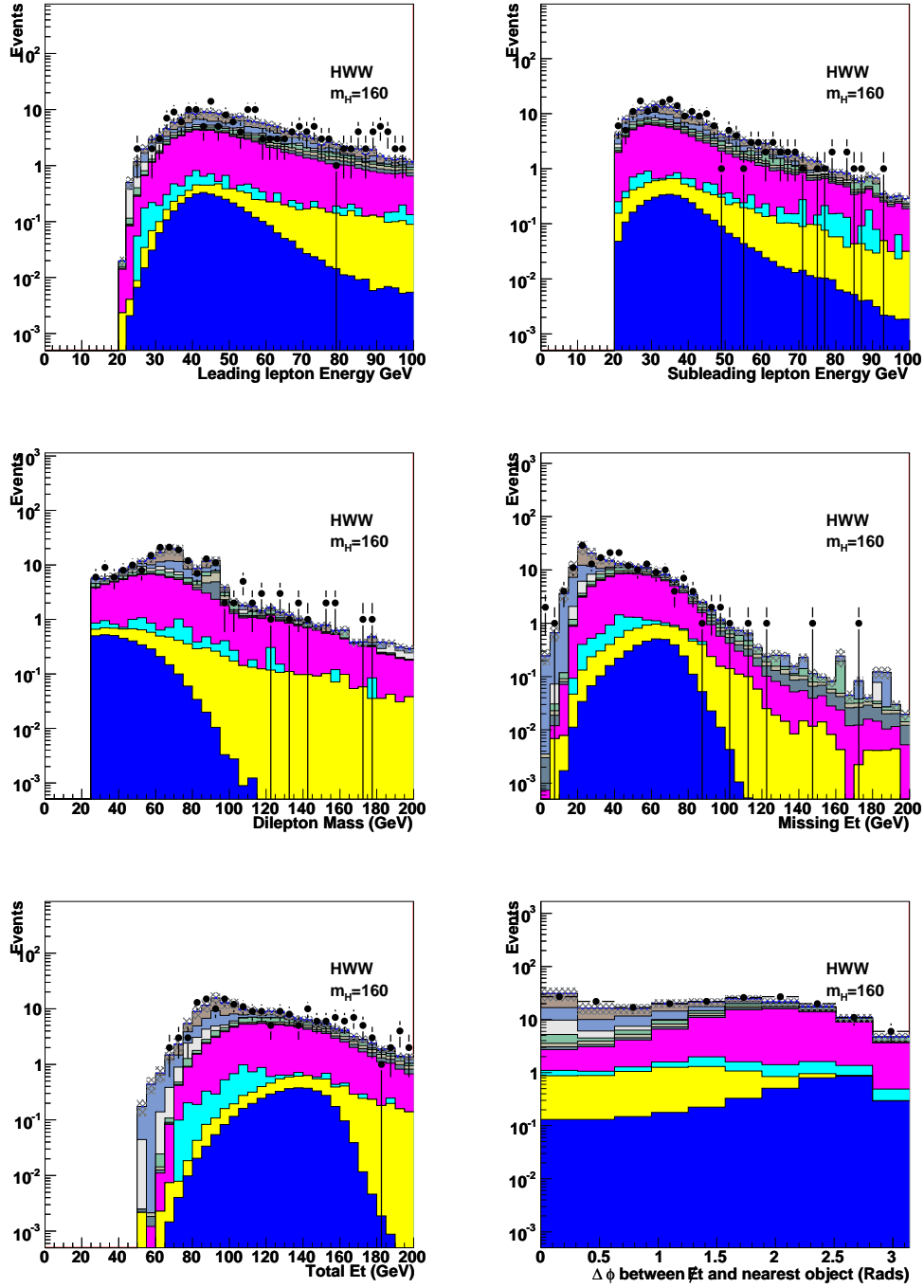


Figure 6.13: Plots of input variables used in the multivariate analysis after the cut on the Drell Yan neural net. Please refer to section 2.7 for a legend.

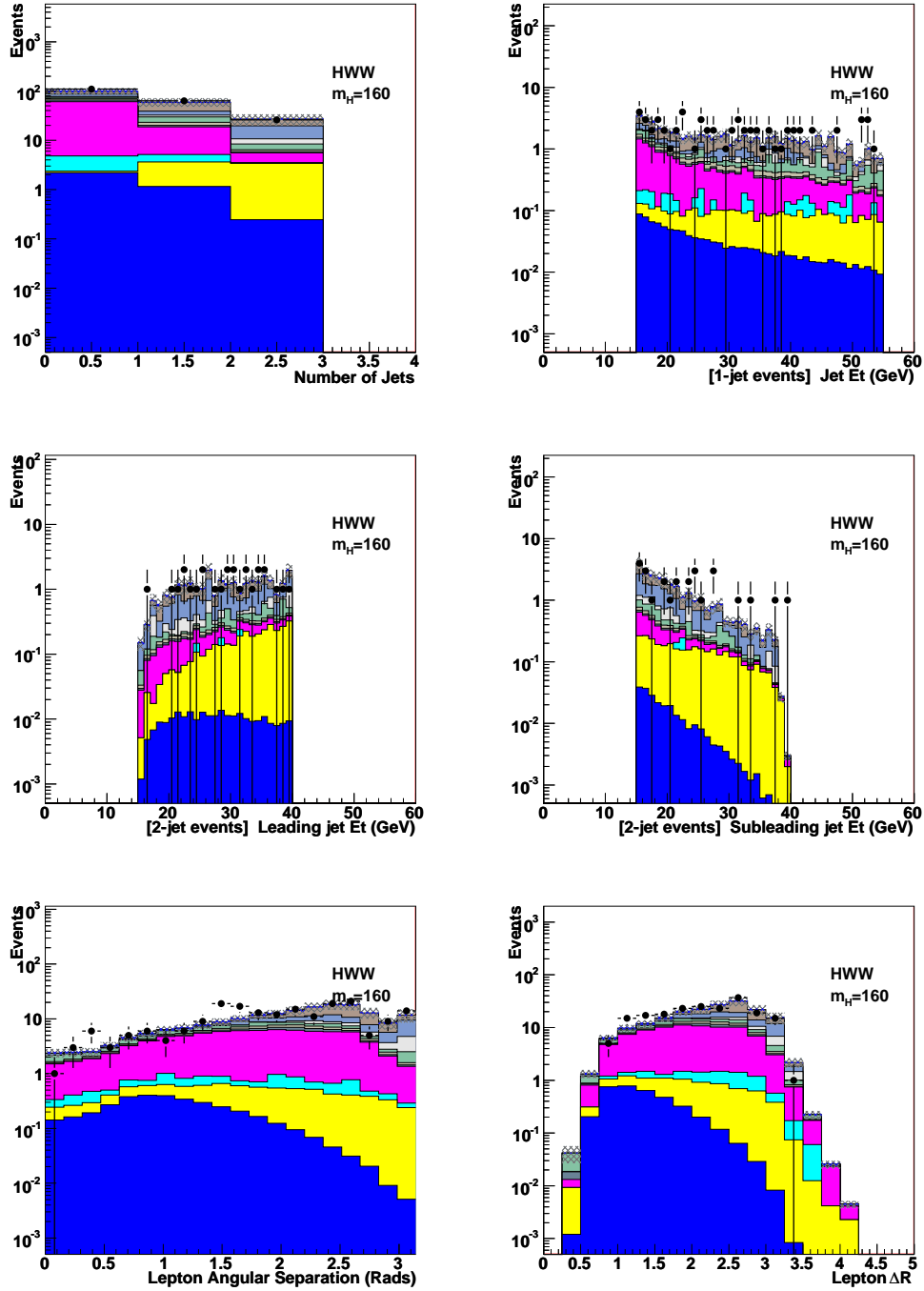


Figure 6.14: Plots of input variables used in the multivariate analysis after the cut on the Drell Yan neural net. Please refer to section 2.7 for a legend.

	ee	$e\mu$	$\mu\mu$	$\ell\ell$
WW	$26.18 \pm 0.14 \pm 3.14$	$28.75 \pm 0.11 \pm 5.04$	$16.83 \pm 0.10 \pm 2.05$	$71.75 \pm 0.20 \pm 9.36$
WZ	$3.34 \pm 0.05 \pm 0.36$	$1.19 \pm 0.01 \pm 0.12$	$2.99 \pm 0.04 \pm 0.32$	$7.51 \pm 0.05 \pm 0.80$
ZZ	$2.85 \pm 0.08 \pm 0.30$	$0.14 \pm 0.01 \pm 0.02$	$3.13 \pm 0.08 \pm 0.33$	$6.12 \pm 0.10 \pm 0.64$
ttbar	$1.70 \pm 0.12 \pm 0.17$	$2.70 \pm 0.14 \pm 0.26$	$1.42 \pm 0.10 \pm 0.14$	$5.82 \pm 0.21 \pm 0.57$
wgamma	$2.75 \pm 0.56 \pm 0.58$	$1.33 \pm 0.24 \pm 0.30$	$0.00 \pm 0.00 \pm 0.00$	$4.08 \pm 0.55 \pm 0.87$
fake	$5.67 \pm 0.56 \pm 0.52$	$5.46 \pm 0.25 \pm 1.08$	$2.80 \pm 0.26 \pm 0.67$	$13.93 \pm 0.52 \pm 2.24$
Drell Yan	$42.94 \pm 11.91 \pm 14.25$	$1.04 \pm 0.20 \pm 0.33$	$28.14 \pm 8.90 \pm 9.47$	$72.11 \pm 10.30 \pm 23.41$
Background Total	$85.43 \pm 0.43 \pm 15.36$	$40.59 \pm 0.15 \pm 5.50$	$55.30 \pm 0.30 \pm 10.23$	$181.32 \pm 0.47 \pm 26.84$
$H \rightarrow WW_{(M_H=110GeV)}$	$0.01 \pm 0.00 \pm 0.00$	$0.02 \pm 0.00 \pm 0.00$	$0.01 \pm 0.00 \pm 0.00$	$0.04 \pm 0.00 \pm 0.01$
$H \rightarrow WW_{(M_H=120GeV)}$	$0.09 \pm 0.00 \pm 0.01$	$0.11 \pm 0.00 \pm 0.01$	$0.07 \pm 0.00 \pm 0.01$	$0.27 \pm 0.00 \pm 0.03$
$H \rightarrow WW_{(M_H=130GeV)}$	$0.27 \pm 0.00 \pm 0.03$	$0.37 \pm 0.00 \pm 0.05$	$0.21 \pm 0.00 \pm 0.03$	$0.84 \pm 0.01 \pm 0.10$
$H \rightarrow WW_{(M_H=140GeV)}$	$0.54 \pm 0.01 \pm 0.07$	$0.77 \pm 0.01 \pm 0.10$	$0.42 \pm 0.01 \pm 0.05$	$1.72 \pm 0.01 \pm 0.21$
$H \rightarrow WW_{(M_H=150GeV)}$	$0.79 \pm 0.01 \pm 0.10$	$1.18 \pm 0.01 \pm 0.15$	$0.60 \pm 0.01 \pm 0.08$	$2.57 \pm 0.01 \pm 0.32$
$H \rightarrow WW_{(M_H=160GeV)}$	$1.02 \pm 0.01 \pm 0.13$	$1.74 \pm 0.01 \pm 0.22$	$0.84 \pm 0.01 \pm 0.11$	$3.60 \pm 0.02 \pm 0.46$
$H \rightarrow WW_{(M_H=170GeV)}$	$0.98 \pm 0.01 \pm 0.13$	$1.68 \pm 0.01 \pm 0.22$	$0.83 \pm 0.01 \pm 0.11$	$3.48 \pm 0.02 \pm 0.46$
$H \rightarrow WW_{(M_H=180GeV)}$	$0.80 \pm 0.01 \pm 0.11$	$1.37 \pm 0.01 \pm 0.19$	$0.68 \pm 0.01 \pm 0.09$	$2.85 \pm 0.01 \pm 0.39$
$H \rightarrow WW_{(M_H=190GeV)}$	$0.54 \pm 0.01 \pm 0.08$	$0.91 \pm 0.01 \pm 0.13$	$0.46 \pm 0.00 \pm 0.06$	$1.91 \pm 0.01 \pm 0.27$
$H \rightarrow WW_{(M_H=200GeV)}$	$0.42 \pm 0.00 \pm 0.06$	$0.70 \pm 0.00 \pm 0.10$	$0.35 \pm 0.00 \pm 0.05$	$1.47 \pm 0.01 \pm 0.22$
data	98.00	40.00	60.00	198.00

Table 6.5: Events passing Drell Yan neural net cuts. Statistical and systematic errors are displayed.

The W^+W^- neural net scores are plotted before and after (Fig. 6.15) the cut, and show good agreement. The limit calculation is performed on the W^+W^- score plots after the Drell Yan rejection cut. Plots of the W^+W^- neural net scores after the Drell Yan neural net cut can be found in Appendix E and F for all masses.

The overall acceptance of the cut is broken down into backgrounds in Table 6.5. Appendix A contains detailed acceptance tables of all samples separated into dilepton types.

6.7 Limit calculation using likelihood estimator

The neural net plots show good agreement between the data and Monte Carlo, and so the data presents no evidence of Higgs events within the data sample and

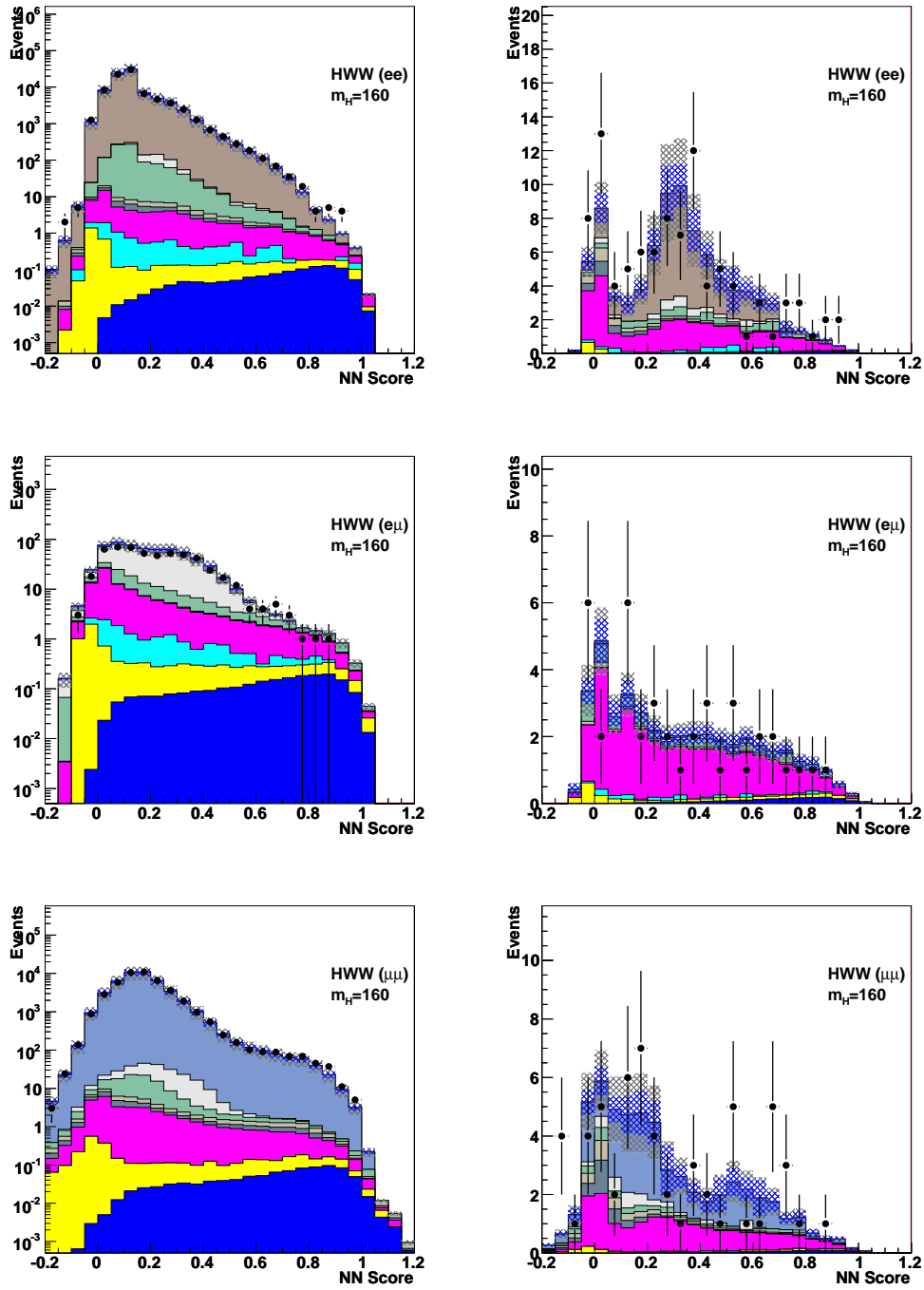


Figure 6.15: Plots of the W^+W^- -trained neural net scores before (left column) and after (right column) the Drell Yan trained neural net has been cut upon. The W^+W^- -trained neural net is trained on events before the Drell Yan neural net is cut upon. The W^+W^- -trained neural net score plots with the Drell Yan trained neural net cut in the second column are the final plots on which a likelihood test is performed. Please refer to section 2.7 for a legend. See Appendix F for more information.

no Higgs production cross section value can be inferred. Therefore, a limit on the maximum cross section of the Higgs production can be calculated given that if it were any bigger than this limit value, the Higgs would become evident in the data. It is often expressed as a multiple of the theoretical value, such that when the ratio of the cross section limit and the theoretical cross section nears 1, the theory value is tested. The cross section limit calculation was calculated using the `mclimit_cms` program which employs a Bayesian log-likelihood technique.^{33,57,60} The Bayesian method is interested in finding the probability that a hypothesis is true (here denoted as a number of signal events, (s)) given that a number of events seen overall is n . This is written as $P(s|n)$. From Monte Carlo, a number of events seen can be predicted given a number of signal events, $P(n|s)$. The Bayesian method is then used to relate these two:

$$P(s|n) = \frac{P(n|s)P(s)}{P(n)} \quad (6.1)$$

where $P(s)$ corresponds to prior beliefs about the signal, and $P(n)$ is found by integrating $P(n|s)$ over all s :

$$P(s|n) = \frac{P(n|s)P(s)}{\int_{-\infty}^{\infty} P(n|s')P(s')ds'} \quad (6.2)$$

Here, $P(s|n)$ is the probability of s higgs events in n events; $P(n|s)$ is the probability of n events given s signal events, and $P(s)$ is the probability of finding s higgs events. The prior beliefs are chosen simply, stating the definite existence of a signal provided the signal cross section is positive.

$$s \geq 0 \rightarrow P(s) = 1; s < 0 \rightarrow P(s) = 0 \quad (6.3)$$

This has the effect of limiting the integral in the numerator:

$$P(s|n) = \frac{P(n|s)P(s)}{\int_0^\infty P(n|s')P(s')ds'} = \frac{P(n|s)P(s)}{\int_0^\infty P(n|s')ds'} \quad (6.4)$$

The aim of the analysis is to place an upper limit on the signal cross section to 95% confidence level. This means that there is only 5% chance of the signal existing ($P(s|n)$) above a certain cross-sectional limit on s :

$$C.L. = 0.95 = \int_0^{s_{up}} P(s|n)ds \quad (6.5)$$

thus, the 95% limit is found by repeatedly increasing s_{up} , the upper limit, until the condition:

$$C.L. = 0.95 = \int_0^{s_{up}} P(s|n)ds = \frac{\int_0^{s_{up}} P(n|s)ds}{\int_0^\infty P(n|s)ds} \quad (6.6)$$

is achieved. In practice, as the cross-section within the denominator integral increases to infinity, the probability of the finite number of data events seen being the result of an extremely large signal tends to zero, and the infinite upper bound of the denominator can be truncated at a reasonably high value. The probability is estimated using the $\Delta\chi^2$. For this analysis, the differences in χ^2 match of the data to Monte Carlo between the background and the signal+background was used:

$$\chi^2(n|s+b) - \chi^2(n|b) = \Delta\chi^2 \quad (6.7)$$

For each mass point, an observed limit and an expected limit is calculated. The observed limit is the limit on the signal cross section as given by the data. This is compared to an expected limit, which is calculated from ‘pseudo-data’, estimated

from Monte Carlo. To get an expected limit in order to incorporate statistical errors the process is repeated with ‘pseudo-data’, in many ‘pseudo experiments’, in this case 10,000 for each higgs mass tested. In each of these, a pseudo-data sample is randomly estimated from the Monte Carlo within the errors; these will give a distribution of limits at 95% CL for all the pseudo experiments for each mass.

The median of this distribution of pseudo limits is taken as the expected limit. The limits which signify 16% and 84% of the pseudo-limit population are considered to be the $\pm 1\sigma$ statistical variance on this, and the limits within 2% and 98% of the pseudo-limits distribution become the $\pm 2\sigma$ statistical variances. The pseudo-data for the experiments is estimated on a bin-by-bin basis by choosing a value randomly fluctuated around the predicted Monte-Carlo within the error prescribed by the systematic errors and the statistical errors of the Monte-Carlo.

The limit calculator takes as its input the neural net score histograms. These are separated into histograms containing ee , $e\mu$ and $\mu\mu$ as in a previous analysis in this channel⁷⁵. This is due to the different profiles of the histograms generated, particularly between $e\mu$ and the same-lepton templates as the $e\mu$ plots are largely free of Drell Yan contamination. The same-lepton histograms ee and $\mu\mu$ are also separated in anticipation of different magnitudes of errors involved in measuring muons and electrons, and also the fake background contributions.

Within the likelihood program, the backgrounds are separated into W^+W^- and non- W^+W^- backgrounds, as in a previous analysis.⁷⁵ This is due to the fact that the neural net scores around the signal are largely only populated by W^+W^- background; varying the errors on the non- W^+W^- background has reduced effect upon the limit outcome which is based upon the signal content at a particular neural net

score. Thus, for every distribution on which the likelihood test is performed, there is a signal template, a W^+W^- -template, and a non- W^+W^- -template used as input to the limit calculator. The non- W^+W^- -template contains all of the non- W^+W^- -backgrounds, and errors on this template are applied to all the events. Studies have shown that the outcome changes negligibly if the non- W^+W^- -background template is broken down further.

6.8 Neural Net improvement investigations

A new method based on neural nets was investigated to improve the signal-to-background ratios of the higher scored neural net bins. A neural net has one set of weights which it optimises over many events in order to get the best overall separation between background and signal. However, the likelihood method above will give lower limits if the signal-to-background ratios of bins are higher; a better limit can be achieved if a single bin can be found with high signal and low background, even if much of the signal is disregarded. To exploit this, a method inspired by neural nets was invented by the author. The formula for a node in a neural net is that of a hyperplane if the sigmoid activation function is not included:

$$0 = \sum_i^n w_i \cdot v_i \quad (6.8)$$

where i runs over the variables, w_i are the coefficients which defines the plane and the v_i are the values of the input variables, which are the dimensions of the space. When an event's value for the variables is placed into the v_i , the sum will be negative or positive, signifying that the event lies on one or other of the sides

of the plane. Events can be sorted in this way into distinct areas.

One of these planes will divide the phase space into 2^1 regions; two hyperplanes will separate the space into 2^2 regions, and so on with n planes splitting the plane up into 2^n regions. The method chooses the best array of hyperplanes to create small regions of high signal to background. The planes were chosen by randomly guessing the plane's coefficients, w_i , until the best configuration could be found using 'simulated annealing' minimisation.

An error is calculated similar to the neural net, except that here, the score is the signal to background ratio of all the areas added up, such that a better score includes many areas where there are a high proportion signal compared with the background. The inverse of this score is then minimised. The method of simulated annealing changes one w_i at a time, accepting and storing any improvements in maximising the signal/background that might happen. However, when a worse score is attained by randomly changing the weight, the weight is accepted with a probability. This probability is based upon a 'temperature' variable within the minimisation program, such that a higher temperature accepts poorer changes more readily. This is to prevent the minimisation getting stuck in false minima. As the process continues, the temperature is gradually lowered such that the chances to get out of the minima are decreased until the function finds the lowest minimum. This is in analogy to real annealing where a metal is heated up and cooled gradually; this gives the atoms in the metal many chances at finding a lowest energy position in a crystal.

In order to prevent the technique from isolating very small numbers of events, the score is modified in a pessimistic way by including the statistical errors in the signal and background counting. Thus in reality, the number of signal in an area,

N_s , is replaced with $N_s - \sqrt{N_s}$ and the number of background in a region, N_b , is replaced with $N_b + \sqrt{N_b}$.

Once the optimal array of hyperplanes is decided upon, the w_i are fixed, and events are tested on each plane by passing their variable values into the v_i , and determining on which side of the plane they lie. This will assign them to one of the 2^n regions, and a score is given to them based upon the signal to background ratio found for that region during the training stage.

This is then added to the neural net score, and increases the performance of the neural net by 3%. However, the effects of errors generated by the method has not been fully investigated, as the technique is essentially a series of tuned cuts; consequently, it is not used in this analysis. Further improvements might involve:

- Training with all the backgrounds combined; this does not suffer in the same way as the neural net because the differences in the numbers of events of signal and background are taken care of by the inclusion of the systematic error in the counting.
- The technique may also be modified using boosted decision tree principles, where the process is repeated many times to create many hyperplane nets, and a score for each event averaged over all the nets.
- The technique may be modified by training the net of hyperplanes to find a ‘hotspot’ of high signal/background, then removing these events. A new net would be trained upon the remaining events. This prevents successive trainings from optimising the same areas.

6.9 Method Summary

After an initial set of cuts to remove $t\bar{t}$ contributions, ten variables were chosen with which to conduct a multivariate analysis. The strongest technique was a neural net trained using BFGS minimisation. The sample was split into $ee, e\mu$ and $\mu\mu$ contributions for training. Two neural nets were trained, both using the Higgs sample as the signal. The first used Drell Yan as background, and the second used W^+W^- as the background. Optimal cut points on the Drell Yan neural net score were discerned which would have the highest signal/background in the passing events. The W^+W^- neural net scores of the events passing these Drell Yan cuts were used as the final discrimination plots. A Bayesian likelihood test was performed on the discriminating plots using both shape and yield errors. An observed limit is found from the data. An expected limit is found by performing 10,000 pseudo experiments in which data is simulated by varying the yields predicted by Monte Carlo randomly within the errors. This is performed 10 times with signal from 10 Higgs masses.

Chapter 7

Systematic Uncertainties

The systematic uncertainties are taken into account by producing an error on the expected limit, as described in chapter 6.7. Two types of error were included, shape errors and yield errors.

Shape errors are errors which differ per bin, such that the error can affect different portions of the phase space differently. They are therefore introduced into the expected limit calculation as an ‘up-error’ plot and a ‘down-error’ plot. Errors on the yield affect all the bins equally in the background contributions.

The errors are collected into errors on the signal, errors on the W^+W^- background as this is the most signal like, and errors on the rest of the backgrounds. This is due to the fact that most background in the signal regions are W^+W^- , with very little contributions from the other backgrounds. If an error is only applicable to one background with in the last of these, is distributed over the whole of the rest of the backgrounds, scaled appropriately to the fraction of that particular background process. Studies have shown this to give indistinguishable results to when the backgrounds are treated separately.

likelihood template	Error (%) ee	Error (%) e μ	Error (%) $\mu\mu$
Higgs	< 0.1	< 0.1	< 0.1
WW	< 0.1	< 0.1	< 0.1
non-WW	-6.8+4.8	-1.6+1.1	-9.3+4.4

Table 7.1: Average errors on the yield from varying the jet energy scale

7.1 Shape Errors

For each of these errors, a upper error and lower error version of each discrimination histogram is created to reflect the maximum effects of the error in question. These are then used within the likelihood calculation in order to estimate a bin-by-bin error variation.

7.1.1 Jet Energy Scale

Jet energy is measured and corrected using the same method as in an earlier analysis.⁹ This uses algorithms in the CDF package JetCorr12⁶³ that use jet momentum balancing in di-jet events to find correction factors for the measured jet energies. The jet energy scale error is the inaccuracy incurred in properly evaluating the energy correction; as a consequence, it is given per jet by the jet energy correction algorithms. For the upper jet energy scale shape errors, the jets' energies are increased by the error, and the \cancel{E}_T is altered accordingly. The event is then fed through the whole analysis again to create upper error plots for the jet energy scale shape errors. The jet energy uncertainty causes an average yield uncertainty shown in Table. 7.1. The shape error plots for input into the likelihood calculation are shown in Fig. 7.1.

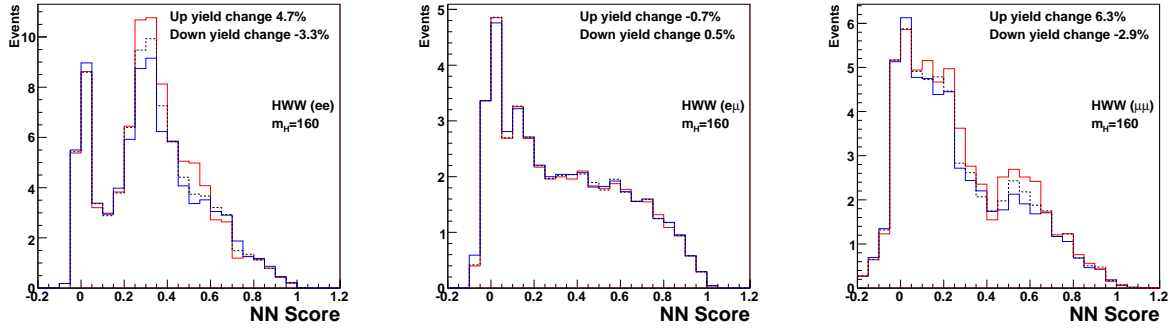


Figure 7.1: Jet energy systematic plots. They are separated into ee , $e\mu$ and $\mu\mu$. The red line shows the neural net background once the maximum positive error is placed upon all the events (denoted ‘Up’ in the plot). The blue line shows the neural net background once the maximum negative error is placed upon all the events (denoted ‘Down’ in the plot). The dashed black line represents the neural net scores without error. The average percentage changes in yield for the ‘Up’ and ‘Down’ errors are given on the plots.

7.1.2 Lepton Energy Scale

The lepton energy scale is the error involved in measuring the lepton energies. The spread of Z masses measured between the di-lepton pair combinations is taken to be the inaccuracy of the lepton energy scale. After energy corrections, the spread from the measured mean data Z mass of $90.88 \text{ GeV}/c^2$ were less than 0.3%, so the highest energy correction was used, 1.4%. To apply the error, the leptons’ four vectors are modified by this amount, and the \cancel{E}_T corrected. The event is then once again passed through the analysis process as with the jet error to create a shape error plots. As with the jet energy scale, small lepton energy changes may cause leptons to fail cuts producing differences in shape and yield. Average yield changes are shown in Table. 7.2. Shape error plots for input into the likelihood calculation are shown in Fig. 7.2.

likelihood template	Error (%) ee	Error (%) $e\mu$	Error (%) $\mu\mu$
Higgs	< 0.1	± 0.9	+0.3-0.1
WW	+0.1-0.2	+0.6-0.8	+0.3-0.4
non-WW	+1.1-1.5	+2.1-0.1	+4.5-1.7

Table 7.2: Average errors on the yield from varying the lepton energy scale

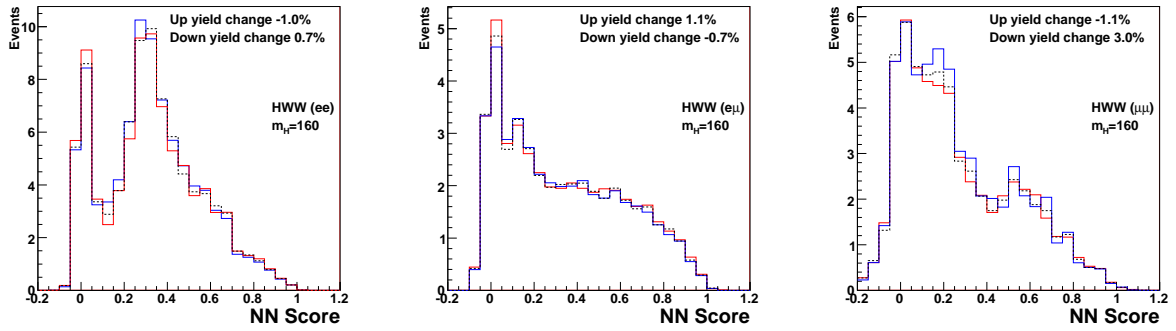


Figure 7.2: Lepton energy systematic plots. They are separated into ee , $e\mu$ and $\mu\mu$. The red line shows the neural net background once the maximum positive error is placed upon all the events (denoted 'Up' in the plot). The blue line shows the neural net background once the maximum negative error is placed upon all the events (denoted 'Down' in the plot). The dashed black line represents the neural net scores without error. The average percentage changes in yield for the 'Up' and 'Down' errors are given on the plots.

7.1.3 Initial State Radiation

Jets within $gg \rightarrow H \rightarrow W^+W^-$ couple strongly, and so to first order, they can originate only from gluons emitted from the initial gluons, otherwise known as initial state radiation. Pythia models this with initial parton showering, where the probability of a gluon escaping to produce a jet is calculated as a function of Q^2 and the sharing fraction of energy amongst the escaping particles, z .⁷⁷ This is also important because it modifies the P_T of the subprocess. The method to determine the error is the same as is used in a previous analysis,²⁸ which varies the showering parameters PARP(62), PARP(64) and PARP(91) of the Pythia framework. The

likelihood template	Error (%) ee	Error (%) $e\mu$	Error (%) $\mu\mu$
Higgs	+0.1-0.5	+ < 0.1 – 0.1	+ < 0.1 – 0.3
WW	+2.0-3.8	+1.7-3.2	+1.9-3.7
non-WW	+1.2-0.4	+0.7-1.5	+0.3– < 0.1

Table 7.3: Average errors on the yield from varying the ISR parameters

change in the P_T spectrum of the Higgs using the modified PARP variable with respect to the P_T spectrum using the tuned values of the variables is measured. The largest effect is seen with PARP(64), so the differences seen in changing this parameter are used for the error. The differences measured within selected P_T bins are taken and used to weight events which have the P_T equal to the specified subprocess P_T in that bin. Average yield changes appear in Table. 7.3, and shape error plots for input into the likelihood calculation are shown in Fig. 7.3.

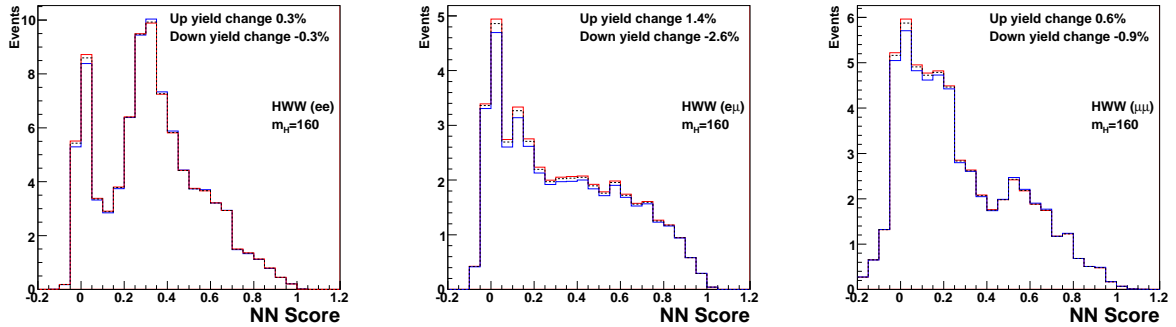


Figure 7.3: Initial state radiation systematic plots. They are separated into ee , $e\mu$ and $\mu\mu$. The red line shows the neural net background once the maximum positive error is placed upon all the events (denoted ‘Up’ in the plot). The blue line shows the neural net background once the maximum negative error is placed upon all the events (denoted ‘Down’ in the plot). The dashed black line represents the neural net scores without error. The average percentage changes in yield for the ‘Up’ and ‘Down’ errors are given on the plots.

7.1.4 Parton Distribution Function

The parton distribution function is a fit to many experiments' results which models the distribution of momenta in the colliding protons and anti-protons. For a simulated event, the momentum of the initial incident partons within the proton/anti-proton are chosen by the generator; however, in reality, the partons' likelihood to exist at that chosen momentum is prescribed by the fraction of partons within the proton of that momentum. Modifying the distribution will therefore create a rate change in the number of events seen, as the simulator would allow more or less events to be created with these momenta. The parton distribution functions are measured by the CTEQ⁷² group and depend on a set of 20 independent parameters, or 'eigenvectors', for which a set of PDF values is chosen for event generation by best fit to numerous experiments. The PDF set used was the CTEQ6M NLO set. The CTEQ group also supply a set of 20 pairs of parton distributions with each of these parameters set to its limit in either direction. To find the error in the rate of production that arises from these PDF uncertainties, each generated event is fed into each of the distributions and a fractional change in weight for each eigenvector is noted, with a fractional upwards or downwards change being taken as the upper limit or lower of the uncertainty's effects. These are then added in quadrature to provide upper and lower errors for the event. As this occurs on an event by event basis, the effect of the errors will not necessarily be constant over all neural net scores, so a shape error plot is made. The PDF uncertainty causes an average yield uncertainty shown in Table. 7.4. The shape error plots for input into the likelihood calculation are shown in Fig. 7.4.

likelihood template	Error (%) ee	Error (%) $e\mu$	Error (%) $\mu\mu$
Higgs	+8.4-8.1	+8.2-7.4	+8.1-7.2
WW	+4.2-4.3	+4.6-4.1	+4.6-4.2
non-WW	+3.9-4.5	+3.1-2.9	+4.9-4.1

Table 7.4: Average errors on the yield from varying the PDF parameters

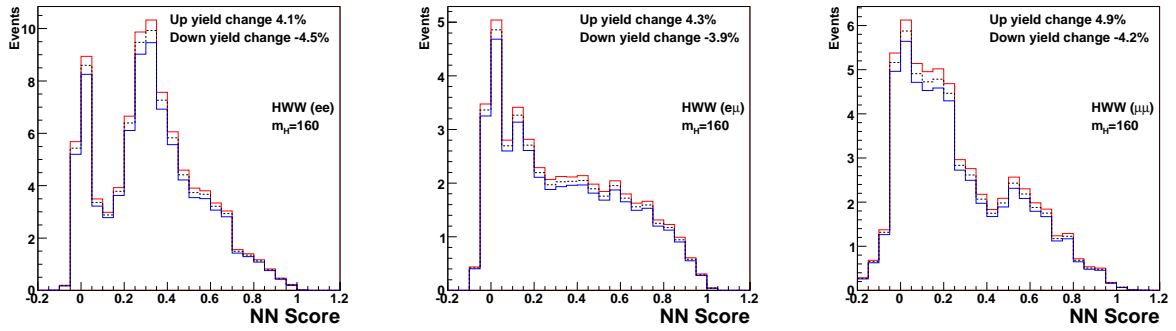


Figure 7.4: PDF Energy systematic plots. They are separated into ee , $e\mu$ and $\mu\mu$. The red line shows the neural net background once the maximum positive error is placed upon all the events (denoted ‘Up’ in the plot). The blue line shows the neural net background once the maximum negative error is placed upon all the events (denoted ‘Down’ in the plot). The dashed black line represents the neural net scores without error. The average percentage changes in yield for the ‘Up’ and ‘Down’ errors are given on the plots.

7.1.5 Fakes

Fake rates are found from jet-triggered samples, each differing by having a trigger jet energy threshold. The spread of fake rates measured from these samples is the error for each fake rate. This is then applied as a rate error to each fake lepton on an event by event basis, and this becomes the shape error for the fake rate. The Fake uncertainty causes an average yield uncertainty shown in Table. 7.5, where the error is only applicable to the non-WW background, as this is where the fakes are included. Shape error plots for input into the likelihood calculation are shown in Fig. 7.5.

likelihood template	Error (%) ee	Error (%) $e\mu$	Error (%) $\mu\mu$
non-WW	± 0.8	± 0.9	± 1.7

Table 7.5: Average errors on the yield from varying the Fake parameters

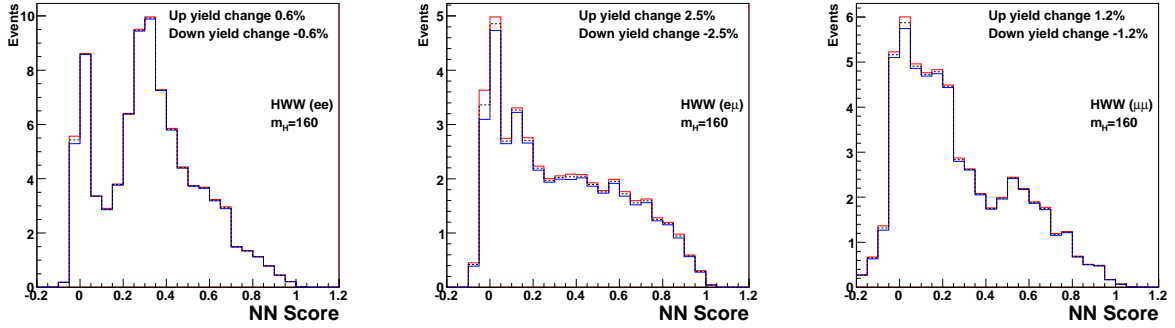


Figure 7.5: Fakes systematic plots. They are separated into ee , $e\mu$ and $\mu\mu$. The red line shows the neural net background once the maximum positive error is placed upon all the events (denoted ‘Up’ in the plot). The blue line shows the neural net background once the maximum negative error is placed upon all the events (denoted ‘Down’ in the plot). The dashed black line represents the neural net scores without error. The average percentage changes in yield for the ‘Up’ and ‘Down’ errors are given shown on the plots.

7.2 Other Errors

These are implemented as overall scale errors only, so each bin of the neural net scores have the same error placed upon them.

7.2.1 Luminosity

The uncertainty on the integrated luminosity is determined to be 6%. This comes from two sources: there is an uncertainty of 4% in the measurement of the $p\bar{p}$ cross section, which is necessary to calculate the total number of collisions occurring. This is added in quadrature with errors involved in measuring the density of protons in the beam bunches, which is also 4%. This is as measured by the CLC

which is responsible for measuring the instantaneous luminosity in each run.¹⁰

7.2.2 Higgs $\rightarrow W^+W^-$ cross section @ NNLO

This is estimated to be 10%, but does not affect any absolute limit placed on the Higgs cross section, as it is only applicable when comparing the measured limit to the theoretically calculated value. It is therefore not included in the likelihood calculations, but only in results which include the theoretical value.

7.2.3 Drell Yan Neural Net Cut Efficiency

This is the difference in the cut efficiency of the Drell Yan neural net cut between Monte Carlo and data. It is found by varying the cut on the Drell Yan neural net in both directions and measuring the change in efficiency within the data and the simulation. The largest difference between the data and Monte Carlo is taken to be the error. This was found in the ee channel and was found to be 20%. Table 7.6 shows the cut acceptance for the data and Monte Carlo, and the ratio between the two for the various cut values. The maximum variation of 20% between data and Monte Carlo acceptances is seen at the neural net cut of 0.991, so this is taken to be the error. However, the size of the error is due to the statistical error on the data as shown in Figure. 6.15.

7.2.4 Lepton ID, reconstruction and trigger efficiencies

These are supplied with the scale factors and trigger rates from the Joint Physics working group. The errors are applied on an event by event basis to achieve an upper and lower limit upon the yield. They are summarised in Table 7.7

cut value	Data acceptance (ϵ_{Data})	Monte Carlo acceptance (ϵ_{MC})	$\epsilon_{Data}/\epsilon_{MC}$
1.001	0.07%	0.07%	1.05 ± 0.13
0.999	0.08%	0.08%	1.11 ± 0.12
0.997	0.09%	0.08%	1.12 ± 0.12
0.995	0.10%	0.09%	1.13 ± 0.12
0.993	0.11%	0.09%	1.19 ± 0.12
0.991	0.11%	0.09%	1.20 ± 0.12
0.989	0.11%	0.10%	1.18 ± 0.11
0.987	0.12%	0.10%	1.17 ± 0.11
0.985	0.12%	0.10%	1.18 ± 0.11

Table 7.6: Evaluation of the Drell Yan neural net cut error is evaluated by varying the ee cut around the analysis cut value of 0.993. The ee channel is chosen because it shows the largest differences between data and Monte Carlo. The largest ratio between the data and Monte Carlo acceptances is found at a cut value of 0.991, and is 20%

likelihood template	Error (%) ee	Error (%) $e\mu$	Error (%) $\mu\mu$
all templates	± 1.0	± 1.6	± 2.1

Table 7.7: Average errors from uncertainties in lepton scale factors, trigger efficiencies and reconstruction

7.2.5 Generator

When $t\bar{t}$ background is independently generated with Herwig¹² it shows a discrepancy in acceptance of 6% compared with Pythia.⁷⁸² This error is therefore included in estimating the yield of the $t\bar{t}$ background. For practical reasons, this is placed on the non- W^+W^- background template in proportion to the $t\bar{t}$ background yield in the template. This is justified by the small quantity of the $t\bar{t}$ in the templates as it has been removed by the jet number cut; it is also justified by the position of the $t\bar{t}$ background in the neural net score, which appears at low neural-net scores, and does not effect the signal area of the scores. This has been tested by separating the $t\bar{t}$ template from the non- W^+W^- background template and performing the likelihood tests with the extra $t\bar{t}$ template, and was found to have negligible affects on the results.

7.2.6 $W\gamma$ conversion error

This is quoted at 20% from conversion error estimations used in current analyses⁷, based on estimations in a previous analysis¹¹. As with the $t\bar{t}$ generator error, this is applied to the non- W^+W^- -background template in proportion to the $W\gamma$ presence in the non- W^+W^- -template. As with the $t\bar{t}$, studies where the $W\gamma$ background has been separated from the non- W^+W^- -template and treated as a separate template have resulted in negligible changes in the calculated limit.

7.2.7 Cross section

Background cross section theoretical uncertainties including those on the next to leading order k-factor are estimated to be 10% for W^+W^- , $W^\pm Z^0$, $Z^0 Z^{05}$, $W\gamma$ and

$t\bar{t}$ ⁶².

7.2.8 Next-to-leading-order acceptance

The uncertainty in acceptance between leading order and next to leading order has been estimated at 6% for W^+W^- and 10% for other backgrounds, as calculated from the ratio of cross sections.

7.2.9 Summary

Table. 7.8 summarises the average systematics used in the analysis. Tables 7.9 and 7.10 show the expected limits at $M_H=160$ GeV with no errors, and with each error individually applied. The largest effect is from the Drell Yan Neural Net cut error.

Error type	likelihood template	Error (%) ee	Error (%) $e\mu$	Error (%) $\mu\mu$
Jet Energy Scale	Higgs	< 0.1	< 0.1	< 0.1
	WW	< 0.1	< 0.1	< 0.1
	non-WW	$-6.8+4.8$	$-1.6+1.1$	$-9.3+4.4$
Lepton Energy Scale	Higgs	< 0.1	± 0.9	$+0.3-0.1$
	WW	$+0.1-0.2$	$+0.6-0.8$	$+0.3-0.4$
	non-WW	$+1.1-1.5$	$+2.1-0.1$	$+4.5-1.7$
Initial State Radiation	Higgs	$+0.1-0.5$	$+ < 0.1 - 0.1$	$+ < 0.1 - 0.3$
	WW	$+2.0-3.8$	$+1.7-3.2$	$+1.9-3.7$
	non-WW	$+1.2-0.4$	$+0.7-1.5$	$+0.3- < 0.1$
Parton Distribution Function	Higgs	$+8.4-8.1$	$+8.2-7.4$	$+8.1-7.2$
	WW	$+4.2-4.3$	$+4.6-4.1$	$+4.6-4.2$
	non-WW	$+3.9-4.5$	$+3.1-2.9$	$+4.9-4.1$
Fake	non-WW	± 0.8	± 0.9	± 1.7
Luminosity	all templates	± 6		
Drell Yan Neural Net cut	all templates	± 20		
Lepton ID	all templates	± 1.0	± 1.6	± 2.1
Generator	non-WW	± 0.2	± 1.3	± 0.3
W-gamma conversion	non-WW	± 0.9	± 2.2	± 0.7
Cross section	all backgrounds	± 10		
NLO acceptance	WW	± 6		
	non-WW	± 10		
	Higgs	± 10		

Table 7.8: Summary of average systematic errors on the yield used in the analysis

Expected limit	-2 σ (pb)	-1 σ (pb)	Median (pb)	+1 σ (pb)	+2 σ (pb)
Statistical error only	0.80	1.05	1.45	2.03	2.79
Jet Energy Scale	0.82	1.09	1.53	2.16	3.02
Lepton Energy Scale	0.80	1.05	1.46	2.03	2.83
Initial State Radiation	0.84	1.11	1.54	2.20	3.02
Parton Distribution Function	0.80	1.08	1.52	2.17	3.01
Fake	0.79	1.05	1.46	2.05	2.84
Luminosity	0.82	1.09	1.50	2.11	2.89
Drell Yan Neural Net cut	0.84	1.11	1.55	2.18	3.01
Lepton ID	0.80	1.04	1.45	2.05	2.79
Generator	0.80	1.06	1.45	2.03	2.81
W-gamma conversion	0.81	1.07	1.48	2.07	2.81
Cross section	0.80	1.06	1.47	2.06	2.82
NLO acceptance	0.81	1.09	1.50	2.11	2.89

Table 7.9: Expected limits to 95% C.L. on $\sigma_{gg \rightarrow H} \cdot BR(H \rightarrow W^+W^- \rightarrow \ell\ell)$ with statistical errors and only one systematic error applied. The results are expressed in pb, and $M_H = 160$ GeV

Expected limit	-2 σ	-1 σ	Median $Limit/\sigma_{gg \rightarrow H}^{theory}$	+1 σ	+2 σ
Statistical error only	2.09	2.74	3.77	5.28	7.26
Jet Energy Scale	2.13	2.84	3.98	5.61	7.86
Lepton Energy Scale	2.09	2.74	3.80	5.30	7.37
Initial State Radiation	2.18	2.88	4.02	5.74	7.85
Parton Distribution Function	2.07	2.82	3.97	5.66	7.84
Fake	2.06	2.74	3.80	5.34	7.39
Luminosity	2.14	2.84	3.91	5.50	7.53
Drell Yan Neural Net cut	2.18	2.88	4.03	5.68	7.83
Lepton ID	2.07	2.72	3.78	5.33	7.27
Generator	2.07	2.75	3.77	5.28	7.31
W-gamma conversion	2.12	2.78	3.86	5.38	7.32
Cross section	2.08	2.77	3.82	5.37	7.34
NLO acceptance	2.11	2.85	3.90	5.49	7.52

Table 7.10: Expected limits to 95% C.L. on $\sigma_{gg \rightarrow H} \cdot BR(H \rightarrow W^+W^- \rightarrow \ell\ell)$ with statistical errors and only one systematic error applied. The results are expressed as a fraction of the theoretical $\sigma_{gg \rightarrow H}$, and $M_H = 160$ GeV

Chapter 8

Measurement

8.1 Results

The measurement is performed with a sample taken with an integrated luminosity of $\int \mathcal{L} dt = 2.4 \text{ fb}^{-1}$ which yields 198 data events after all cut have been applied (see Table 6.5 and Appendix A). The calculated limits found are listed in Table. 8.1 and are displayed in Fig. 8.3. Individual plots of pseudo experiments for each mass point can be seen in Fig. 8.1 and Fig. 8.2. The expected limits are lowest at the $M_H=160 \text{ GeV}$ and 170 GeV mass points due the both W bosons being released on-shell between these points. The observed limit remains within one σ of the expected limit for masses of 150 and below and are within 2σ for the mass points M_H 160 GeV to 190 GeV. Table 8.3 contains the limits from the $M_H=160 \text{ GeV}$ mass point split into the three channels, and shows that most discriminating power comes from the ee channel; the discrepancy between the expected and observed limits at this point is shown also to originate mostly in the $e\mu$ and $\mu\mu$ channels.

M_H (GeV)	110	120	130	140	150	160	170	180	190	200
-2 σ (pb)	9.55	3.76	2.38	1.72	1.39	0.82	0.75	0.83	0.93	1.04
-1 σ (pb)	13.17	5.23	3.35	2.43	1.90	1.12	1.03	1.14	1.30	1.47
Median (pb)	19.13	7.45	4.80	3.51	2.74	1.60	1.47	1.62	1.87	2.13
+1 σ (pb)	27.63	10.88	6.97	5.08	3.98	2.29	2.12	2.35	2.72	3.12
+2 σ (pb)	39.33	15.50	9.74	7.28	5.64	3.25	2.97	3.36	3.88	4.44
Observed Limit (pb)	25.58	7.02	4.04	5.08	3.31	2.63	2.97	2.68	3.46	2.83

Table 8.1: Measured observed and expected limits to 95% C.L. on $\sigma_{gg \rightarrow H} \cdot BR(H \rightarrow W^+W^- \rightarrow \ell\ell)$ expressed in pb

M_H (GeV)	110	120	130	140	150	160	170	180	190	200
-2 σ	169.96	28.65	10.58	5.57	3.90	2.14	2.24	3.04	4.97	6.95
-1 σ	234.40	39.91	14.93	7.85	5.35	2.93	3.07	4.18	6.92	9.81
Median $Limit/\sigma_{gg \rightarrow H}^{theory}$	340.55	56.84	21.38	11.34	7.71	4.17	4.36	5.98	9.99	14.22
+1 σ	491.78	83.01	31.00	16.43	11.19	5.98	6.29	8.66	14.53	20.84
+2 σ	700.10	118.21	43.34	23.55	15.85	8.47	8.82	12.38	20.73	29.65
Observed Limit/ $\sigma_{gg \rightarrow H}^{theory}$	455.29	53.58	17.97	16.43	9.30	6.85	8.81	9.87	18.46	18.89

Table 8.2: Measured observed and expected limits to 95% C.L. on $\sigma_{gg \rightarrow H}$ expressed as a fraction of the theoretical $\sigma_{gg \rightarrow H}$

Channel	ee	$e\mu$	$\mu\mu$
-2 σ	1.21	2.18	2.19
-1 σ	1.62	2.91	2.85
Median (pb)	2.31	4.12	3.95
+1 σ	3.43	5.94	5.66
+2 σ	4.95	8.62	8.06
Observed Limit (pb)	2.72	6.80	6.41

Table 8.3: Measured observed and expected limits to 95% C.L. on $\sigma_{gg \rightarrow H} \cdot BR(H \rightarrow W^+W^- \rightarrow \ell\ell)$ expressed in pb at $M_H = 160$ GeV and split into channels

Channel	ee	$e\mu$	$\mu\mu$
-2σ	3.40	6.12	6.15
-1σ	4.55	8.17	8.01
Median $Limit/\sigma_{gg\rightarrow H}^{theory}$	6.49	11.57	11.10
$+1\sigma$	9.63	16.69	15.90
$+2\sigma$	13.90	24.21	22.64
Observed Limit/ $\sigma_{gg\rightarrow H}^{theory}$	7.64	19.10	18.01

Table 8.4: Measured observed and expected limits to 95% C.L. on $\sigma_{gg\rightarrow H}$ expressed as a fraction of the theoretical $\sigma_{gg\rightarrow H}$ at $M_H = 160$ GeV and split into channels

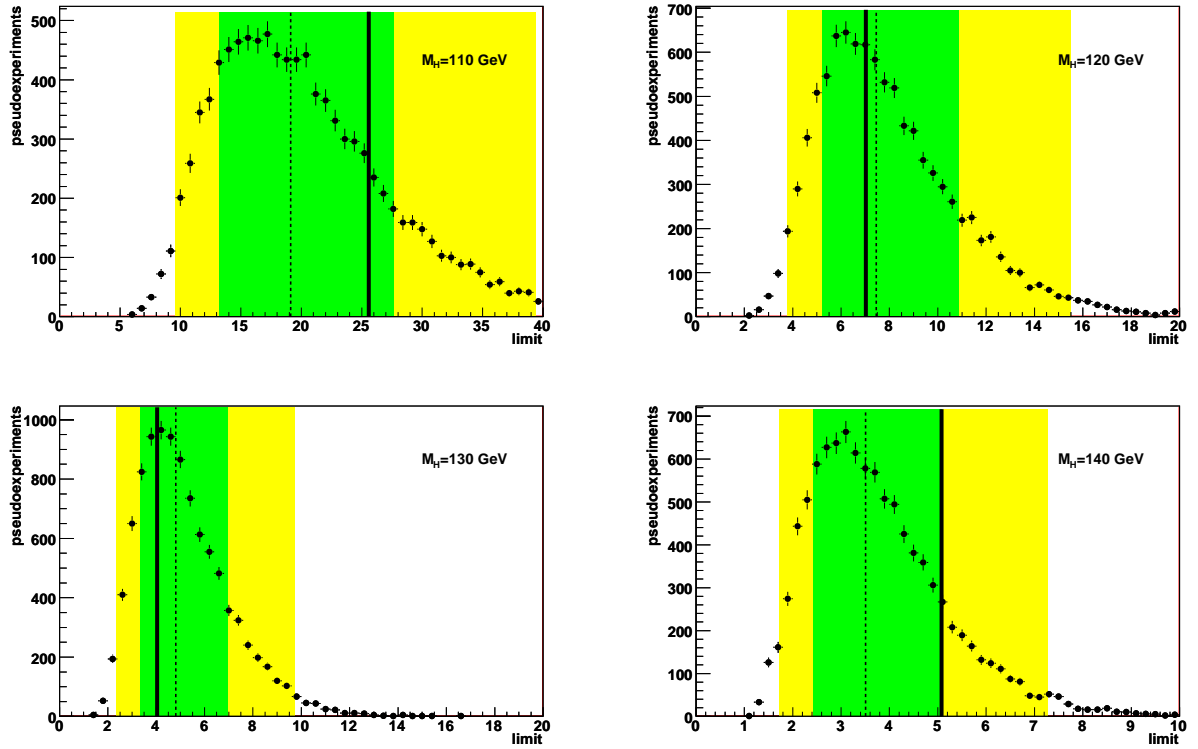


Figure 8.1: Plots of the limits set by the pseudo experiments with the resultant expected limit with errors. The observed limit is shown as a bold line. The 1σ error band is the green band, and the 2σ error band is shown by the yellow band.

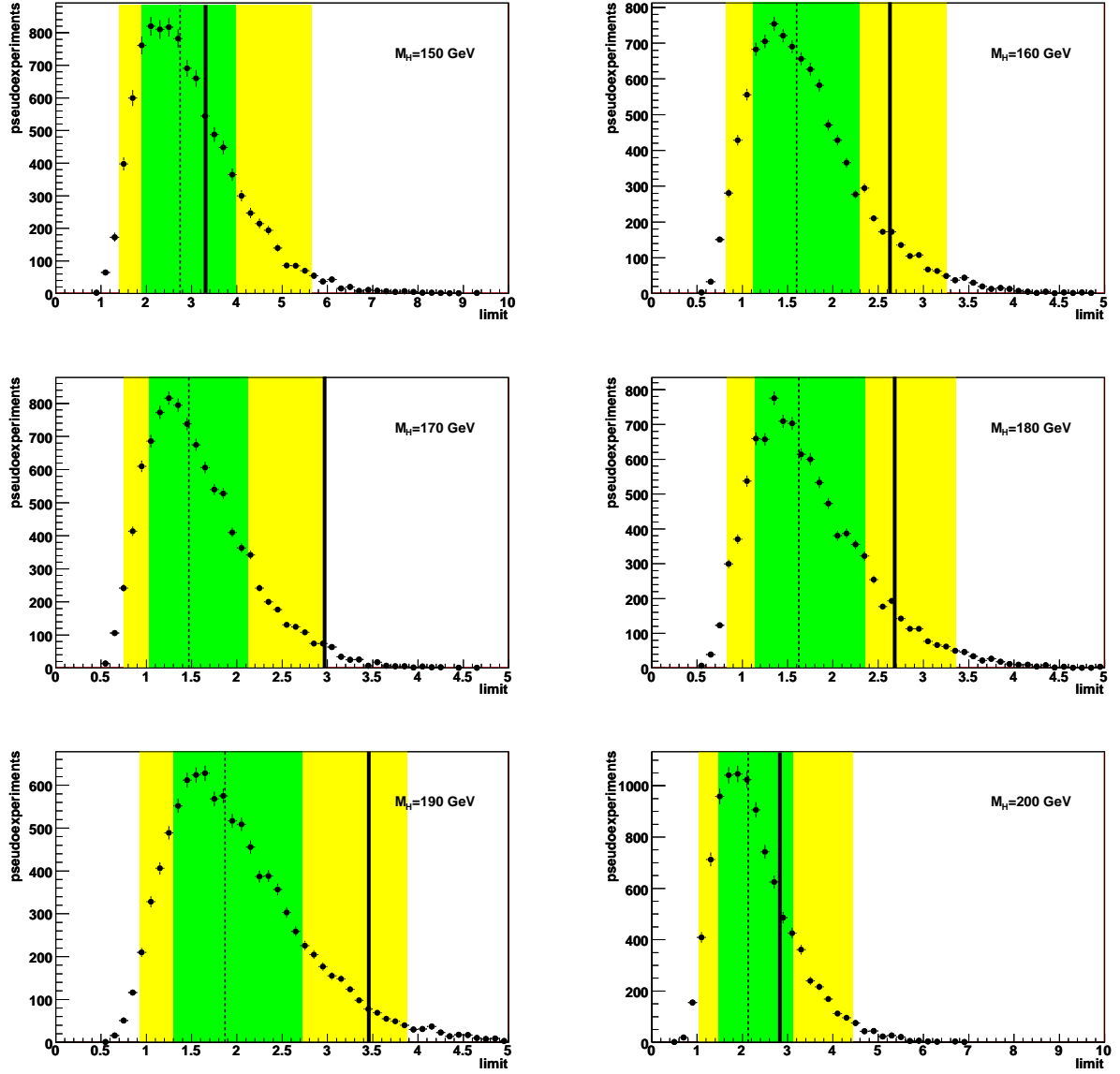


Figure 8.2: Plots of the limits set by the pseudo experiments with the resultant expected limit with errors. The observed limit is shown as a bold line. The 1σ error band is the green band, and the 2σ error band is shown by the yellow band.

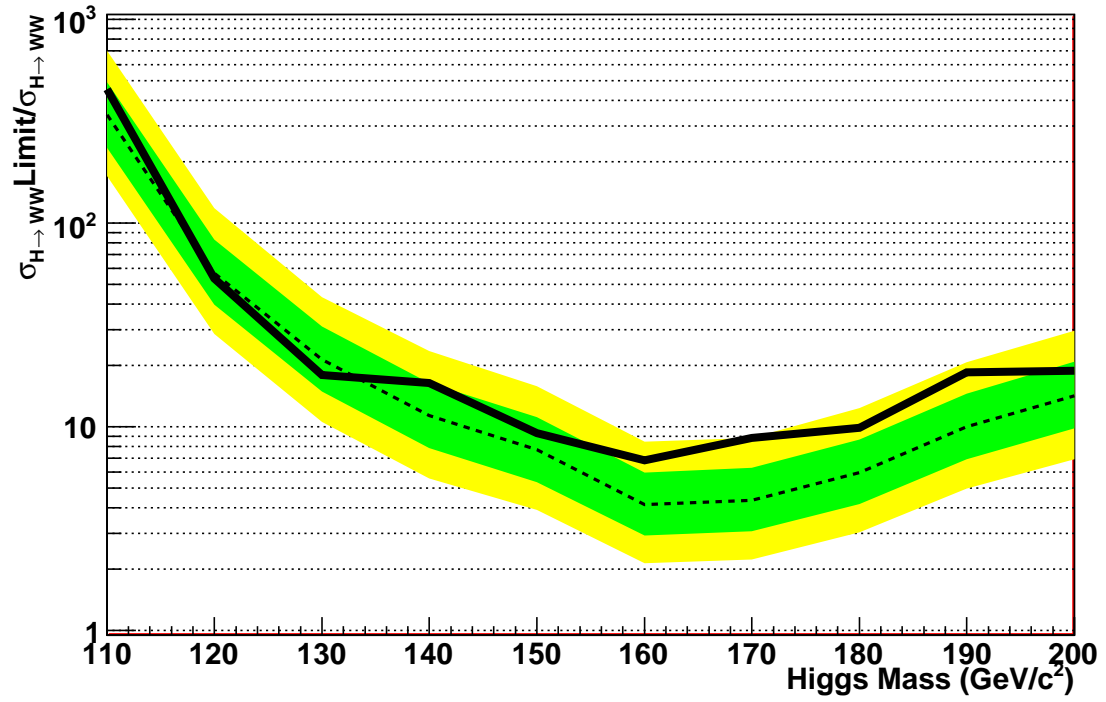


Figure 8.3: Expected and observed limits on $gg \rightarrow H$ plotted as a fraction of the theoretical standard model cross section. The dashed line represents the expected limits, with the observed limit shown by the bold line. The 1σ error band is the green band, and the 2σ error band is shown by the yellow band.

Chapter 9

Conclusion

A neural net was used to discriminate the $gg \rightarrow H \rightarrow W^+W^-$ signal from the background, and a likelihood test was performed on the resulting plots to obtain a limit on the cross section. Upper limits at 95% C.L. have been placed upon $\sigma(gg \rightarrow H \rightarrow W^+W^-) \cdot BR(W \rightarrow e, \mu)$. The lowest expected limit found was at a Mass of $M_H = 160$ GeV, with an expected limit of 4.17 times the Standard Model cross section. The observed limit was within one σ of the expected limit below $M_H = 160$ GeV, but showed an excess within two σ of the expected limit between the masses of $M_H = 160$ GeV and $M_H = 190$ GeV.

The effectiveness of the analysis is difficult to compare with the recent published CDF result⁸⁰ which found a minimal expected limit at 95% C.L. of $2.2 \cdot \sigma_{SM}$, as there were many differences in the implementation:

- There are different lepton types used in the published result to increase acceptance. These leptons more than double the signal, but in doing so increase the backgrounds significantly, specifically 399% for the $W\gamma$ background and 267% for the fake background. The fake backgrounds also contain large er-

rors due to much higher fake errors, which inflate the expected limits. The increase in sensitivity is therefore difficult to gauge.

- This analysis uses a cut on a neural net score to reject the Drell Yan, which is more efficient than a cut on \cancel{E}_T -based variable as used in the published result, but the published result also trains on the Drell Yan in the final score.
- The published result combines two techniques, the neural net and a matrix element technique, but the neural net strength is not evaluated in isolation. A direct comparison is therefore difficult.
- This analysis incorporates events with two jets to increase acceptance. These are not included in the explicit matrix element calculation used to generate likelihood ratios, and so are omitted from published result.
- The published result does not employ shape errors in the likelihood calculation, due to the necessity of recalculating matrix element score which are very CPU intensive.
- The published result includes 0.6 fb^{-1} extra luminosity.

A variety of multivariate techniques were tested with the neural net found to be the most discriminating. A variety of training methods were also tested, with the BFGS method proving the most effective. The limit calculation was performed on samples separated by physical lepton type, which is made possible due to the lepton types chosen in the analysis which are well identified. A method for improving signal to background ratio was suggested and tested, resulting in a potential 3% increase in sensitivity, but remains to be fully developed.

The analysis has prospects for improvement by including more luminosity and combining the multiple multivariate techniques tested here. Ultimately, combination with other channels will have the power to reduce the expected limits at $M_H=160$ GeV from CDF to that of the Standard Model in the near future.

Bibliography

- [1] The CDF Collaboration A. Abulencia et al. Search for a neutral higgs boson decaying to a w boson pair in p anti-p collisions at $\sqrt{s} = 1.96$ tev. *Phys. Rev. Lett.*, 97(081802), 2006.
- [2] Robert G. Wagner (ANL). Understanding and using lshr. CDF Internal Note 6249.
- [3] Veronique Boisvert. Trigger efficiencies for the high e_t central electrons in the gen6 data. CDF Internal Note 7939.
- [4] R. Mills C. N. Yang. Conservation of isotopic spin and isotopic gauge invariance. *Phys. Rev.*, 96:191, 1954.
- [5] J. M. Campbell and R. K. Ellis. Update on vector boson pair production at hadron colliders. *Phys. Rev. D*, 60:113006, 1999.
- [6] M. Carena, J. S. Conway, H. E. Haber, and J. D. Hobbs. Report of the higgs working group of the tevatron run 2 susy/higgs workshop. hep-ph/0010338v2, 2000.
- [7] et al CDF Collaboration: D.Acosta. Measurement of the w^+w^- produc-

- tion cross section in $p\bar{p}$ collisions at $\sqrt{s}=1.96$ tev using dilepton events. *Phys.Rev.Lett.*, 94(hep-ex/0501050v2):211–801, 2005.
- [8] Aidan Robson Cigdem Issever, Bob Wagner and Corrinne Mills. Plug electron baseline cuts as defined in summer 2003 and their efficiencies. CDF Internal Note 6789.
- [9] The CDF collaboration. Top mass measurement in the lepton + jets channel using a matrix element method with quasi-monte carlo integration and in situ jet calibration with 1.9 fb^{-1} . CDF Public Note 9301.
- [10] The CDF collaboration. The performance of the cdf luminosity monitor. *Nucl. Instr. Meth.*, A494:57–62, 2002.
- [11] The CDF collaboration. Measurement of $w\gamma$ and $z\gamma$ production in $p\bar{p}$ collisions at \sqrt{s} 1.96 tev. *Physics Review Letters*, 94(041803), 2005.
- [12] G. Corcella, I.G. Knowles, G. Marchesini, S. Moretti, K. Odagiri, P. Richardson, M.H. Seymour, and B.R. Webber. Herwig 6.5. *JHEP*, 0101(hep-ph/0210213):010, 2001.
- [13] P. M. Zerwas D. Graudenz, M. Spira. Qcd corrections to higgs-boson production at proton-proton colliders. *Phys. Rev. Lett.*, 70(10):1372–1375, 1993.
- [14] S. Rolli D. Hare, E. Halkiadakis. Electron id efficiencies and scale factors for periods 9 to 12. CDF Internal Note 9148.
- [15] T. Spreitzer D. Hare, E. Halkiadakis. Electron id efficiency and scale factors for winter 2007 analyses. CDF Internal Note 8614.

- [16] W. David Dagenhart. Measurement of the z production cross section. CDF Internal Note 8471.
- [17] D.Hidas, D.Benjamin, M.Kruse, T.Davies, A.Robson, P.Bussey, R.St.Denis, and A.S.Thompson. Fake lepton studies for hww analysis with 1 fb^{-1} . CDF Internal Note 8649.
- [18] M. Dittmar and H. Dreiner. How to find a higgs boson with a mass between 115 ad 180 gev at the cern lhc. *Phys. Rev. D*, 55(1):167–172, 1997.
- [19] Fermilab Accelerator Division. The fermilab main injector technical design handbook. http://www-fni.fnal.gov/fmiinternal/MI_Technical_Design/index.html.
- [20] Fermilab Accelerator Division. Tevatron data summary tables. <http://www-bd.fnal.gov/ppplot/today/DataSummaryTables.html>.
- [21] Fermilab Accelerator Division. Fermilab Linac upgrade conceptual design revision 4A. *FERMILAB-LU-CONCEPTUAL-DESIGN*, 1989. <http://lss.fnal.gov/archive/linac/fermilab-lu-999.shtml>.
- [22] A. Djouadi, J.Kalinowski, and M. Spira. Hdecay: a program for higgs decays in the standard model and its supersymmetric extension. hep-ph/9704448v1, 1997.
- [23] T. Dorigo. The muon system upgrade for the cdf ii experiment. *Nucl. Instrum. Methods*, A461:560–562, 2001.
- [24] Brian Drendel. 2008 pbar rookie book update. <http://www-drendel.fnal.gov/documents/2007-Pbar-Rookie-Book.htm>.

- [25] M. Tecchio E. Halkiadakis, C. Hays and W. Yao. A conversion removal algorithm for the 2003 winter conferences. CDF Internal Note 6250.
- [26] J. Elias, S. Klimenko, J. konisberg, A. Korytov, G. Mitselmakher, A. Nomerotski, D. Northacker, A. Safonov, and R. Vidal. Luminosity montior based on cherenkov counters for $p\bar{p}$ colliders. CDF Internal Note 5003, 1999.
- [27] Franois Englert and Robert Brout. Broken symmetry and the mass of gauge vector mesons. *Phys. Rev. Lett*, 13:321–23, 1964.
- [28] A Abulencia et al. Measurements of inclusive w and z cross sections in $p\bar{p}$ collisions at $\sqrt{s} = 19.6$ tev. *J.Phys. G:Nucl.Part. Phys.*, 34:2457–2544, 2007.
- [29] A. Affolder et al. Isl: Intermediate silicon layers detector for the cdf experiment. *Nucl. Instrum. Methods*, A453:84, 2000.
- [30] A. Affolder et al. Cot central outer tracker. *Nucl. Instrum. Methods*, A526:249, 2004.
- [31] A. Hocker et Al. Tmva - toolkit for multivariate data analysis. physics/0703039, 2007.
- [32] A. Sill et al. SvX-ii: Cdf run ii silicon tracking projects. *Nucl. Instrum. Methods*, A447:1, 2000.
- [33] C. Amsler et al. The review of particle physics. *Physics Letters B*, 667(1), 2008.
- [34] C. S. Hill et al. L00: Operational experience and performance of the cdf ii silicon detector. *Nucl. Instrum. Methods*, A530:1, 2004.

- [35] F. Abe et al. The cdf ii detector: Technical design report. Tech. Report FERMILAB-Pub-96/390-E, 1996.
- [36] G. Apollinari et al. Shower maximum detector for the cdf plug upgrade calorimeter. *Nucl. Instrum. Methods*, A412:515, 1998.
- [37] G. Ascoli et al. The cdf central muon detector. *Nucl. Instrum. Methods*, A268:33, 1998.
- [38] L. Balka et al. The cdf central electromagnetic calorimeter. *Nucl. Instrum. Methods*, A267:272–279, 1988.
- [39] M. Albrow et al. The cdf plug upgrade electromagnetic calorimeter: Test beam result. *Nucl. Instrum. Methods*, A480:524–546, 2002.
- [40] R.V. Harlander et al. A logical calculus of the ideas immanent in nervous activity. *Phys. Rev. Lett.*, 88:201801, 2002.
- [41] S. Bertolucci et al. The cdf central and endwall hadronic calorimeters. *Nucl. Instrum. Methods*, A267:301, 1988.
- [42] Richard Fernow. *Introduction to Experimental Particle Physics*. Cambridge University Press, 1986.
- [43] Gregorio Bernardi (for the CDF and D0 Collaboration). Searches and prospects for standard model higgs boson at the tevatron. arXiv:0809.5265v1 [hep-ex], 2008.
- [44] CDF Framework. <http://cdfkits.fnal.gov/CdfCode/source/Stntuple/top/CalConstants.hh#017> <http://cdfkits.fnal.gov/CdfCode/source/CalorGeometry/src/TowerKey.cc#046>.

- [45] CDF Framework. http://cdfkits.fnal.gov/CdfCode/source/Electron/src/emobj_alg.cc#1499.
- [46] CDF Framework. <http://cdfkits.fnal.gov/CdfCode/source/Stntuple/Stntuple/obj/TStnElectron.hh#269>.
- [47] CDF Framework. <http://cdfkits.fnal.gov/CdfCode/source/ElectronObjects/src/CdfEmObject.cc#704>.
- [48] CDF Framework. <http://cdfkits.fnal.gov/CdfCode/source/ElectronUser/ElectronUser/StdCEMElectron.icc#088>.
- [49] CDF Framework. <http://cdfkits.fnal.gov/CdfCode/source/Electron/src/PEMChiSquare.cc>.
- [50] David Griffiths. *Introduction to Elementary Particles*. John Wiley and Sons, 1987.
- [51] CDF Higgs Group. <http://www-cdf.fnal.gov/stdenis/internal/NVertStudyMetSumEt.html#SumEtUE>.
- [52] The TEVNPH Working Group. Combined cdf and d0 upper limits on standard model higgs boson production at high mass ($155200 \text{ geV}/c^2$) with 3fb^{71} of data. CDF Internal Note 9465, 2008.
- [53] U. Grundler, L. Lovas, and A. Taffard. High- p_t muons recommended cuts and efficiencies for winter 2007. CDF Internal Note 8618, 2006.
- [54] T. Hambye and K. Riesselmann. Matching conditions and higgs boson mass upper bounds re-examined. *Phys. Rev. D*, 7255(55), 1997.

- [55] Bo-Young Han and Veronique Boisvert. Trigger efficiencies for high e_t central electrons in the gen6 data. CDF Internal Note 8629, 2006.
- [56] Boyoung Han. Met pem trigger efficiency for phoenix electrons. CDF Internal Note 7940.
- [57] Joel Heinrich, Craig Blocker, John Conway, Luc Demoritier, Louis Lyons, Giovanni Punzi, and Pekka K. Sinervo. Interval estimation in the presence of nuisance parameters. 1 bayesian approach. physics/0409129, 2004.
- [58] Peter Higgs. Broken symmetries and the masses of gauge bosons. *Phys. Rev. Lett*, 13:508–09, 1964.
- [59] Yoshio Ishizawa and Jason Nielson. Trigger efficiencies for high e_t electrons. CDF Internal Note 7401, 2005.
- [60] Tom Junk. Sensitivity, exclusion and discovery with small signals, large backgrounds, and large systematic uncertainties. CDF Internal Note 8312.
- [61] Michio Kaku. *Quantum Field Theory: a Modern Introduction*. Oxford University Press, 1993.
- [62] Nikolaos Kidonakis and Ramona Vogt. Next-to-next-to-leading order soft-gluon corrections in top quark hadroproduction. hep-ph/0308222v1, 2003.
- [63] P. Lujan, A. Galtieri, J. Lys, J. Freeman, J. Nielsen, and I. Volobouev. Top mass measurement in the lepton + jets channel with the mtm3 matrix element method using 1.9 fb^{-1} . CDF Internal Note 9245.
- [64] Ernie Malamud. Fermilab’s chain of accelerators, accelerator details. <http://www-bd.fnal.gov/public/>.

- [65] Victoria Martin. Inclusive w and z cross section measurements at the fermilab tevatron. CDF Internal Note 7313, 2004.
- [66] Elliott McCrory. Fermilab linac department. <http://linac.fnal.gov/>.
- [67] W. McCulloch and W. Pitts. A logical calculus of the ideas immanent in nervous activity. *Bulletin of Mathematical Biophysics*, 7:115 – 133, 1943.
- [68] Sarah Lockwitz Mircea Coca, Eva Halkiadakis. Central electron identification efficiencies for the 200 pb^{-1} run 2 dataset. CDF Internal Note 6580.
- [69] Charles A. Nelson. Correlation between decay planes in higgs-boson decays into a w pair (into a z pair). *Phys. Rev. D*, 37(5):1220–1225, 1988.
- [70] T.K. Nelson. The cdf-ii silicon tracking system. *Nucl. Instrum. Methods*, A485:1–5, 2002.
- [71] Michael E. Peskin and Daniel V. Schroeder. *An Introduction to Quantum Field Theory*. Westview Press, 1995.
- [72] J. Pumplin, D.R. Stump, J Houston, H.L. Lai, P. Nadolsky, and W.K Tung. New generation of parton distributions with uncertainties from global analysis. [ph/0201195v3](#), 2008.
- [73] KURT RIESSELMANN. Limitations of a standard model higgs boson. [arXiv:hep-ph/9711456v1](#), 1997.
- [74] Raul Rojas. *Neural Networks: A Systematic Introduction*. Springer, 1996.
- [75] M. Kruse S. Chuang, M. Coca. Search for $h \rightarrow ww^*$ in the dilepton channel with 360 pb^{-1} of run ii data. CDF Internal Note 7708.

- [76] W.K. Sakumoto. Event $|z_{vtx}| < 60$ cm cut acceptance for run ii. CDF Internal Note 7935, 2005.
- [77] Torbjorn Sjostrand, Leif Lonnblad, Stephen Mrenna, and Peter Skands. Pythia 6.3 physics and manual. ph/0308153, 2003.
- [78] Torbjorn Sjostrand, Stephen Mrenna, and Peter Skands. Pythia 6.4 physics and manual. hep-ph/0603175v2, 2006.
- [79] T. Spreitzer and J. Incandela C, Mills. Electron id efficiency and scale factor with topntuple 6.1.4 for summer 2006. CDF Internal Note 8274.
- [80] The CDF Collaboration T. Aaltonen et al. Search for a higgs boson decaying to two w bosons at cdf. arXiv:0809.3930v1 [hep-ex], 2008.
- [81] J. Incandela T. Spreitzer, C. Mills. Electron identification in offline release 6.1.2. CDF Internal Note 7950.
- [82] M. Teccio. Acceptance and background systematics for the top dilepton cross section measurement. CDF Public Note 6590.
- [83] The Trigger and Datasets Working Group. The cdf run ii trigger table and datasets plan. CdfNote 4718, 1998.
- [84] The Trigger and Datasets Working Group. S. belforte et al. CdfNote 6362, 2002.
- [85] X. Zhang U. Grundler, A. Taffard. High- p_t muons recommended cuts and efficiencies for summer 2006. CDF Internal Note 8262.

- [86] Accelerator Update. Accelerator report no. 1: The cockcroft-walton.
http://www.fnal.gov/pub/news04/update_archive/update_9-10.html.
- [87] Accelerator Update. Accelerator report no. 10: The tevatron.
http://www.fnal.gov/pub/news04/update_archive/update_11-18.html.
- [88] Accelerator Update. Accelerator report no. 2: The fermi accelerator complex.
http://www.fnal.gov/pub/news04/update_archive/update_9-15.html.
- [89] Accelerator Update. Accelerator report no. 4: The linac.
http://www.fnal.gov/pub/news04/update_archive/update_10-1.html.
- [90] Accelerator Update. Accelerator report no. 5: The linac side-coupled cavities.
http://www.fnal.gov/pub/news04/update_archive/update_10-6.html.
- [91] Accelerator Update. Accelerator report no. 7: The booster.
http://www.fnal.gov/pub/news04/update_archive/update_10-22.html.
- [92] Accelerator Update. Accelerator report no. 9: The main injector.
http://www.fnal.gov/pub/news04/update_archive/update_11-10.html.
- [93] Bruce Worthel. Fermilab booster department. <http://www-bd.fnal.gov/proton/booster.html>.
- [94] Bruce Worthel. *Booster Rookie Book*, 2005. http://www-bdnew.fnal.gov/operations/rookie_books/Booster_V3_1.pdf.

Appendix A

Acceptance Tables

This appendix contains acceptance tables for all the samples broken down into dilepton types. No weights have been applied to the events. For Monte Carlo, the initial number of events is the number of generated events.

Category	no cut	Lepton ID	$M_{\ell\ell} > 25$	jet veto	opp sign	DYNN
TCE-TCE	2.25766e+07	0 0.00+-0.00	0 0+-0	0 0+-0	0 0+-0	0 0+-0
TCE-PHX	2.15487e+07	0 0+-0	0 0+-0	0 0+-0	0 0+-0	0 0+-0
e e Subtotal		0 0.00+-0.00	0 0+-0	0 0+-0	0 0+-0	0 0+-0
TCE-CMUP	2.22148e+07	990 0.00+-0.00	923 93.23+-0.80	807 87.43+-1.09	579 71.75+-1.58	1 0.17+-0.17
TCE-CMU	2.22148e+07	112 0.00+-0.00	111 99.11+-0.89	96 86.49+-3.24	87 90.62+-2.97	0 0.00+-0.00
TCE-CMP	2.22148e+07	154 0.00+-0.00	149 96.75+-1.43	119 79.87+-3.29	92 77.31+-3.84	0 0.00+-0.00
TCE-CMX	2.16576e+07	488 0.00+-0.00	455 93.24+-1.14	376 82.64+-1.78	270 71.81+-2.32	1 0.37+-0.37
PHX-CMUP	2.11928e+07	1778 0.01+-0.00	1771 99.61+-0.15	1705 96.27+-0.45	848 49.74+-1.21	6 0.71+-0.29
PHX-CMU	2.11928e+07	292 0.00+-0.00	289 98.97+-0.59	275 95.16+-1.26	135 49.09+-3.01	0 0.00+-0.00
PHX-CMP	2.11928e+07	309 0.00+-0.00	309 100.00+-0.00	299 96.76+-1.01	143 47.83+-2.89	0 0.00+-0.00
PHX-CMX	2.07108e+07	1034 0.00+-0.00	992 95.94+-0.61	960 96.77+-0.56	512 53.33+-1.61	2 0.39+-0.28
e mu Subtotal		5157 0.02+-0.00	4999 96.94+-0.24	4637 92.76+-0.37	2666 57.49+-0.73	10 0.38+-0.12
CMUP-CMUP	2.25592e+07	288047 1.28+-0.00	287424 99.78+-0.01	279393 97.21+-0.03	279393 100.00+-0.00	132 0.05+-0.00
CMUP-CMU	2.25592e+07	125979 0.56+-0.00	125786 99.85+-0.01	122068 97.04+-0.05	122068 100.00+-0.00	53 0.04+-0.01
CMUP-CMP	2.25592e+07	158402 0.70+-0.00	158198 99.87+-0.01	153440 96.99+-0.04	153440 100.00+-0.00	83 0.05+-0.01
CMUP-CMX	2.16866e+07	295523 1.36+-0.00	294961 99.81+-0.01	286219 97.04+-0.03	286217 100.00+-0.00	135 0.05+-0.00
CMX-CMX	2.19837e+07	86566 0.39+-0.00	86450 99.87+-0.01	84354 97.58+-0.05	84354 100.00+-0.00	65 0.08+-0.01
CMX-CMU	2.16866e+07	62451 0.29+-0.00	62407 99.93+-0.01	60772 97.38+-0.06	60772 100.00+-0.00	38 0.06+-0.01
CMX-CMP	2.16866e+07	68432 0.32+-0.00	68345 99.87+-0.01	66277 96.97+-0.07	66277 100.00+-0.00	51 0.08+-0.01
mu mu Subtotal		1085400 4.90+-0.00	1083571 99.83+-0.00	1052523 97.13+-0.02	1052521 100.00+-0.00	557 0.05+-0.00
Total	2.31597e+07	1090557 4.71+-0.00	1088570 99.82+-0.00	1057160 97.11+-0.02	1055187 99.81+-0.00	567 0.05+-0.00

Table A.1: $Z \rightarrow \mu^- \mu^+$ acceptances

Category	no cut	Lepton ID	$M_{\ell\ell} > 25$	jet veto	opp sign	DYNN
TCE-TCE	2.26115e+07	918185 4.06+-0.00	916088 99.77+-0.00	836531 91.32+-0.03	835863 99.92+-0.00	584 0.07+-0.00
TCE-PHX	2.16042e+07	1190839 5.51+-0.00	1189628 99.90+-0.00	1135527 95.45+-0.02	1009204 88.88+-0.03	198 0.02+-0.00
e e Subtotal		2109024 9.57+-0.01	2105716 99.84+-0.00	1972058 93.65+-0.02	1845067 93.56+-0.02	782 0.04+-0.00
TCE-CMUP	2.2247e+07	2 0.00+-0.00	2 100.00+-0.00	1 50.00+-35.36	1 100.00+-0.00	0 0.00+-0.00
TCE-CMU	2.2247e+07	0 0+-0	0 0+-0	0 0+-0	0 0+-0	0 0+-0
TCE-CMP	2.2247e+07	2 0.00+-0.00	1 50.00+-35.36	1 100.00+-0.00	1 100.00+-0.00	0 0.00+-0.00
TCE-CMX	2.17149e+07	0 0+-0	0 0+-0	0 0+-0	0 0+-0	0 0+-0
PHX-CMUP	2.12456e+07	1 0.00+-0.00	1 100.00+-0.00	0 0.00+-0.00	0 0+-0	0 0+-0
PHX-CMU	2.12456e+07	0 0+-0	0 0+-0	0 0+-0	0 0+-0	0 0+-0
PHX-CMP	2.12456e+07	2 0.00+-0.00	2 100.00+-0.00	2 100.00+-0.00	2 100.00+-0.00	0 0.00+-0.00
PHX-CMX	2.07704e+07	2 0.00+-0.00	2 100.00+-0.00	2 100.00+-0.00	1 50.00+-35.36	0 0.00+-0.00
e mu Subtotal		9 0.00+-0.00	8 88.89+-10.48	6 75.00+-15.31	5 83.33+-15.21	0 0.00+-0.00
CMUP-CMUP	2.25925e+07	0 0+-0	0 0+-0	0 0+-0	0 0+-0	0 0+-0
CMUP-CMU	2.25925e+07	0 0+-0	0 0+-0	0 0+-0	0 0+-0	0 0+-0
CMUP-CMP	2.25925e+07	0 0+-0	0 0+-0	0 0+-0	0 0+-0	0 0+-0
CMUP-CMX	2.17423e+07	0 0+-0	0 0+-0	0 0+-0	0 0+-0	0 0+-0
CMX-CMX	2.20421e+07	0 0+-0	0 0+-0	0 0+-0	0 0+-0	0 0+-0
CMX-CMU	2.17423e+07	0 0+-0	0 0+-0	0 0+-0	0 0+-0	0 0+-0
CMX-CMP	2.17423e+07	0 0+-0	0 0+-0	0 0+-0	0 0+-0	0 0+-0
mu mu Subtotal		0 0+-0	0 0+-0	0 0+-0	0 0+-0	0 0+-0
Total	2.31956e+07	2109033 9.09+-0.01	2105724 99.84+-0.00	1972064 93.65+-0.02	1845072 93.56+-0.02	782 0.04+-0.00

Table A.2: $Z \rightarrow e^-e^+$ acceptances

Category	no cut	Lepton ID	$M_{\ell\ell} > 25$	jet veto	opp sign	DYNN
TCE-TCE	9.52313e+06	398585 4.19+-0.01	394356 98.94+-0.02	171428 43.47+-0.08	157228 91.72+-0.07	27212 17.31+-0.10
TCE-PHX	9.15391e+06	417753 4.56+-0.01	416625 99.73+-0.01	193294 46.40+-0.08	156967 81.21+-0.09	24261 15.46+-0.09
e e Subtotal		816338 8.75+-0.01	810981 99.34+-0.01	364722 44.97+-0.06	314195 86.15+-0.06	51473 16.38+-0.07
TCE-CMUP	9.38816e+06	65279 0.70+-0.00	59915 91.78+-0.11	44656 74.53+-0.18	22836 51.14+-0.24	7225 31.64+-0.31
TCE-CMU	9.38816e+06	13030 0.14+-0.00	12253 94.04+-0.21	9236 75.38+-0.39	4629 50.12+-0.52	1520 32.84+-0.69
TCE-CMP	9.38816e+06	16196 0.17+-0.00	15067 93.03+-0.20	11262 74.75+-0.35	5632 50.01+-0.47	1993 35.39+-0.64
TCE-CMX	9.1552e+06	33304 0.36+-0.00	31461 94.47+-0.13	23771 75.56+-0.24	12022 50.57+-0.32	3337 27.76+-0.41
PHX-CMUP	9.02126e+06	35748 0.40+-0.00	35589 99.56+-0.04	28079 78.90+-0.22	14235 50.70+-0.30	2740 19.25+-0.33
PHX-CMU	9.02126e+06	7080 0.08+-0.00	7000 98.87+-0.13	5531 79.01+-0.49	2792 50.48+-0.67	599 21.45+-0.78
PHX-CMP	9.02126e+06	9321 0.10+-0.00	9304 99.82+-0.04	7360 79.11+-0.42	3700 50.27+-0.58	769 20.78+-0.67
PHX-CMX	8.82636e+06	16870 0.19+-0.00	16294 96.59+-0.14	12942 79.43+-0.32	6470 49.99+-0.44	1099 16.99+-0.47
e mu Subtotal		196828 2.14+-0.00	186883 94.95+-0.05	142837 76.43+-0.10	72316 50.63+-0.13	19282 26.66+-0.16
CMUP-CMUP	9.52681e+06	128971 1.35+-0.00	126862 98.36+-0.04	66123 52.12+-0.14	58684 88.75+-0.12	13133 22.38+-0.17
CMUP-CMU	9.52681e+06	57663 0.61+-0.00	57002 98.85+-0.04	29314 51.43+-0.21	26049 88.86+-0.18	6333 24.31+-0.27
CMUP-CMP	9.52681e+06	73336 0.77+-0.00	72399 98.72+-0.04	37792 52.20+-0.19	33775 89.37+-0.16	7636 22.61+-0.23
CMUP-CMX	9.1934e+06	130220 1.42+-0.00	128894 98.98+-0.03	66628 51.69+-0.14	58475 87.76+-0.13	14122 24.15+-0.18
CMX-CMX	9.29385e+06	31454 0.34+-0.00	31130 98.97+-0.06	16626 53.41+-0.28	14554 87.54+-0.26	3236 22.23+-0.34
CMX-CMU	9.1934e+06	24067 0.26+-0.00	23883 99.24+-0.06	12744 53.36+-0.32	11234 88.15+-0.29	2725 24.26+-0.40
CMX-CMP	9.1934e+06	30736 0.33+-0.00	30489 99.20+-0.05	15932 52.25+-0.29	14035 88.09+-0.26	3666 26.12+-0.37
mu mu Subtotal		476447 5.08+-0.01	470659 98.79+-0.02	245159 52.09+-0.07	216806 88.43+-0.06	50851 23.45+-0.09
Total	9.74616e+06	1489613 15.28+-0.01	1468523 98.58+-0.01	752718 51.26+-0.04	603317 80.15+-0.05	121606 20.16+-0.05

Table A.3: $W^\pm Z^0$ acceptances

Category	no cut	Lepton ID	$M_{\ell\ell} > 25$	jet veto	opp sign	DYNN
TCE-TCE	2.24393e+08	34772 0.02+-0.00	33917 97.54+-0.08	24327 71.73+-0.24	22266 91.53+-0.18	148 0.66+-0.05
TCE-PHX	2.12299e+08	28129 0.01+-0.00	27884 99.13+-0.06	22235 79.74+-0.24	18096 81.39+-0.26	122 0.67+-0.06
e e Subtotal		62901 0.03+-0.00	61801 98.25+-0.05	46562 75.34+-0.17	40362 86.68+-0.16	270 0.67+-0.04
TCE-CMUP	2.20565e+08	254640 0.12+-0.00	7676 3.01+-0.03	5122 66.73+-0.54	3495 68.24+-0.65	244 6.98+-0.43
TCE-CMU	2.20565e+08	58842 0.03+-0.00	1304 2.22+-0.06	896 68.71+-1.28	547 61.05+-1.63	56 10.24+-1.30
TCE-CMP	2.20565e+08	14667 0.01+-0.00	1839 12.54+-0.27	1261 68.57+-1.08	908 72.01+-1.26	67 7.38+-0.87
TCE-CMX	2.1416e+08	98593 0.05+-0.00	5626 5.71+-0.07	3982 70.78+-0.61	2504 62.88+-0.77	188 7.51+-0.53
PHX-CMUP	2.08574e+08	3279 0.00+-0.00	3214 98.02+-0.24	2456 76.42+-0.75	1267 51.59+-1.01	79 6.24+-0.68
PHX-CMU	2.08574e+08	648 0.00+-0.00	608 93.83+-0.95	450 74.01+-1.78	230 51.11+-2.36	19 8.26+-1.82
PHX-CMP	2.08574e+08	1105 0.00+-0.00	1092 98.82+-0.32	903 82.69+-1.14	577 63.90+-1.60	22 3.81+-0.80
PHX-CMX	2.03272e+08	2643 0.00+-0.00	2347 88.80+-0.61	1869 79.63+-0.83	998 53.40+-1.15	74 7.41+-0.83
e mu Subtotal		434417 0.20+-0.00	23706 5.46+-0.03	16939 71.45+-0.29	10526 62.14+-0.37	749 7.12+-0.25
CMUP-CMUP	2.26043e+08	4114 0.00+-0.00	3706 90.08+-0.47	3400 91.74+-0.45	3004 88.35+-0.55	127 4.23+-0.37
CMUP-CMU	2.26043e+08	1807 0.00+-0.00	1718 95.07+-0.51	1613 93.89+-0.58	1512 93.74+-0.60	40 2.65+-0.41
CMUP-CMP	2.26043e+08	1652 0.00+-0.00	1532 92.74+-0.64	1454 94.91+-0.56	1344 92.43+-0.69	42 3.12+-0.47
CMUP-CMX	2.16313e+08	4437 0.00+-0.00	4138 93.26+-0.38	3843 92.87+-0.40	3187 82.93+-0.61	187 5.87+-0.42
CMX-CMX	2.19412e+08	1437 0.00+-0.00	1228 85.46+-0.93	1154 93.97+-0.68	925 80.16+-1.17	67 7.24+-0.85
CMX-CMU	2.16313e+08	844 0.00+-0.00	815 96.56+-0.63	765 93.87+-0.84	706 92.29+-0.96	31 4.39+-0.77
CMX-CMP	2.16313e+08	701 0.00+-0.00	677 96.58+-0.69	625 92.32+-1.02	569 91.04+-1.14	28 4.92+-0.91
mu mu Subtotal		14992 0.01+-0.00	13814 92.14+-0.22	12854 93.05+-0.22	11247 87.50+-0.29	522 4.64+-0.20
Total	2.54491e+08	512310 0.20+-0.00	99321 19.39+-0.06	76355 76.88+-0.13	62135 81.38+-0.14	1541 2.48+-0.06

Table A.4: fake acceptances

Category	no cut	Lepton ID	$M_{\ell\ell} > 25$	jet veto	opp sign	DYNN
TCE-TCE	2.24393e+08	47583 0.02+-0.00	46871 98.50+-0.06	41967 89.54+-0.14	41891 99.82+-0.02	58 0.14+-0.02
TCE-PHX	2.12299e+08	53258 0.03+-0.00	53110 99.72+-0.02	50533 95.15+-0.09	45076 89.20+-0.14	40 0.09+-0.01
e e Subtotal		100841 0.05+-0.00	99981 99.15+-0.03	92500 92.52+-0.08	86967 94.02+-0.08	98 0.11+-0.01
TCE-CMUP	2.20565e+08	501 0.00+-0.00	481 96.01+-0.87	419 87.11+-1.53	396 94.51+-1.11	23 5.81+-1.18
TCE-CMU	2.20565e+08	67 0.00+-0.00	64 95.52+-2.53	52 81.25+-4.88	52 100.00+-0.00	1 1.92+-1.90
TCE-CMP	2.20565e+08	94 0.00+-0.00	91 96.81+-1.81	80 87.91+-3.42	78 97.50+-1.75	4 5.13+-2.50
TCE-CMX	2.1416e+08	259 0.00+-0.00	248 95.75+-1.25	221 89.11+-1.98	203 91.86+-1.84	7 3.45+-1.28
PHX-CMUP	2.08574e+08	287 0.00+-0.00	282 98.26+-0.77	258 91.49+-1.66	187 72.48+-2.78	3 1.60+-0.92
PHX-CMU	2.08574e+08	37 0.00+-0.00	36 97.30+-2.67	31 86.11+-5.76	22 70.97+-8.15	0 0.00+-0.00
PHX-CMP	2.08574e+08	42 0.00+-0.00	42 100.00+-0.00	36 85.71+-5.40	25 69.44+-7.68	1 4.00+-3.92
PHX-CMX	2.03272e+08	177 0.00+-0.00	159 89.83+-2.27	154 96.86+-1.38	100 64.94+-3.85	1 1.00+-0.99
e mu Subtotal		1464 0.00+-0.00	1403 95.83+-0.52	1251 89.17+-0.83	1063 84.97+-1.01	40 3.76+-0.58
CMUP-CMUP	2.26043e+08	13027 0.01+-0.00	12824 98.44+-0.11	12424 96.88+-0.15	12423 99.99+-0.01	18 0.14+-0.03
CMUP-CMU	2.26043e+08	5348 0.00+-0.00	5301 99.12+-0.13	5139 96.94+-0.24	5138 99.98+-0.02	13 0.25+-0.07
CMUP-CMP	2.26043e+08	6643 0.00+-0.00	6575 98.98+-0.12	6338 96.40+-0.23	6337 99.98+-0.02	10 0.16+-0.05
CMUP-CMX	2.16313e+08	14263 0.01+-0.00	14141 99.14+-0.08	13720 97.02+-0.14	13718 99.99+-0.01	11 0.08+-0.02
CMX-CMX	2.19412e+08	4392 0.00+-0.00	4347 98.98+-0.15	4229 97.29+-0.25	4228 99.98+-0.02	4 0.09+-0.05
CMX-CMU	2.16313e+08	2733 0.00+-0.00	2721 99.56+-0.13	2646 97.24+-0.31	2646 100.00+-0.00	2 0.08+-0.05
CMX-CMP	2.16313e+08	3003 0.00+-0.00	2980 99.23+-0.16	2876 96.51+-0.34	2875 99.97+-0.03	2 0.07+-0.05
mu mu Subtotal		49409 0.02+-0.00	48889 98.95+-0.05	47372 96.90+-0.08	47365 99.99+-0.01	60 0.13+-0.02
Total	2.54491e+08	151714 0.06+-0.00	150273 99.05+-0.02	141123 93.91+-0.06	135395 95.94+-0.05	198 0.15+-0.01

Table A.5: data acceptances

Category	no cut	Lepton ID	$M_{\ell\ell} > 25$	jet veto	opp sign	DYNN
TCE-TCE	1.58483e+07	5888 0.04+-0.00	5875 99.78+-0.06	5553 94.52+-0.30	5506 99.15+-0.12	33 0.60+-0.10
TCE-PHX	1.51068e+07	5902 0.04+-0.00	5892 99.83+-0.05	5652 95.93+-0.26	4967 87.88+-0.43	33 0.66+-0.12
e e Subtotal		11790 0.08+-0.00	11767 99.80+-0.04	11205 95.22+-0.20	10473 93.47+-0.23	66 0.63+-0.08
TCE-CMUP	1.55529e+07	6456 0.04+-0.00	6445 99.83+-0.05	6207 96.31+-0.23	6184 99.63+-0.08	7 0.11+-0.04
TCE-CMU	1.55529e+07	1002 0.01+-0.00	1000 99.80+-0.14	967 96.70+-0.56	966 99.90+-0.10	0 0.00+-0.00
TCE-CMP	1.55529e+07	1264 0.01+-0.00	1263 99.92+-0.08	1213 96.04+-0.55	1210 99.75+-0.14	2 0.17+-0.12
TCE-CMX	1.47587e+07	3110 0.02+-0.00	3106 99.87+-0.06	2975 95.78+-0.36	2966 99.70+-0.10	1 0.03+-0.03
PHX-CMUP	1.48158e+07	2862 0.02+-0.00	2861 99.97+-0.03	2762 96.54+-0.34	2421 87.65+-0.63	0 0.00+-0.00
PHX-CMU	1.48158e+07	540 0.00+-0.00	539 99.81+-0.19	530 98.33+-0.55	459 86.60+-1.48	0 0.00+-0.00
PHX-CMP	1.48158e+07	558 0.00+-0.00	558 100.00+-0.00	538 96.42+-0.79	469 87.17+-1.44	0 0.00+-0.00
PHX-CMX	1.41946e+07	1771 0.01+-0.00	1769 99.89+-0.08	1714 96.89+-0.41	1523 88.86+-0.76	0 0.00+-0.00
e mu Subtotal		17563 0.12+-0.00	17541 99.87+-0.03	16906 96.38+-0.14	16198 95.81+-0.15	10 0.06+-0.02
CMUP-CMUP	1.57057e+07	1941 0.01+-0.00	1938 99.85+-0.09	1881 97.06+-0.38	1881 100.00+-0.00	12 0.64+-0.18
CMUP-CMU	1.57057e+07	598 0.00+-0.00	598 100.00+-0.00	575 96.15+-0.79	575 100.00+-0.00	10 1.74+-0.55
CMUP-CMP	1.57057e+07	784 0.00+-0.00	784 100.00+-0.00	756 96.43+-0.66	756 100.00+-0.00	4 0.53+-0.26
CMUP-CMX	1.4718e+07	1695 0.01+-0.00	1694 99.94+-0.06	1638 96.69+-0.43	1638 100.00+-0.00	17 1.04+-0.25
CMX-CMX	1.49114e+07	471 0.00+-0.00	471 100.00+-0.00	458 97.24+-0.75	458 100.00+-0.00	11 2.40+-0.72
CMX-CMU	1.4718e+07	251 0.00+-0.00	251 100.00+-0.00	241 96.02+-1.23	241 100.00+-0.00	3 1.24+-0.71
CMX-CMP	1.4718e+07	257 0.00+-0.00	256 99.61+-0.39	249 97.27+-1.02	249 100.00+-0.00	1 0.40+-0.40
mu mu Subtotal		5997 0.04+-0.00	5992 99.92+-0.04	5798 96.76+-0.23	5798 100.00+-0.00	58 1.00+-0.13
Total	1.60857e+07	35350 0.22+-0.00	35300 99.86+-0.02	33909 96.06+-0.10	32469 95.75+-0.11	134 0.41+-0.04

Table A.6: $Z \rightarrow \tau^- \tau^+$ acceptances

Category	no cut	Lepton ID	$M_{\ell\ell} > 25$	jet veto	opp sign	DYNN
TCE-TCE	8.96708e+06	136829 1.53+-0.00	127118 92.90+-0.07	115438 90.81+-0.08	115278 99.86+-0.01	50069 43.43+-0.15
TCE-PHX	8.57205e+06	113012 1.32+-0.00	110546 97.82+-0.04	103523 93.65+-0.07	91553 88.44+-0.10	31634 34.55+-0.16
e e Subtotal		249841 2.84+-0.01	237664 95.13+-0.04	218961 92.13+-0.06	206831 94.46+-0.05	81703 39.50+-0.11
TCE-CMUP	8.83964e+06	156445 1.77+-0.00	144206 92.18+-0.07	134056 92.96+-0.07	133943 99.92+-0.01	41224 30.78+-0.13
TCE-CMU	8.83964e+06	30791 0.35+-0.00	29163 94.71+-0.13	27136 93.05+-0.15	27116 99.93+-0.02	8561 31.57+-0.28
TCE-CMP	8.83964e+06	39794 0.45+-0.00	37285 93.70+-0.12	34603 92.81+-0.13	34582 99.94+-0.01	11950 34.56+-0.26
TCE-CMX	8.61767e+06	73764 0.86+-0.00	69614 94.37+-0.08	64785 93.06+-0.10	64728 99.91+-0.01	15913 24.58+-0.17
PHX-CMUP	8.44679e+06	63431 0.75+-0.00	63016 99.35+-0.03	60376 95.81+-0.08	53387 88.42+-0.13	8886 16.64+-0.16
PHX-CMU	8.44679e+06	13043 0.15+-0.00	12857 98.57+-0.10	12341 95.99+-0.17	10889 88.23+-0.29	2017 18.52+-0.37
PHX-CMP	8.44679e+06	16292 0.19+-0.00	16245 99.71+-0.04	15540 95.66+-0.16	13628 87.70+-0.26	2621 19.23+-0.34
PHX-CMX	8.26226e+06	32091 0.39+-0.00	30691 95.64+-0.11	29484 96.07+-0.11	25977 88.11+-0.19	4082 15.71+-0.23
e mu Subtotal		425651 4.91+-0.01	403077 94.70+-0.03	378321 93.86+-0.04	364250 96.28+-0.03	95254 26.15+-0.07
CMUP-CMUP	8.96979e+06	45338 0.51+-0.00	41254 90.99+-0.13	39214 95.06+-0.11	39214 100.00+-0.00	16030 40.88+-0.25
CMUP-CMU	8.96979e+06	18525 0.21+-0.00	17349 93.65+-0.18	16564 95.48+-0.16	16564 100.00+-0.00	7469 45.09+-0.39
CMUP-CMP	8.96979e+06	24159 0.27+-0.00	22356 92.54+-0.17	21269 95.14+-0.14	21269 100.00+-0.00	9467 44.51+-0.34
CMUP-CMX	8.65312e+06	42913 0.50+-0.00	40435 94.23+-0.11	38659 95.61+-0.10	38658 100.00+-0.00	15927 41.20+-0.25
CMX-CMX	8.74783e+06	9856 0.11+-0.00	9282 94.18+-0.24	8886 95.73+-0.21	8886 100.00+-0.00	3179 35.78+-0.51
CMX-CMU	8.65312e+06	7210 0.08+-0.00	6821 94.60+-0.27	6503 95.34+-0.26	6503 100.00+-0.00	2843 43.72+-0.62
CMX-CMP	8.65312e+06	9167 0.11+-0.00	8727 95.20+-0.22	8251 94.55+-0.24	8251 100.00+-0.00	3855 46.72+-0.55
mu mu Subtotal		157168 1.78+-0.00	146224 93.04+-0.06	139346 95.30+-0.06	139345 100.00+-0.00	58770 42.18+-0.13
Total	9.17034e+06	832660 9.08+-0.01	786965 94.51+-0.02	736628 93.60+-0.03	710426 96.44+-0.02	235727 33.18+-0.06

Table A.7: W^+W^- acceptances

Category	no cut	Lepton ID	$M_{\ell\ell} > 25$	jet veto	opp sign	DYNN
TCE-TCE	9.06702e+06	288778 3.18+-0.01	282878 97.96+-0.03	111806 39.52+-0.09	110639 98.96+-0.03	18202 16.45+-0.11
TCE-PHX	8.69049e+06	242876 2.79+-0.01	241251 99.33+-0.02	101193 41.95+-0.10	88526 87.48+-0.10	15253 17.23+-0.13
e e Subtotal		531654 5.98+-0.01	524129 98.58+-0.02	212999 40.64+-0.07	199165 93.51+-0.05	33455 16.80+-0.08
TCE-CMUP	8.93748e+06	12592 0.14+-0.00	11750 93.31+-0.22	6265 53.32+-0.46	3696 58.99+-0.62	758 20.51+-0.66
TCE-CMU	8.93748e+06	2244 0.03+-0.00	2128 94.83+-0.47	1095 51.46+-1.08	639 58.36+-1.49	147 23.00+-1.66
TCE-CMP	8.93748e+06	2938 0.03+-0.00	2776 94.49+-0.42	1430 51.51+-0.95	808 56.50+-1.31	212 26.24+-1.55
TCE-CMX	8.80289e+06	5918 0.07+-0.00	5636 95.23+-0.28	3074 54.54+-0.66	1790 58.23+-0.89	294 16.42+-0.88
PHX-CMUP	8.56316e+06	5471 0.06+-0.00	5449 99.60+-0.09	3326 61.04+-0.66	1769 53.19+-0.87	167 9.44+-0.70
PHX-CMU	8.56316e+06	1047 0.01+-0.00	1028 98.19+-0.41	631 61.38+-1.52	323 51.19+-1.99	42 13.00+-1.87
PHX-CMP	8.56316e+06	1300 0.02+-0.00	1296 99.69+-0.15	775 59.80+-1.36	434 56.00+-1.78	51 11.75+-1.55
PHX-CMX	8.43815e+06	2749 0.03+-0.00	2653 96.51+-0.35	1634 61.59+-0.94	928 56.79+-1.23	70 7.54+-0.87
e mu Subtotal		34259 0.39+-0.00	32716 95.50+-0.11	18230 55.72+-0.27	10387 56.98+-0.37	1741 16.76+-0.37
CMUP-CMUP	9.06845e+06	98169 1.08+-0.00	95769 97.56+-0.05	43534 45.46+-0.16	42491 97.60+-0.07	11286 26.56+-0.21
CMUP-CMU	9.06845e+06	41801 0.46+-0.00	41144 98.43+-0.06	18496 44.95+-0.25	18044 97.56+-0.11	4978 27.59+-0.33
CMUP-CMP	9.06845e+06	55630 0.61+-0.00	54558 98.07+-0.06	24491 44.89+-0.21	23943 97.76+-0.09	6651 27.78+-0.29
CMUP-CMX	8.83791e+06	90407 1.02+-0.00	89059 98.51+-0.04	39807 44.70+-0.17	38654 97.10+-0.08	10770 27.86+-0.23
CMX-CMX	8.93385e+06	20909 0.23+-0.00	20450 97.80+-0.10	9536 46.63+-0.35	9268 97.19+-0.17	2289 24.70+-0.45
CMX-CMU	8.83791e+06	16406 0.19+-0.00	16142 98.39+-0.10	7491 46.41+-0.39	7283 97.22+-0.19	2006 27.54+-0.52
CMX-CMP	8.83791e+06	20947 0.24+-0.00	20737 99.00+-0.07	9313 44.91+-0.35	9045 97.12+-0.17	2610 28.86+-0.48
mu mu Subtotal		344269 3.84+-0.01	337859 98.14+-0.02	152668 45.19+-0.09	148728 97.42+-0.04	40590 27.29+-0.12
Total	9.27832e+06	910182 9.81+-0.01	894704 98.30+-0.01	383897 42.91+-0.05	358280 93.33+-0.04	75786 21.15+-0.07

Table A.8: $Z^0 Z^0$ acceptances

Category	no cut	Lepton ID	$M_{\ell\ell} > 25$	jet veto	opp sign	DYNN
TCE-TCE	7.1103e+06	14070 0.20+-0.00	13277 94.36+-0.19	1353 10.19+-0.26	1353 100.00+-0.00	587 43.39+-1.35
TCE-PHX	6.65356e+06	7867 0.12+-0.00	7687 97.71+-0.17	806 10.49+-0.35	718 89.08+-1.10	193 26.88+-1.65
e e Subtotal		21937 0.32+-0.00	20964 95.56+-0.14	2159 10.30+-0.21	2071 95.92+-0.43	780 37.66+-1.06
TCE-CMUP	6.91055e+06	16464 0.24+-0.00	15494 94.11+-0.18	1696 10.95+-0.25	1693 99.82+-0.10	615 36.33+-1.17
TCE-CMU	6.91055e+06	3127 0.05+-0.00	3011 96.29+-0.34	331 10.99+-0.57	331 100.00+-0.00	118 35.65+-2.63
TCE-CMP	6.91055e+06	4271 0.06+-0.00	4052 94.87+-0.34	400 9.87+-0.47	400 100.00+-0.00	168 42.00+-2.47
TCE-CMX	6.4918e+06	6309 0.10+-0.00	6008 95.23+-0.27	654 10.89+-0.40	653 99.85+-0.15	202 30.93+-1.81
PHX-CMUP	6.45817e+06	4774 0.07+-0.00	4747 99.43+-0.11	508 10.70+-0.45	464 91.34+-1.25	107 23.06+-1.96
PHX-CMU	6.45817e+06	798 0.01+-0.00	784 98.25+-0.46	95 12.12+-1.17	77 81.05+-4.02	24 31.17+-5.28
PHX-CMP	6.45817e+06	1104 0.02+-0.00	1101 99.73+-0.16	134 12.17+-0.99	116 86.57+-2.95	33 28.45+-4.19
PHX-CMX	6.11429e+06	1901 0.03+-0.00	1808 95.11+-0.49	185 10.23+-0.71	166 89.73+-2.23	36 21.69+-3.20
e mu Subtotal		38748 0.58+-0.00	37005 95.50+-0.11	4003 10.82+-0.16	3900 97.43+-0.25	1303 33.41+-0.76
CMUP-CMUP	7.06326e+06	4785 0.07+-0.00	4469 93.40+-0.36	511 11.43+-0.48	511 100.00+-0.00	244 47.75+-2.21
CMUP-CMU	7.06326e+06	1914 0.03+-0.00	1810 94.57+-0.52	195 10.77+-0.73	195 100.00+-0.00	94 48.21+-3.58
CMUP-CMP	7.06326e+06	2717 0.04+-0.00	2553 93.96+-0.46	294 11.52+-0.63	294 100.00+-0.00	156 53.06+-2.91
CMUP-CMX	6.50944e+06	3942 0.06+-0.00	3746 95.03+-0.35	391 10.44+-0.50	391 100.00+-0.00	155 39.64+-2.47
CMX-CMX	6.64451e+06	727 0.01+-0.00	684 94.09+-0.87	75 10.96+-1.19	75 100.00+-0.00	22 29.33+-5.26
CMX-CMU	6.50944e+06	584 0.01+-0.00	560 95.89+-0.82	60 10.71+-1.31	60 100.00+-0.00	30 50.00+-6.45
CMX-CMP	6.50944e+06	834 0.01+-0.00	809 97.00+-0.59	84 10.38+-1.07	84 100.00+-0.00	34 40.48+-5.36
mu mu Subtotal		15503 0.23+-0.00	14631 94.38+-0.19	1610 11.00+-0.26	1610 100.00+-0.00	735 45.65+-1.24
Total	7.32459e+06	76188 1.04+-0.00	72600 95.29+-0.08	7772 10.71+-0.11	7581 97.54+-0.18	2818 37.17+-0.56

Table A.9: $t\bar{t}$ acceptances

Category	no cut	Lepton ID	$M_{\ell\ell} > 25$	jet veto	opp sign	DYNN
TCE-TCE	4.79382e+06	446 0.01+-0.00	182 40.81+-2.33	171 93.96+-1.77	89 52.05+-3.82	10 11.24+-3.35
TCE-PHX	4.57464e+06	1165 0.03+-0.00	871 74.76+-1.27	832 95.52+-0.70	418 50.24+-1.73	47 11.24+-1.55
e e Subtotal		1611 0.03+-0.00	1053 65.36+-1.19	1003 95.25+-0.66	507 50.55+-1.58	57 11.24+-1.40
TCE-CMUP	4.7049e+06	355 0.01+-0.00	144 40.56+-2.61	132 91.67+-2.30	69 52.27+-4.35	5 7.25+-3.12
TCE-CMU	4.7049e+06	27 0.00+-0.00	7 25.93+-8.43	6 85.71+-13.23	1 16.67+-15.21	0 0.00+-0.00
TCE-CMP	4.7049e+06	26 0.00+-0.00	10 38.46+-9.54	10 100.00+-0.00	4 40.00+-15.49	1 25.00+-21.65
TCE-CMX	4.54756e+06	172 0.00+-0.00	93 54.07+-3.80	83 89.25+-3.21	43 51.81+-5.48	4 9.30+-4.43
PHX-CMUP	4.48729e+06	566 0.01+-0.00	516 91.17+-1.19	502 97.29+-0.72	252 50.20+-2.23	13 5.16+-1.39
PHX-CMU	4.48729e+06	82 0.00+-0.00	71 86.59+-3.76	70 98.59+-1.40	36 51.43+-5.97	1 2.78+-2.74
PHX-CMP	4.48729e+06	85 0.00+-0.00	82 96.47+-2.00	80 97.56+-1.70	38 47.50+-5.58	1 2.63+-2.60
PHX-CMX	4.353e+06	457 0.01+-0.00	273 59.74+-2.29	266 97.44+-0.96	143 53.76+-3.06	5 3.50+-1.54
e mu Subtotal		1770 0.04+-0.00	1196 67.57+-1.11	1149 96.07+-0.56	586 51.00+-1.47	30 5.12+-0.91
CMUP-CMUP	4.79782e+06	0 0+-0	0 0+-0	0 0+-0	0 0+-0	0 0+-0
CMUP-CMU	4.79782e+06	0 0+-0	0 0+-0	0 0+-0	0 0+-0	0 0+-0
CMUP-CMP	4.79782e+06	0 0+-0	0 0+-0	0 0+-0	0 0+-0	0 0+-0
CMUP-CMX	4.56524e+06	0 0+-0	0 0+-0	0 0+-0	0 0+-0	0 0+-0
CMX-CMX	4.63499e+06	0 0+-0	0 0+-0	0 0+-0	0 0+-0	0 0+-0
CMX-CMU	4.56524e+06	0 0+-0	0 0+-0	0 0+-0	0 0+-0	0 0+-0
CMX-CMP	4.56524e+06	0 0+-0	0 0+-0	0 0+-0	0 0+-0	0 0+-0
mu mu Subtotal		0 0+-0	0 0+-0	0 0+-0	0 0+-0	0 0+-0
Total	4.95244e+06	3381 0.07+-0.00	2249 66.52+-0.81	2152 95.69+-0.43	1093 50.79+-1.08	87 7.96+-0.82

Table A.10: $W\gamma$ acceptances

Category	no cut	Lepton ID	$M_{\ell\ell} > 25$	jet veto	opp sign	DYNN
TCE-TCE	1.16797e+06	9498 0.81+-0.01	5955 62.70+-0.50	4923 82.67+-0.49	4920 99.94+-0.04	793 16.12+-0.52
TCE-PHX	1.10849e+06	4411 0.40+-0.01	3390 76.85+-0.64	2980 87.91+-0.56	2776 93.15+-0.46	323 11.64+-0.61
e e Subtotal		13909 1.21+-0.01	9345 67.19+-0.40	7903 84.57+-0.37	7696 97.38+-0.18	1116 14.50+-0.40
TCE-CMUP	1.14845e+06	11357 0.99+-0.01	7191 63.32+-0.45	6094 84.74+-0.42	6092 99.97+-0.02	953 15.64+-0.47
TCE-CMU	1.14845e+06	1552 0.14+-0.00	1032 66.49+-1.20	865 83.82+-1.15	865 100.00+-0.00	197 22.77+-1.43
TCE-CMP	1.14845e+06	1994 0.17+-0.00	1256 62.99+-1.08	1020 81.21+-1.10	1019 99.90+-0.10	283 27.77+-1.40
TCE-CMX	1.11907e+06	4753 0.42+-0.01	3240 68.17+-0.68	2814 86.85+-0.59	2813 99.96+-0.04	248 8.82+-0.53
PHX-CMUP	1.08949e+06	1914 0.18+-0.00	1733 90.54+-0.67	1572 90.71+-0.70	1482 94.27+-0.59	14 0.94+-0.25
PHX-CMU	1.08949e+06	378 0.03+-0.00	279 73.81+-2.26	243 87.10+-2.01	224 92.18+-1.72	2 0.89+-0.63
PHX-CMP	1.08949e+06	331 0.03+-0.00	310 93.66+-1.34	270 87.10+-1.90	244 90.37+-1.80	6 2.46+-0.99
PHX-CMX	1.06461e+06	1621 0.15+-0.00	1058 65.27+-1.18	941 88.94+-0.96	867 92.14+-0.88	18 2.08+-0.48
e mu Subtotal		23900 2.12+-0.01	16099 67.36+-0.30	13819 85.84+-0.27	13606 98.46+-0.10	1721 12.65+-0.28
CMUP-CMUP	1.17628e+06	3483 0.30+-0.01	2077 59.63+-0.83	1780 85.70+-0.77	1780 100.00+-0.00	355 19.94+-0.95
CMUP-CMU	1.17628e+06	975 0.08+-0.00	627 64.31+-1.53	528 84.21+-1.46	528 100.00+-0.00	147 27.84+-1.95
CMUP-CMP	1.17628e+06	1322 0.11+-0.00	839 63.46+-1.32	699 83.31+-1.29	699 100.00+-0.00	191 27.32+-1.69
CMUP-CMX	1.12958e+06	2736 0.24+-0.00	1869 68.31+-0.89	1632 87.32+-0.77	1632 100.00+-0.00	261 15.99+-0.91
CMX-CMX	1.14567e+06	547 0.05+-0.00	342 62.52+-2.07	309 90.35+-1.60	309 100.00+-0.00	39 12.62+-1.89
CMX-CMU	1.12958e+06	287 0.03+-0.00	201 70.03+-2.70	172 85.57+-2.48	172 100.00+-0.00	40 23.26+-3.22
CMX-CMP	1.12958e+06	394 0.03+-0.00	277 70.30+-2.30	229 82.67+-2.27	229 100.00+-0.00	65 28.38+-2.98
mu mu Subtotal		9744 0.84+-0.01	6232 63.96+-0.49	5349 85.83+-0.44	5349 100.00+-0.00	1098 20.53+-0.55
Total	1.21413e+06	47553 3.92+-0.02	31676 66.61+-0.22	27071 85.46+-0.20	26651 98.45+-0.08	3935 14.76+-0.22

Table A.11: $gg \rightarrow H \rightarrow W^+W^-$ acceptances, assuming $M_H^{\text{SM}} = 110$ GeV

Category	no cut	Lepton ID	$M_{\ell\ell} > 25$	jet veto	opp sign	DYNN
TCE-TCE	1.17306e+06	12543 1.07+-0.01	8795 70.12+-0.41	7303 83.04+-0.40	7298 99.93+-0.03	2320 31.79+-0.55
TCE-PHX	1.1134e+06	6234 0.56+-0.01	5195 83.33+-0.47	4520 87.01+-0.47	4161 92.06+-0.40	894 21.49+-0.64
e e Subtotal		18777 1.63+-0.01	13990 74.51+-0.32	11823 84.51+-0.31	11459 96.92+-0.16	3214 28.05+-0.42
TCE-CMUP	1.15354e+06	14565 1.26+-0.01	9967 68.43+-0.39	8380 84.08+-0.37	8377 99.96+-0.02	2388 28.51+-0.49
TCE-CMU	1.15354e+06	2195 0.19+-0.00	1601 72.94+-0.95	1324 82.70+-0.95	1323 99.92+-0.08	450 34.01+-1.30
TCE-CMP	1.15354e+06	2914 0.25+-0.00	2057 70.59+-0.84	1699 82.60+-0.84	1699 100.00+-0.00	675 39.73+-1.19
TCE-CMX	1.12416e+06	6225 0.55+-0.01	4573 73.46+-0.56	3945 86.27+-0.51	3944 99.97+-0.03	756 19.17+-0.63
PHX-CMUP	1.0944e+06	2917 0.27+-0.00	2737 93.83+-0.45	2447 89.40+-0.59	2263 92.48+-0.53	73 3.23+-0.37
PHX-CMU	1.0944e+06	526 0.05+-0.00	454 86.31+-1.50	409 90.09+-1.40	376 91.93+-1.35	36 9.57+-1.52
PHX-CMP	1.0944e+06	462 0.04+-0.00	439 95.02+-1.01	390 88.84+-1.50	359 92.05+-1.37	11 3.06+-0.91
PHX-CMX	1.06952e+06	2123 0.20+-0.00	1508 71.03+-0.98	1333 88.40+-0.82	1216 91.22+-0.78	64 5.26+-0.64
e mu Subtotal		31927 2.81+-0.01	23336 73.09+-0.25	19927 85.39+-0.23	19557 98.14+-0.10	4453 22.77+-0.30
CMUP-CMUP	1.18138e+06	4334 0.37+-0.01	2855 65.87+-0.72	2454 85.95+-0.65	2454 100.00+-0.00	898 36.59+-0.97
CMUP-CMU	1.18138e+06	1442 0.12+-0.00	1017 70.53+-1.20	860 84.56+-1.13	860 100.00+-0.00	402 46.74+-1.70
CMUP-CMP	1.18138e+06	1947 0.16+-0.00	1325 68.05+-1.06	1115 84.15+-1.00	1115 100.00+-0.00	529 47.44+-1.50
CMUP-CMX	1.13468e+06	3785 0.33+-0.01	2790 73.71+-0.72	2402 86.09+-0.66	2402 100.00+-0.00	729 30.35+-0.94
CMX-CMX	1.15078e+06	690 0.06+-0.00	485 70.29+-1.74	430 88.66+-1.44	430 100.00+-0.00	137 31.86+-2.25
CMX-CMU	1.13468e+06	465 0.04+-0.00	360 77.42+-1.94	319 88.61+-1.67	319 100.00+-0.00	123 38.56+-2.73
CMX-CMP	1.13468e+06	621 0.05+-0.00	458 73.75+-1.77	401 87.55+-1.54	401 100.00+-0.00	177 44.14+-2.48
mu mu Subtotal		13284 1.14+-0.01	9290 69.93+-0.40	7981 85.91+-0.36	7981 100.00+-0.00	2995 37.53+-0.54
Total	1.21923e+06	63988 5.25+-0.02	46616 72.85+-0.18	39731 85.23+-0.16	38997 98.15+-0.07	10662 27.34+-0.23

Table A.12: $gg \rightarrow H \rightarrow W^+W^-$ acceptances, assuming $M_H^{\text{SM}} = 120$ GeV

Category	no cut	Lepton ID	$M_{\ell\ell} > 25$	jet veto	opp sign	DYNN
TCE-TCE	1.15414e+06	14575 1.26+-0.01	10830 74.31+-0.36	8968 82.81+-0.36	8960 99.91+-0.03	3968 44.29+-0.52
TCE-PHX	1.09457e+06	7608 0.70+-0.01	6610 86.88+-0.39	5795 87.67+-0.40	5335 92.06+-0.36	1759 32.97+-0.64
e e Subtotal		22183 1.96+-0.01	17440 78.62+-0.28	14763 84.65+-0.27	14295 96.83+-0.14	5727 40.06+-0.41
TCE-CMUP	1.13666e+06	17306 1.52+-0.01	12555 72.55+-0.34	10395 82.80+-0.34	10390 99.95+-0.02	4277 41.16+-0.48
TCE-CMU	1.13666e+06	2834 0.25+-0.00	2168 76.50+-0.80	1805 83.26+-0.80	1805 100.00+-0.00	847 46.93+-1.17
TCE-CMP	1.13666e+06	3830 0.34+-0.01	2895 75.59+-0.69	2392 82.63+-0.70	2390 99.92+-0.06	1281 53.60+-1.02
TCE-CMX	1.1053e+06	7229 0.65+-0.01	5566 77.00+-0.49	4690 84.26+-0.49	4689 99.98+-0.02	1344 28.66+-0.66
PHX-CMUP	1.07758e+06	3646 0.34+-0.01	3491 95.75+-0.33	3138 89.89+-0.51	2920 93.05+-0.45	203 6.95+-0.47
PHX-CMU	1.07758e+06	674 0.06+-0.00	610 90.50+-1.13	552 90.49+-1.19	487 88.22+-1.37	75 15.40+-1.64
PHX-CMP	1.07758e+06	623 0.06+-0.00	606 97.27+-0.65	546 90.10+-1.21	495 90.66+-1.25	48 9.70+-1.33
PHX-CMX	1.05075e+06	2469 0.23+-0.00	1878 76.06+-0.86	1630 86.79+-0.78	1477 90.61+-0.72	181 12.25+-0.85
e mu Subtotal		38611 3.46+-0.02	29769 77.10+-0.21	25148 84.48+-0.21	24653 98.03+-0.09	8256 33.49+-0.30
CMUP-CMUP	1.16449e+06	5222 0.45+-0.01	3602 68.98+-0.64	3065 85.09+-0.59	3065 100.00+-0.00	1481 48.32+-0.90
CMUP-CMU	1.16449e+06	1922 0.17+-0.00	1423 74.04+-1.00	1205 84.68+-0.95	1205 100.00+-0.00	696 57.76+-1.42
CMUP-CMP	1.16449e+06	2496 0.21+-0.00	1803 72.24+-0.90	1549 85.91+-0.82	1549 100.00+-0.00	946 61.07+-1.24
CMUP-CMX	1.11786e+06	4433 0.40+-0.01	3425 77.26+-0.63	2981 87.04+-0.57	2981 100.00+-0.00	1216 40.79+-0.90
CMX-CMX	1.13191e+06	866 0.08+-0.00	644 74.36+-1.48	565 87.73+-1.29	565 100.00+-0.00	186 32.92+-1.98
CMX-CMU	1.11786e+06	622 0.06+-0.00	477 76.69+-1.70	407 85.32+-1.62	407 100.00+-0.00	188 46.19+-2.47
CMX-CMP	1.11786e+06	768 0.07+-0.00	622 80.99+-1.42	540 86.82+-1.36	540 100.00+-0.00	303 56.11+-2.14
mu mu Subtotal		16329 1.43+-0.01	11996 73.46+-0.35	10312 85.96+-0.32	10312 100.00+-0.00	5016 48.64+-0.49
Total	1.20031e+06	77123 6.43+-0.02	59205 76.77+-0.15	50223 84.83+-0.15	49260 98.08+-0.06	18999 38.57+-0.22

Table A.13: $gg \rightarrow H \rightarrow W^+W^-$ acceptances, assuming $M_H^{\text{SM}} = 130$ GeV

Category	no cut	Lepton ID	$M_{\ell\ell} > 25$	jet veto	opp sign	DYNN
TCE-TCE	1.1678e+06	16686 1.43+-0.01	12907 77.35+-0.32	10546 81.71+-0.34	10540 99.94+-0.02	5913 56.10+-0.48
TCE-PHX	1.10837e+06	8586 0.77+-0.01	7618 88.73+-0.34	6584 86.43+-0.39	6015 91.36+-0.35	2482 41.26+-0.63
e e Subtotal		25272 2.20+-0.01	20525 81.22+-0.25	17130 83.46+-0.26	16555 96.64+-0.14	8395 50.71+-0.39
TCE-CMUP	1.14827e+06	19638 1.71+-0.01	14986 76.31+-0.30	12577 83.92+-0.30	12571 99.95+-0.02	6334 50.39+-0.45
TCE-CMU	1.14827e+06	3396 0.30+-0.01	2763 81.36+-0.67	2309 83.57+-0.70	2308 99.96+-0.04	1319 57.15+-1.03
TCE-CMP	1.14827e+06	4683 0.41+-0.01	3612 77.13+-0.61	2997 82.97+-0.63	2997 100.00+-0.00	1869 62.36+-0.88
TCE-CMX	1.1189e+06	8195 0.73+-0.01	6615 80.72+-0.44	5574 84.26+-0.45	5572 99.96+-0.03	2144 38.48+-0.65
PHX-CMUP	1.08936e+06	4366 0.40+-0.01	4241 97.14+-0.25	3793 89.44+-0.47	3514 92.64+-0.42	477 13.57+-0.58
PHX-CMU	1.08936e+06	810 0.07+-0.00	744 91.85+-0.96	652 87.63+-1.21	600 92.02+-1.06	143 23.83+-1.74
PHX-CMP	1.08936e+06	814 0.07+-0.00	799 98.16+-0.47	712 89.11+-1.10	648 91.01+-1.07	122 18.83+-1.54
PHX-CMX	1.06449e+06	2817 0.26+-0.00	2232 79.23+-0.76	1956 87.63+-0.70	1786 91.31+-0.64	304 17.02+-0.89
e mu Subtotal		44719 3.96+-0.02	35992 80.48+-0.19	30570 84.94+-0.19	29996 98.12+-0.08	12712 42.38+-0.29
CMUP-CMUP	1.17611e+06	5950 0.51+-0.01	4356 73.21+-0.57	3684 84.57+-0.55	3684 100.00+-0.00	2197 59.64+-0.81
CMUP-CMU	1.17611e+06	2300 0.20+-0.00	1776 77.22+-0.87	1510 85.02+-0.85	1510 100.00+-0.00	1014 67.15+-1.21
CMUP-CMP	1.17611e+06	3004 0.26+-0.00	2292 76.30+-0.78	1941 84.69+-0.75	1941 100.00+-0.00	1317 67.85+-1.06
CMUP-CMX	1.12941e+06	5136 0.45+-0.01	4194 81.66+-0.54	3549 84.62+-0.56	3549 100.00+-0.00	1903 53.62+-0.84
CMX-CMX	1.14551e+06	1059 0.09+-0.00	827 78.09+-1.27	734 88.75+-1.10	734 100.00+-0.00	304 41.42+-1.82
CMX-CMU	1.12941e+06	702 0.06+-0.00	569 81.05+-1.48	488 85.76+-1.46	488 100.00+-0.00	291 59.63+-2.22
CMX-CMP	1.12941e+06	969 0.09+-0.00	813 83.90+-1.18	669 82.29+-1.34	669 100.00+-0.00	443 66.22+-1.83
mu mu Subtotal		19120 1.65+-0.01	14827 77.55+-0.30	12575 84.81+-0.29	12575 100.00+-0.00	7469 59.40+-0.44
Total	1.21396e+06	89111 7.34+-0.02	71344 80.06+-0.13	60275 84.49+-0.14	59126 98.09+-0.06	28576 48.33+-0.21

Table A.14: $gg \rightarrow H \rightarrow W^+W^-$ acceptances, assuming $M_H^{\text{SM}} = 140$ GeV

Category	no cut	Lepton ID	$M_{\ell\ell} > 25$	jet veto	opp sign	DYNN
TCE-TCE	1.15053e+06	17804 1.55+-0.01	14041 78.86+-0.31	11402 81.21+-0.33	11389 99.89+-0.03	7335 64.40+-0.45
TCE-PHX	1.09098e+06	9430 0.86+-0.01	8557 90.74+-0.30	7339 85.77+-0.38	6668 90.86+-0.34	3201 48.01+-0.61
e e Subtotal		27234 2.41+-0.01	22598 82.98+-0.23	18741 82.93+-0.25	18057 96.35+-0.14	10536 58.35+-0.37
TCE-CMUP	1.131e+06	21404 1.89+-0.01	16684 77.95+-0.28	13682 82.01+-0.30	13679 99.98+-0.01	8093 59.16+-0.42
TCE-CMU	1.131e+06	3918 0.35+-0.01	3202 81.73+-0.62	2645 82.60+-0.67	2644 99.96+-0.04	1706 64.52+-0.93
TCE-CMP	1.131e+06	5388 0.48+-0.01	4272 79.29+-0.55	3477 81.39+-0.60	3477 100.00+-0.00	2356 67.76+-0.79
TCE-CMX	1.10162e+06	8822 0.80+-0.01	7152 81.07+-0.42	5974 83.53+-0.44	5973 99.98+-0.02	2883 48.27+-0.65
PHX-CMUP	1.07197e+06	4801 0.45+-0.01	4686 97.60+-0.22	4137 88.28+-0.47	3789 91.59+-0.43	777 20.51+-0.66
PHX-CMU	1.07197e+06	877 0.08+-0.00	826 94.18+-0.79	730 88.38+-1.12	664 90.96+-1.06	210 31.63+-1.80
PHX-CMP	1.07197e+06	895 0.08+-0.00	888 99.22+-0.29	798 89.86+-1.01	724 90.73+-1.03	218 30.11+-1.70
PHX-CMX	1.0471e+06	2923 0.28+-0.01	2375 81.25+-0.72	2047 86.19+-0.71	1851 90.43+-0.65	456 24.64+-1.00
e mu Subtotal		49028 4.41+-0.02	40085 81.76+-0.17	33490 83.55+-0.19	32801 97.94+-0.08	16699 50.91+-0.28
CMUP-CMUP	1.15839e+06	6577 0.57+-0.01	4898 74.47+-0.54	4100 83.71+-0.53	4100 100.00+-0.00	2762 67.37+-0.73
CMUP-CMU	1.15839e+06	2574 0.22+-0.00	2033 78.98+-0.80	1702 83.72+-0.82	1702 100.00+-0.00	1186 69.68+-1.11
CMUP-CMP	1.15839e+06	3432 0.30+-0.01	2564 74.71+-0.74	2149 83.81+-0.73	2149 100.00+-0.00	1557 72.45+-0.96
CMUP-CMX	1.11169e+06	5509 0.50+-0.01	4560 82.77+-0.51	3833 84.06+-0.54	3833 100.00+-0.00	2326 60.68+-0.79
CMX-CMX	1.12778e+06	1016 0.09+-0.00	798 78.54+-1.29	699 87.59+-1.17	699 100.00+-0.00	340 48.64+-1.89
CMX-CMU	1.11169e+06	811 0.07+-0.00	653 80.52+-1.39	549 84.07+-1.43	549 100.00+-0.00	345 62.84+-2.06
CMX-CMP	1.11169e+06	1154 0.10+-0.00	979 84.84+-1.06	841 85.90+-1.11	841 100.00+-0.00	592 70.39+-1.57
mu mu Subtotal		21073 1.85+-0.01	16485 78.23+-0.28	13873 84.16+-0.28	13873 100.00+-0.00	9108 65.65+-0.40
Total	1.19477e+06	97335 8.15+-0.03	79168 81.34+-0.12	66104 83.50+-0.13	64731 97.92+-0.06	36343 56.14+-0.20

Table A.15: $gg \rightarrow H \rightarrow W^+W^-$ acceptances, assuming $M_H^{\text{SM}} = 150$ GeV

Category	no cut	Lepton ID	$M_{\ell\ell} > 25$	jet veto	opp sign	DYNN
TCE-TCE	1.16252e+06	19556 1.68+-0.01	15250 77.98+-0.30	12102 79.36+-0.33	12090 99.90+-0.03	9062 74.95+-0.39
TCE-PHX	1.10288e+06	9638 0.87+-0.01	8687 90.13+-0.30	7342 84.52+-0.39	6698 91.23+-0.33	3692 55.12+-0.61
e e Subtotal		29194 2.56+-0.01	23937 81.99+-0.22	19444 81.23+-0.25	18788 96.63+-0.13	12754 67.88+-0.34
TCE-CMUP	1.143e+06	23826 2.08+-0.01	18400 77.23+-0.27	15056 81.83+-0.28	15047 99.94+-0.02	10890 72.37+-0.36
TCE-CMU	1.143e+06	4565 0.40+-0.01	3646 79.87+-0.59	2996 82.17+-0.63	2996 100.00+-0.00	2262 75.50+-0.79
TCE-CMP	1.143e+06	6396 0.56+-0.01	5034 78.71+-0.51	4080 81.05+-0.55	4077 99.93+-0.04	3255 79.84+-0.63
TCE-CMX	1.11531e+06	9559 0.86+-0.01	7761 81.19+-0.40	6454 83.16+-0.42	6449 99.92+-0.03	4054 62.86+-0.60
PHX-CMUP	1.08388e+06	4758 0.44+-0.01	4659 97.92+-0.21	4068 87.31+-0.49	3731 91.72+-0.43	1172 31.41+-0.76
PHX-CMU	1.08388e+06	920 0.08+-0.00	867 94.24+-0.77	751 86.62+-1.16	684 91.08+-1.04	349 51.02+-1.91
PHX-CMP	1.08388e+06	951 0.09+-0.00	945 99.37+-0.26	821 86.88+-1.10	758 92.33+-0.93	334 44.06+-1.80
PHX-CMX	1.06067e+06	3292 0.31+-0.01	2667 81.01+-0.68	2299 86.20+-0.67	2092 91.00+-0.60	776 37.09+-1.06
e mu Subtotal		54267 4.82+-0.02	43979 81.04+-0.17	36525 83.05+-0.18	35834 98.11+-0.07	23092 64.44+-0.25
CMUP-CMUP	1.17083e+06	7432 0.63+-0.01	5457 73.43+-0.51	4570 83.75+-0.50	4570 100.00+-0.00	3585 78.45+-0.61
CMUP-CMU	1.17083e+06	3018 0.26+-0.00	2361 78.23+-0.75	1983 83.99+-0.75	1983 100.00+-0.00	1581 79.73+-0.90
CMUP-CMP	1.17083e+06	4068 0.35+-0.01	3059 75.20+-0.68	2568 83.95+-0.66	2568 100.00+-0.00	2135 83.14+-0.74
CMUP-CMX	1.12583e+06	5970 0.53+-0.01	4952 82.95+-0.49	4208 84.98+-0.51	4208 100.00+-0.00	3023 71.84+-0.69
CMX-CMX	1.14193e+06	1132 0.10+-0.00	834 73.67+-1.31	697 83.57+-1.28	697 100.00+-0.00	415 59.54+-1.86
CMX-CMU	1.12583e+06	934 0.08+-0.00	742 79.44+-1.32	625 84.23+-1.34	625 100.00+-0.00	480 76.80+-1.69
CMX-CMP	1.12583e+06	1334 0.12+-0.00	1103 82.68+-1.04	940 85.22+-1.07	940 100.00+-0.00	765 81.38+-1.27
mu mu Subtotal		23888 2.07+-0.01	18508 77.48+-0.27	15591 84.24+-0.27	15591 100.00+-0.00	11984 76.86+-0.34
Total	1.20869e+06	107349 8.88+-0.03	86424 80.51+-0.12	71560 82.80+-0.13	70213 98.12+-0.05	47830 68.12+-0.18

Table A.16: $gg \rightarrow H \rightarrow W^+W^-$ acceptances, assuming $M_H^{\text{SM}} = 160$ GeV

Category	no cut	Lepton ID	$M_{\ell\ell} > 25$	jet veto	opp sign	DYNN
TCE-TCE	1.17066e+06	20459 1.75+-0.01	16549 80.89+-0.27	12997 78.54+-0.32	12984 99.90+-0.03	10016 77.14+-0.37
TCE-PHX	1.11099e+06	10390 0.94+-0.01	9517 91.60+-0.27	7969 83.73+-0.38	7239 90.84+-0.32	4025 55.60+-0.58
e e Subtotal		30849 2.68+-0.01	26066 84.50+-0.21	20966 80.43+-0.25	20223 96.46+-0.13	14041 69.43+-0.32
TCE-CMUP	1.15213e+06	24761 2.15+-0.01	19779 79.88+-0.25	16026 81.03+-0.28	16022 99.98+-0.01	11784 73.55+-0.35
TCE-CMU	1.15213e+06	4662 0.40+-0.01	3865 82.90+-0.55	3171 82.04+-0.62	3171 100.00+-0.00	2361 74.46+-0.77
TCE-CMP	1.15213e+06	6678 0.58+-0.01	5394 80.77+-0.48	4367 80.96+-0.53	4362 99.89+-0.05	3493 80.08+-0.60
TCE-CMX	1.12237e+06	10166 0.91+-0.01	8586 84.46+-0.36	7055 82.17+-0.41	7053 99.97+-0.02	4560 64.65+-0.57
PHX-CMUP	1.09299e+06	5260 0.48+-0.01	5169 98.27+-0.18	4477 86.61+-0.47	4089 91.33+-0.42	1618 39.57+-0.76
PHX-CMU	1.09299e+06	1026 0.09+-0.00	983 95.81+-0.63	867 88.20+-1.03	791 91.23+-0.96	414 52.34+-1.78
PHX-CMP	1.09299e+06	1078 0.10+-0.00	1068 99.07+-0.29	950 88.95+-0.96	870 91.58+-0.90	469 53.91+-1.69
PHX-CMX	1.06773e+06	3310 0.31+-0.01	2752 83.14+-0.65	2347 85.28+-0.68	2146 91.44+-0.58	875 40.77+-1.06
e mu Subtotal		56941 5.02+-0.02	47596 83.59+-0.16	39260 82.49+-0.17	38504 98.07+-0.07	25574 66.42+-0.24
CMUP-CMUP	1.17836e+06	7777 0.66+-0.01	5994 77.07+-0.48	4907 81.87+-0.50	4907 100.00+-0.00	3905 79.58+-0.58
CMUP-CMU	1.17836e+06	3167 0.27+-0.00	2609 82.38+-0.68	2191 83.98+-0.72	2191 100.00+-0.00	1826 83.34+-0.80
CMUP-CMP	1.17836e+06	4348 0.37+-0.01	3393 78.04+-0.63	2807 82.73+-0.65	2807 100.00+-0.00	2322 82.72+-0.71
CMUP-CMX	1.13129e+06	6298 0.56+-0.01	5368 85.23+-0.45	4518 84.17+-0.50	4518 100.00+-0.00	3369 74.57+-0.65
CMX-CMX	1.14738e+06	1223 0.11+-0.00	980 80.13+-1.14	829 84.59+-1.15	829 100.00+-0.00	549 66.22+-1.64
CMX-CMU	1.13129e+06	1062 0.09+-0.00	877 82.58+-1.16	734 83.69+-1.25	734 100.00+-0.00	591 80.52+-1.46
CMX-CMP	1.13129e+06	1471 0.13+-0.00	1314 89.33+-0.81	1103 83.94+-1.01	1103 100.00+-0.00	911 82.59+-1.14
mu mu Subtotal		25346 2.18+-0.01	20535 81.02+-0.25	17089 83.22+-0.26	17089 100.00+-0.00	13473 78.84+-0.31
Total	1.21522e+06	113136 9.31+-0.03	94197 83.26+-0.11	77315 82.08+-0.12	75816 98.06+-0.05	53088 70.02+-0.17

Table A.17: $gg \rightarrow H \rightarrow W^+W^-$ acceptances, assuming $M_H^{\text{SM}} = 170$ GeV

Category	no cut	Lepton ID	$M_{\ell\ell} > 25$	jet veto	opp sign	DYNN
TCE-TCE	1.14988e+06	20473 1.78+-0.01	17497 85.46+-0.25	13612 77.80+-0.31	13598 99.90+-0.03	9794 72.03+-0.38
TCE-PHX	1.09033e+06	11267 1.03+-0.01	10610 94.17+-0.22	8832 83.24+-0.36	7963 90.16+-0.32	4241 53.26+-0.56
e e Subtotal		31740 2.81+-0.02	28107 88.55+-0.18	22444 79.85+-0.24	21561 96.07+-0.13	14035 65.09+-0.32
TCE-CMUP	1.13036e+06	24818 2.20+-0.01	20860 84.05+-0.23	16688 80.00+-0.28	16682 99.96+-0.01	11465 68.73+-0.36
TCE-CMU	1.13036e+06	4844 0.43+-0.01	4234 87.41+-0.48	3399 80.28+-0.61	3396 99.91+-0.05	2427 71.47+-0.77
TCE-CMP	1.13036e+06	6804 0.60+-0.01	5824 85.60+-0.43	4705 80.79+-0.52	4702 99.94+-0.04	3495 74.33+-0.64
TCE-CMX	1.10153e+06	10169 0.92+-0.01	8842 86.95+-0.33	7194 81.36+-0.41	7186 99.89+-0.04	4383 60.99+-0.58
PHX-CMUP	1.07133e+06	6081 0.57+-0.01	6001 98.68+-0.15	5154 85.89+-0.45	4723 91.64+-0.39	1874 39.68+-0.71
PHX-CMU	1.07133e+06	1167 0.11+-0.00	1130 96.83+-0.51	950 84.07+-1.09	852 89.68+-0.99	425 49.88+-1.71
PHX-CMP	1.07133e+06	1336 0.12+-0.00	1329 99.48+-0.20	1155 86.91+-0.93	1038 89.87+-0.89	541 52.12+-1.55
PHX-CMX	1.047e+06	3349 0.32+-0.01	2883 86.09+-0.60	2433 84.39+-0.68	2193 90.14+-0.60	833 37.98+-1.04
e mu Subtotal		58568 5.27+-0.02	51103 87.25+-0.14	41678 81.56+-0.17	40772 97.83+-0.07	25443 62.40+-0.24
CMUP-CMUP	1.15819e+06	7864 0.68+-0.01	6474 82.32+-0.43	5297 81.82+-0.48	5297 100.00+-0.00	4041 76.29+-0.58
CMUP-CMU	1.15819e+06	3114 0.27+-0.00	2687 86.29+-0.62	2229 82.95+-0.73	2229 100.00+-0.00	1754 78.69+-0.87
CMUP-CMP	1.15819e+06	4239 0.37+-0.01	3462 81.67+-0.59	2814 81.28+-0.66	2814 100.00+-0.00	2260 80.31+-0.75
CMUP-CMX	1.11204e+06	6532 0.59+-0.01	5796 88.73+-0.39	4875 84.11+-0.48	4875 100.00+-0.00	3569 73.21+-0.63
CMX-CMX	1.12814e+06	1159 0.10+-0.00	973 83.95+-1.08	810 83.25+-1.20	810 100.00+-0.00	521 64.32+-1.68
CMX-CMU	1.11204e+06	1018 0.09+-0.00	880 86.44+-1.07	736 83.64+-1.25	736 100.00+-0.00	530 72.01+-1.65
CMX-CMP	1.11204e+06	1480 0.13+-0.00	1357 91.69+-0.72	1130 83.27+-1.01	1130 100.00+-0.00	903 79.91+-1.19
mu mu Subtotal		25406 2.23+-0.01	21629 85.13+-0.22	17891 82.72+-0.26	17891 100.00+-0.00	13578 75.89+-0.32
Total	1.1946e+06	115714 9.69+-0.03	100839 87.15+-0.10	82013 81.33+-0.12	80224 97.82+-0.05	53056 66.13+-0.17

Table A.18: $gg \rightarrow H \rightarrow W^+W^-$ acceptances, assuming $M_H^{\text{SM}} = 180$ GeV

Category	no cut	Lepton ID	$M_{\ell\ell} > 25$	jet veto	opp sign	DYNN
TCE-TCE	1.16288e+06	20980 1.80+-0.01	18613 88.72+-0.22	14268 76.66+-0.31	14256 99.92+-0.02	9476 66.47+-0.40
TCE-PHX	1.10392e+06	12134 1.10+-0.01	11603 95.62+-0.19	9516 82.01+-0.36	8592 90.29+-0.30	4338 50.49+-0.54
e e Subtotal		33114 2.90+-0.02	30216 91.25+-0.16	23784 78.71+-0.24	22848 96.06+-0.13	13814 60.46+-0.32
TCE-CMUP	1.1436e+06	25238 2.21+-0.01	22135 87.71+-0.21	17557 79.32+-0.27	17541 99.91+-0.02	10997 62.69+-0.37
TCE-CMU	1.1436e+06	4955 0.43+-0.01	4494 90.70+-0.41	3627 80.71+-0.59	3624 99.92+-0.05	2377 65.59+-0.79
TCE-CMP	1.1436e+06	6817 0.60+-0.01	6107 89.58+-0.37	4870 79.74+-0.51	4868 99.96+-0.03	3337 68.55+-0.67
TCE-CMX	1.11354e+06	10541 0.95+-0.01	9546 90.56+-0.28	7643 80.06+-0.41	7638 99.93+-0.03	4277 56.00+-0.57
PHX-CMUP	1.08516e+06	6846 0.63+-0.01	6786 99.12+-0.11	5788 85.29+-0.43	5276 91.15+-0.37	2008 38.06+-0.67
PHX-CMU	1.08516e+06	1188 0.11+-0.00	1161 97.73+-0.43	977 84.15+-1.07	858 87.82+-1.05	416 48.48+-1.71
PHX-CMP	1.08516e+06	1614 0.15+-0.00	1609 99.69+-0.14	1349 83.84+-0.92	1198 88.81+-0.86	569 47.50+-1.44
PHX-CMX	1.05961e+06	3427 0.32+-0.01	3125 91.19+-0.48	2684 85.89+-0.62	2392 89.12+-0.60	854 35.70+-0.98
e mu Subtotal		60626 5.40+-0.02	54963 90.66+-0.12	44495 80.95+-0.17	43395 97.53+-0.07	24835 57.23+-0.24
CMUP-CMUP	1.17143e+06	7790 0.66+-0.01	6715 86.20+-0.39	5490 81.76+-0.47	5490 100.00+-0.00	3972 72.35+-0.60
CMUP-CMU	1.17143e+06	3228 0.28+-0.00	2881 89.25+-0.55	2361 81.95+-0.72	2361 100.00+-0.00	1780 75.39+-0.89
CMUP-CMP	1.17143e+06	4233 0.36+-0.01	3682 86.98+-0.52	3002 81.53+-0.64	3002 100.00+-0.00	2220 73.95+-0.80
CMUP-CMX	1.1243e+06	6674 0.59+-0.01	6090 91.25+-0.35	5081 83.43+-0.48	5081 100.00+-0.00	3506 69.00+-0.65
CMX-CMX	1.14016e+06	1185 0.10+-0.00	1057 89.20+-0.90	870 82.31+-1.17	870 100.00+-0.00	540 62.07+-1.65
CMX-CMU	1.1243e+06	1055 0.09+-0.00	938 88.91+-0.97	752 80.17+-1.30	752 100.00+-0.00	527 70.08+-1.67
CMX-CMP	1.1243e+06	1534 0.14+-0.00	1453 94.72+-0.57	1199 82.52+-1.00	1199 100.00+-0.00	911 75.98+-1.23
mu mu Subtotal		25699 2.23+-0.01	22816 88.78+-0.20	18755 82.20+-0.25	18755 100.00+-0.00	13456 71.75+-0.33
Total	1.20905e+06	119439 9.88+-0.03	107995 90.42+-0.09	87034 80.59+-0.12	84998 97.66+-0.05	52105 61.30+-0.17

Table A.19: $gg \rightarrow H \rightarrow W^+W^-$ acceptances, assuming $M_H^{\text{SM}} = 190$ GeV

Category	no cut	Lepton ID	$M_{\ell\ell} > 25$	jet veto	opp sign	DYNN
TCE-TCE	1.16124e+06	21431 1.85+-0.01	19537 91.16+-0.19	14996 76.76+-0.30	14977 99.87+-0.03	9091 60.70+-0.40
TCE-PHX	1.10338e+06	12743 1.15+-0.01	12325 96.72+-0.16	10051 81.55+-0.35	9000 89.54+-0.31	4209 46.77+-0.53
e e Subtotal		34174 3.00+-0.02	31862 93.23+-0.14	25047 78.61+-0.23	23977 95.73+-0.13	13300 55.47+-0.32
TCE-CMUP	1.14174e+06	25758 2.26+-0.01	23315 90.52+-0.18	18293 78.46+-0.27	18283 99.95+-0.02	10579 57.86+-0.37
TCE-CMU	1.14174e+06	4986 0.44+-0.01	4651 93.28+-0.35	3715 79.88+-0.59	3714 99.97+-0.03	2203 59.32+-0.81
TCE-CMP	1.14174e+06	7022 0.62+-0.01	6452 91.88+-0.33	5097 79.00+-0.51	5092 99.90+-0.04	3141 61.68+-0.68
TCE-CMX	1.11655e+06	10633 0.95+-0.01	9833 92.48+-0.26	7828 79.61+-0.41	7825 99.96+-0.02	4026 51.45+-0.56
PHX-CMUP	1.0844e+06	7273 0.67+-0.01	7231 99.42+-0.09	6104 84.41+-0.43	5542 90.79+-0.37	2040 36.81+-0.65
PHX-CMU	1.0844e+06	1287 0.12+-0.00	1266 98.37+-0.35	1069 84.44+-1.02	936 87.56+-1.01	440 47.01+-1.63
PHX-CMP	1.0844e+06	1699 0.16+-0.00	1698 99.94+-0.06	1467 86.40+-0.83	1305 88.96+-0.82	624 47.82+-1.38
PHX-CMX	1.06187e+06	3426 0.32+-0.01	3153 92.03+-0.46	2652 84.11+-0.65	2356 88.84+-0.61	766 32.51+-0.97
e mu Subtotal		62084 5.53+-0.02	57599 92.78+-0.10	46225 80.25+-0.17	45053 97.46+-0.07	23819 52.87+-0.24
CMUP-CMUP	1.16936e+06	7623 0.65+-0.01	6841 89.74+-0.35	5626 82.24+-0.46	5626 100.00+-0.00	3710 65.94+-0.63
CMUP-CMU	1.16936e+06	3216 0.28+-0.00	2949 91.70+-0.49	2356 79.89+-0.74	2356 100.00+-0.00	1615 68.55+-0.96
CMUP-CMP	1.16936e+06	4175 0.36+-0.01	3707 88.79+-0.49	3028 81.68+-0.64	3028 100.00+-0.00	2089 68.99+-0.84
CMUP-CMX	1.12707e+06	6612 0.59+-0.01	6139 92.85+-0.32	5064 82.49+-0.49	5064 100.00+-0.00	3342 66.00+-0.67
CMX-CMX	1.14316e+06	1387 0.12+-0.00	1261 90.92+-0.77	1095 86.84+-0.95	1095 100.00+-0.00	654 59.73+-1.48
CMX-CMU	1.12707e+06	1115 0.10+-0.00	1045 93.72+-0.73	859 82.20+-1.18	859 100.00+-0.00	598 69.62+-1.57
CMX-CMP	1.12707e+06	1576 0.14+-0.00	1501 95.24+-0.54	1224 81.55+-1.00	1224 100.00+-0.00	877 71.65+-1.29
mu mu Subtotal		25704 2.23+-0.01	23443 91.20+-0.18	19252 82.12+-0.25	19252 100.00+-0.00	12885 66.93+-0.34
Total	1.20501e+06	121962 10.12+-0.03	112904 92.57+-0.08	90524 80.18+-0.12	88282 97.52+-0.05	50004 56.64+-0.17

Table A.20: $gg \rightarrow H \rightarrow W^+W^-$ acceptances, assuming $M_H^{\text{SM}} = 200$ GeV

Appendix B

Detailed Input plots

This Appendix contains plots of the input variables separated into ee , $e\mu$ and $\mu\mu$.

The Higgs signal from the $M_H=160$ GeV mass point is included in the plots.

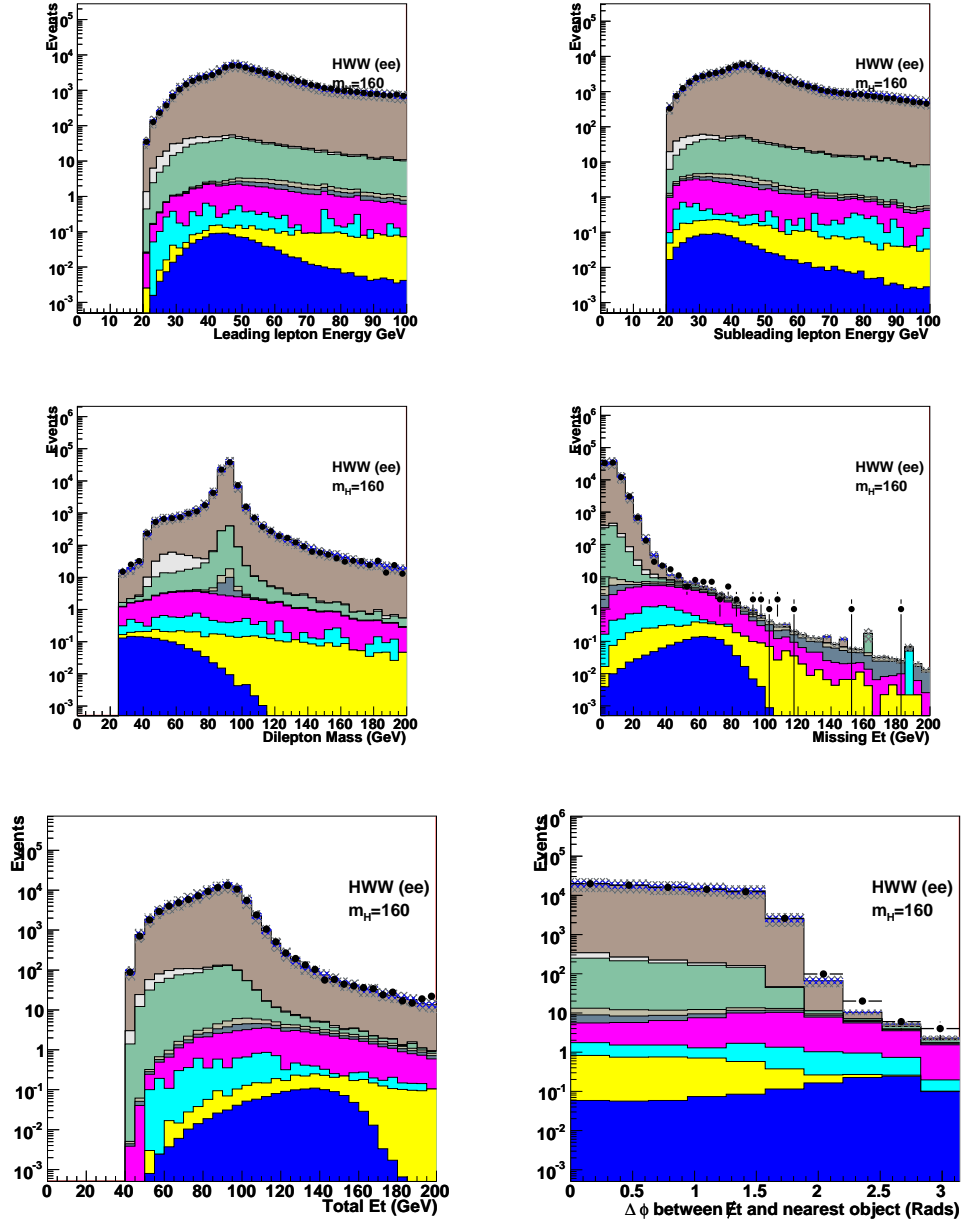


Figure B.1: Plots of input variables used in the multivariate analysis including only the ee dileptons. Please refer to section 2.7 for a legend.

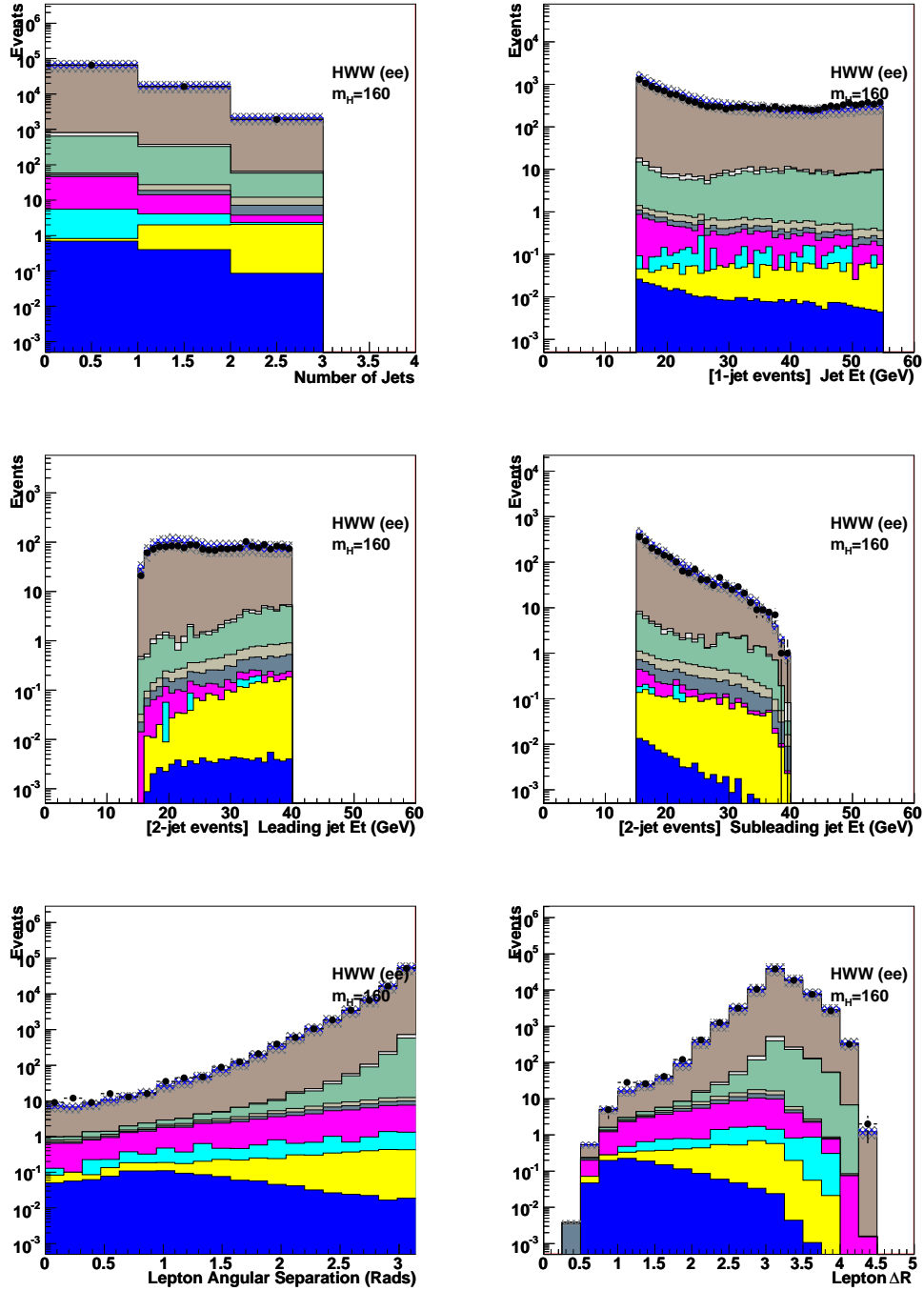


Figure B.2: Plots of input variables used in the multivariate analysis including only the ee dileptons. Please refer to section 2.7 for a legend.

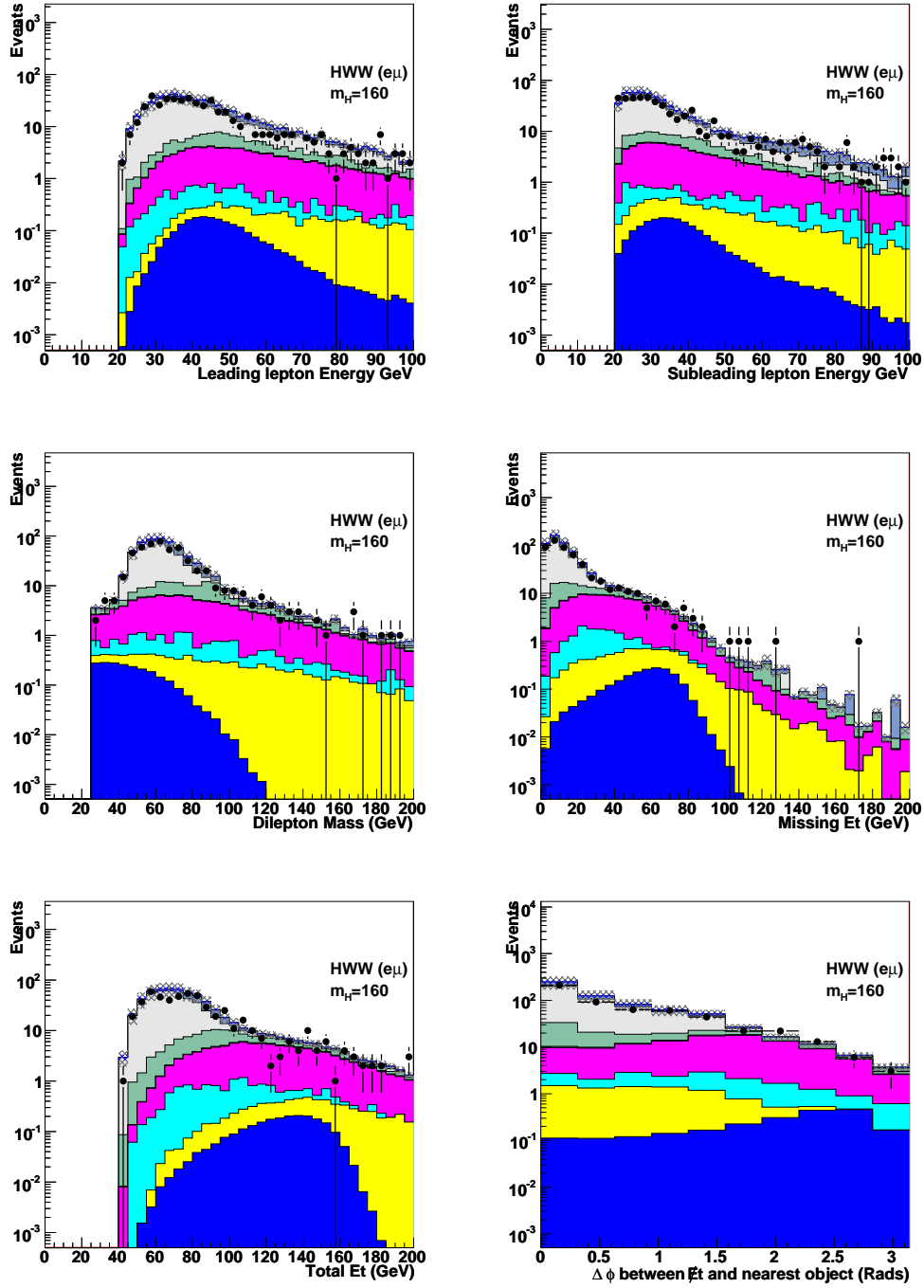


Figure B.3: Plots of input variables used in the multivariate analysis including only the $e\mu$ dileptons. Please refer to section 2.7 for a legend.

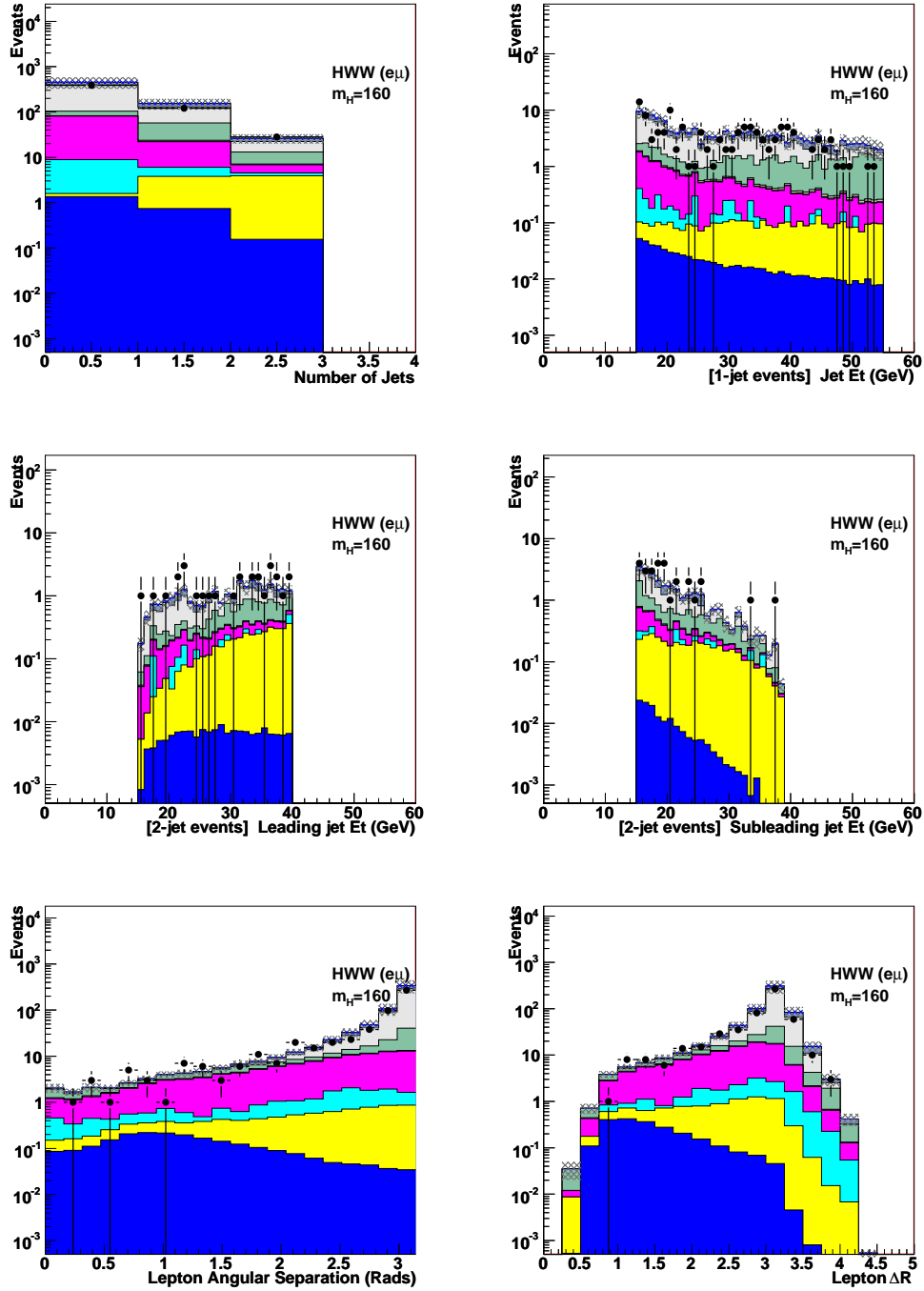


Figure B.4: Plots of input variables used in the multivariate analysis including only the $e\mu$ dileptons. Please refer to section 2.7 for a legend.

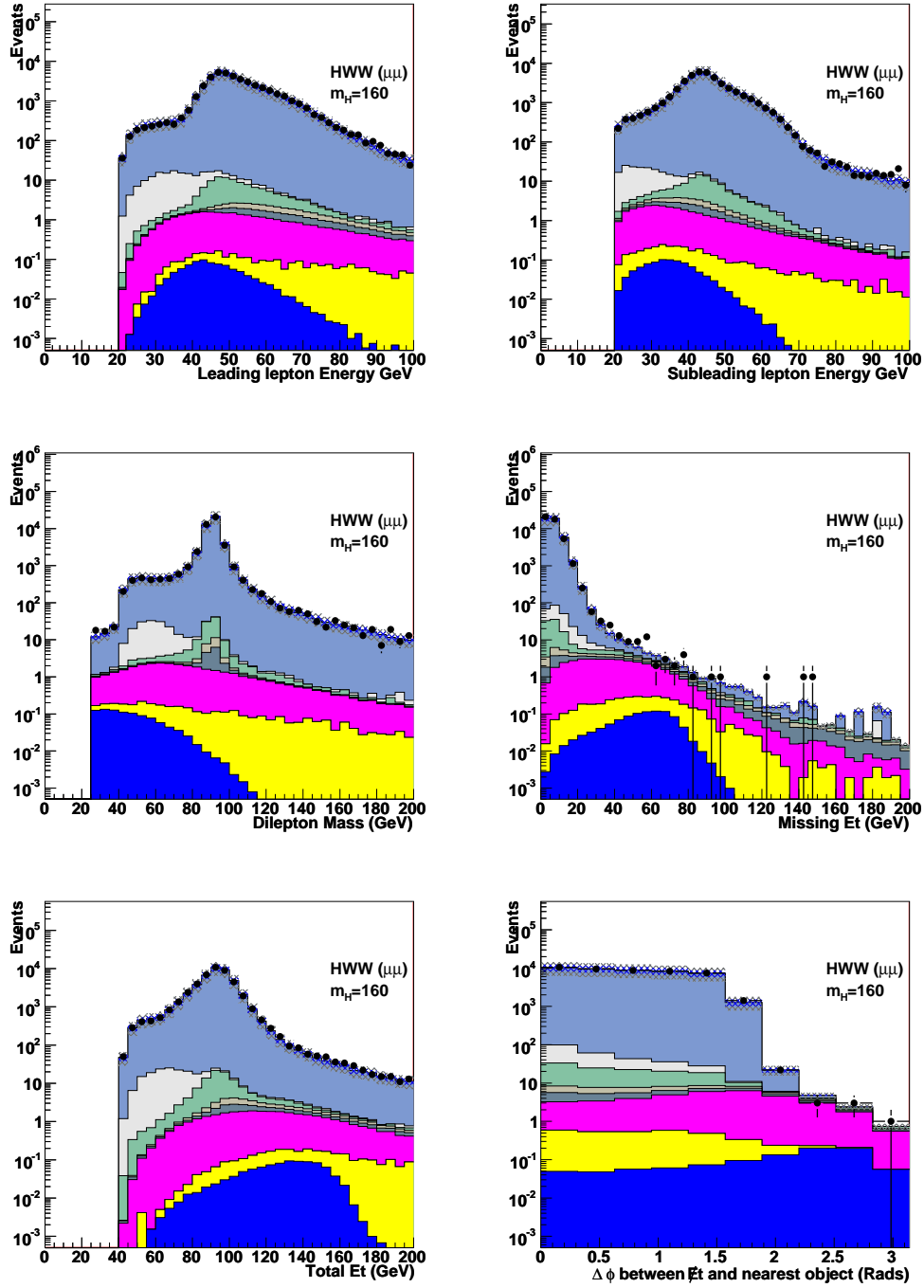


Figure B.5: Plots of input variables used in the multivariate analysis including only the $\mu\mu$ dileptons. Please refer to section 2.7 for a legend.

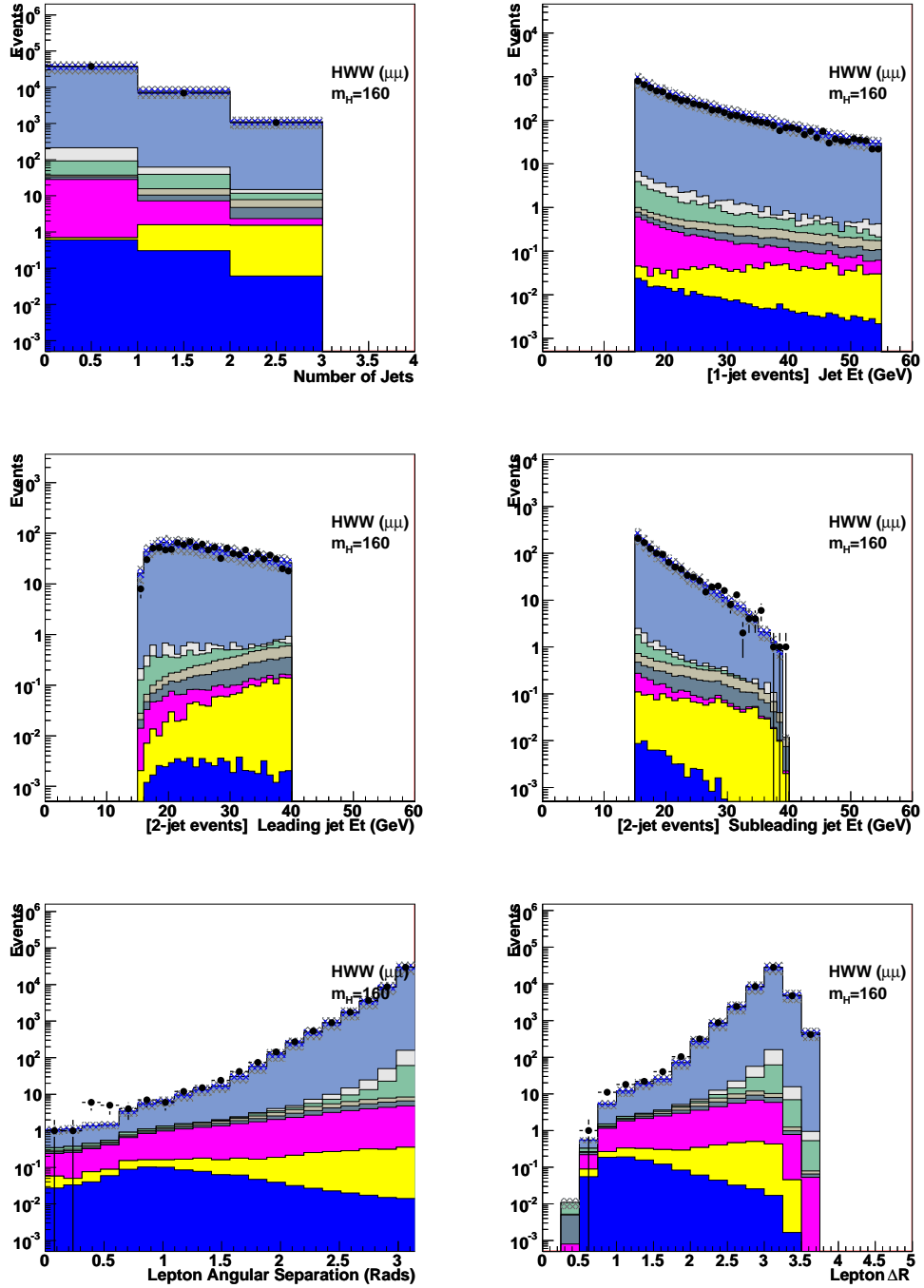


Figure B.6: Plots of input variables used in the multivariate analysis including only the $\mu\mu$ dileptons. Please refer to section 2.7 for a legend.

Appendix C

Detailed Input plots after the Drell Yan cut

This Appendix contains plots of the input variables once the Drell Yan neural net has been cut upon separated into ee , $e\mu$ and $\mu\mu$. The Higgs signal from the $M_H=160$ GeV mass point is included in the plots.

APPENDIX C. DETAILED INPUT PLOTS AFTER THE DRELL YAN CUT182

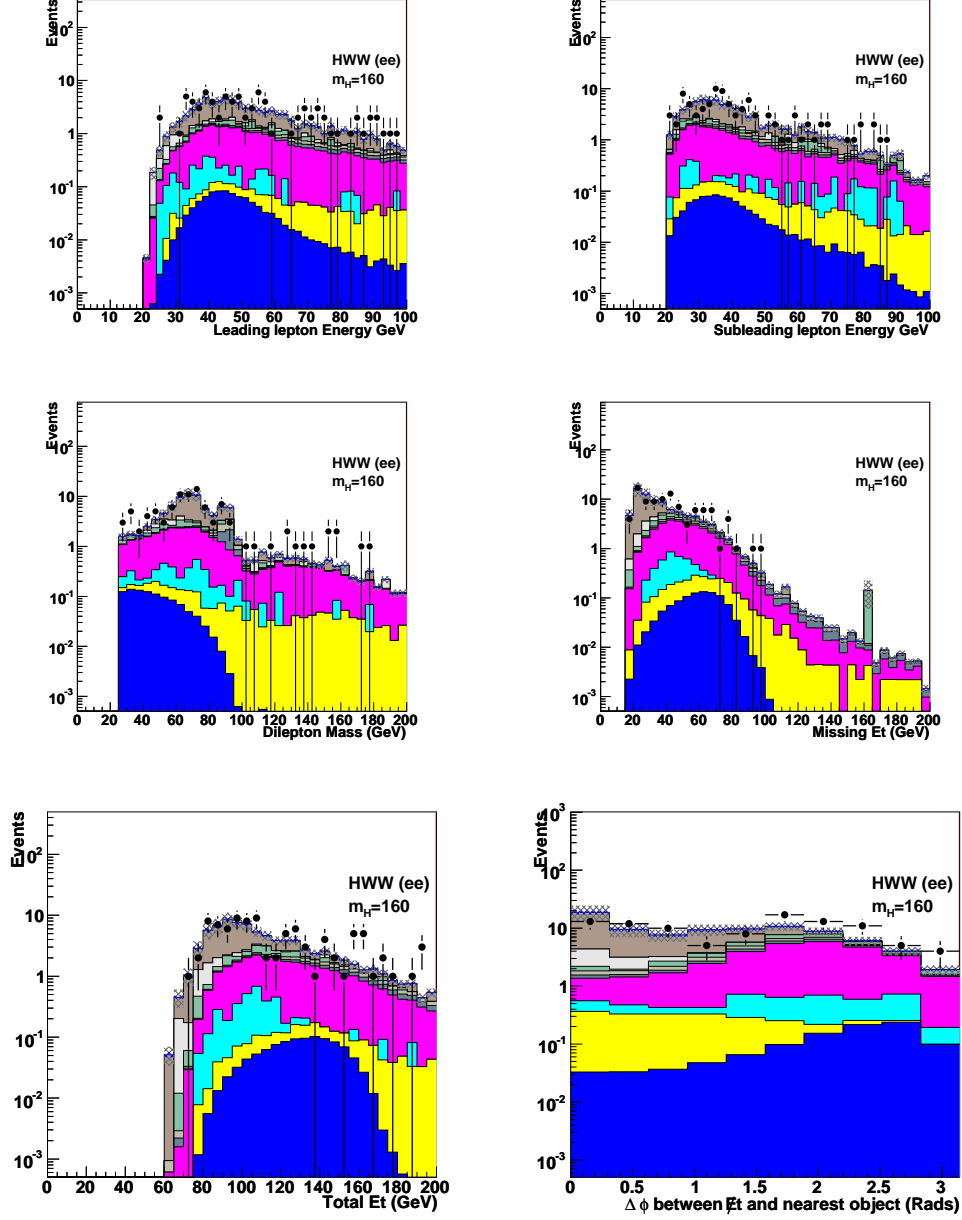


Figure C.1: Plots of input variables used in the multivariate analysis after the cut on the Drell Yan neural net including only the ee dileptons assuming $M_H^{\text{SM}} = 160$ GeV. Please refer to section 2.7 for a legend.

APPENDIX C. DETAILED INPUT PLOTS AFTER THE DRELL YAN CUT183

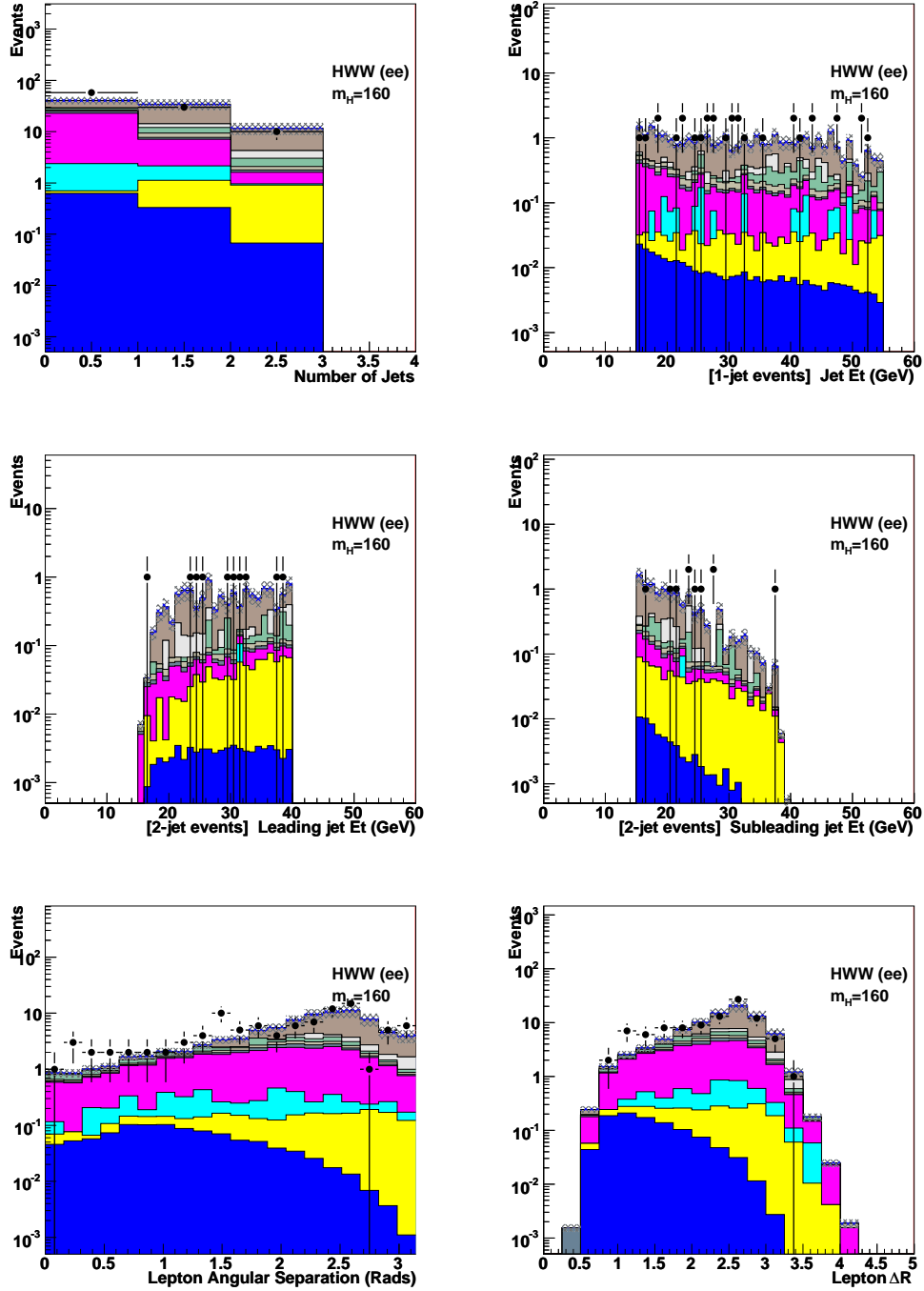


Figure C.2: Plots of input variables used in the multivariate analysis after the cut on the Drell Yan neural net including only the ee dileptons assuming $M_H^{\text{SM}} = 160$ GeV. Please refer to section 2.7 for a legend.

APPENDIX C. DETAILED INPUT PLOTS AFTER THE DRELL YAN CUT¹⁸⁴

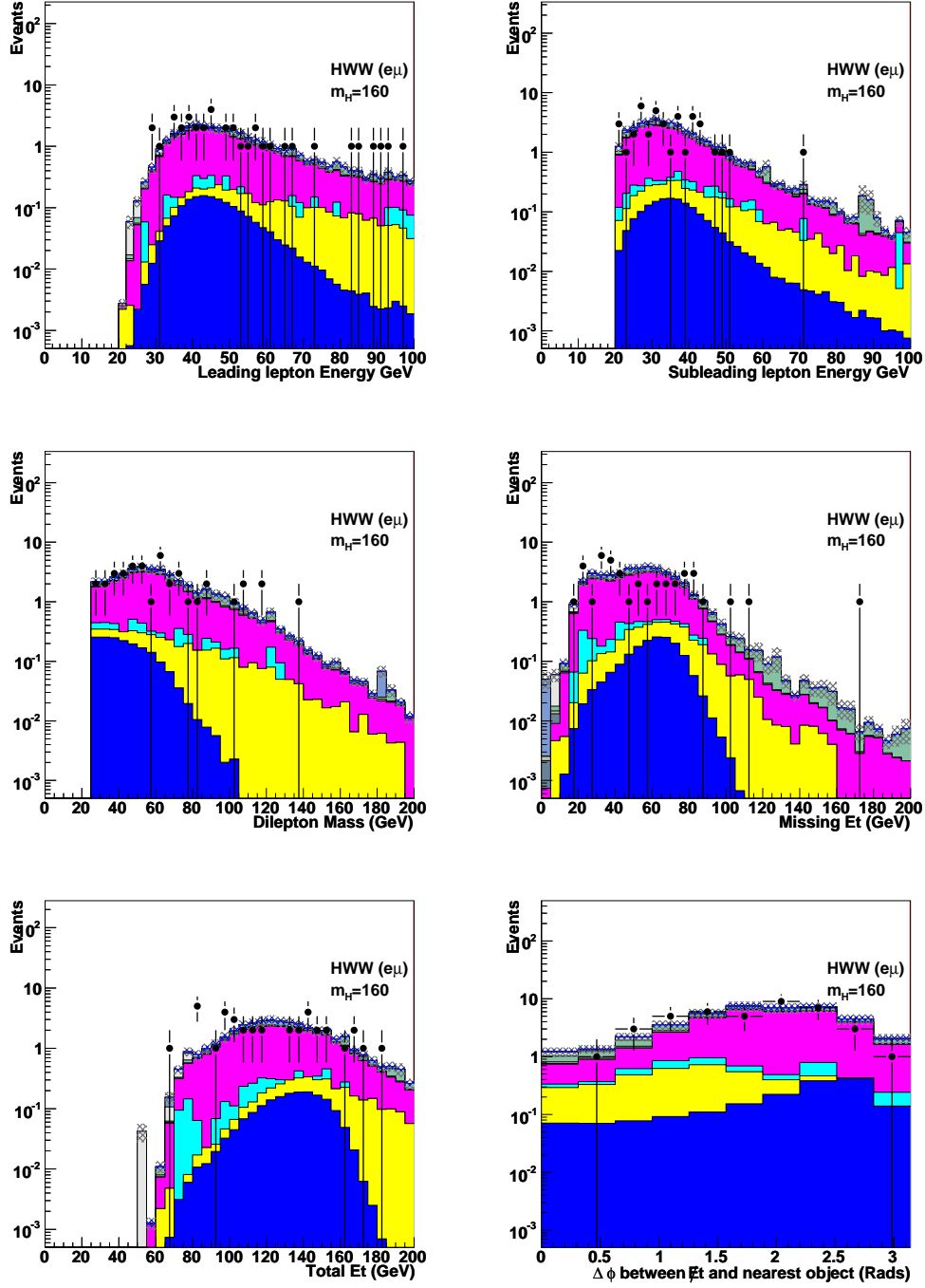


Figure C.3: Plots of input variables used in the multivariate analysis after the cut on the Drell Yan neural net including only the $e\mu$ dileptons assuming $M_H^{\text{SM}} = 160$ GeV. Please refer to section 2.7 for a legend.

APPENDIX C. DETAILED INPUT PLOTS AFTER THE DRELL YAN CUT¹⁸⁵

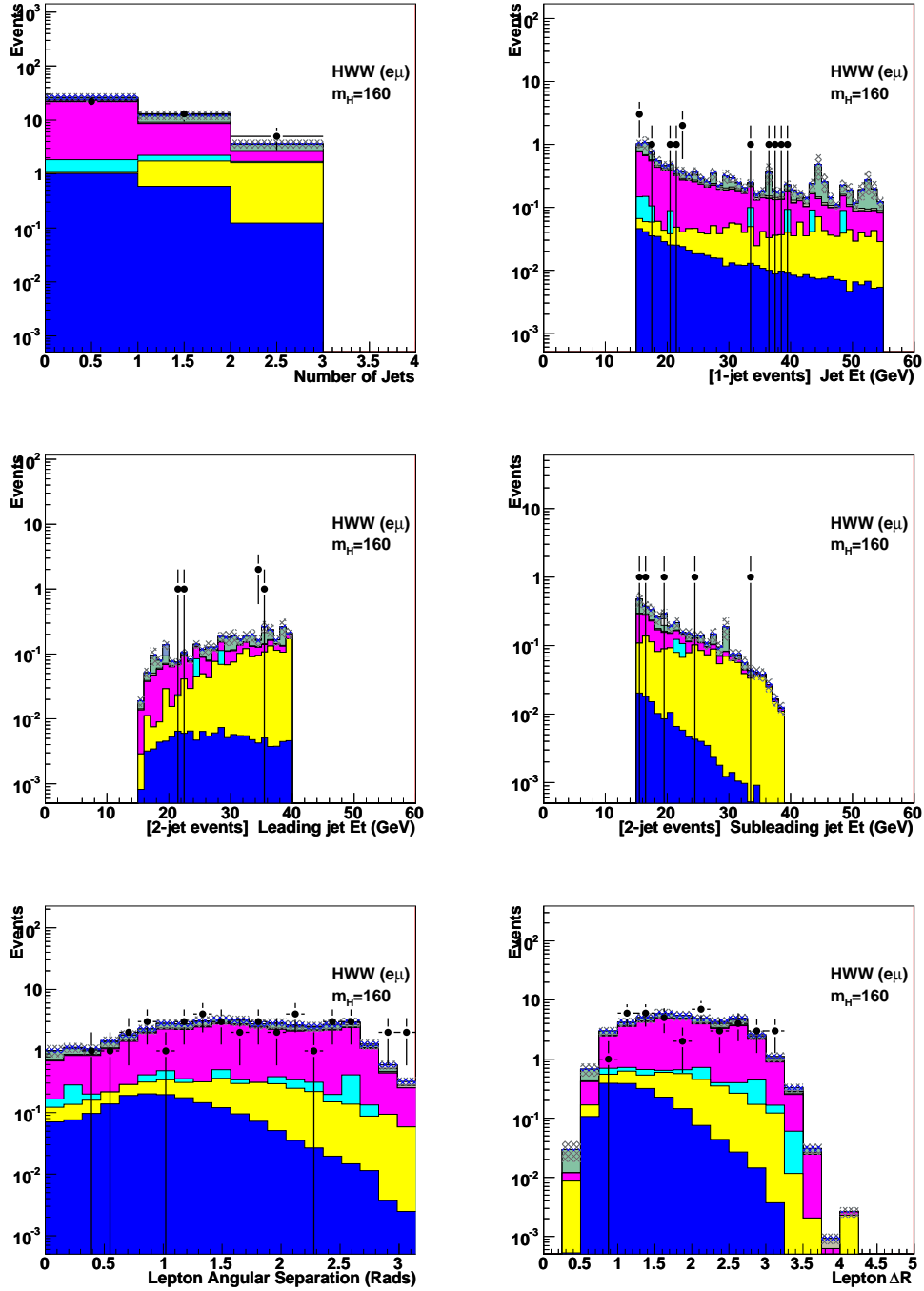


Figure C.4: Plots of input variables used in the multivariate analysis after the cut on the Drell Yan neural net including only the $e\mu$ dileptons assuming $M_H^{\text{SM}} = 160$ GeV. Please refer to section 2.7 for a legend.

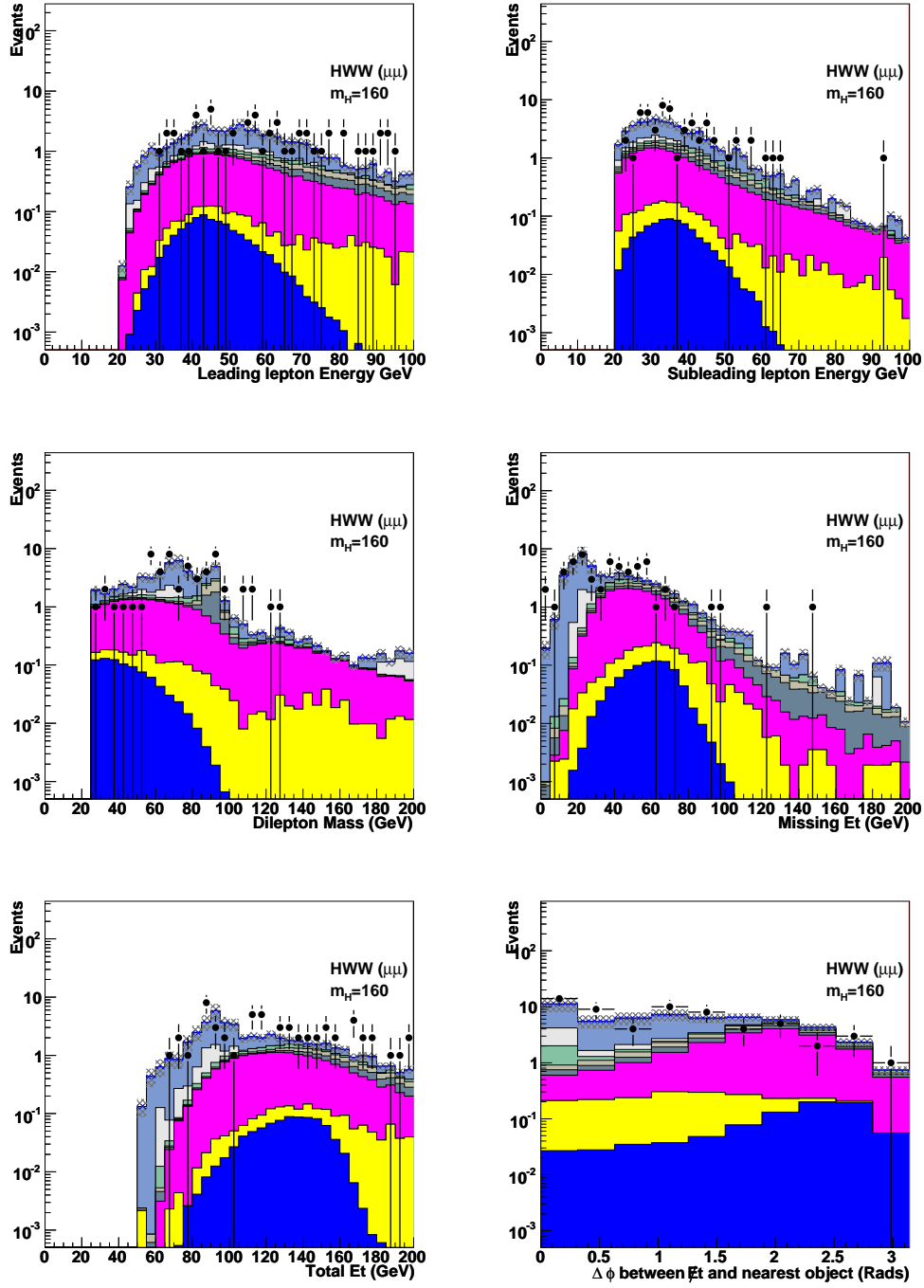


Figure C.5: Plots of input variables used in the multivariate analysis after the cut on the Drell Yan neural net including only the $\mu\mu$ dileptons assuming $M_H^{\text{SM}} = 160$ GeV. Please refer to section 2.7 for a legend.

APPENDIX C. DETAILED INPUT PLOTS AFTER THE DRELL YAN CUT¹⁸⁷

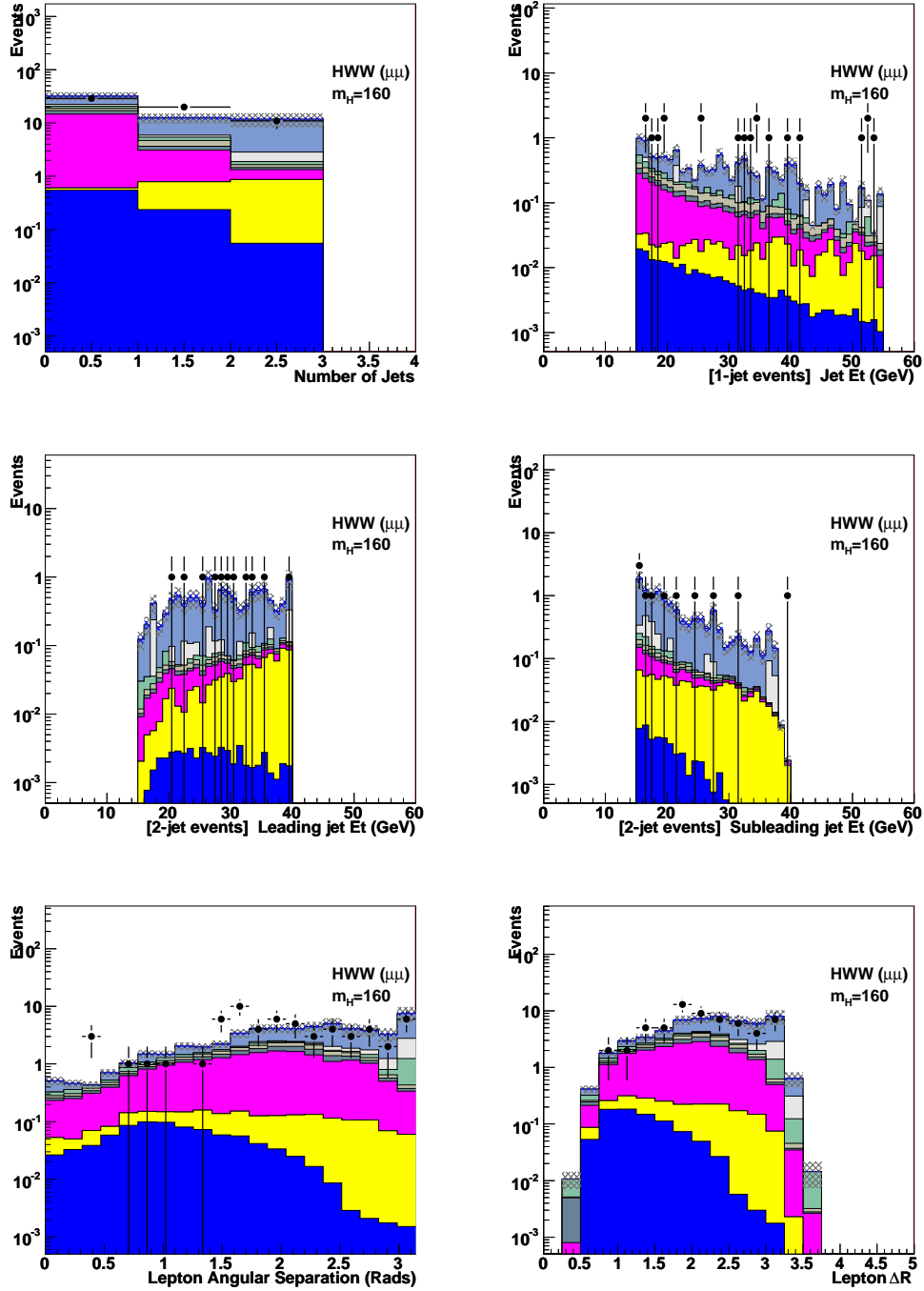


Figure C.6: Plots of input variables used in the multivariate analysis after the cut on the Drell Yan neural net including only the $\mu\mu$ dileptons assuming $M_H^{\text{SM}} = 160$ GeV. Please refer to section 2.7 for a legend.

Appendix D

Neural net training outputs

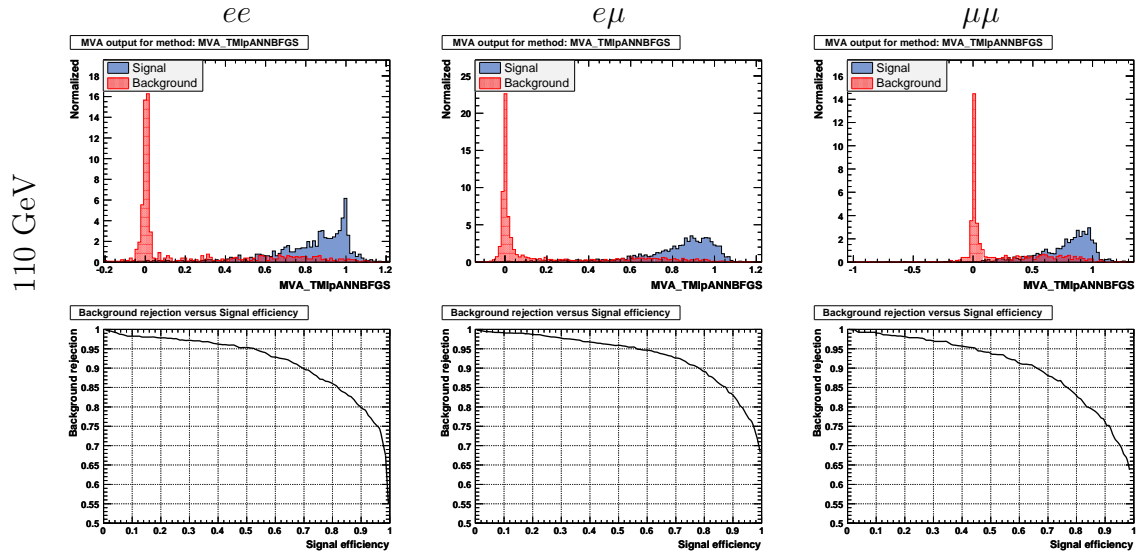


Figure D.1: W^+W^- -neural net training plots at $M_H = 110$ GeV. The top plots are separation output from the neural net training, and the bottom plots are the corresponding signal efficiency vs. background rejection plots.

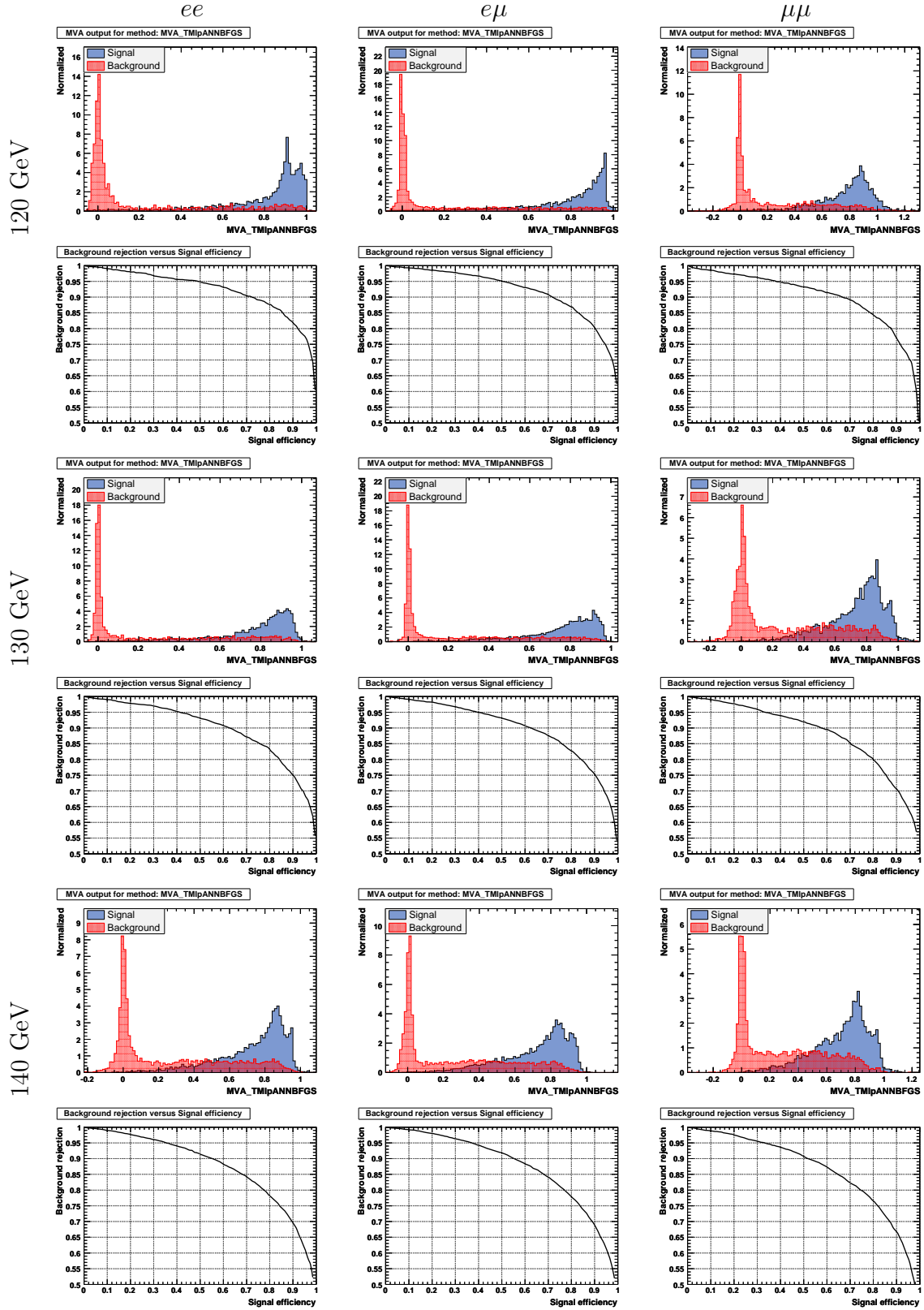


Figure D.2: W^+W^- neural net training plots at $M_H = 120, 130,$ and 140 GeV. The top plots are separation output from the neural net training, and the bottom plots are the corresponding signal efficiency vs. background rejection plots.

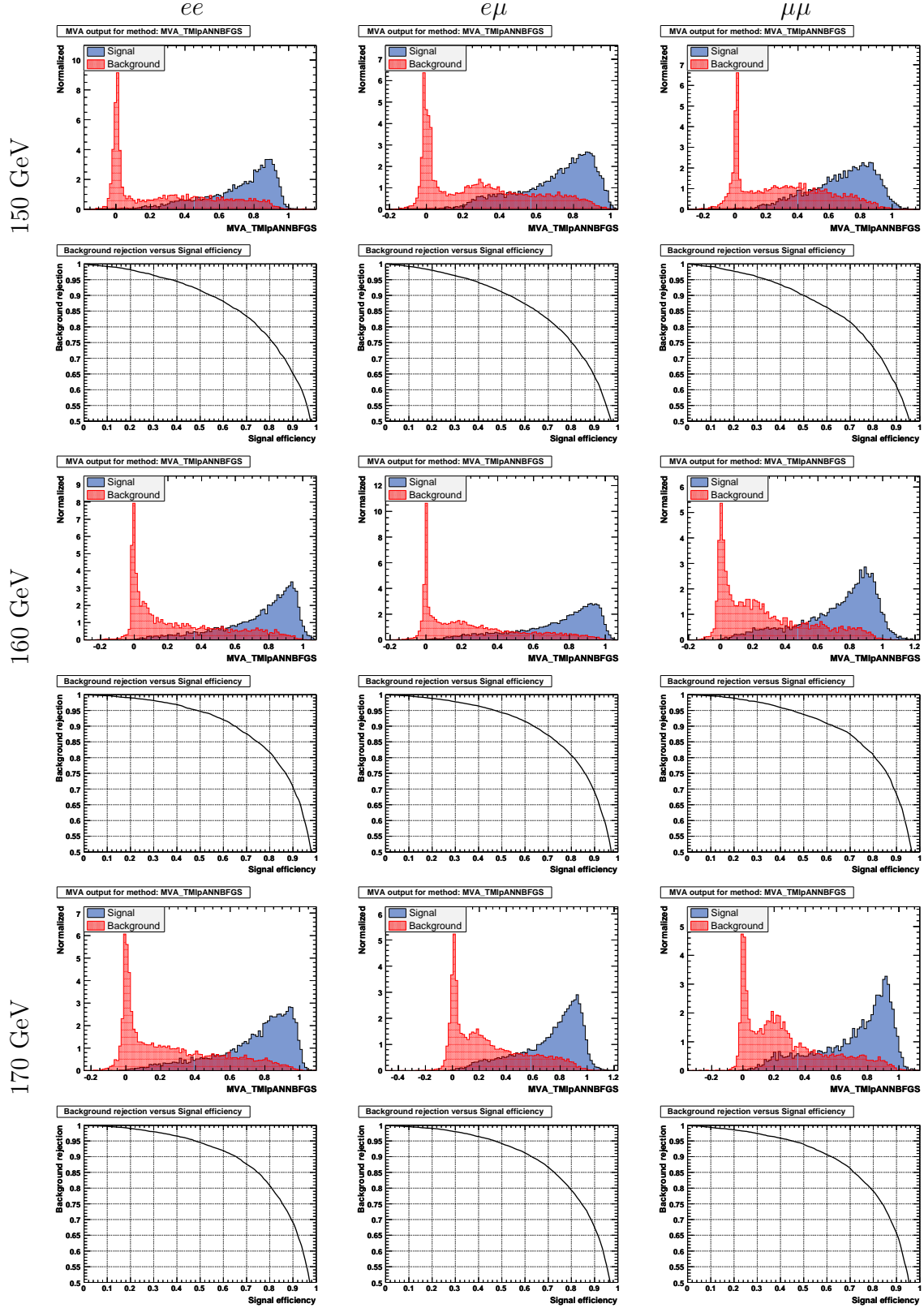


Figure D.3: W^+W^- neural net training plots at $M_H = 150, 160,$ and 170 GeV. The top plots are separation output from the neural net training, and the bottom plots are the corresponding signal efficiency vs. background rejection plots.

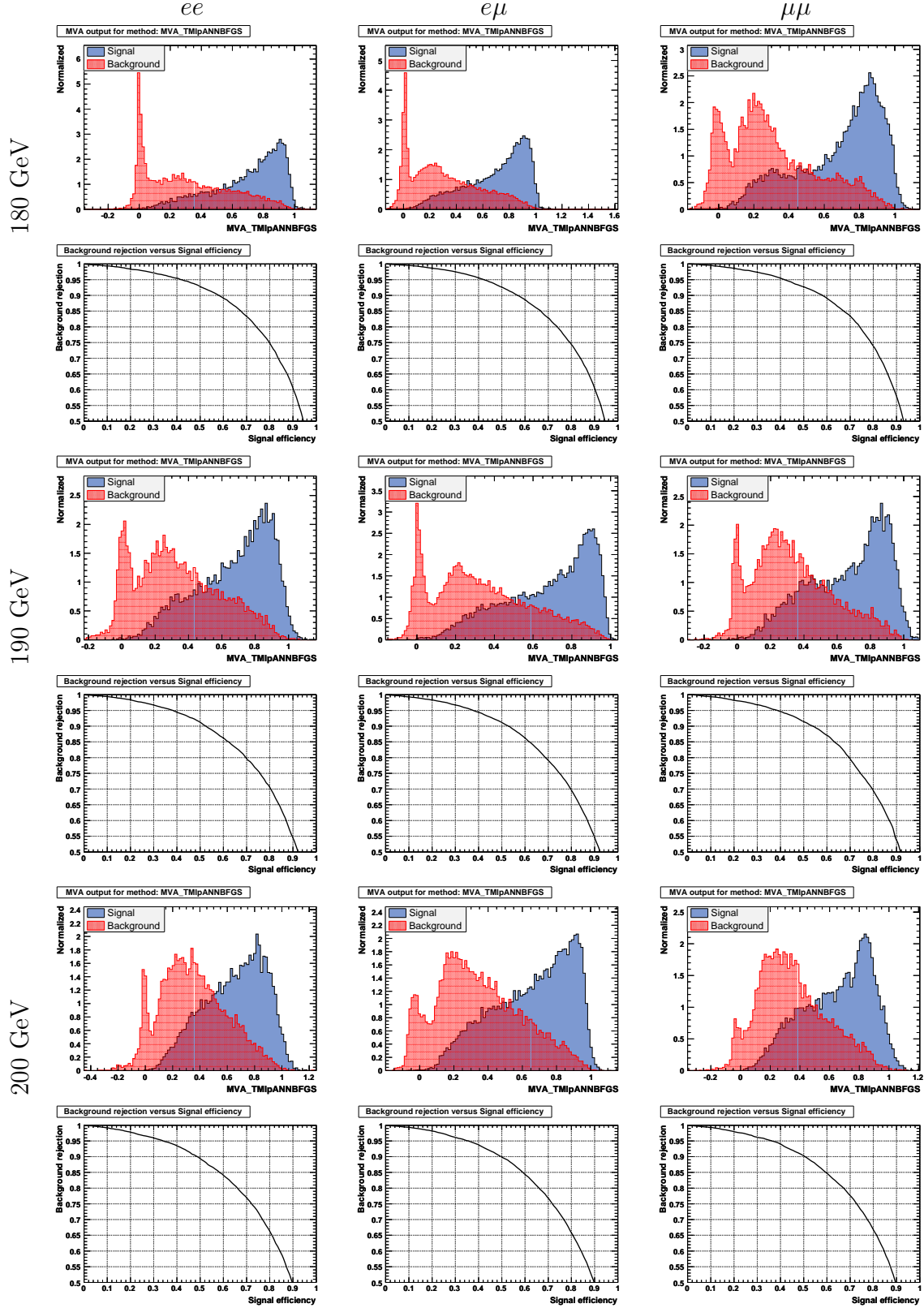


Figure D.4: W^+W^- neural net training plots at $M_H = 180, 190,$ and 200 GeV. The top plots are separation output from the neural net training, and the bottom plots are the corresponding signal efficiency vs. background rejection plots.

Appendix E

Likelihood Input Plots (linear)

This appendix contains the W^+W^- -neural net plots after the Drell Yan neural net has been cut upon for all masses split into ee , $e\mu$, and $\mu\mu$. These are the input plots to the likelihood limit calculator. The plots are shown with a linear y-axis.

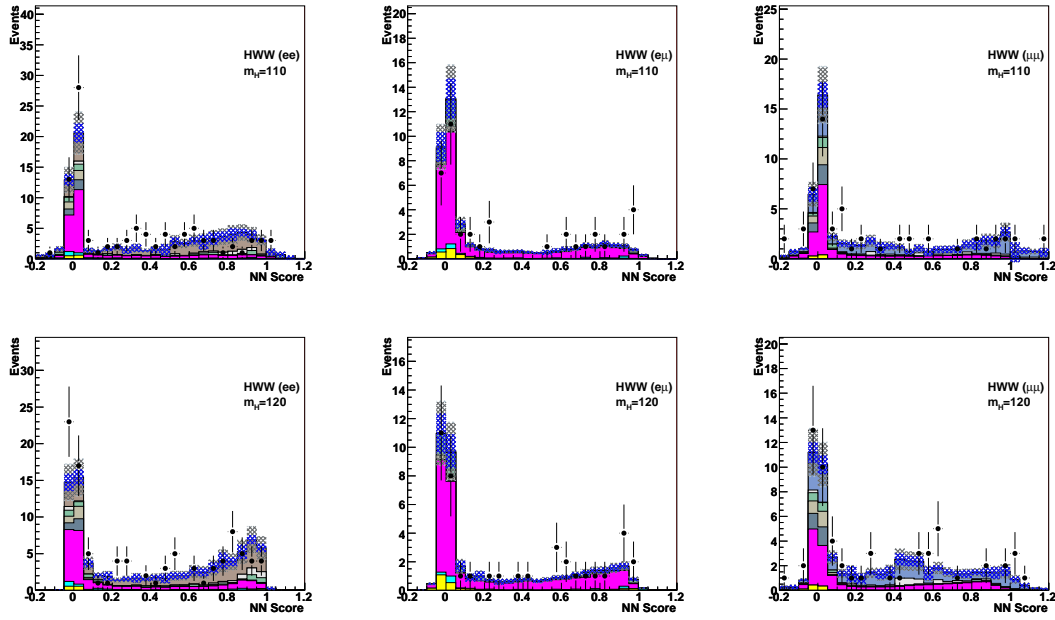


Figure E.1: Plots of the W^+W^- -trained neural net scores after the Drell Yan trained neural net has been cut upon. These final plots on which a likelihood test is performed. Please refer to section 2.7 for a legend.

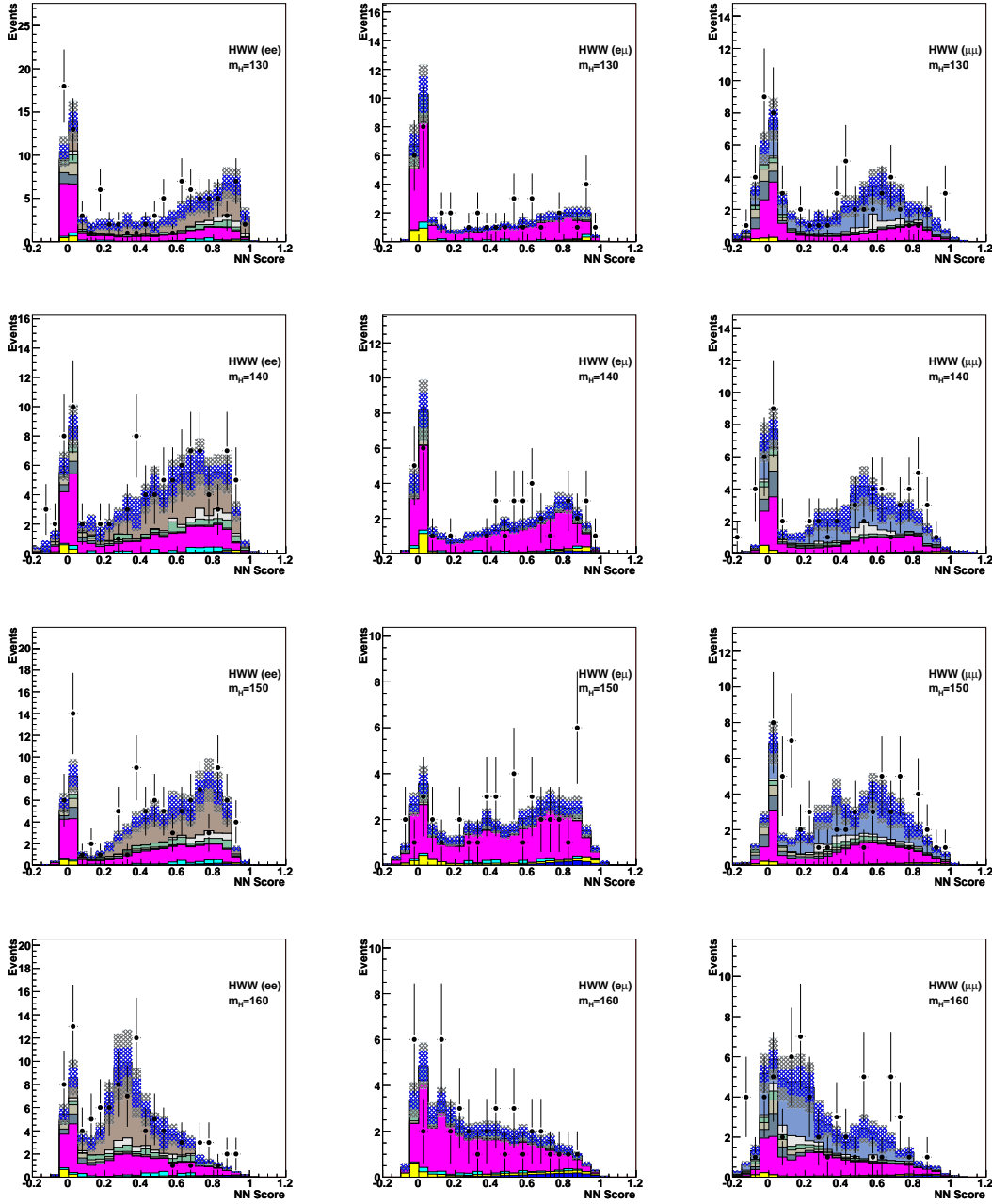


Figure E.2: Plots of the W^+W^- -trained neural net scores after the Drell Yan trained neural net has been cut upon. These final plots on which a likelihood test is performed. Please refer to section 2.7 for a legend.

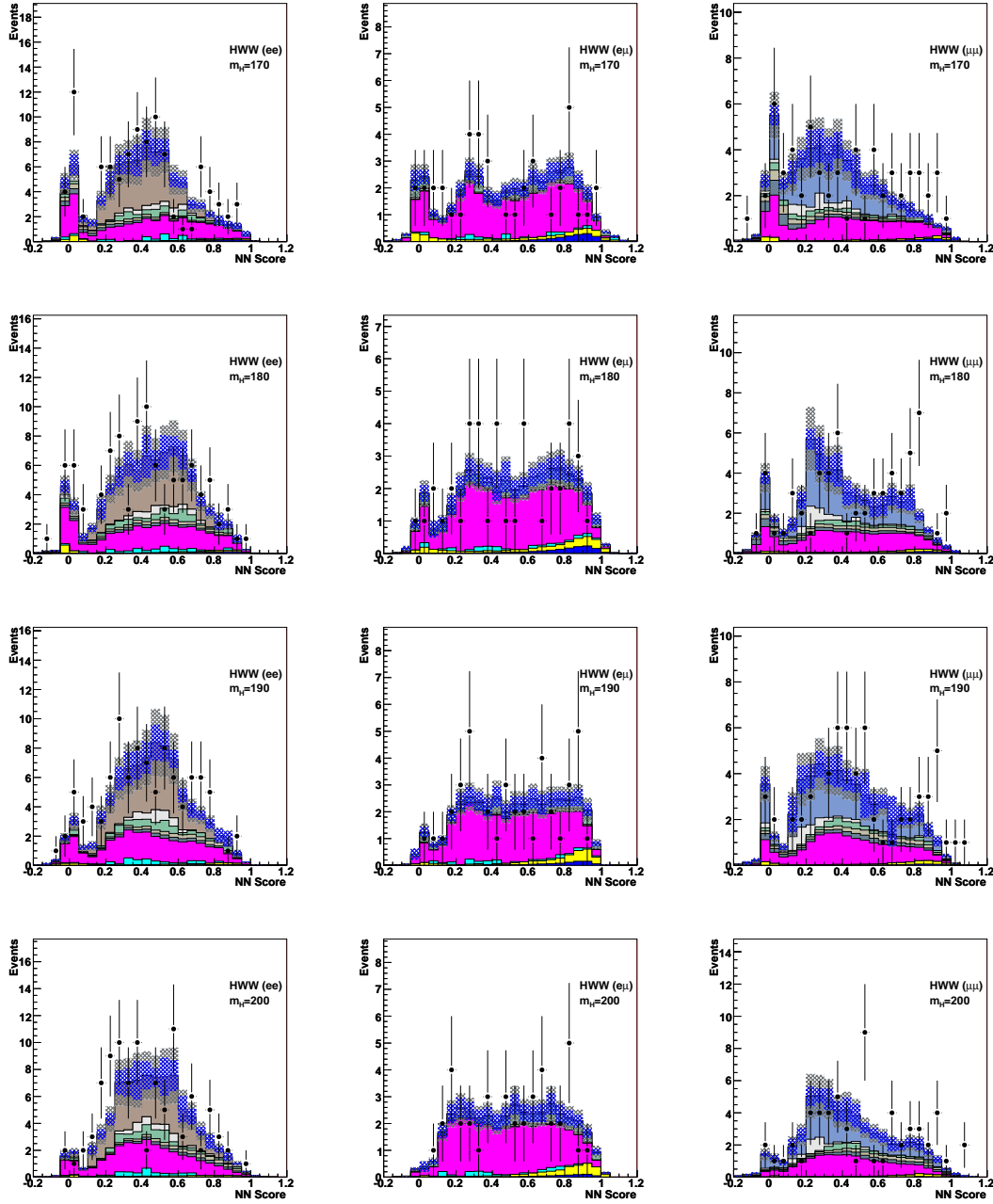


Figure E.3: Plots of the W^+W^- -trained neural net scores after the Drell Yan trained neural net has been cut upon. These final plots on which a likelihood test is performed. Please refer to section 2.7 for a legend.

Appendix F

Likelihood Input Plots (log)

This appendix contains the W^+W^- -neural net plots after the Drell Yan neural net has been cut upon for all masses split into ee , $e\mu$, and $\mu\mu$. These are the input plots to the likelihood limit calculator. The plots are shown with a logarithmic y-axis.

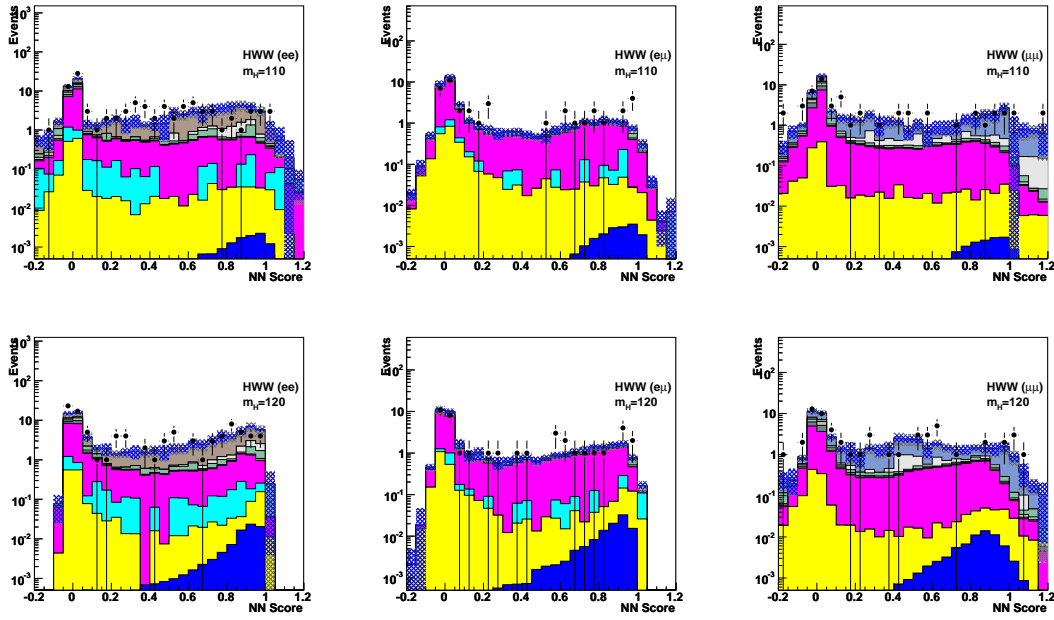


Figure F.1: Plots of the W^+W^- -trained neural net scores after the Drell Yan trained neural net has been cut upon. These final plots on which a likelihood test is performed. Please refer to section 2.7 for a legend.

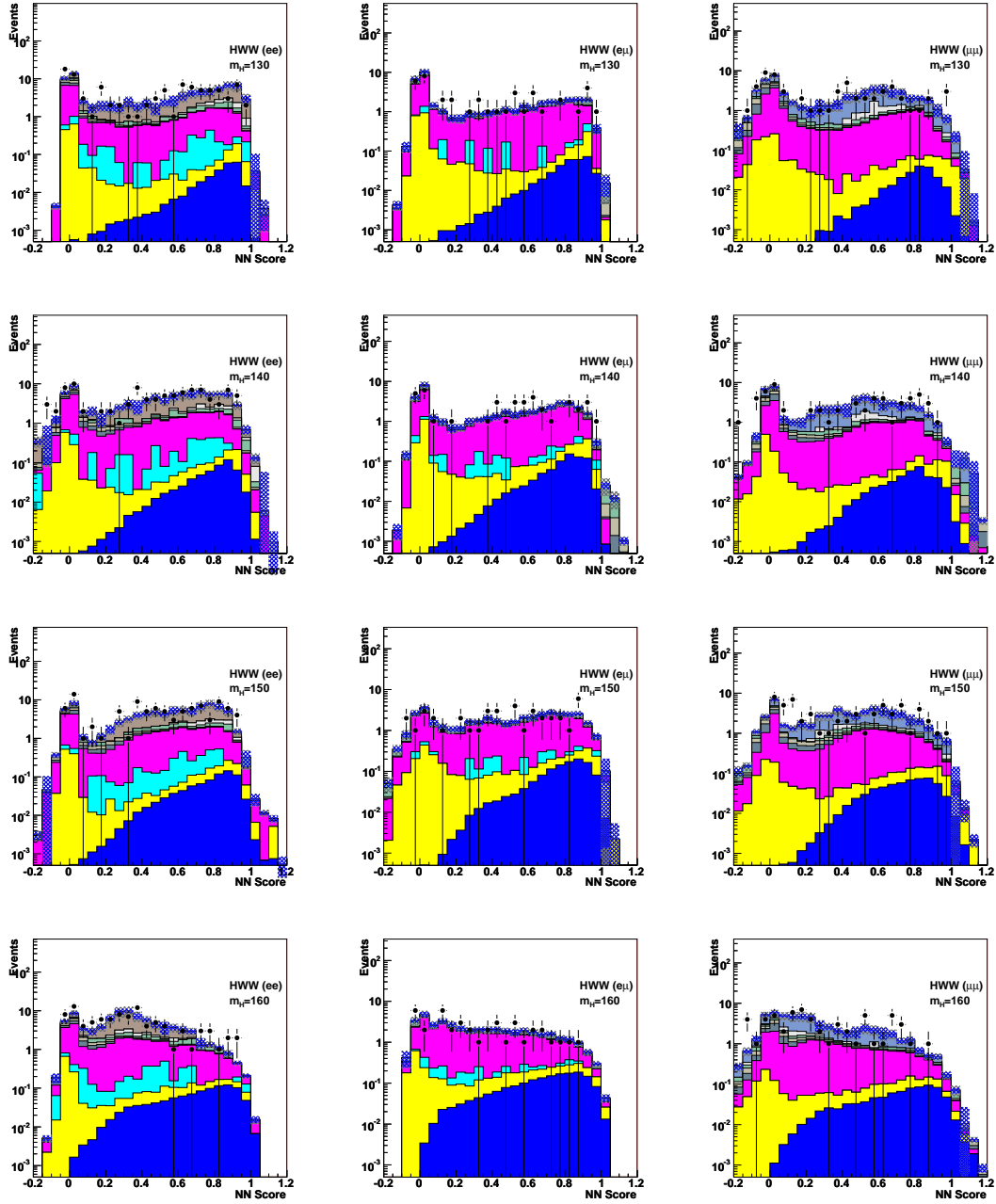


Figure F.2: Plots of the W^+W^- -trained neural net scores after the Drell Yan trained neural net has been cut upon. These final plots on which a likelihood test is performed. Please refer to section 2.7 for a legend.

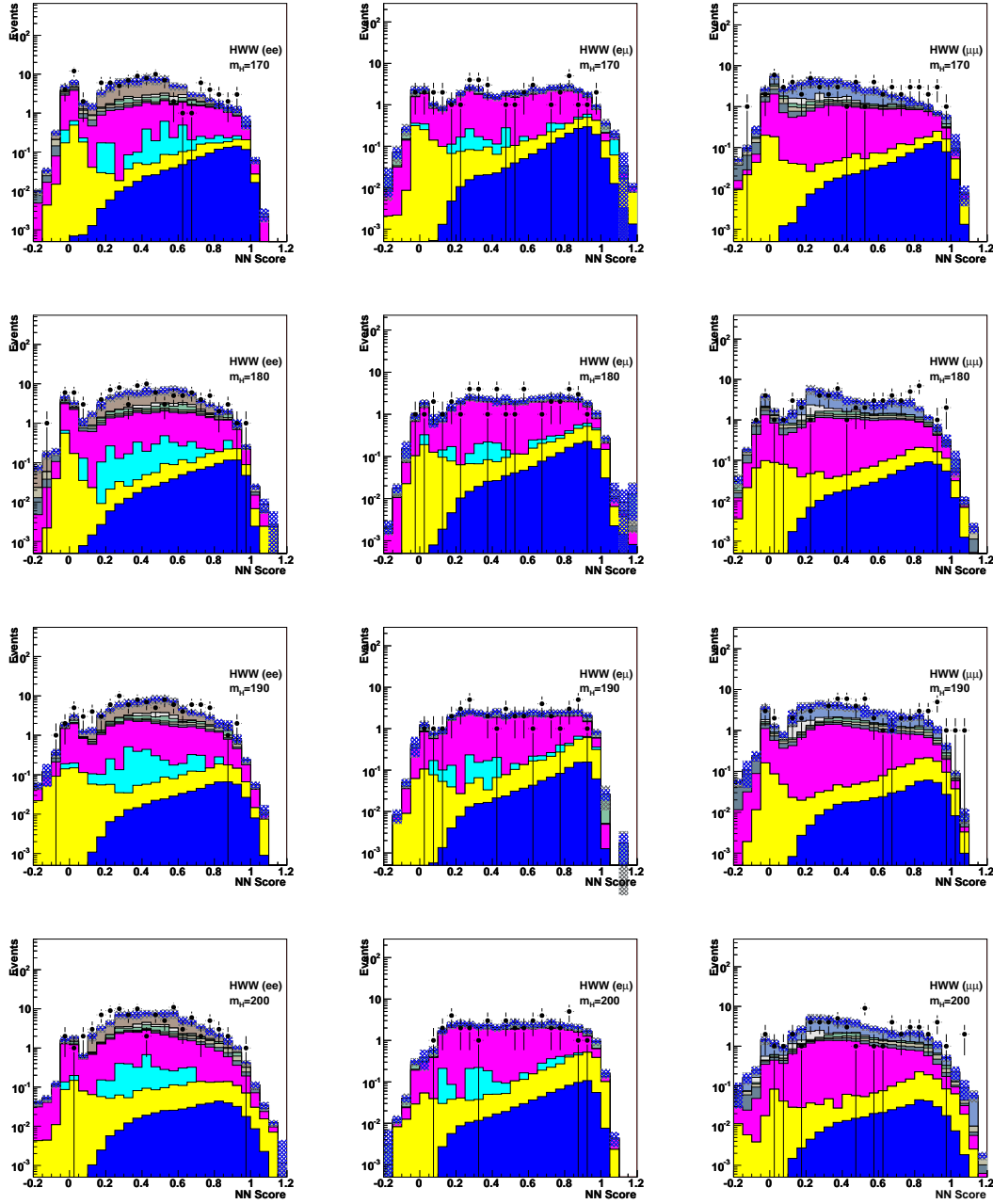


Figure F.3: Plots of the W^+W^- -trained neural net scores after the Drell Yan trained neural net has been cut upon. These final plots on which a likelihood test is performed. Please refer to section 2.7 for a legend.